

Ministry of Education and Science of the Russian Federation
Saint Petersburg National Research University of Information
Technologies, Mechanics, and Optics

NANOSYSTEMS:

PHYSICS, CHEMISTRY, MATHEMATICS

2014, volume 5(1)

Special Issue

*Proceedings of the 11th Biennial International
Conference “Advanced Carbon Nanostructures”*

Наносистемы: физика, химия, математика

2014, том 5, № 1



NANOSYSTEMS:

PHYSICS, CHEMISTRY, MATHEMATICS

ADVISORY BOARD MEMBERS

Chairman: V.N. Vasiliev (*St. Petersburg, Russia*),
V.M. Ievlev (*Voronezh*), P.S. Kop'ev (*St. Petersburg, Russia*),
V.N. Parmon (*Novosibirsk*), A.I. Rusanov (*St. Petersburg, Russia*).

EDITORIAL BOARD

Editor-in-Chief: N.F. Morozov (*St. Petersburg, Russia*)
Deputy Editor-in-Chief: I.Yu. Popov (*St. Petersburg, Russia*)

Section Co-Editors:

Physics – V.M. Uzdin (*St. Petersburg, Russia*),
Chemistry, material science – V.V. Gusarov (*St. Petersburg, Russia*),
Mechanics – A.K. Belyaev (*St. Petersburg, Russia*),
Mathematics – I.Yu. Popov (*St. Petersburg, Russia*).

Editorial Board Members:

V.M. Adamyan (*Odessa, Ukraine*); O.V. Al'myasheva (*St. Petersburg, Russia*); S. Bechta (*Stockholm, Sweden*); V.G. Bepalov (*St. Petersburg, Russia*); A. Chatterjee (*Hyderabad, India*); S.A. Chivilikhin (*St. Petersburg, Russia*); A.V. Chizhov (*Dubna, Russia*); P.P. Fedorov (*Moscow, Russia*); E.A. Gudilin (*Moscow, Russia*); D.A. Indeitsev (*St. Petersburg, Russia*); A.L. Ivanovskii (*Ekaterinburg, Russia*); H. Jónsson (*Reykjavik, Iceland*); A.A. Kiselev (*Madison, USA*); Yu.S. Kivshar (*Canberra, Australia*); S.A. Kozlov (*St. Petersburg, Russia*); Yu.B. Kudasov (*Sarov, Russia*); S.E. Kul'kova (*Tomsk, Russia*); P.A. Kurasov (*Stockholm, Sweden*); A.V. Lukashin (*Moscow, Russia*); V.A. Margulis (*Saransk, Russia*); I.V. Melikhov (*Moscow, Russia*); G.P. Miroshnichenko (*St. Petersburg, Russia*); H. Neidhardt (*Berlin, Germany*); K. Pankrashkin (*Orsay, France*); B.S. Pavlov (*Auckland, New Zealand*); A.V. Ragulya (*Kiev, Ukraine*); V. Rajendran (*Tamil Nadu, India*); V.P. Romanov (*St. Petersburg, Russia*); V.Ya. Rudyak (*Novosibirsk, Russia*); V.M. Talanov (*Novocherkassk, Russia*); A.Ya. Vul' (*St. Petersburg, Russia*).

Editors:

I.V. Blinova; A.I. Popov; M.A. Skryabin; A.I. Trifanov; E.S. Trifanova (*St. Petersburg, Russia*),
R. Simoneaux (*USA*).

Address: University ITMO, Kronverkskiy pr., 49, St. Petersburg 197101, Russia.

Phone: +7(812)232-67-65, **Journal site:** <http://nanojournal.ifmo.ru/>,

E-mail: popov1955@gmail.com

AIM AND SCOPE

The scope of the journal includes all areas of nano-sciences. Papers devoted to basic problems of physics, chemistry, material science and mathematics inspired by nanosystems investigations are welcomed. Both theoretical and experimental works concerning the properties and behavior of nanosystems, problems of its creation and application, mathematical methods of nanosystem studies are considered.

The journal publishes scientific reviews (up to 30 journal pages), research papers (up to 15 pages) and letters (up to 5 pages). All manuscripts are peer-reviewed. Authors are informed about the referee opinion and the Editorial decision.

Content

From the Editorial Board	5
<i>Special Issue: Proceedings of the 11th Biennial International Conference “Advanced Carbon Nanostructures” (ACNS’2013)</i>	
K. Takeuchi, T. Hayashi, Y. A. Kim, K. Fujisawa, M. Endo The state-of-the-art science and applications of carbon nanotubes	15
T. Hashimoto, S. Kamikawa, Y. Yagi, J. Haruyama, H. Yang, M. Chshiev Graphene edge spins: spintronics and magnetism in graphene nanomeshes	25
<u>FULLERENS</u>	
N.B. Tamm, S.I. Troyanov Synthesis, isolation, and X-ray structural characterization of trifluoromethylated C₉₀ fullerenes: C₉₀(30)(CF₃)₁₈ and C₉₀(35)(CF₃)₁₄	39
I.V. Mikheev, D.S. Volkov, M.A. Proskurnin, N.V. Avramenko, M.V. Korobov Preparation and characterization of a new clustered {C₇₀}_n fullerene material	46
M. Yesilbas, T. L. Makarova, I. Zakharova Fullerene films with suppressed polymerizing ability	53
A.A. Bogdanov, A.P. Voznyakovskii, A.O. Pozdnyakov UV-Vis diagnostics of the PMMA - C₆₀ composite system and the kinetics of its thermal decomposition	62
Y. Mackeyev, M. Raof, B. Cisneros, N. Koshkina, C.S. Berger, L.J. Wilson, S.A. Curley Toward paclitaxel-[60]fullerene immunoconjugates as a targeted prodrug against cancer	67
L.B. Piotrovsky, B.L. Milman, D.N. Nikolaev, N.V. Lugovkina, E.V. Litasova, M.A. Dumpis Characterization of fullerene derivatives by MALDI LIFT-TOF/TOF mass spectrometry	76
E.O. Petrenko, M.V. Makarets, V.M. Mikoushkin, V.M. Pugach Simulation of secondary electron transport in thin metal and fullerite films	81
<u>NANOTUBES</u>	
K. Schneider, B. Stamm, K. Gutöhrlein, C. Burkhardt, A. Stett, D.P. Kern CVD growth of carbon nanotubes with a Ni catalyst in a polyimide trench	86
N.N. Konobeeva, M.B. Belonenko Propagation of femtosecond pulses in carbon nanotubes	91
A.A. Kravchenko, T.A. Ermakova, O.A. Davletova, I.V. Zaporotskova, T.K. Korchagina, U.V. Popov, G.A. Kalmikova The semi-empirical research of the adsorption of biologically active molecules on the outer surface of carbon nanotubes	98
N.P. Polikarpova, I.V. Zaporotskova, D.E. Vilkeeva, D.I. Polikarpov Sensor properties of carboxyl-modified carbon nanotubes	101
S. Boroznin, E. Boroznina, I.V. Zaporotskova, P.A. Zaporotskov, O.A. Davletova Migration processes on the surface of carbon nanotubes with substitute boron atoms	107
<u>GRAPHENE</u>	
V.V. Afrosimov, A.T. Dideykin, V.I. Sakharov, I.T. Serenkov, S.P. Vul Utilizing of the medium-energy ion scattering spectrometry for the composition investigation of graphene oxide films on silicon surface	113

O.V. Kononenko, V.N. Matveev, D.P. Field, D.V. Matveev, S.I. Bozhko, D.V. Roshchupkin, E.E. Vdovin, A.N. Baranov	
Investigation of structure and transport properties of graphene grown by low-pressure no flow CVD on polycrystalline Ni films	117
V.A. Ponomarchuk, A.T. Titov, T.N. Moroz, A.N. Pyryaev, A.V. Ponomarchuk	
Hierarchically porous graphene in natural graphitic globules from silicate magmatic rocks	123
D.M. Sedlovets, A.N. Redkin	
The influence of the ambient conditions on the electrical resistance of graphene-like films	130
E.F. Sheka, V.A. Popova, N.A. Popova	
Topological mechanochemistry of graphene	134
S.V. Koniakhin, E.D. Eidelman	
The electron-phonon matrix element in the Dirac point of graphene	142
N.A. Lvova, O.Yu. Ananina	
The adsorption properties of polycrystalline graphene: quantum-chemical simulation	148
A.V. Pak, M.B. Belonenko	
The evolution of few cycles optical pulses in a double-layer graphene – boron nitride taking into account nonlinearity of a medium	155
<u>NANODIAMONDS</u>	
M. Ivanov, Z.Mahbooba, D. Ivanov, S.Smirnov, S.Pavlyshko, E.Osawa, D.Brenner, O.Shenderova	
Nanodiamond-based oil lubricants on steel-steel and stainless steel – hard alloy high load contact: investigation of friction surfaces	160
<u>OTHERS</u>	
V.A. Davydov, A.V. Rakhmanina, V.N. Agafonov, V.N. Khabashesku	
Synergistic influence of fluorine and hydrogen on processes of thermal transformations of carbon-containing systems under high pressures	167
K.V. Mironovich, V.A. Krivchenko, P.V. Voronin, S.A. Evlashin	
Secondary nucleation on nanostructured carbon films in the plasma of direct current glow discharge	172
V.S. Protopopova, M.V. Mishin, A.V. Arkhipov, S.I. Krel, P.G. Gabdullin	
Field electron emission from a nickel-carbon nanocomposite	178
S.S. Bukalov, Ya.V. Zubavichus, L.A. Leites, A.I. Sorokin, A.S. Kotosonov	
Structural changes in industrial glassy carbon as a function of heat treatment temperature according to Raman spectroscopy and X-ray diffraction data	186
S.V. Kozyrev, V.I. Ivanov-Omskii, S.G. Yastrebov, T.K. Zvonareva, M.S. Chekulaev, A.V. Siklitskaya	
Carbon encapsulation of magnetic metal nanoparticles: correlation between nanoscale structure of carbon matrix and electromagnetic properties	192
S.A. Burikov, S.A. Dolenko, K.A. Laptinskiy, I.V. Plastinin, A.M. Vervalde, I.I. Vlasov, T.A. Dolenko	
Using artificial neural networks for elaboration of fluorescence biosensors on the basis of nanoparticles	195

FROM THE EDITORIAL BOARD

*Special Issue: Proceedings of the 11th Biennial International Conference
“Advanced Carbon Nanostructures” (ACNS’2013)*

Organizers

- Ioffe Physical-Technical Institute, St.Petersburg, Russia
- St. Petersburg Nuclear Physics Institute, Russia
- National Research Center "Kurchatov Institute", Moscow, Russia
- St. Petersburg State Institute of Technology (Technical University),
Russia

Official Partners

- Russian Foundation for Basic Research
- Department of General Physics and Astronomy of the Russian
Academy of Sciences
- Fund for Infrastructure and Educational Programs
- Government of Saint Petersburg

International Advisory Committee

F. Banhart	Strasbourg University, France
J. Davidson	Vanderbilt University, USA
M. Dresselhaus	Massachusetts Institute of Technology, USA
L. Echegoyen	University of Texas At El Paso, USA
T. Enoki	Tokyo Institute of Technology, Japan
D. Gruen	Argonne National Laboratory, USA
D. Guldi	University of Erlangen-Nurnberg, Germany
R. Kalish	Israel Institute of Technology, Technion, Israel
W. Kraetschmer	Max-Planck Institute, Germany
H. Kroto	Florida State University, USA
E. Osawa	Nanocarbon Research Institute Ltd., Japan
H. Shinohara	Nagoya University, Japan
F. Wudl	University of California, USA

Organizing Committee

A.Ya. Vul' (Conference Chair)	Ioffe Institute, St. Petersburg, Russia
S.V. Kidalov (Chair)	Ioffe Institute, St. Petersburg, Russia
B.B. Chaivanov	National Research Center "Kurchatov Institute", Russia
V.F. Ezhov	St Petersburg Nuclear Physics Institute, Russia

A.V. Kirillin	Russian Foundation for Basic Research, Russia
P.S. Kop'ev	Ioffe Institute, St. Petersburg, Russia
V.V. Kveder	Institute of Solid State Physics, Chernogolovka, Russia
N.V. Lisitsyn	St. Petersburg State Institute of Technology, Russia
O.M. Nefedov	Branch of Chemistry and Material Sciences of the Russian Academy of Sciences, Russia
M.Yu. Romanovsky	Department of General Physics, Russian Academy of Science
S.A. Tsyganov	Russian Foundation for Basic Research, Russia
A.G. Zabrodsky	Ioffe Institute, Russia

International Program Committee

M.V. Baidakova (Co-Chair)	Ioffe Institute, St. Petersburg, Russia
A.T. Dideikin (Co-Chair)	Ioffe Institute, St. Petersburg, Russia
A.E. Aleksensky	Ioffe Institute, St. Petersburg, Russia
A.S. Artjomov	Lebedev Physical Institute, Moscow, Russia
V.Yu. Dolmatov	Federal State Unitary Enterprise "Special Design and Technological Office "Technolog", St. Petersburg, Russia
Yu.S. Grushko	St. Petersburg Nuclear Physics Institute, Russia
A.V. Eletsii	National Research Center "Kurchatov Institute", Russia
M. Korobov	Moscow State University, Russia
S.V. Kozyrev	Center for Advanced Studies of St. Petersburg State Polytechnical University, St. Petersburg, Russia
A.V. Krestinin	Institute of Problems of Chemical Physics, Russia
I.I. Kulakova	Moscow State University, Russia
V.L. Kuznetsov	Boreskov Institute of Catalysis, Novosibirsk, Russia
L.B. Piotrovsky	Institute of Experimental Medicine North-West Branch of RAMS, St. Petersburg, Russia
O.A. Shenderova	International Technology Center, USA
A.M. Shikin	St. Petersburg State University, Russia
V.I. Sokolov	Institute of Organoelement Compounds, Moscow, Russia
V.M. Titov	Institute of Hydrodynamics, Novosibirsk, Russia
A.P. Vozniakovskii	Federal State Unitary Enterprise Scientific Research Institute for Synthetic Rubber, St. Petersburg, Russia

Local Organizing Committee

I.V. Vorobyova (Chair)	Ioffe Institute, St. Petersburg, Russia
N.A. Dobriakova	JSC "Intellect" Account manager
T.P. Kazantseva	Ioffe Institute, St. Petersburg, Russia
B.M. Silin	Ioffe Institute, St. Petersburg, Russia
L.V. Sharonova	Ioffe Institute, St. Petersburg, Russia
L.A. Zaytseva	Ioffe Institute, St. Petersburg, Russia

Technical Group

D.B. Shustov	Web-site, Ioffe Institute, St. Petersburg, Russia
A.N. Trofimov	Ioffe Institute, St. Petersburg, Russia
K.N. Guliaeva	Ioffe Institute, St. Petersburg, Russia
In association with Agency for Science and Technology "Intellect"	

List of Participants ACNS'2013

- Agafonov Viatcheslav** France
Francois Rabelais University of Tours
- Ahmadishina Karina** Russia
National Research University of Electronic Technology
- Akhmetov Arslan** Russia
Institute of Petrochemistry and Catalysis RAS
- Andreev Sergey** Russia
NRC Institute of Immunology
- Antonova Irina** Russia
A.V.Rzhanov Institute of Semiconductor Physics SB RAS
- Apenova Marina** Russia
Lomonosov Moscow State University
- Aqnazarova Shafoat** Tadjikistan
Tajik National University, Research Department of Physics of the Condensed Environments of the Tajik National University
- Aramini Matteo** Italy
Department of Physics – University of Parma
- Arkhipov Alexander** Russia
St.Petersburg State Polytechnic University
- Avdeev Mikhail** Russia
Joint Institute for Nuclear Research
- Baidakova Marina** Russia
Ioffe Physical-Technical Institute
- Barnard Amanda** Australia
CSIRO Materials Science and Engineering
- Bashkatova Elena** Russia
NRC Institute of Immunology FMBA, Russia
- Biloivan Olga** Ukraine
Institute of Molecular Biology and Genetics
- Bolotin Kirill** United States
Physics Dept, Vanderbilt Univeristy
- Boroznin Sergey** Russia
Volgograd State University
- Brotsman Victor** Russia
Lomonosov Moscow State University
- Buchatskaya Yulia** Russia
Lomonosov Moscow State University
- Bukalov Sergey** Russia
Institute of Organoelement Compounds Russian Academy of Science
- Burikov Sergey** Russia
Moscow State University
- Bykov Victor** Russia
Institute of Physical Problems named F.V. Lukin
- Cavallari Chiara** France
Institut Laue Langevin
- Cherdyntseva Svetlana** Russia
Karpov Institute of Physical Chemistry
- Chernov Valerii** Russia
IAP RAS
- Chernozatonskii Leonid** Russia
Emanuel Institute of Biochemical Physics RAS
- Churilov Grigory** Russia
L.V. Kirensky Institute of Physics SB RAS
- Davletova Olessya** Russia
Volgograd State University
- Davydov Valeriy** Russia
L.F. Vereshchagin Insnitute for High Pressure Physics
- Davydov Vladimir** Russia
M.V. Lomonosov Moscow State University
- Demin Victor** Russia
IBCP RAS

Dideikin Artur	Russia	Gazizov Ruslan	Russia
<i>Ioffe Physical-Technical Institute</i>		<i>Moscow State University</i>	
Dolenko Tatiana	Russia	Generalov Alexander	Russia
<i>Moscow State University</i>		<i>V.A. Fock Institute of Physics, St. Petersburg State University</i>	
Dolmatov Valery	Russia	Golubina Elena	Russia
<i>FGUP "SCTB "Technolog"</i>		<i>M.V.Lomonosov Moscow State University</i>	
Duong Tran	Russia	Gorodetskiy Dmitriy	Russia
<i>D. Mendeleev University of Chemical Technology</i>		<i>Nikolaev Institute of Inorganic Chemistry SB RAS</i>	
Elbakyan Lusine	Russia	Goryunkov Alexey	Russia
<i>Volgograd State University</i>		<i>Lomonosov Moscow State University</i>	
Eletskii Alexander	Russia	Guenther Steffen	Switzerland
<i>National Research Center "Kurchatov Institute"</i>		<i>Reishauer AG</i>	
Emelianov Alexey	Russia	Guliaeva Kseniia	Russia
<i>St. Petersburg State Polytechnic University</i>		<i>Ioffe Physical-Technical Institute</i>	
Endo Morinobu	Japan	Haruyama Junji	Japan
<i>Shinshu University</i>		<i>Aoyama Gakuin University</i>	
Enoki Toshiaki	Japan	Ibragimov Ramil	Russia
<i>Tokyo Institute of Technology</i>		<i>National Research University of Electronic Technology</i>	
Erokhin Aleksey	Russia	Ichkitidze Levan	Russia
<i>Lomonosov Moscow State University</i>		<i>National Reserch Univerity MIET</i>	
Eydelman Evgeny	Russia	Ishikawa Manabu	Japan
<i>St.-Petersburg Chemical-Pharmaseutical Academy, Ioffe Physical-Technical Institute</i>		<i>Kyoto University</i>	
Fedorov Georgy	Russia	Ivanov Michail	Russia
<i>Kurchatov Institute</i>		<i>Ural Federal University</i>	
Fedorovskaya Ekaterina	Russia	Kalish Rafi	Israel
<i>Nikolaev Institute of Inorganic Chemistry SB RAS</i>		<i>Physics Dept and Solid State Inst. Technion</i>	
Fursikov Pavel	Russia	Katkov Mikhail	Russia
<i>Institute of Problems of Chemical Physics RAS</i>		<i>Nikolaev Institute of Inorganic Chemistry</i>	
Gaboardi Mattia	Italy	Katz Evgeni	Israel
<i>Department of Physics and Earth Science – Parma</i>		<i>Ben-Gurion University of the Negev</i>	
Gaeth Wilhelm	Germany	Khamatgalimov Ayrat	Russia
<i>Gaeth-Diamant</i>		<i>A.E. Arbuzov Institute of Organic and Physical Chemistry Kazan S</i>	
Garashchenko Viktor	Ukraine	Kharlamova Marianna	Russia
<i>V. Bakul Institute for Superhard Materials</i>		<i>Lomonosov Moscow State University</i>	
		Khomich Andrew	Russia
		<i>Prokhorov General Physics Institute</i>	

Kidalov Sergey	Russia	Kremlev Kirill	Russia
<i>Ioffe Physical-Technical Institute</i>		<i>G.A.Razuvaev Institute of Organometallic Chemistry</i>	
Klimovskikh Ilya	Russia	Krivosenko Yury	Russia
<i>Saint Petersburg State University</i>		<i>St. Petersburg State University</i>	
Kocherga Evgeniy	Russia	Krutoyarov Aleksey	Russia
<i>Snezhinsk Institute of Physics and Technology, National Research</i>		<i>Volgograd State University</i>	
Kolomiets Nadiia	Ukraine	Ktitorov Sergey	Russia
<i>Kyiv National Taras Shevchenko University</i>		<i>Ioffe Physical-Technical Institute</i>	
Konarev Dmitri	Russia	Kudashova Yulia	Russia
<i>Institute of Problems of Chemical Physics RAS</i>		<i>Ioffe Physical-Technical Institute</i>	
Koniakhin Sergei	Russia	Kulakova Inna	Russia
<i>Ioffe Physical-Technical Institute</i>		<i>Lomonosov Moscow State University</i>	
Konobeeva Natalia	Russia	Kurkin Tikhon	Russia
<i>Volgograd State University</i>		<i>Enikolopov Institute of Synthetic Polymeric Materials</i>	
Kononenko Oleg	Russia	Kvashnin Dmitry	Russia
<i>Institute of Microelectronics Technology and High Purity Materia</i>		<i>Emanuel Institute of Biochemical Physics RAS</i>	
Korepanov Vitaly	Taiwan	Kvashnina Yulia	Russia
<i>National Chiao Tung University</i>		<i>Technological Institute for Superhard and Novel Carbon Materials</i>	
Korobov Mikhail	Russia	Lebedev Alexander	Russia
<i>Department of Chemistry, Moscow State University</i>		<i>Ioffe Physical-Technical Institute</i>	
Korolev Konstantin	Russia	Lebedev Vasily	Russia
<i>Federal State Unitary Enterprise "Special Construction-Technolog</i>		<i>Petersburg Nuclear Physics Institute</i>	
Kosakovskii German	Russia	Leonidov Nikolay	Russia
<i>Kotel'nikov Institute of Radioengineering and Electronics of RAS</i>		<i>Pavlov Ryazan State Medical University</i>	
Kotin Igor	Russia	Levin Denis	Russia
<i>Rzhanov Institute of Semiconductor Physics</i>		<i>National Research University of Electronic Technology (MIET)</i>	
Kovalenko Valerii	Russia	Levinson Olga	Israel
<i>Arbuzov IOPC KazSC RAS</i>		<i>Ray Techniques Ltd</i>	
Kozyrev Sergey	Russia	Liu Fupin	China
<i>SPbSPU, Center for Advanced Studies</i>		<i>University of Science and Technology of China</i>	
Kramberger Christian	Austria	Lozovik Yurii	Russia
<i>University of Vienna</i>		<i>Institute of Spectroscopy</i>	
Krel Svyatoslav	Russia	Lvova Natalia	Russia
<i>St. Petersburg State Polytechnic University</i>		<i>Technological Institute for Superhard and Novel Carbon Materials</i>	

Mackeyev Yuri United States
Rice University

Makarov Ivan Russia
SCTB "Technolog"

Malovichko Anton Russia
National Research University of Electronic Technology

Markovic Zoran Serbia
Vinca Institute of Nuclear Sciences, University of Belgrade

Mazaleva Olga Russia
Moscow State University

Meletov Konstantin Russia
Institute of Solid State Physics of RAS

Meylakhs Alexander Russia
Ioffe Physical-Technical Institute

Mikhailova Svetlana Kazakhstan
Al-Farabi Kazakh National University

Mikheev Ivan Russia
Lomonosov Moscow State University

Mikushkin Valery Russia
Ioffe Physical-Technical Institute

Mironovich Kirill Russia
Skobeltsyn Institute of Nuclear Physics, Lomonosov Moscow State University

Moos Evgeny Russia
Ryazan State University

Morimune Seira Japan
Kobe University

Nakano Yoshiaki Japan
Kyoto University

Nasibulin Albert Finland
Aalto Univeristy

Nebogatikova Nadezhda Russia
Institute of Semiconductor Physics of SB RAS

Nesterenko Pavel Australia
University of Tasmania

Nikitin Evgeny Russia
SIDAL

Nikonova Roza Russia
Physical-Technical Institute of the Ural Branch of Russian Academy of Sciences

Okotrub Alexander Russia
Nikolaev Institute of Inorganic Chemistry SB RAS

Orlova Tatiana Russia
Ioffe Physical-Technical Institute

Osipov Vladimir Russia
Ioffe Physical-Technical Institute

Otsuka Akihiro Japan
Kyoto University

Ozawa Masaki Japan
Meijo University

Pak Anastasia Russia
Volgograd State University

Panova Anna Ukraine
ISM - V.Bakul Institute of Superhard Materials, National Academ

Petrenko Ievgenii Ukraine
Kiev Institute for Nuclear Research NAS of Ukraine

Petrova Natalia Russia
South Ural State University

Petukhov Vladimir Russia
MIET

PICHOT Vincent France
NS3E, French-German Research Institute of Saint-Louis

Piotrovskiy Levon Russia
Institute of Experimental Medicine

Polikarpov Dmitriy Russia
Volgograd State University

Polikarpova Natalia Russia
Volgograd State University

Polozkov Roman Russia
Saint Petersburg State Polytechnical University

Pontiroli Daniele Italy
University of Parma

Popov Vladimir	Russia	Rudometkin Kirill	Russia
<i>National University of Science and Technology "MISIS"</i>		<i>FGUP "SCTB "Technolog"</i>	
Popova Nadezhda	Russia	Rukhov Artem	Russia
<i>Peoples' Friendship University of Russia</i>		<i>Tambov State Technical University</i>	
Potapova Iraida	Russia	Rybalchenko Alexey	Russia
<i>A.A. Baikov Institute of Metallurgy and Material Science of RAS</i>		<i>Moscow State University</i>	
Pozdnyakov Aleksei	Russia	Sabirov Denis	Russia
<i>Ioffe Physical-Technical Institute</i>		<i>Institute of Petrochemistry and Catalysis RAS</i>	
Prato Maurizio	Italy	Sadykov Nail	Russia
<i>University of Trieste</i>		<i>Snezhinsk Institute of Physics and Technology, National Research</i>	
Prikhodko Aleksandr	Russia	Sakharov Vladimir	Russia
<i>St.Petersburg State Polytechnical University</i>		<i>Ioffe Physical-Technical Institute</i>	
Pyryaev Aleksandr	Russia	Samoylova Nataliya	Russia
<i>Institute of Geology and Mineralogy SB RAS</i>		<i>Lomonosov MSU University</i>	
Razbirin Boris	Russia	Saroka Vasil	Belarus
<i>Ioffe Physical-Technical Institute</i>		<i>Research Institute for Nuclear Problems</i>	
Reich Konstantin	Russia	Savkin Dmitry	Russia
<i>Ioffe Physical-Technical Institute</i>		<i>Russian Federal Nuclear Centre</i>	
Ricco Mauro	Italy	Schneider Kerstin	Germany
<i>Dipartimento di Fisica e Scienze della Terra, Parma University</i>		<i>Institute for Applied Physics, University of Tübingen</i>	
Rintala Perttu	Finland	Sedelnikova Olga	Russia
<i>Carbodeon Ltd Oy</i>		<i>Nikolaev Institute of Inorganic Chemistry</i>	
Romanova Natalia	Russia	Sedlovets Daria	Russia
<i>M.V. Lomonosov Moscow State University</i>		<i>Institute of Microelectronics Technology and High Purity Materials RAS</i>	
Rosenholm Jessica	Finland	Shakhov Fedor	Russia
<i>Abo Akademi University</i>		<i>Ioffe Physical-Technical Institute</i>	
Rostedt Niko	Finland	Shames Alexander	Israel
<i>Carbodeon Ltd Oy</i>		<i>Department of Physics, Ben-Gurion University of the Negev</i>	
Rozanov Roman	Russia	Sheka Elena	Russia
<i>National Research University of Electronic Technology</i>		<i>Peoples' Friendship University of Russia</i>	
Rozhkova Natalia	Russia	Shenderova Olga	United States
<i>Institute of Geology Karelian Research Center RAS</i>		<i>International Technology Center</i>	
Rudolf Petra	Netherlands	Shestakov Mikhail	Russia
<i>University of Groningen, Groningen, The Netherlands</i>		<i>Ioffe Physical-Technical Institute</i>	

Shinohara Hisanori	Japan	Tur Viacheslav	Russia
<i>Nagoya University</i>		<i>Nikolaev Institute of Inorganic Chemistry SB RAS</i>	
Shnitov Vladimir	Russia	Urbanovich Uladimir	Belarus
<i>Ioffe Physical-Technical Institute</i>		<i>Scientific-Practical Materials Research Centre NAS of Belarus</i>	
Shvidchenko Aleksander	Russia	Urvanov Sergey	Russia
<i>Ioffe Physical-Technical Institute</i>		<i>Technological Institute for Superhard and Novel Materials</i>	
Sinitza Alexander	Russia	Usachev Dmitry	Russia
<i>National Research Centre "Kurchatov Institute"</i>		<i>St. Petersburg State University</i>	
Skokan Eugenii	Russia	Ustimenko Kseniya	Russia
<i>Moscow State University, Department of Chemistry</i>		<i>Moscow State University</i>	
Solomatin Andrey	Russia	Uzbekov Rustem	France
<i>Lomonosov Moscow State University</i>		<i>University Francois Rabelais</i>	
Sominski Gennadi	Russia	Valynets Nadzeya	Belarus
<i>Saint Petersburg State Polytechnical University</i>		<i>Research Institute for Nuclear Problems</i>	
Tai Nyan-Hwa	Taiwan	Vancso Peter	Hungary
<i>National Tsing-Hua University</i>		<i>Institute of Technical Physics and Materials Science, Centre for Natural Sciences</i>	
Takai Kazuyuki	Japan	Varanovich Sofiya	Belarus
<i>Hosei University</i>		<i>Research Institute for Nuclear Problems of Belarusian State Univ</i>	
Terranova Maria Letizia	Italy	Vasilyeva Ekaterina	Russia
<i>University of Rome Tor Vergata</i>		<i>Saint Petersburg State Polytechnical University</i>	
Tikhomirova Galina	Russia	Vazquez Fernandez-Pacheco Ester	Spain
<i>Ural Federal University</i>		<i>Universidad de Castilla la Mancha</i>	
Tomchuk Oleksandr	Russia	Verkhovtsev Alexey	Germany
<i>Frank Laboratory of Neutron Physics, Joint Institute for Nuclear</i>		<i>Frankfurt Institute for Advanced Studies</i>	
Tomchuk Alina	Russia	Vershinin Nikolay	Russia
<i>Frank Laboratory of Neutron Physics</i>		<i>Institute of Problems of Chemical Physics</i>	
Troyanov Sergey	Russia	Vilkov Oleg	Russia
<i>Moscow State University, Chemistry Department</i>		<i>St. Petersburg State University</i>	
 TSAI I-SHOU	Taiwan	Vinogradov Andrey	Russia
<i>Feng Chia University</i>		<i>Ioffe Physical-Technical Institute</i>	
Tsalenchuk Alexander	United Kingdom	Vlasov Igor	Russia
<i>National Physical Laboratory</i>		<i>General Physics Institute</i>	
Tuktarov Airat	Russia	Volkov Dmitry	Russia
<i>Institute of Petrochemistry and Catalysis of RAS</i>		<i>Lomonosov Moscow State University, Chemistry Department</i>	

Vorobyova Irina Russia
Organazing Committee

Voropaev Sergey Russia
*Vernadsky Institute of Geochemistry
(GEOKHI) RAS*

Voznyakovskii Alexandr Russia
*S.V.Lebedev Research Institute
for Synthetic Rubber*

Vul' Alexander Russia
Ioffe Physical-Technical Institute

Wei Tao China
*University of Science and Technology of
China*

Xie Su-Yuan China
Xiamen University

Yakovlev Ruslan Russia
Pavlov Ryazan State Medical Universiry

Yang Shangfeng China
*University of Science and Technology of
China*

Yastrebov Sergey Russia
Ioffe Physical-Technical Institute

Yemelyanov Aleksei Russia
*National Research University of Electronic
Technology (MIET)*

Zagrebina Elena Russia
*Fock Institute of Physics, St. Peterburg
State University*

Zakharova Irina Russia
St. Petersburg State Technical University

Zharikova Evgeniya Russia
*N. S. Kurnakov Institute of General and
Inorganic Chemistry Russian Academy of
Sciences*

Zhizhin Evgeny Russia
Saint Petersburg State University

From Guest Editorial

This special volume of “**NANOSYSTEMS: PHYSICS, CHEMISTRY, MATHEMATICS**” presents the Proceedings of the 11th Biennial International Conference "Advanced Carbon Nanostructures" (ACNS'2013) held July 1-5, 2013 in St.Petersburg, Russia.

The tradition of the Conference takes its beginning in 1993 in St.Petersburg from the first International Workshop "Fullerenes and Atomic Clusters" (IWFAC). And since that time it is still held every two years, attracting nanocarbon community from all over in the world. In the year 2011 the Conference has been joined with International Symposium "Detonation Nanodiamonds: Technology, Properties and Applications" under the title “Advanced Carbon Nanostructures”. More than 250 participants from the leading scientific centers and universities of Russia, Ukraine, Belarus, Austria, Australia, China, Finland, France, Germany, Hungary, Italy, Israel, Japan, Netherlands, Serbia, Spain, Switzerland, and the UK took part in the Conference.

We believe that ACNS'2013 has become one of the most representative meetings in the field of the nanocarbon science. All aspects of the nanocarbon science were covered by the Conference and the appropriate papers were included in the Proceedings. The topics of the papers include not only many questions of physics, chemistry of fullerenes, nanotubes, graphene and other nanocarbon materials but also covered wide range of applications of these promising materials.

The ACNS'2013, was organized by Ioffe Physical-Technical Institute, St.Petersburg Nuclear Physics Institute, National Research Center "Kurchatov Institute", Moscow, Russia, and St. Petersburg State Institute of Technology (Technical University). We would like to express our gratitude to the official partners of the ACNS'2013 – Russian Foundation for Basic Researches, Department of General Physics and Astronomy of the Russian Academy of Sciences, Fund for Infrastructure and Educational Programs of the Government of Saint Petersburg as well as the Journal “Nanosystems: Physics, Chemistry, Mathematics”. We greatly appreciate the active help of the International Advisory Committee and Program Committee members for their important advices in determining of the scope of the ACNS'2013 the list of invited and oral speakers as well as the help in reviewing the manuscripts for Proceedings.

Taking into account the wishes of all participants of our conference it was decided to organize the next conference “Advanced Carbon Nanostructures” in July 2015, so we are pleased to welcome the members of world nanocarbon community to St. Petersburg.

Marina V. Baidakova, Artur T. Dideikin and Larisa V. Sharonova.

Guest editors of ACNS'2013

THE STATE-OF-THE-ART SCIENCE AND APPLICATIONS OF CARBON NANOTUBES

K. Takeuchi¹, T. Hayashi², Y. A. Kim², K. Fujisawa², M. Endo¹

¹Institute of Science and Technology, Shinshu University, Nagano, Japan

²Faculty of Engineering, Shinshu University, Nagano, Japan

endo@endomoribu.shinshu-u.ac.jp

PACS 73.63.Fg; 61.48.De

Extra-ordinary chemical and physical properties of carbon nanotubes (CNTs) also the success of large-scale production by a catalytic chemical vapor deposition method. It should be noted that lots of CNT-derived products are already in use and their viability strongly depend on their commercialization. We describe the synthesis techniques of various CNTs, and structural characterizations will be discussed, and finally their practical applications of these CNTs will be described from the industrial point of view as well as safety issue of CNTs.

Keywords: Carbon nanotube, Nanostructure, Chemical vapor deposition, Synthesis, Application.

1. Introduction

Carbon nanotubes (CNTs) have attracted lots of attention from scientists in various fields because they exhibit extraordinary physical and chemical properties due to their intrinsic nano-sized and carbon-based natures. Various synthetic methods for producing carbon nanotubes have been reported. The dominant process is to synthesize carbon nanotubes using a catalytic chemical vapor deposition (CCVD) method because this technique is a very effective tool for producing on a large scale and controlling the number of carbon shells, using nanosized iron particles that are dispersed on the substrate or a floating reactant technique [1-4]. Noticeably, highly crystalline and pure CNTs are commercially produced in a semi-continuous system through the right combination of the CCVD method and the subsequent high-temperature thermal treatment.

In this paper, firstly, the current usage of carbon nanotubes in energy storage devices as one of the important components of lithium ion secondary batteries is shown, and supercapacitor and fuel cell applications are demonstrated with a special emphasis on their morphology and texture [4]. The effectiveness of the addition of carbon nanotubes to both the cathode and anode electrode on the performance of lithium ion secondary batteries will be discussed [5]. Second, the application of CNTs as the electrode for supercapacitor will be described in terms of their pore size and distributions [6]. It is thought that the usage of nanotubes in the commercialized energy storage devices will only increase when considering the nature of our energy-oriented society. Third, the industrial usages of CNTs as multi-functional filler in rubber nanocomposites will be described. Finally, for successful developments of CNT's, the safety and toxicity of carbon nanotubes are the most important issue [7-11]. By sharing the all information on risks [7-11] and benefits of the materials with everyone having a stake in their use, we are able to prove CNTs to be green and safe innovative materials, by the responsible productions and uses, as one of the 21st century's leading materials.

2. Synthesis and structures of CNTs by CCVD method

Currently, it is well known that the CCVD method is most commonly used for the synthesis of single-walled CNTs (SWCNTs), double-walled CNTs (DWCNTs), and MWCNTs (Fig. 1) [12,13]. For example, SWCNTs were synthesized by the floating method, and the obtained SWCNTs were directly used to form CNT ropes. In 1988, the industrialization of MWCNTs began experimentally, and the supply of MWCNTs samples began; to this day, the most frequently used catalyst in this synthetic method is iron. Now, many production systems for the industrial-scale synthesis of MWCNTs by various processes using the fluidization CCVD method as a basis have been established; MWCNTs have been industrialized in several countries, such as Germany, France, Japan, the US, Belgium, China, the UK and others. Depending on the intended use, there are several types, including as-deposited MWCNTs and those thermally treated at high temperatures (Fig. 1(b)). Since the 1990's, basic and applied research and the development of single-, double- and multi-walled CNTs, have been accelerated, thus making carbon fibers (CFs) and these materials the leading causes for the worldwide interest in nanotechnology.

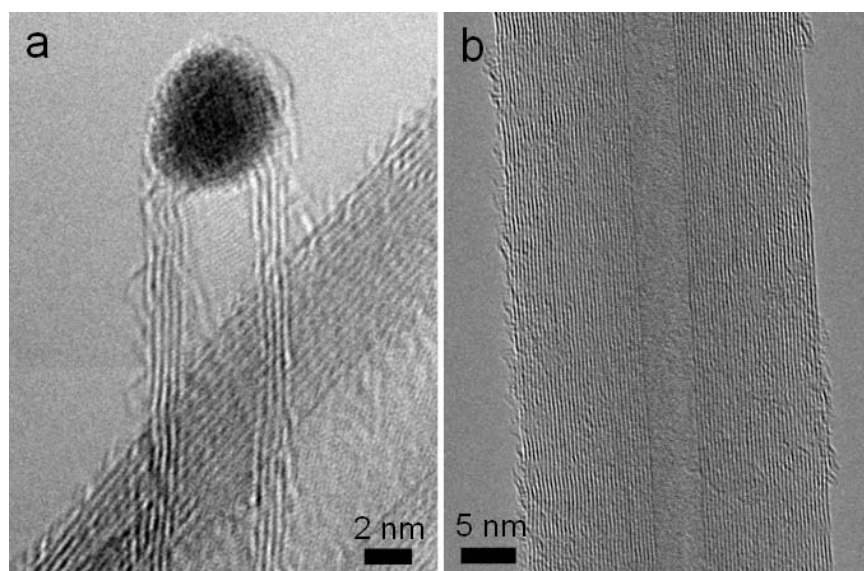


FIG. 1. TEM images of (a) four-walled CNT formed through catalytic effect of iron particles and (b) thermally treated MWCNT

An important factor required for the use of CNTs as a nanotechnology material is the precise control of growth for structures suitable for the required functions. By using the CCVD method, the number of layers, such as single, double, and multiwalled, as described above, can be controlled; we have succeeded in the synthesis of highly-pure DWCNTs with high structural perfection by the seeding method using an iron catalyst, that is, the CCVD method. Other major methods reported for DWCNT synthesis include high-temperature pulsed arc discharge [14] and thermal treatment of peapods, i.e., fullerenes encapsulated in SWCNTs [15]. Iron and cobalt particles, as well as molybdenum alloy particles, are primarily used as catalysts in the CCVD method, and in these methods, the catalyst particle size is precisely controlled on alumina and zeolite supports. We have developed a synthetic method for DWCNTs in which the reaction temperature and the catalyst particle size in particular were optimized using magnesium-oxide and iron catalysts [Fig. 2(a)] [16]. It is worthwhile to note that the high-purity DWCNTs had a small diameter almost equivalent to that of

SWCNTs, with a narrow diameter distribution. Furthermore, we could fabricate paper-like DWCNTs with high flexibility [16]. By thinning the film, the fabrication of a conductive transparent film is possible, 14) and the application of the film as a transparent and conductive film is expected. Additionally, DWCNTs have interesting adsorption characteristics; hydrogen is well adsorbed in nanospaces of DWCNTs [17]. Because the diameter of DWCNTs is approximately 1 nm, which is comparable to that of SWCNTs, it is expected that DWCNTs with properties arising from the double-wall structure will be utilized in electronic and energy device applications. It is even possible to form a hybrid double-wall structure in which only the electronic properties of the outer tube are changed to that of an insulator, by fluorinating the outer tube of the coaxial double wall yet maintaining the intrinsic physical and chemical properties of the inner tube [Fig. 2(b)] [18].

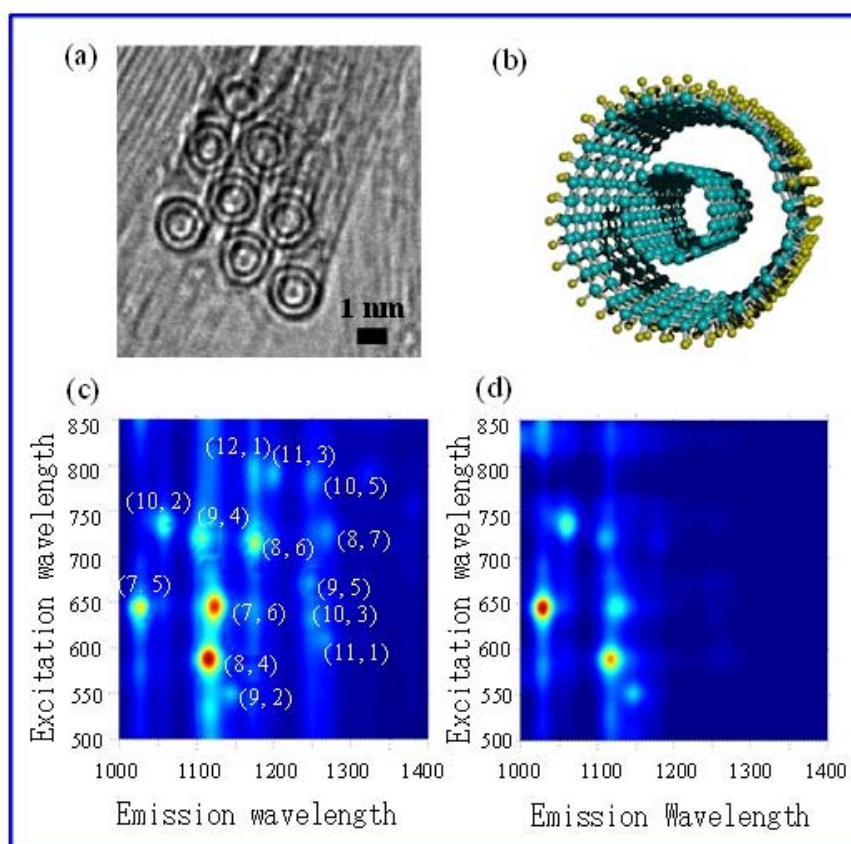


FIG. 2. (a) TEM image of DWCNT and (c) its photoluminescence map; (b) structural model of fluorinated DWCNT and (d) its photoluminescence map[16,18,19]

Figure 3(a) shows a TEM image of a DWCNT with a fluorinated outer tube. As shown in the figure, the shape of the DWCNT was unchanged by fluorination; the shape of the coaxial double-wall structure remains the same. From the Raman spectra acquired with three different laser lines (532, 633, and 785 nm), the Raman radial breathing mode (RBM), which is a vibration mode in the radial direction unique to CNTs, is selectively suppressed in the outer tube ($< 200 \text{ cm}^{-1}$) owing to fluorination. Conversely, this vibrational mode is maintained in the inner tube ($> 200 \text{ cm}^{-1}$) [Fig. 3(b)]. It is possible to observe the distribution of the chirality (geometrical helical structure) of semiconducting CNTs by photoluminescence (PL) measurement of DWCNTs. SWCNTs are well known to become

a metal or a semiconductor depending on the chirality, and Fig. 2(c) shows the PL map for pristine DWCNTs (without fluorination). The map shows the chirality distribution for the inner tube of DWCNTs; three strong PL peaks were ascribed to the inner tubes with chiralities (7, 6), (8, 4), and (7,5). In contrast, Fig. 2(d) shows the photoluminescence map for fluorinated DWCNTs, where the signals corresponding to some chiralities disappeared after fluorination. On the basis of this finding, it was concluded that the electronic states of the inner tube are unaffected by fluorination of the outer tube, indicating that the electronic states of only the outer tube are selectively changed by fluorination. Namely, even when functionalization, such as the modification of a DWCNT with functional groups and the adhesion of metal catalysts, is carried out on the outer tube, the effects of functionalization on the structure and properties of the inner tube are very limited. An ideal property can be maintained in the inner tube because of the double-wall structure with high structural perfection, which is an advantage of DWCNTs when they are applied as a material in electronic devices and sensors, and as a composite material. This could be referred to as “DWCNT chemistry”.

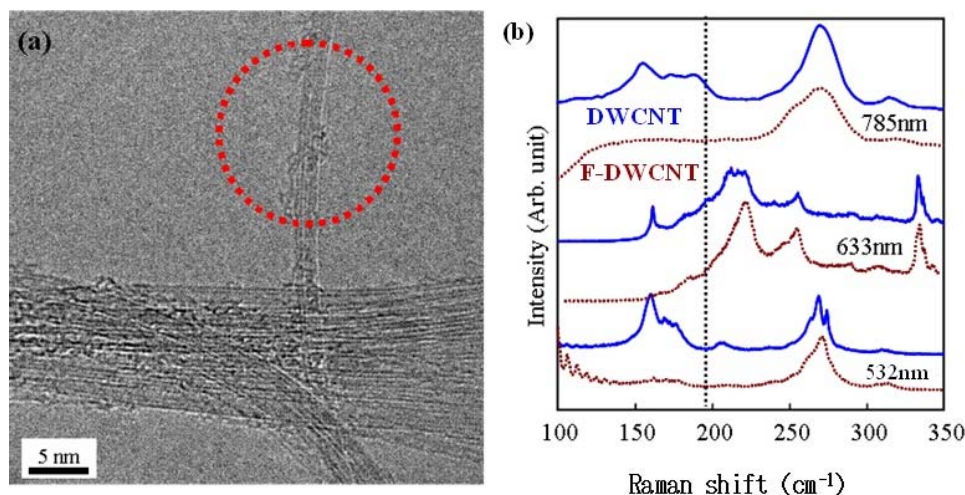


FIG. 3. (a) TEM image of fluorinated DWCNT and (b) Raman spectra of pristine and fluorinated DWCNTs[19]

Due to their unique characteristic of a hollow core, DWCNTs have been considered as templates for metal nanowires, with the encapsulation of lanthanum (La) [19] and gadolinium (Gd) [20] atoms already having been reported. We produced nanowires by a one-dimensional alignment of molybdenum (Mo) and platinum (Pt) atoms inside the DWCNTs [21], aiming at the use of these atoms as new catalysts (Fig. 4). In particular, a unique application of DWCNTs, in which the outer and inner tubes have different functions, is expected; for example, the outer tube may be modified with functional groups to add functions and the inner tube with high structural perfection may be used as a conductive or semiconductive SWCNT. In the future, the exploration of methods of mass-synthesizing high-purity DWCNTs by the floating method and the development of their unique applications are expected. The research achievement on DWCNTs by Shinohara et al. [14] is noteworthy and the research on DWCNTs is one of the scientific fields in which Japan has taken a worldwide leading role.

3. Development of CNTs applications

CNTs were first practically applied because of their mechanical properties. Even when CNTs are subjected to a kneading process within a matrix, the integrity of the tube shape is maintained, which was not the case for conventional carbon fibers (CFs). Therefore, it is possible to add mechanical, electrical, and thermal conductive functions that are derived from a thin laminated graphene cylindrical structure with high structural perfection to various composite materials.

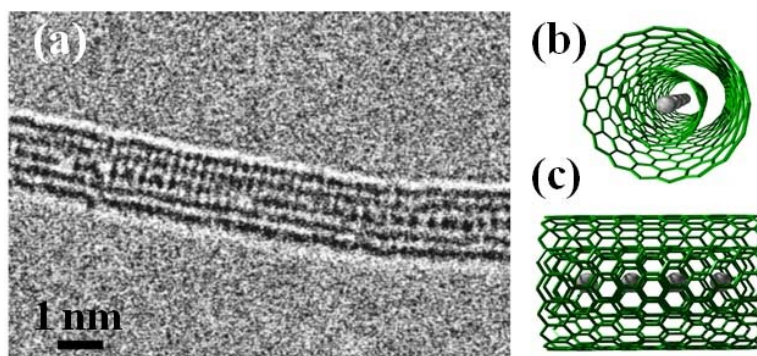


FIG. 4. (a) Encapsulation of Mo atoms inside DWCNT and (b) its structural model[22]

MWCNTs have been practically used as an electrode additive in lithium-ion batteries (LIBs) from relatively early in their development, and have accumulated market achievements.[5] A MWCNT electrode additive has contributed to the improvement of LIB performance and great expectations are placed on plug-in hybrid cars and electric vehicles equipped with LIBs. Figure 4 shows a SEM image of LIB graphite anode to which MWCNTs have been added and are uniformly distributed among graphite particles. Depending on the proportion of MWCNTs added to the LIB anode graphite, the cycle life, namely the cyclability, of the battery is significantly improved; the cycle life increases with an increasing proportion of MWCNTs [5]. This improvement is considered to be due to the formation of a flexible conductive network between particles owing to the highest resiliency of MWCNTs resulting from their carbon nanostructure among various materials. Also, it is expected that the addition of CNTs will enhance the electrochemical performance of the LIB, such as rate capability. MWCNTs can also be used as an additive to the cathode of LIBs; the practical application of MWCNTs in this field is already under way. The contribution and application ranges of MWCNTs in power sources other than LIBs for portable electronic devices have been increasing. The use of MWCNTs in lead-acid batteries and electric double-layer capacitors is also strongly expected.

The advantage of the electric double-layer capacitor (EDLC) is considered to be its high discharge rate [18], thus making it applicable as a hybrid energy source for electric vehicles and portable electric devices [19]. EDLC containing carbon nanotubes in the electrode exhibited relatively high capacitances resulting from the high surface area accessible to the electrolyte [17,20,21]. On the other hand, the most important factor in commercial EDLC is considered to be the overall resistance on the cell system. In this context, carbon nanotubes and nanofibers with enhanced electrical and mechanical properties can be applied as an electrically conductive additive in the electrode of the EDLC. The addition of carbon nanotubes has been shown to result in an enhanced capacity at higher current densities, when compared with electrodes containing carbon black [22].

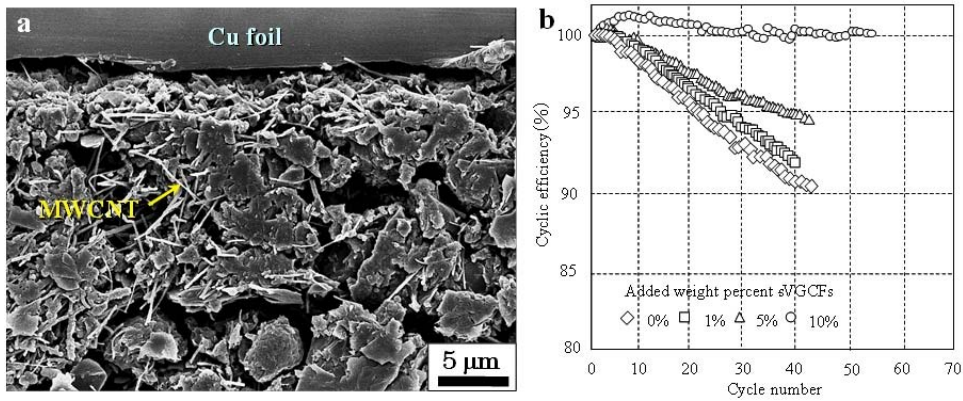


FIG. 5. (a) SEM image of anode sheet containing MWCNTs in commercial LIB, and (b) cyclic efficiency of synthetic graphite, heat-treated at 2900 °C, as a function of weight percent, from 0 to 1.5V, with a current density of 0.2mA/cm²[5]

The applications of composite materials of various matrix resins, rubber, and metals using MWCNTs as a filler are being developed. Research on the practical use of MWCNTs, such as for containers used in semiconductor fabrication, automobile parts, and windmills for wind power generation, has been active. MWCNTs are expected to add new functions, e.g. as the third additive for the PAN-based CF composite material, in order to strengthen such as compressive strength. In addition, the composite of MWCNTs with aluminum is applied to a plate with high thermal conductivity. SWCNTs and MWCNTs are expected to have a high thermal conductivity of 3,000–6,000 W/mK at room temperature, which may open up new applications in the fields of metal composite materials used for electronic devices and the cooling of laser elements. Because of this, an advanced composite metal with a light density, comparable to that of plastics, can be expected.

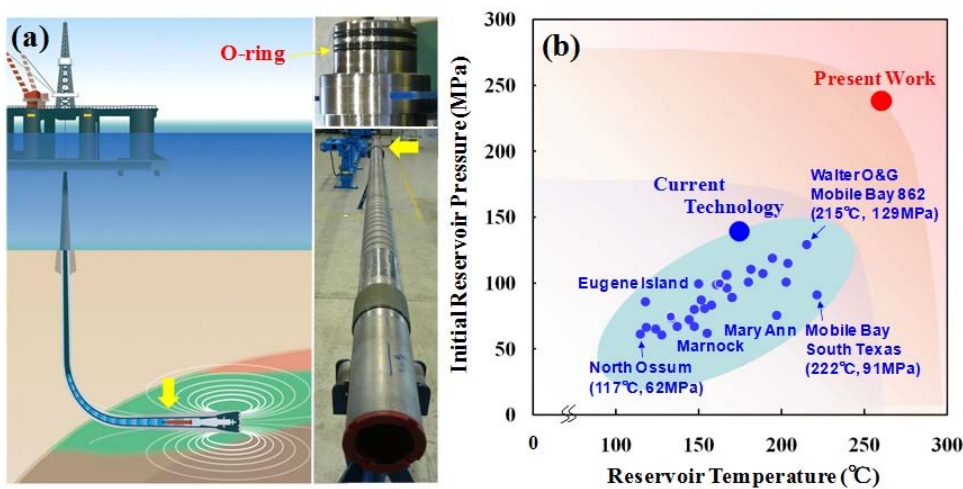


FIG. 6. (a) Downhaul devices in underground resources probing using rubber seals as a key component and (b) the distribution of temperature and pressure of the current oil wells, for example (Schlumberger Oilfield Review, 50-67, 1998)[23]

The technologies for oil development and exploration are used under harsh conditions; the temperature and pressure of oil wells are as high as 175 ° C and 140 MPa, respectively. That pressure corresponds to the hydraulic pressure in the sea at a depth of 14,000 m. An innovative improvement of rubber functions was achieved through the use of a CNT composite rubber, as realized by the cellulated structure in which CNTs are dispersed in rubber matrices as if they are cell membranes [23]. An environmentally resistant rubber seal (CNT/fluoroelastomer (FKM) composite) with a sealing ability of 260 ° C and 239 MPa, which far exceeds the current sealing ability (175 ° C and 140 MPa, standard specification), has already been developed (Fig. 6) [23]. Thanks to this development, the drilling rate of raw oil is expected to significantly improve, contributing to the stable supply of oil resources.

The 21st century is called the century of water. Humans face water shortages and conflicts over the water supply because of rapid industrialization and population expansion. However, considerable amounts of water are being lost due to leaks; the leakage rate is the lowest at about 3 % in Germany, but it is very high even in developed countries, for example, in the UK with over 20 %, France with 30 %, and the US with 20 %. The predominant reason for such leaks is known to be the premature failure of rubber sealants (e.g., O-ring packing and gaskets) in valves by the presence of chlorine in tap water. There is a strong demand for developing a chemically and environmentally sustainable nanocomposite-rubber sealant to prevent such water leakage. The incorporation of the optimum surface-modified and high-crystalline carbon nanotubes allows rubber sealants to maintain their sealing properties without any distinctive degradation over a wide range of temperatures and environmental conditions for the expected lifetime. The addition of carbon black is generally known to improve strength, but deteriorate chlorine-resistance of the rubber composite. We have demonstrated that the surface-modified MWCNT-incorporated rubber composite exhibits outstanding resistance to chlorine (Fig. 7) [24], as well as excellent mechanical and thermal properties. Our developed MWCNTs-incorporated rubber nanocomposites are very promising as high-performance sealants to transport tap water and hot water (or steam) without water-leakage and chlorine-contamination, which can also contribute as a green technology to saving electric power in the water century.

The expected application areas of CNTs range widely. The commercialization of the PAN-based CFs started from fishing rods and golf clubs; then in approximately 10 years, it expanded to aerospace-related fields. Since then, the demand for carbon fibers in common industries has also been increasing. CNTs appear to be heading in a similar direction of development, and scientific support for the development of CNTs from fundamental to application fields is hoped for in the future.

4. Safety, responsible production and uses of CNTs

The development of CNT-related material technology should be based on the concept of “safety for success” and abide by the correct risk control, from the initial to the final processes of products, following the principle of “responsible production and application” [25-28]. It is important to establish and share international evaluation criteria developed for the complete safety and toxicity evaluation of CNTs; moreover, it is hoped that the development of the CNTs applications will be promoted further on the basis of such criteria. As Takagi et al. [7] reported, malignant mesothelioma was induced in mice in which CNTs had been intraperitoneally administered. Without question, we must pay special attention to all processes related to CNTs until a socially acceptable risk control system can be established. The practice of responsible production, application, distribution, and disposal should be carried out under a life-cycle assessment for the commercialization of CNTs. I hope that a leading

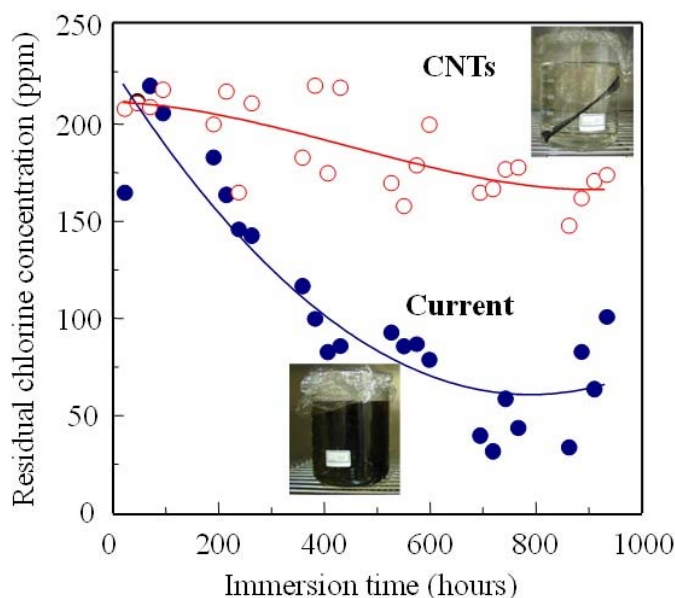


FIG. 7. Variations of the chlorine concentrations of chlorine solutions containing the carbon black (Current) - and multi-walled carbon nanotubes - incorporated rubber composites as a function of immersion time. The chlorine solution containing the current sample become opaque whereas there is no changes in the solution[24]

model to promote scientific and technological research and industrial promotion of CNTs will be established on the basis of the precautionary approach or control banding, which all of academia should pay attention and expend effort to this end. To achieve this, the risks and benefits of CNTs should be correctly understood. At the same time, it is necessary for all stakeholders to participate in open discussion, and for the use of CNTs to be widely accepted by society through the disclosure of information, promoting to a safe and green innovation of using CNTs under social agreement beyond the scheme of science and technology. Steady progress in the safety evaluation of CNTs will lead to great success for CNTs (safety for success) [25,29]. It is hoped that CNT science and technology, expected to greatly contribute to green technology, can serve as a 21st-century model of material development.

5. Conclusion

In this paper, we have shown the synthesis of CNTs by the CCVD method, and their practical applications in energy storage devices such as lithium-ion secondary batteries, supercapacitors, and as multi-functional filler in rubber nanocomposites. Finally, the safety studies of carbon nanomaterials were shown. By using the CCVD method, we are expecting improvements such as the precise control of chirality, the suitable and designed length control and synthesis efficiency of CNT. The advancement of the applied and basic science used to create innovative applications, performing biological safety evaluation that will encourage the social acceptance of CNTs, and the development of safe-controlled CNT structures are highly anticipated in the near future. Through these activities, CNTs will surely contribute to green innovations in the 21st century.

Acknowledgment

The present review paper is described as the proceedings of the conference ACNS2013 together with the quotation and published original papers by the authors elsewhere [4]. The authors would like to show sincere thanks to the conference organizers for the kind invitation.

References

- [1] A. Oberlin, M. Endo, T. Koyama. Filamentous growth of carbon through benzene decomposition. *J. Crystal Growth*, **32**, P. 335–349 (1976).
- [2] M. Endo. Grow Carbon Fibers in the Vapor Phase. *ChemTech*, P. 568–576 (1988).
- [3] M. Endo, H. Muramatsu, T. Hayashi, Y.A. Kim, M. Terrones, M.S. Dresselhaus, 'Buckypaper' from coaxial nanotubes. *Nature*, **433**, P. 476 (2005).
- [4] M. Endo. Carbon Nanotube Research: Past and Future. *Jpn. J. Appl. Phys.*, **51**, P. 040001(1-8) (2012).
- [5] M. Endo, Y.A. Kim, T. Hayashi, K. Nishimura, T. Matsushita, K. Miyashita, M.S. Dresselhaus. Vapor-grown carbon fibers (VGCFs). Basic properties and battery application. *Carbon*, **39**, P. 1287–1297 (2001).
- [6] Y. J. Kim, C.-M. Yang, K.C. Park, K. Kaneko, Y.A. Kim, M. Noguchi, T. Fujino, S. Oyama, M. Endo. Edge-enriched, porous carbon-based, high energy density supercapacitors for Hybrid electric vehicles. *ChemSusChem*, **5**(3), P. 535–541 (2012).
- [7] A. Takagi, A. Hirose, T. Nishimura, N. Fukumori, A. Ogata, N. Ohashi, S. Kitajima, J. Kanno. Induction of mesothelioma in p53+/- mouse by intraperitoneal application of multi-wall carbon nanotube. *J. Toxicol. Sci.*, **33**, P. 105–116 (2008).
- [8] C. A. Poland, R. Duffin, I. Kinloch, A. Maynard, W.A.H. Wallace, A. Seaton, V. Stone, S. Brown, W. Macnee, K. Donaldson. Carbon nanotubes introduced into the abdominal cavity of mice show asbestos-like pathogenicity in a pilot study. *Nature Nanotechnology*, **3**(7), P. 423–428 (2008).
- [9] D.W. Porter, A.F. Hubbs, R.R. Mercer, N. Wu, M.G. Wolfarth, K. Sriram, S. Leonard, L. Battelli, D. Schwegler-Berry, S. Friend, M. Andrew, B.T. Chen, S. Tsuruoka, M. Endo, V. Castranova. Mouse pulmonary dose-and time course-responses induced by exposure to multi-walled carbon nanotubes. *Toxicology*, **269**, P. 136–147 (2010).
- [10] NIOSH, Progress Toward Safe Nanotechnology in the Work Places (2007).
- [11] J. Nakanishi. Risk Assessment of Manufactured Nanomaterials: Approaches - Overview of Approaches and Results. Final report issued on August 17, 2011. NEDO
- [12] M. Endo, K. Takeuchi, S. Igarashi, K. Kobori, M. Shiraishi, H.W. Kroto. The production and structure of pyrolytic carbon nanotubes (PCNTs). *J. Phys. Chem. Solids*, **54**, P. 1841–1848 (1993).
- [13] M. Endo, K. Takeuchi, K. Kobori, K. Takahashi, H.W. Kroto, A. Sarkar. Pyrolytic Carbon Nanotubes from Vapor-Grown Carbon Fibers. *Carbon*, **33**, P. 873–881 (1995).
- [14] T. Sugai, H. Yoshida, T. Shimada, T. Okazaki, H. Shinohara, S. Bandow. New Synthesis of High-Quality Double-Walled Carbon Nanotubes by High-Temperature Pulsed Arc Discharge. *Nano Lett.*, **3**, P. 769–773 (2003).
- [15] S. Bandow, M. Takizawa, K. Hirahara, M. Yudasaka, S. Iijima. Raman scattering study of double-wall carbon nanotubes derived from the chains of fullerenes in single-wall carbon nanotubes. *Chem. Phys. Lett.*, **337**, P. 48–54 (2001).
- [16] M. Endo, H. Muramatsu, T. Hayashi, Y.A. Kim, M. Terrones, M.S. Dresselhaus 'Buckypaper' from coaxial nanotubes. *Nature*, **433**, P. 476 (2005).
- [17] Y.C. Jung, D. Shimamoto, H. Muramatsu, Y.A. Kim, T. Hayashi, M. Terrones, M. Endo. Robust, Conducting, and Transparent Polymer Composites Using Surface-Modified and Individualized Double-Walled Carbon Nanotubes. *Adv. Mater.*, **20**(23), P. 4509–4512 (2008).
- [18] Y. Tao, H. Muramatsu, M. Endo, K. Kaneko. Evidence of Water Adsorption in Hydrophobic Nanospaces of Highly Pure Double-Walled Carbon Nanotubes. *J. Am. Chem. Soc.*, **132**(4), P. 1214–1215 (2010).
- [19] T. Hayashi, D. Shimamoto, Y.A. Kim, H. Muramatsu, F. Okino, H. Touhara, T. Shimada, Y. Miyauchi, S. Maruyama, M. Terrones, M.S. Dresselhaus, M. Endo. Selective Optical Property Modification of Double-Walled Carbon Nanotubes by Fluorination. *ACS Nano*, **2**, P. 485–488 (2008).
- [20] L. Guan, K. Suenaga, S. Okubo, T. Okazaki, S. Iijima. Metallic Wires of Lanthanum Atoms Inside Carbon Nanotubes. *J. Am. Chem. Soc.*, **130**, P. 2162–2163 (2008).

- [21] R. Kitaura, N. Imazu, K. Kobayashi, H. Shinohara. Fabrication of Metal Nanowires in Carbon Nanotubes via Versatile Nano-Template Reaction. *Nano Lett.*, **8**(2), P. 693–699 (2008).
- [22] H. Muramatsu, T. Hayashi, Y.A. Kim, D. Shimamoto, M. Endo, M. Terrones, M.S. Dresselhaus. Synthesis and Isolation of Molybdenum Atomic Wires. *Nano Lett.*, **8**, P. 237–240 (2008).
- [23] M. Endo, T. Noguchi, M. Ito, K. Takeuchi, T. Hayashi, Y.A. Kim, Wanibuchi T., Jinnai H., Terrones M., Dresselhaus M.S. Extreme-Performance Rubber Nanocomposites for probing and Excavating Deep Oil Resources Using Multi-Walled Carbon Nanotubes. *Adv. Func. Mat.*, **18**, P. 3403–3409 (2008).
- [24] M. Endo, K. Takeuchi, T. Noguchi, Y. Asano, K. Fujisawa, Y.A. Kim, T. Hayashi, H. Ueki, S. Iinou. *Ind. Eng. Chem. Res.*, **49**, P. 9798 (2010).
- [25] EPA. Nanotechnology White Paper, February (2007).
- [26] Report on strategic survey of ultraprecision technology development and industry exploration, FY 2006 (Research on appropriate control method at the nanotechnology-related research and production sites, FY 2006 entrusted research supported by Ministry of Economy, Trade and Industry) March 2007 (in Japanese).
- [27] Material from a briefing session on the safety of nanomaterials organized by Ministry of Health, Labour and Welfare, Ministry of Economy, Trade and Industry, and Ministry of the Environment, 19 May 2009 (in Japanese).
- [28] Notification on Precautionary Measures for Prevention of Exposure etc. to Nanomaterials (LSB Notification No.0331011), Labour Standards Bureau, Ministry of Health, Labour and Welfare, 31 March 2009 (in Japanese).
- [29] Toxicology Topics: Developing Safe Products Using Nanotechnology, Society of Toxicology (2010). <http://www.toxicology.org/gp/toxtopics.asp>

GRAPHENE EDGE SPINS: SPINTRONICS AND MAGNETISM IN GRAPHENE NANOMESHES

T. Hashimoto¹, S. Kamikawa¹, Y. Yagi¹, J. Haruyama^{1*}, H. Yang², M. Chshiev²

¹Faculty of Science and Engineering, Aoyama Gakuin University, Kanagawa, Japan

²SPINTEC, CEA/CNRS/UJF-Grenoble 1/Grenoble-INP, 38054, Grenoble cedex 9, France

*J-haru@ee.aoyama.ac.jp

PACS 75.70.-i, 75.30.-m, 75.50.Dd, 75.75.-c

We have fabricated low-defect graphene nanomeshes (GNMs) by using a non-lithographic method and observed large-amplitude ferromagnetism even at room temperature, only when pore edges of the GNMs were hydrogen-terminated. The observed correlation between the inter-pore spacing and magnetism and also magnetic force microscope observations suggest that it is attributed to polarized electron spins localized at the zigzag-type atomic structured pore-edges. The magnetic moment per edge dangling bond ($\sim 0.3 \mu\text{B}$) is also in quantitative agreement with two theories. Moreover, a spin pumping effect is found for fields applied in parallel with the GNM planes in few-layer ferromagnetic GNMs, while a magnetoresistance (MR) hysteresis loop is observed under perpendicular fields. The present ferromagnetic GNMs must also realize rare-element free, invisible, flexible, and ultra-light (wearable) magnets and spintronic devices, which can overcome environmental and material-resource problems.

Keywords: Graphene, Edges, Polarized spins, Magnetism, Spintronics, Flat band.

1. Introduction

Graphenes, a mono-atomic carbon layer, has attracted considerable attention from many viewpoints. A variety of electronic structures, physical phenomena, and applications have already been reported. However, there is one issue, on which little data have been experimentally reported. That is edge-based phenomena. There are two different kinds of edge atomic structures for graphenes. One is the so-called arm chair, while the other is zigzag. It is theoretically well-known that zigzag edges can produce a flat energy band, where electrons have infinite effective mass and, hence, localize, resulting in extremely high electronic density of states (EDOS); the so-called edge states. Due to the edge states, spin interaction is significantly induced. Then, electron spin polarization (e.g., (anti)ferromagnetism) can appear spontaneously [1–7, 10–22, 28–31].

In the case of a graphene nanoribbon (GNR), which is an one-dimensional strip line of graphene with edges on both longitudinal sides, the edge-based spin configuration is very complicated and thus, interesting [1–7]. Assuming perfect edges for GNRs without any defects allows the electron spins localized at zigzag edges [1, 10] to be stabilized toward polarization (i.e., (anti)ferromagnetism) due to the exchange interaction between the two edges, which produces a maximum spin ordering in these orbitals as well as those in graphene nanomeshes (GNMs) with hexagonal nanopore arrays (Fig.1) [13, 29], and in graphene nanoflakes [14]. This is similar to the case of Hund's rule for atoms. Moreover, the spin configuration depends on different kinds of atoms (e.g., hydrogen (H) and oxygen (O)), which terminate edge carbon dangling bonds [3, 31].

Conversely, assuming the presence of defects in the ensemble of carbon atoms (e.g. graphene flakes) yields a net magnetism, which is interpreted by Lieb's theorem. It predicts the emergence of ferromagnetism by an increase in the difference between the number of removed A

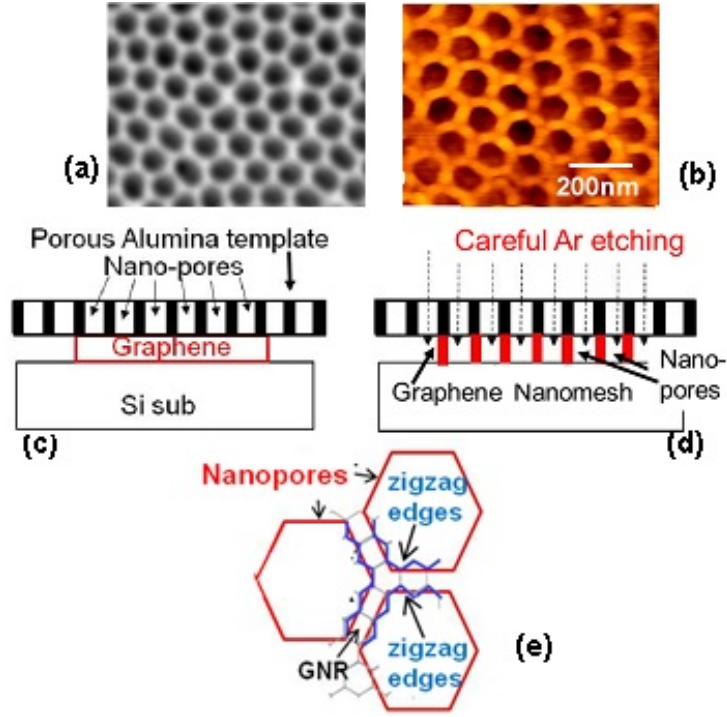


FIG. 1. (a) SEM top view of an NPAT, which shows honeycomb-like array of hexagonal nano-pores. (b) AFM image of a GNM formed by using (a) as an etching mask, which proves hexagonal shape of pores with mean diameter $\phi \sim 80$ nm and mean inter-pore distance $W \sim 20$ nm. (c)(d) Schematic cross sectional views of fabrication process of a GNM. (c) NPAT is located on graphene as an etching mask. (d) The graphene is carefully etched by Ar gas, resulting in a GNM. (e) Schematic view of a GNM with the zigzag-type pore-edge. Narrow regions sandwiched by two pores with width (W) correspond to GNRs. Actual structure includes a larger number of hexagonal carbon unit cells per inter-pore region with ~ 40 nm length and $W \sim 20$ nm. This GNM structure brings at least three large advantages

and B sites (Δ_{AB}) of the graphene bipartite lattice at zigzag edges [14,29,31]. The magnitude of the ferromagnetism increases with increasing values of Δ_{AB} .

Moreover, many theoretical works have predicted spin-based phenomena realizable using graphene edges. For instance, a spin-filtering effect predicted that GNRs with antiferromagnetic spin alignment on two edges can transport only electron spins with the same moment, which can be controlled by applying electric fields [22]. Realization of (quantum) spin Hall effect (SHE) as topological insulator (TI) was also theoretically predicted by resolving double degeneration of edge spin bands (e.g., by introducing spin orbit interaction (SOI)) and controlling two spins with opposite moments existing in two different bands by applying electric fields [25–27]. Indeed, one group reported on the observation of SHE in dihydrogenated graphenes. Using a specified resist (MSQ) and irradiating electron beam with changing the amount of dose allowed dihydrogenation of the graphenes including edges. This resulted in the appearance of sp^3 hybridized orbitals and, hence, introduction of strong SOI and SHE. These are strongly expected to make possible novel spintronic devices.

No works, however, have reported experimental observation of magnetism and spin-based phenomena arising from graphene zigzag edges, although the observation of graphene

edge-atomic structures has been carried out in some systems (e.g., in overlapped graphenes with Joule heating [15], GNRs [17–19], and GNMs with pore edges [20,21]). This is because edge-related phenomena are easily destroyed by disorder (damage, defects) introduced during the fabrication process (e.g., by lithographic methods). We have, therefore, developed two non-lithographic fabrication methods for graphene edges; i.e., (1) GNRs derived from unzipping of carbon nanotubes combined with air blow and three-step annealing [17] and (2) GNMs fabricated using a nanoporous alumina template (NPAT) [33]. In the present work, magnetism and spin-related phenomena are reported for GNMs made using the latter process.

2. Experimental results and discussion

2.1. Ferromagnetism arising from pore edges

(a) Sample fabrication

Low-defect GNMs with honeycomb-like arrays of hexagonal nanopores (Figs. 1(b) and 1(e)) were fabricated on a large ensemble of mechanically exfoliated graphenes (or CVD-synthesized graphenes on a SiC substrate) by using NPAT (Fig. 1(a)) [23] as an etching mask (Fig. 1(c)), following our previous method [33]. The NPAT, which consists of a honeycomb-like array of hexagonal-shaped nanopores, was fabricated by the anodic oxidation of a pure aluminum (Al) substrate (Al = 99.99%) using electrochemical methods with a carbon cathode [23]. Due to self-organization, a NPAT provides structure parameters (e.g., pore diameter ϕ and interpore space w) with exceptionally high regularity and high reproducibility. After the formation, the NPAT with an area of 1 cm² was detached from the Al substrate by alternating the polarity of the two electrodes. The detached NPATs were then placed onto the graphenes on Si(SiO₂) substrate as etching masks.

The thin-multilayer (< 10 layers) and monolayer graphene samples which were used as the base for formation of GNMs were extracted from bulk Kish graphite (Toshiba Ceramics) onto degenerately doped Si wafers with a 250-nm-thick SiO₂ surface layer by means of mechanical exfoliation. Interference-induced color shifts in an optical microscope (3D-CCD), Raman spectroscopy, and cross-correlation with an AFM profile allowed us to identify the number of deposited graphene layers of all graphene flakes, which ranged from 1 to ~10.

Using the NPAT as a mask, the assembled graphenes were etched by a carefully optimized low-power Ar gas (e.g., 200–600 V for 10–40 min) to avoid damage. We carried out the low-power etching step by step. After each 10 minute etching, we performed a FESEM (or AFM) measurement and checked for the formation of nanopores on the Si-substrate under the NPAT mask. Until the formation of nanopores on the Si-substrate was confirmed, we repeated the low-power etching. This is a very important process which avoids damaging the pore edges. The boundaries of nanopores are not aligned along the hexagonal carbon lattice of graphene in this process. Consequently, naomesh of the NPAT was transferred to graphene. After formation of the GNM, the NPAT mask was entirely dissolved by a H₃PO₄ solution or detached mechanically from the GNMs in some cases. Either method left no contamination remaining from the NPAT mask. Then, all multi-layer GNM flakes (i.e., except for monolayer GNMs), which existed under the NPAT, were entirely removed by the mechanical method (i.e, by plastic tweezers) one by one to measure the magnetization of only monolayer GNMs. After removing, the absence of the multi-layer GNM flakes was reconfirmed following the above-mentioned method.

All GNMs fabricated through these processes (including Figs. 2(c) and 2(f) sample) were annealed at 800 °C under high vacuum (10⁻⁶ Torr) for 0.5–3 days with constant gas pumping and, then, under hydrogen gas by a field-emission-type radical CVD system under greater than

1MPa pressure for at least for 3 hours for all the measurements. The first annealing is for deoxygenation of the pore edges and recovering all damages and defects, while the second annealing is for termination of the carbon atoms at the pore edges by hydrogen atoms.

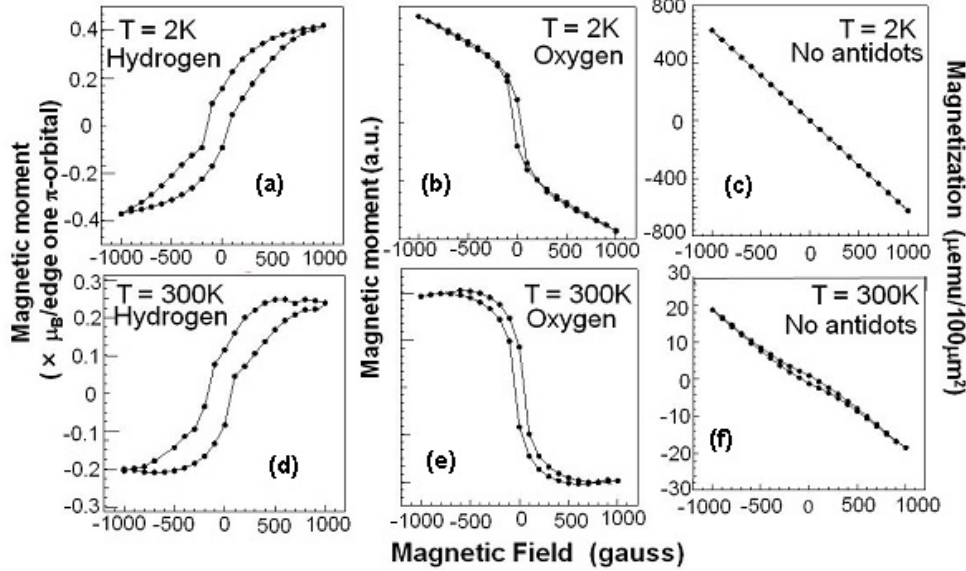


FIG. 2. Magnetization of monolayer GNMs with $\phi \sim 80$ nm and $W \sim 20$ nm for (a)(d) hydrogen-terminated edges; (b)(e) oxygen-terminated edges; and (c)(f) bulk graphene without pore arrays. DC magnetization was measured by a superconducting quantum interference device (SQUID; Quantum Design). Magnetic fields were applied perpendicular to GNMs. The vertical axes in panels (a) and (d) denote magnetic moment per localized-edge orbital, assuming mono-hydrogenation of individual edge carbon atoms

The observation of the features shown in Figs. 2(b) and 2(e) were made after the observation of the feature in Fig. 2(a), and subsequent annealing at 800 °C under high vacuum (10^{-6} Torr) for 3 days with constant gas pumping for dehydrogenation of the edges and, then, under an oxygen atmosphere for 1 hour for oxidization of the pore edges. SQUID measurements were carried out immediately after annealing.

Consequently, a large ensemble of monolayer GNMs with a total area $\sim 4 \times 1$ cm² was prepared for magnetization measurements (Fig. 2) (i.e., one sample consists of at least 4 substrates with monolayer GNMs. The total area does not include the area of the nano-pores. The total number of measured samples was 11). In order to confirm the lack of contribution from NPATs and Si-substrates, the magnetization of the Si-substrates assembled with only NPATs (i.e., without GNMs) was measured as well as the NPATs for Figs. 2(c) and 2(f) (Si-sub + bulk graphenes) and the absence of ferromagnetism was confirmed.

This method offers the following three significant advantages. (1) It gives less damage and defects to the GNMs because of the non-lithographic method. (2) Moreover, the honeycomb-like array of hexagonal nanopores can result in the formation of a large ensemble of GNRs and pore edges with sufficient lengths (e.g., 40 nm in the present case), because the regions between two pores can be GNRs and the presence of six boundaries of hexagonal pore among the neighboring six pores produces six GNR (Fig. 1(e)). In the actual GNM, it is speculated that a mixture of zigzag and armchair edges may exist in one GNR (one pore edge), as confirmed by the STM observation [9]. Even in that case, a large number of GNRs in the present GNMs can

yield a large area of assembled zigzag-edge GNRs. This is extremely effective to detect small magnetic and electric signals arising from pore edges. (3) From a topological reason, when the atomic structure of one pore boundary is aligned with the hexagonal carbon lattice of graphenes (e.g., to zigzag), the other five pore boundaries can have the same edge atomic structure (e.g. zigzag).

In the present experiment, the pore-edge atomic structures could not be intentionally controlled to zigzag type unlike Ref. [20]. However, in Ref. [33], we indirectly proved the presence of zigzag atomic structure at the pore edges by observation of the small ratios of D/G peak heights (< 0.2) in Raman spectroscopy, which were realized by reconstruction of edge atomic structure to a zigzag type by high-temperature annealing, in comparison with previous reports [20, 30]. Indeed, the presence of polarized spins in such H-terminated GNMs was confirmed in inter-pore regions and also at some pore edges by observations using magnetic force microscopy [33]. Moreover, the observed anomalous magnetoresistance (MR) oscillation turned out to be due to the presence of localized electrons at the pore edges in the H-terminated zigzag-type GNMs with ~ 10 layers [33].

(b) Magnetism due to H-terminated pore edges

The magnetization curve measured for the H-terminated monolayer GNM, which showed the low D/G peak ratio values (< 0.2), is shown in Fig. 2(a). A ferromagnetic-hysteresis loop with large amplitude is clearly observed. In addition to this sample, three other samples with low D/G peak heights in Raman spectroscopy exhibited similar ferromagnetism. In contrast, O-terminated GNMs exhibited a diamagnetism-like weak hysteresis loop (Fig. 2(b)). This is consistent with Ref. [6], which reported that the formation of a spin-paired C–O chemical bond drastically reduces the local atomic magnetic moment of carbon at the zigzag edge of GNRs and suppresses the emergence of ferromagnetism. Reference [6] reported that the formation of a spin-paired C=O chemical bond drastically reduces the local atomic magnetic moment of carbon at the zigzag edge of GNRs and suppresses the emergence of ferromagnetism. The disappearance of ferromagnetism in Figs. 2(b) and 2(e) is qualitatively consistent with this theory.

Bulk graphenes without any pores and those assembled with NPATs show few such features, even after H_2 annealing (Figs. 2(c) and 2(f)), implying no contribution of parasitic factors (e.g., defects, impurities) from bulk graphenes. Moreover, presence of less damage or impurities was reconfirmed in most of the bulk-graphene regions, because mechanically exfoliated bulk graphenes showed extremely low D/G peak heights ($\ll 0.1$) and high 2D peak intensity in Raman spectroscopy. These results strongly suggest that the observed ferromagnetism is associated with polarized spins localized at the H-terminated zigzag-pore edges. The ferromagnetism observed at 2 K appears even at room temperature with a larger magnitude for the hysteresis loops (Fig. 2(d)). In Figs. 2(b) and 2(e), even the diamagnetism of graphene has mostly disappeared. One of the reasons is attributed to the formation of a nanopore array, because such an array drastically reduces the bulk graphene area available for the presence of loop currents which produce diamagnetism at the currently applied magnetic-field levels (i.e., corresponding to only GNRs with $W \sim 20$ nm between nanopores; Fig. 1(e)). The radius of the cyclotron motion for electrons is given by $R_c = (\pi n_s)^{1/2} (h/2\pi) / eB$. By observing the magnetoresistance (i.e., commensurability peak), we calculate n_s to be $\sim (4 \times 10^{11}) \text{ cm}^{-2}$ in the present GNMs. Based on this n_s value, R_c is calculated to be as large as ~ 400 nm, even for the largest applied magnetic field of 1000 gauss in Fig. 2. Indeed, this R_c value is 20 times larger than $W \sim 20$ nm between the present nanopores, and it prohibits the emergence of loop currents for the formation of diamagnetism.

Figure 3 shows the correlation between the inter-pore spacing (corresponding to the width of the GNR, W ; Fig.1(e)) and the magnetization. The magnitude of the hysteresis loop was found to decrease with increasing W . In particular, the residual magnetization is inversely proportional to the W value (inset of Fig. 3(c)). This result is qualitatively consistent with theories for the GNR model, according to which, the edge spin stability and ordering of a zigzag-edge GNR are determined by the exchange interaction between the two edges leading to vanishing of ferromagnetic edge spin ordering with increased W [2,5].

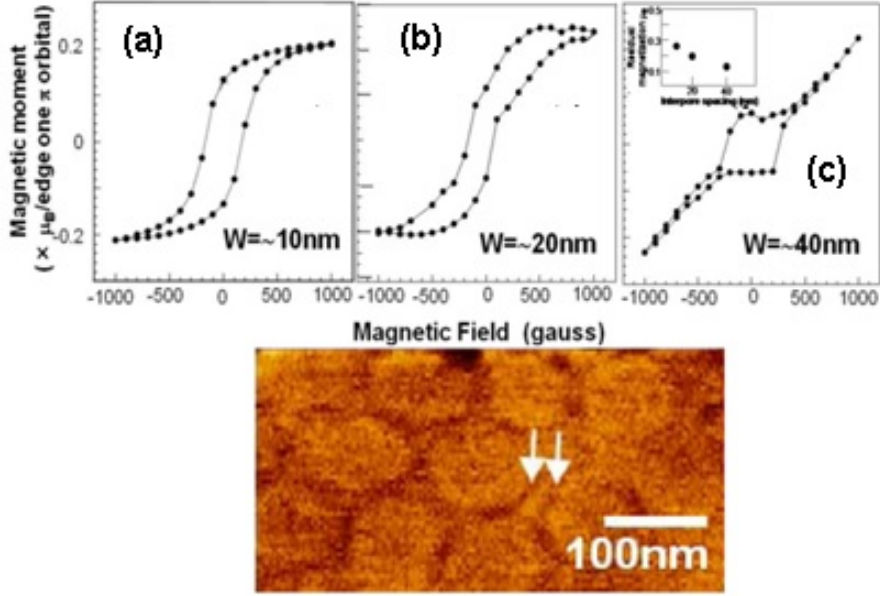


FIG. 3. (a)–(c) Correlation of the magnetization with the mean inter-pore spacing W of monolayer GNMs at $T = 300$ K. Mean pore diameter ($\phi \sim 80$ nm) was kept through all samples. For Figs. 3 (a)–(c), difference in magnetic moment between upper and lower curves of hysteresis loop at $H = 0$ (residual magnetization $B_r \times 2$) is $\sim 0.28 \mu_B$, $\sim 0.2 \mu_B$, $\sim 0.12 \mu_B$ and the loop width at zero magnetic moment (coercivity $H_c \times 2$) is ~ 400 gauss, ~ 260 gauss, ~ 500 gauss, respectively. Inset of (c); B_r at 300 K as a function of W . (d) Magnetic force microscope image of a ferromagnetic GNM. CoPtCr-coated Si-probe was used for measurement with a tapping mode. Darker color means higher densities of polarized spins. In particular, the parts indicated by two arrows evidently show presence of pore-edge localized spins

Such a correlation cannot be understood by ferromagnetism originating from the defects located only at the pore edges or in the bulk graphene between pores. In the former case, the ferromagnetism amplitude should be mostly independent of W , because defects are located only at pore edges. In the latter case, the ferromagnetism amplitude should increase with an increase of W , because the defect density increases. Consequently, we conclude that the observed ferromagnetism is not due to parasitic origins (e.g., defects, impurities) but should be truly attributed to H-terminated zigzag pore edges.

This is also consistent with magnetic force microscope (MFM) observations (Fig. 3(d)). Although the space resolution is poor, we can actually confirm the presence of high densities of polarized spins at the inter-pore regions and also some pore edges under slight magnetic fields. To date, approximately 50% of the samples, which include samples showing the low D/G peak heights, have shown ferromagnetism.

As mentioned above, we could not intentionally form zigzag-type pore-edge atomic structure. Refs. [15] and [16], however, suggested that zigzag edges are the most stable chemically and that arm chair-based edges are reconstructed to zigzag after STM Joule heating for long edges of overlapped graphenes [15] and electron beam (EB) irradiation for pore edges [16].

Ref. [30] reported that edge chirality can be distinguished by the observation that the $I(D)$ for graphene edges were stronger (weaker) at the armchair (zigzag) edges. This is because the double resonance process, which induces the D peak, can only be fulfilled at an armchair edge, when the one-dimensional character of the edge is considered. Indeed, Ref. [30] exhibited $I(D)/I(G)$ value < 0.1 for observation of zigzag edge of graphene flakes by using angle-dependent Raman spectroscopy with a polarized laser beam. This is qualitatively consistent with Fig. 1(e).

The low $I(D)/I(G)$ values are also qualitatively consistent with those reported for GNPs in Ref. [20], whose hexagonal-pore boundaries are intentionally aligned along the carbon hexagonal lattice by specified method, resulting in the formation of pure zigzag pore edges.

There are three different edge structures: zigzag, armchair, and a mixture of the two. Because the possibility of the formation of each structure is basically equal ($\sim 33\%$), the value of 50% for formation of a zigzag edge (samples 1–4) indicates that almost half of the edges for the case of the mixtures (i.e., $\sim 33\%/2 = \sim 17\%$), which are close to the behavior of a zigzag edge, can be reconverted to a zigzag edge by annealing (i.e., $\sim 33\% + \sim 17\% = \sim 50\%$). The remaining 50% of the samples will have armchair edges or large-volume defects.

The stability may be simply understood by the difference in the number of carbon atoms bonded to two neighboring carbon atoms (dangling bonds) for zigzag edge (i.e., one such atom) and arm chair edges (two such atoms) [16]. After removal of such atoms, the arm chair edge requires twice as much energy as the zigzag in order to repair the removed atoms and, thus, becomes unstable. In our system, we carried out high -temperature annealing for narrow ($W \sim 20$ nm) GNRs (i.e., narrow inter-pore spacing). This might bring the energy similar to those in Refs. [15,16] and cause the reconversion of edge atomic structures to zigzag.

However, this is strongly case-dependent. Edge reconstruction occurs under some conditions; e.g., electron beam (EB) irradiation during HRTEM observation (Ref. [16]), Joule heating by a STM probe (Ref. [15]), and high temperature annealing. Thus, the exact values of activation energy for cutting and reconstructing edge C-C bonds should be experimentally investigated and be determined as universal values in the future.

Currently, refs. [15] and [16] argue that the zigzag edge is the most stable and arm chair-based edges are reconverted to zigzag ones after EB irradiation for pore edges and STM Joule heating for long edges of overlapped graphenes, while “PRL 101, 115502” and “PRB 80, 073401” interestingly argues that 5–7 zigzag edge is stable after EB irradiation. These results may look controversial.

However, to the best of our knowledge and experience, 5–7 edge structures have been merely observed and reported to date, because they consist of peculiar polygons except for hexagon. Indeed, the “PRB 80, 073401” exhibited only very small parts of the edges. Thus, we don’t think that the 5–7 edge can stably exist within a long range along long edges like our hexagonal nanopore with a 40 nm length for one boundary. Moreover, 5–7 edge can be one of disordered edge structures and, hence, large $I(D)/I(G)$ ratios should be observed in Raman spectroscopy. This is not consistent with our results. Therefore, we concur with the argument put forth in refs. [15] and [16].

The observation of edge atomic structures is indispensable for present experiments. However, it is extremely difficult to do this at this time, because for HRTEM observation,

GNMs cannot be fabricated on a TEM grid, and for STM observation, the GNMs do not have a large enough conductivity for such measurements. The GNMs formed on Cu substrates may solve this problem for STM observations, because such a substrate provides a high conductivity, although the atomic edge structures may be affected by the Cu substrate.

(c) *Theoretical discussion of edge magnetization values*

Here, employing the GNR model, which assumes pure zigzag pore edges (i.e., without any defects) at all regions, allows one to estimate the magnetic moment of edge carbon atoms that contribute to the ferromagnetism observed in Fig. 2. Assuming that only edge dangling bonds have localized spin moments, the magnetic moment per edge dangling bond prior to H termination is estimated to be $(1.2 \times 10^{-23}) / (\mu_B = 9.3 \times 10^{-24}) \sim 1.3\mu_B$, where μ_B is the Bohr magneton, as follows.

(1) The total area of assembled bulk graphenes used for the pore array formation is $\sim 4 \text{ cm}^2$. (2) The area of one hexagonal unit cell with a pore is $S = 6(3^{-1/2}/2)(a/2)^2 \sim 4300 \text{ nm}^2$, where $a = [80 \text{ nm (pore diameter)} + 20 \text{ nm (interpore spacing)}]$. (3) Thus, the total number of pores is $(4 \text{ cm}^2)/(4300 \text{ nm}^2) \sim 1011 [(1)/(2)]$. (4) The total number of dangling bonds per hexagonal pore is $(40 \text{ nm})/(0.142 \text{ nm} \times 3^{1/2}) \times 6 = 166 \times 6 \sim 1000$. (5) The total number of edge dangling bonds of the GNM used for the SQUID measurement is $1014 [(3) \times (4)]$.

Therefore, using (5), the saturation magnetization per edge dangling bond is estimated to be $1.2 \times 10^{-6} \text{ (emu)} \times 10^{-3}/10^{14} = 1.2 \times 10^{-23} \text{ (J/T)}$. Thus, the magnetic moment per edge dangling bond is estimated to be $(1.2 \times 10^{-23})/(\mu_B = 9.3 \times 10^{-24}) \sim 1.3 \mu_B$. This value is very large compared with previous theoretical predictions. Conventionally, GNRs with no H-termination of dangling bonds should show antiferromagnetism, theoretically. However, in the above estimation, the observed total magnetization was divided by estimated number of edge dangling bonds in the GNM, neglecting this theory. This led to the problem.

Next, after H annealing at high temperature, edge dangling bonds of a GNR are terminated by H atoms [3, 5–7, 9]. The following three types of H terminations are theoretically possible. (1) All edge dangling bonds are each terminated by one H atom on both -side zigzag edge. This provides a flat band for $2\pi/3 \leq k \leq \pi$ in the Brillouin zone. Electrons are well localized at the edges. (2) All the edge dangling bonds of one side are each terminated by two H atoms (so that the edge carbon atom becomes tetrahedrally coordinated; a bearded edge), while the opposite-side dangling bonds are terminated by a single H atom. The GNR provides a flat band for $0 \leq k \leq \pi$, resulting in a completely localized “on-bonding state” around the Fermi level (E_F). This leads to the spin polarization of all carbon atoms. (3) The double H atom termination of the zigzag-edge carbon atoms on both sides of a GNR provides a flat band for $0 \leq k \leq 2\pi/3$ and creates a modified zigzag edge.

The type of edge H-termination could not be observed in the present experiment. However, our case should correspond to case (1) for the following reason; the mono-H termination of the edge dangling bond decreases its magnetic moment to one μ_B . The magnetic moment of one localized-edge π orbital is, therefore, estimated to be as large as $(\sim 1.3\mu_B - 1 \mu_B) = \sim 0.3 \mu_B$. This is in fairly good agreement with the theoretical contribution of the π -orbital state to the edge magnetic moment of $\sim 0.3 \mu_B$ in a zigzag-edged GNR within the ferromagnetically ordered spin configuration [5].

We have estimated the edge magnetization based on a GNR model with zigzag edges, assuming the presence of perfect zigzag-pore edges at all parts of our GNMs. In contrast, even a small defect may still be present in actual pore edges. In order to elucidate the influence of such residual small-volume edge disorder on GNM magnetism, we performed systematic first-principles calculations of magnetic properties of quasi-GNR structures (Fig. 4(a), corresponding

to the inter-pore region) based on Lieb's theorem [29], which assumes slight disorder at the upper edge. Interestingly, the ground state of quasi-GNR structure turned out to be ferromagnetic in Fig. 4(b). The calculated net magnetic moment follows Lieb's theorem with local moments up to $0.2 \mu_B/\text{edge atom}$ and depends on magnitude of the assumed edge disorder. These values agree fairly well with the value estimated from the GNR model. In order to determine which models are more relevant to the actual structures, observation of pore edge atomic structures is indispensable.

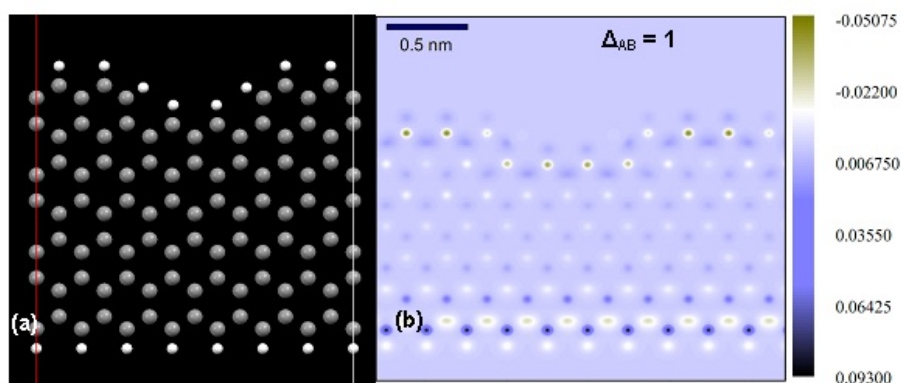


FIG. 4. Model and calculation result for net magnetism (Lieb's theorem) (a) Structure of hydrogen-passivated quasi-GNR, which employs slight curvature (disorder) with $\Delta_{AB} = 1$ (the difference between the number of removed A and B sites of the graphene sublattices at zigzag edges) on the upper edge, used for first-principles calculations based on Lieb's theorem. The dark and white atoms are carbon and hydrogen, respectively. (b) Calculated spin-density distribution of quasi-GNR for (a), which gives the edge magnetic moment of $0.2 \mu_B$ to the lower edge

2.2. Novel spin-phenomena in few-layer ferromagnetic GNMs

Although we have reported spin polarization at the pore edges of monolayer GNMs in the present study, the GNMs didn't show clear electronic features, because lithography was used for electrode formation on the monolayer GNM. This method introduced contamination and disorder to the pore edges. The resistivity of the GNMs was also very high.

In contrast, as mentioned above, we reported periodic MR oscillations arising from electrons localized at H-terminal pore edges in weak-ferromagnetic GNMs with ~ 10 layers, when magnetic fields were applied perpendicularly to the GNMs layers [33]. The observed oscillation period proved that the electron orbit localizing at the pore edges produced the oscillation with a period, which is shorter than those caused by cyclotron-motion electrons due to applied fields. This result suggested that contamination and disorder exist only around the topmost surface or the sub-surface layers, while lower layers (e.g., the fifth layer) should have mostly no such influence. Thus, also in the present measurements, we measured MR behaviors of H-terminated GNMs with ~ 5 layers. Although the magnitude of spin polarization at pore edges becomes weaker in the ~ 5 layer GNMs compared with that of monolayer GNMs, the GNMs actually exhibited small -magnitude but evident ferromagnetism in magnetization measurements and proved presence of polarized edge spins [28].

Figure 5(a) and 5(b) show typical drain current (I_{sd}) vs. drain voltage (V_{sd}) and I_{sd} vs. back-gate voltage (V_{bg}) behaviors for a ~ 5 layer ferromagnetic GNM, respectively. In Fig.5(a), a strong zero-bias anomaly was observed. That can be attributed to either a single electron charging effect in narrow GNR regions among the nano-pores or poor interface between the Au electrodes and the GNM. Figure 5(b) displays an n-type semiconductive behavior, also due to narrow inter-pore GNR regions, which can introduce energy band gaps [17]. Because the band gaps are attributed to confinement of electrons into the one-dimensional space of the inter-pore regions (i.e., GNRs) [17], it is consistent with the presence of zigzag pore edges.

(a) Spin pumping effect under parallel fields

Figures 5(c) and 5(d) show MR (R_{xx}) behaviors for two different- W -value ferromagnetic GNMs ($W \sim 30$ nm and ~ 40 nm) for inset of Fig. 5(a)-pattern under a constant current (I_{sd}) mode of a four probe measurement, when magnetic fields are applied in parallel with the GNM planes ($B_{||}$). They show saw-tooth like MR oscillations, in which the MR monotonically increases with increasing fields, while it abruptly drops at a critical field and starts to increase

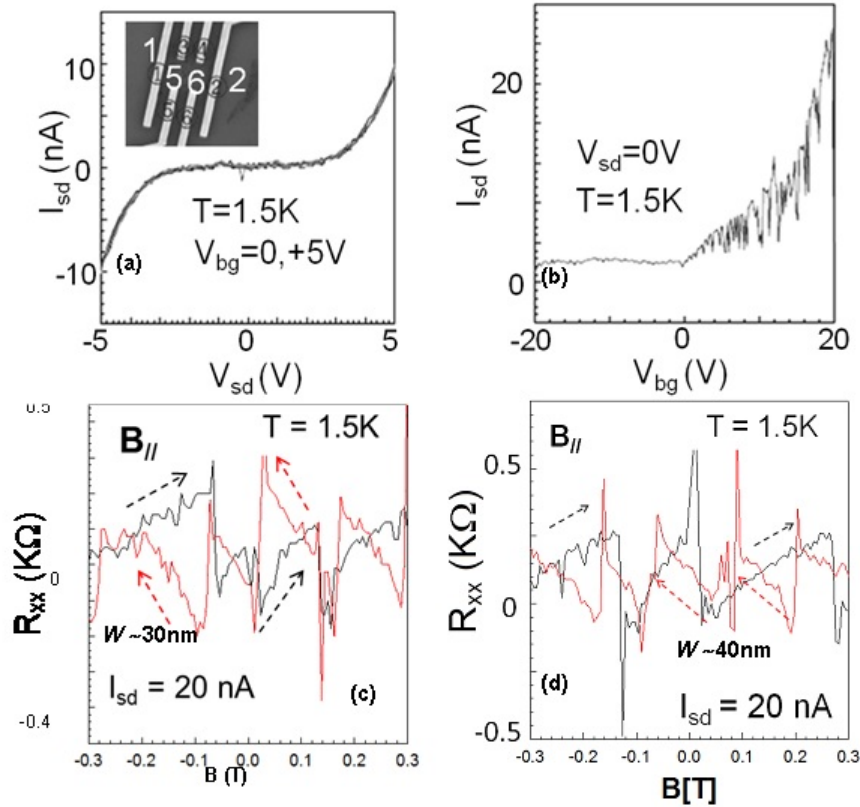


FIG. 5. (a)(b) Typical I_{sd} vs. V_{sd} (a) and I_{sd} vs. V_{bg} (b) behaviors measured between electrodes 1 and 2 (inset) in a ferromagnetic GNM with ~ 5 layers. (a) exhibits an n-type semiconductive behavior due to the narrow inter-pore regions (i.e., GNRs) (Fig. 1(e)). Inset: SEM image of Hall pattern (six probes) formed on a GNM with ~ 5 layers. MR (R_{xx}) between electrodes 5 and 6 was measured under a constant I_{sd} of 20 nA between electrodes 1 and 2. (c) (d) MR (R_{xx}) behaviors under parallel fields in different two samples with ~ 5 layers (i.e., $W \sim 30$ nm for (c) and ~ 40 nm for (d), $\phi \sim 80$ nm is common). V_{bg} was set to +20 V. Arrows mean sequence of applied B (e.g., from -0.3 T to $+0.3$ T or from $+0.3$ T to -0.3 T)

again in a repeated manner. In Fig. 5(c) for $W \sim 40$ nm, at $B < -0.05$ and $0.15 < B$, the oscillation periods are larger than those in two oscillations around $B = 0$. The periods for all oscillations are the same for increasing and decreasing B . In contrast, in Fig. 5(d) for $W \sim 40$ nm, the oscillation becomes ambiguous. We call this saw-tooth like MR oscillation as spin pumping effect. The effect means a repeated cycle of accumulation (increased number) of polarized spins and its abrupt emission (decreased number) at critical fields, depending on the applied fields. Such anomalous behaviors cannot be interpreted by any previous MR phenomena (e.g., ferromagnetic MR behavior, giant MR, tunnel MR, and spin valve effect).

In the present case, spin-polarized electrons localize at the pore edges under thermal equilibrium. However, under non-thermal equilibrium, caused by a constant current flow for Fig. 5(b), the flat bands at the pore edges are modulated and, thus, some of polarized edge-electron-spins don't localize at the pore edges and can flow through bulk graphene regions amongst the pores. In our previous ~ 10 -layer GNMs with $W \sim 20$ nm [33], the spin pumping effect was not observed under parallel fields, although MR oscillation arising from pore-edge localized electrons was found under perpendicular fields. This implies that enough inter-pore space W for electron transport between electrodes is indispensable for the spin flow and detection of the spin pumping effect (Fig. 6).

One of the qualitatively possible interpretations for the spin pumping effect might be as follows. When the applied magnetic field increases, the number of accumulated polarized-spins increase at the pore edges. Moreover, other electrons, which are flowing in bulk graphene regions among the pores, also accumulate at the flat energy band of the pore edges. However, the accumulation of edge-polarized-spins saturate and the excess spins are abruptly emitted at a critical field, as parallel magnetic fields increase further, because the flat band is modulated in the GNM plane by increasing parallel fields, more or less. After the emission of the accumulated excess spins, the flat band partially recovers to near the initial condition and the pore edges can allow further accumulation of spins. Then, MR starts to increase again. In Fig. 5(d) with $W \sim 40$ nm, the oscillation becomes ambiguous as mentioned above. This is qualitatively consistent with decrease in the ferromagnetism amplitude shown in Fig. 3(c), that is, reduction of amplitude of polarized spins at the pore edges in monolayer GNMs. This suggests the presence of optimized W values (e.g., 30 nm), which are most suitable for the appearance of a spin pumping effect. Large W values weaken the magnitude of polarized spins at the pore edges, while small W values obstruct spin flow between electrodes and make spin flow detection difficult (Fig. 6). Further clarification of the exact mechanism is expected in near future.

(b) Hysteresis loop in MR under perpendicular fields

More importantly, we confirm presence of a ferromagnetic-like MR hysteresis loop (Fig. 7), when a magnetic field is applied perpendicularly to the ferromagnetic GNM plane with $W \sim 30$ nm. Although the loop is not perfectly evident, it is somewhat reproducible. This observation can also be understood from polarized-spin transverse between electrodes due to the presence of enough interpore space as mentioned above (Fig. 6). This result is extremely important and is useful to realize all-carbon spintronic devices like magnetic semiconductors (e.g., (In, Mn), As). Indeed, this loop disappears when V_{bg} is set to -20 V in Fig. 5(b). Thus, one can control the switching of the MR hysteresis loop by changing V_{bg} . This makes feasible spin memory devices despite the absence of magnetic atoms. Magnetic semiconductors cannot work at room temperature, while the present feature in ferromagnetic GNMs appears even at room temperature (Fig. 2(d)). It, therefore, must open a new door to magnetic-atom free spintronics to resolve present environmental and resource problems.

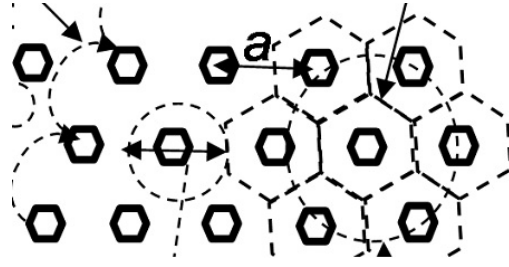


FIG. 6. Schematic top view of a GNM with current path. Under enough large W (i.g., > 30 nm), electrons including pore-edge localized spins can transvers between electrodes because of the reduced pore scattering. Cyclotron-motion electrons also form a runaway orbit and transvers, when the diameter of the motion agrees with the unit cell diameter, a

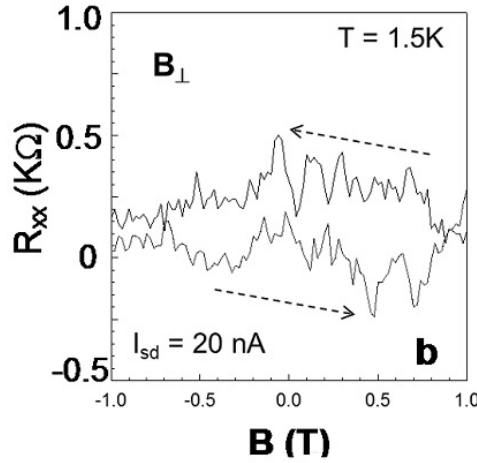


FIG. 7. MR (R_{xx}) behaviors under perpendicular fields in the sample for Fig. 5(c) with $W \sim 30$ nm. V_{bg} was also set to $+20$ V. Arrows mean sequence of applied B

3. Conclusion

In conclusion, we have successfully fabricated low-defect mono-layer GNMs by using a non-lithographic method (i.e., using NPATs as etching masks) and found the emergence of large-amplitude ferromagnetism even at room temperature, only when pore edges of the GNMs were H-terminated. The observed correlation between the inter-pore spacing and magnetism and also MFM observation supported that this was attributed to polarized electron spins localized at the zigzag pore-edges. The magnetic moment per edge dangling bond ($\sim 0.3\mu_B$) was also quantitatively in good agreement with theories for pure zigzag-GNR and also defected-GNR models (Lieb's theorem). Moreover, a spin pumping effect was found for fields applied in parallel to the GNM planes in few-layer ferromagnetic GNMs, while the MR hysteresis loop was observed under perpendicular fields. The optimized inter-pore spacing was found to be useful for detection of evident spin pumping effect and the MR hysteresis loop as well.

As mentioned in introduction, spin-based phenomena in graphenes, which were once only predicted by theories [22,25–27], have now been observed experimentally. One experiment reported on the observation of a large spin diffusion current due to the large spin coherence in high-quality graphene on a hexagonal boron-nitride substrate [32]. The other experiment mentioned in its introduction a report on the observation of SHE in dihydrogenated graphenes

by possibly introducing strong SOI, although some questions still remain. These suggest that spin-based phenomena in graphenes are approaching new stages and also the observations of present edge-spin phenomena open a new door towards the creation of novel spintronic devices. The present ferromagnetic GNMs must also be rare-element free, invisible and flexible in order to be utilized in ultra-light (wearable) magnets and spintronic devices, which can circumvent environmental and material-resource problems.

Acknowledgement

The authors thank K. Fujita, Y. Hashimoto, E. Endo, Y. Iye, S. Katsumoto, M. Yamamoto, S. Tarucha, T. Ando, T. Enoki, M. Koshino, J. Akimitsu, T. Muranaka, H. Aoki, S. Roche, P. Kim, X. Jia, and M. S. Dresselhaus for their technical contribution, fruitful discussions, and encouragement. This work at Aoyama Gakuin was partly supported by a Grant-in-aid for Scientific Research (Basic research A: 24241046) in MEXT, a High-Technology Research Center Project for private universities in MEXT, and also AFOSR grant. M.C. and H. X.Y. acknowledge support by French ANR PNANO project “Nanosim -Graphene” and Grenoble Nanosciences Foundation.

References

- [1] Nakada K., Fujita M., Dresselhaus G., Dresselhaus M. S. Edge state in graphene ribbons: Nanometer size effect and edge shape dependence. *Phys. Rev. B*, **54**, P. 17954 (1996) .
- [2] Fujita M., Wakabayashi K., Nakada K., Kusakabe K. Peculiar Localized State at Zigzag Graphite Edge. *J. Phys. Soc. Jpn.*, **65**, P. 1920 (1996).
- [3] Kusakabe K., Maruyama M. Magnetic nanographite. *Phys. Rev. B*, **67**, P. 092406(4p) (2003).
- [4] Okada S., Oshiyama A. Magnetic Ordering in Hexagonally Bonded Sheets with First-Row Element. *Phys. Rev. Lett.*, **87**, P. 146803(6p) (2001).
- [5] Lee H., Son Y.-W., et al. Magnetic ordering at the edges of graphitic fragments: Magnetic tail interactions between the edge-localized states. *Phys. Rev. B*, **72**, P. 174431 (2005).
- [6] Veiga R.G.A., Miwa R.H., Srivastava G.P. Quenching of local magnetic moment in oxygen adsorbed graphene nanoribbons. *J. Chem. Phys.*, **128**, P. 201101(3p) (2008).
- [7] Lee H., Park N., et al. Ferromagnetism at the edges of the stacked graphitic fragments: an ab initio study. *Chem. Phys. Lett.*, **398**, P. 207–201 (2004).
- [8] Asano H., Muraki S., et al. Strong magnetism observed in carbon nanoparticles produced by the laser vaporization of a carbon pellet in hydrogen-containing Ar balance gas. *J. Phys.: Cond. Mat.*, **22**, P. 334209(4p) (2010).
- [9] Enoki T., Takai K. The edge state of nanographene and the magnetism of the edge-state spins. *Sol. State Commun.*, **149**, P. 1144–1150 (2009).
- [10] Niimi Y., Matsui T., et al. Scanning tunneling microscopy and spectroscopy of the electronic local density of states of graphite surfaces near monoatomic step edges. *Phys. Rev. B*, **73**, P. 085421 (2006).
- [11] Son Y.-W., Cohen M.L., Louie S.G. Energy Gaps in Graphene Nanoribbons. *Phys. Rev. Lett.*, **97**, P. 216803(4p) (2006).
- [12] Yang L., Louie S.G., et al. Quasiparticle Energies and Band Gaps in Graphene Nanoribbons. *Phys. Rev. Lett.*, **99**, P. 186801(4p) (2007).
- [13] Shima N., Aoki H. Electronic structure of super-honeycomb systems: A peculiar realization of semimetal/semiconductor classes and ferromagnet. *Phys. Rev. Lett.*, **71**, P. 4389–4392 (1993).
- [14] Rosser J.F., Palacios J.J. Magnetism in Graphene Nanoislands. *Phys. Rev. Lett.*, **99**, P. 177204 (2007)s.
- [15] Jia X., Hofmann M., et al. Controlled Formation of Zigzag and Armchair Edges in Graphene Nanoribbons by Joule Heating. *Science*, **323**, P. 1701 (2009).
- [16] Girit C.O., Meyer J.C., et al. Graphene at the edge: Stability and Dynamics. *Science*, **323**, P. 1705 (2009).
- [17] Shimizu T., Haruyama J., et al. Large intrinsic energy bandgaps in annealed nanotube-derived graphene nanoribbons. *Nature Nanotech.*, **6**, P. 45–50 (2011).
- [18] Han M.Y., Brant J.C., Kim P. nsElectron Transport in Disordered Graphene Nanoribbons. *Phys. Rev. Lett.*, **104**, P. 056801(4p) (2010).

- [19] Wang X., Ouyang Y., et al. Room-Temperature All-Semiconducting Sub-10-nm Graphene Nanoribbon Field-Effect Transistors. *Phys. Rev. Lett.*, **100**, P. 206803(4p) (2008).
- [20] Krauss B., Nemes-Incze P., et al. Raman Scattering at Pure Graphene Zigzag Edges. *Nano Lett.*, **10**, P. 4544–4548 (2010).
- [21] Bai J., Zhong X., et al. Graphene nanomesh. *Nature Nanotech.*, **5**, P. 190–194 (2010).
- [22] Son Y.-W., Cohen M.L., Louie S.G. Half-metallic graphene nanoribbons. *Nature*, **444**, P. 347–349 (2006).
- [23] Takesue I., Haruyama J., et al. Superconductivity in Entirely End-Bonded Multiwalled Carbon Nanotubes. *Phys. Rev. Lett.*, **96**, P. 057001(4p) (2006).
- [24] Murakami S., Nagaosa N., Zhang S.-C. Dissipationless Quantum Spin Current at Room Temperature. *Science*, **301**, P. 1348–1351 (2003).
- [25] Kane C.L., Mele E.J. Quantum Spin Hall Effect in Graphen. *Phys. Rev. Lett.*, **95**, P. 226801(4p) (2005).
- [26] Kane C.L. Graphene and the Quantum Spin Hall Effect. *Int. J. Modern Phys. B*, **21**, P. 1155–1164 (2007).
- [27] Schmidt M.J., Loss D. Edge states and enhanced spin-orbit interaction at graphene/graphane interfaces. *Phys. Rev. B*, **81**, P. 165439(12p) (2010).
- [28] Otani M., Koshino M., Takagi Y., Okada S. Intrinsic magnetic moment on (0001) surfaces of rhombohedral graphite. *Phys. Rev. B*, **81**, P. 161403(R)(4p) (2010).
- [29] Yang H., Chshiev M., et al. Inducing and Optimizing Magnetism in Graphene Nanomesh. URL: <http://arxiv.org/abs/1103.4188>.
- [30] You Y.-M., Ni Z.-H., Yu T., Shen Z.X. Edge chirality determination of graphene by Raman spectroscopy. *Appl. Phys. Lett.*, **93**, P. 163112(1–3) (2008).
- [31] Soriano D., Leconte N., et al. Magnetoresistance and Magnetic Ordering Fingerprints in Hydrogenated Graphene. *Phys. Rev. Lett.*, **107**, P. 016602(4p) (2011).
- [32] Abanin D.A., Morozov S.V., et al. Giant nonlocality near the Dirac point in graphene. *Science*, **332** (6027), P. 328–330 (2011).
- [33] Shimizu T., Nakamura J., et al. Magnetoresistance oscillations arising from edge-localized electrons in low-defect graphene antidot-lattices. *Appl. Phys. Lett.*, **100**, P. 023104 (2012).

SYNTHESIS, ISOLATION, AND X-RAY STRUCTURAL CHARACTERIZATION OF TRIFLUOROMETHYLATED C₉₀ FULLERENES: C₉₀(30)(CF₃)₁₈ AND C₉₀(35)(CF₃)₁₄

N. B. Tamm¹, S. I. Troyanov¹

¹Department of Chemistry, Moscow State University, Moscow, Russia

tamm@thermo.chem.msu.ru, stroyano@thermo.chem.msu.ru

PACS 61.48.-c

Two CF₃ derivatives of C₉₀, C₉₀(30)(CF₃)₁₈ and C₉₀(35)(CF₃)₁₄, have been isolated via HPLC from the products of a high-temperature trifluoromethylation of a C₇₆–C₉₆ fullerene mixture with CF₃I. Their molecular structures were determined by single crystal X-ray crystallography using synchrotron radiation. The addition patterns of the new compounds are discussed in comparison with those of the corresponding chlorinated C₉₀.

Keywords: Fullerenes, C₉₀, Trifluoromethylation, HPLC, Structure elucidation.

1. Introduction

Compared to C₆₀ and C₇₀, the investigation of higher fullerenes has been hampered by their relatively low abundance in fullerene soot and due to the existence of cage isomers [1]. Structural characterization of pristine higher fullerenes is typically accomplished by means of ¹³C NMR spectroscopy, which provides information on molecular symmetries. However, identification of higher fullerenes by this conventional method is not unambiguous in many cases since several isomers may exhibit the same molecular symmetry [2,3]. An efficient alternative is chemical derivatization of higher fullerenes followed by isolation and structural characterization of the derivatives thus obtained, as exemplified by several examples for C₇₆–C₉₆ [4–12].

C₉₀ belongs to the group of higher fullerenes with magic (6*n*) number of carbon atoms, which usually possess higher abundance and richer isomerism compared to their neighboring members [13]. For C₉₀, there are 46 topologically possible isomers obeying the Isolated Pentagon Rule (IPR) [1]. Experimentally, ¹³C NMR spectra of chromatographic C₉₀ fractions were interpreted as showing the existence of five isomers of C_{2v}, C_s, C₂, C₁, and C₂ symmetry [14,15]. A comparison between the experimental and theoretically predicted ¹³C NMR shifts allowed the establishment of most probable carbon cages, 28 (C₂), 30 (C₁), 32 (C₁), 35 (C_s), 40 (C₂), 45 (C₂) and 46 (C_{2v}), which are present in the C₉₀ fractions [16]. X-ray crystallographic study of co-crystals of C₉₀ from three HPLC fractions (obtained from arc-discharge of Sm₂O₃-doped graphite rods) with Ni^{II}(OEP) (OEP - octaethylporphirin) resulted in the structural confirmation of three isomers of pristine C₉₀, 1 (D_{5h}), 30, and 32 [17,18].

A trifluoromethylated derivative of C₉₀, C₉₀(CF₃)₁₂, was suggested to contain C₁-C₉₀(32) cage on the basis of its ¹⁹F NMR spectrum [19]. X-ray crystallographic investigation of C₉₀Cl_{*n*} (*n* = 22, 24, 28, and 32) unambiguously confirmed the C₉₀ cages nos. 28, 30, 32,

34 (C_s), 35, and 46 and significantly contributed to the study of their reactivity towards inorganic chlorides [20,21].

Herein, we report the synthesis, HPLC isolation, and X-ray structure elucidation of trifluoromethylated derivatives of two C_{90} isomers, $C_{90}(30)(CF_3)_{18}$ and $C_{90}(35)(CF_3)_{14}$. Addition patterns are discussed and compared with those of the corresponding chlorinated C_{90} .

2. Results

A starting higher fullerene mixture (35-45 mg; MER Corp.) contained C_{76} – C_{96} fullerenes with the highest abundance of C_{84} and small admixtures of C_{60} and C_{70} [22]. The reaction with CF_3I was performed at 420 °C in a glass ampoule for 48 h, whereas the reaction at 560 °C (in a quartz ampoule) lasted only 1 h (see [23] for more details). In both cases, the trifluoromethylation products sublimed in the colder parts of the ampoules contained mixtures of fullerene(CF_3) $_{2n}$ derivatives with $2n$ in the range of 12 – 20 according to MALDI TOF mass spectrometric analyses (fig. 1).

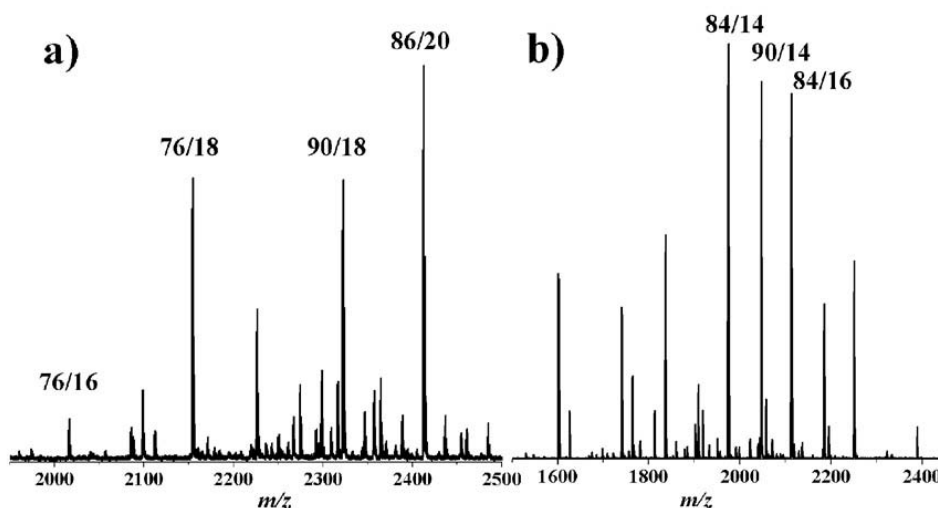


FIG. 1. Mass spectra of trifluoromethylation products. (a) reaction at 420 °C; (b) reaction at 560 °C. The compositions of $C_{2m}(CF_3)_{2n}$ derivatives are given as $2m/2n$.

The product obtained at 420 °C was subjected to a two-step HPLC separation in hexane (Buckyprep column, 10 mm i.d. \times 250 mm, flow rate 4.6 mL min $^{-1}$, monitored at 290 nm). The fraction collected at 13.5 min in the second HPLC step contained mainly a $C_{90}(CF_3)_{18}$ species. Slow concentration of the solution afforded small orange crystals of $C_{90}(CF_3)_{18}\cdot 1.5$ Hexane, which have been investigated by single crystal X-ray diffraction using synchrotron radiation.

The sublimation product from the synthesis at 560 °C was first separated by HPLC in toluene at the same chromatographic conditions; the fraction eluted between 6.3 and 6.6 min was further separated using a toluene/hexane (1/1) mixture as the eluent. The fraction eluted at 19.4 min contained $C_{90}(CF_3)_{14}$ species (fig. 2). Recrystallization from *o*-dichlorobenzene (*o*-DCB) afforded small red crystals. The crystal structure of $C_{90}(CF_3)_{14}\cdot 2.5$ (*o*-DCB) was determined by X-ray single crystal crystallography using synchrotron radiation.

Synchrotron X-ray data were collected at 100 K at the BL14.2 at the BESSY storage ring (PSF at the Free University of Berlin, Germany) using a MAR225 CCD detector. Crystallographic data along with some details of data collection and structure refinements are

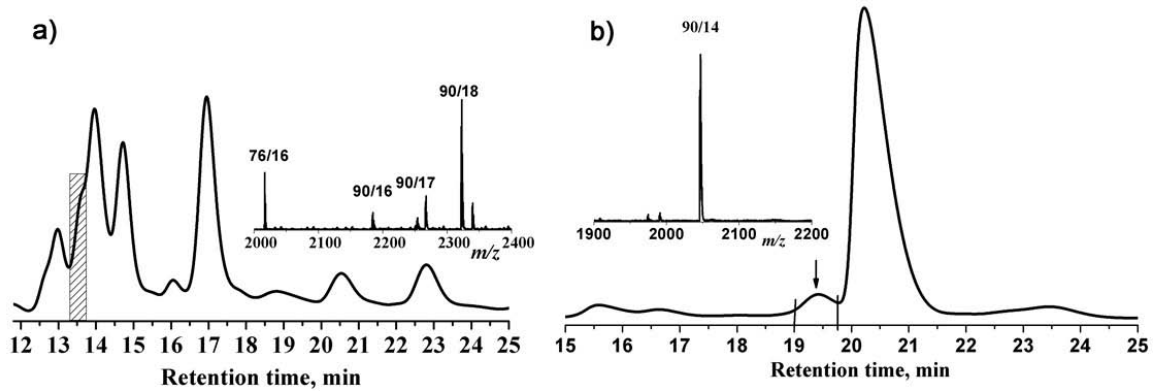


FIG. 2. Chromatographic isolation $C_{90}(CF_3)_{18}$ (a) and $C_{90}(CF_3)_{14}$ (b). The fractions collected are indicated by hatching (a) or arrow (b). Insets show mass spectra of the collected fractions. The compositions of $C_{2m}(CF_3)_{2n}$ derivatives are given as $2m/2n$.

TABLE 1. Crystallographic data and some details of data collection and refinement for $C_{90}(CF_3)_{18} \cdot 1.5\text{Hexane}$ and $C_{90}(CF_3)_{14} \cdot 2.5(o\text{-DCB})$

Compound	$C_{90}(CF_3)_{18} \cdot 1.5\text{Hexane}$	$C_{90}(CF_3)_{14} \cdot 2.5(o\text{-DCB})$
M_r	2452.34	2427.41
Crystal system	Monoclinic	Triclinic
Space group	$C2/c$	$P\bar{1}$
a [Å]	47.661(4)	14.206(1)
b [Å]	22.404(2)	24.343(2)
c [Å]	16.352(1)	25.359(2)
α [°]	90	93.312(3)
β [°]	97.516(6)	99.786(8)
γ [°]	90	102.104(3)
V [Å ³]	17311(2)	8410.0(11)
Z	8	4
D_c [g cm ⁻³]	1.882	1.907
Crystal size [mm]	0.02×0.02×0.01	0.05×0.02×0.01
Detector; λ [Å]	MAR225 / 0.9050	MAR225 / 0.8856
Temperature [K]	100	100
$\theta(\text{max})$ [deg]	36.94	36.67
Refs collected / $R(\text{int})$	121922 / 0.051	122394 / 0.191
Data / parameters	17704 / 1712	33354 / 3099
R_1 [$I \geq 2\sigma(I)$] / wR_2 (all)	0.060 / 0.160	0.090 / 0.216
$\Delta\rho$ (max / min) [e Å ⁻³]	1.107 / -1.265	0.391 / -0.426

presented in Table 1. The structures were solved with SHELXD and anisotropically refined with SHELXL. In the crystal structure of $C_{90}(CF_3)_{18} \cdot 1.5\text{Hexane}$, seven CF_3 groups and solvated hexane molecules are strongly disordered. In the crystal structure of $C_{90}(CF_3)_{14} \cdot 2.5(o\text{-}C_6H_4Cl_2)$, there are two crystallographically independent $C_{90}(CF_3)_{14}$ molecules. One CF_3 group and three of six independent dichlorobenzene molecules are disordered. Crystallographic data are deposited under CCDC-917604 and -917603, respectively.

3. Discussion

Mass spectrometric MALDI analyses of trifluoromethylation products demonstrate the presence of $C_{90}(CF_3)_{2n}$ species with $2n$ ranging from 12 to 20, however, without information concerning the C_{90} cage connectivity and CF_3 addition patterns. HPLC separation supported by subsequent MALDI MS analyses of separated fractions indicates the occurrence of several different $C_{90}(CF_3)_{2n}$ isomers of the same composition whereas their assignment to specific C_{90} cages remained unknown. Growing crystals from separated fractions followed by X-ray crystallographic structure determination using synchrotron radiation was successful in only two cases of $C_{90}(CF_3)_{14}$ and $C_{90}(CF_3)_{18}$, which are the first examples of unambiguous structural characterization of CF_3 derivatives of C_{90} fullerene (fig. 3).

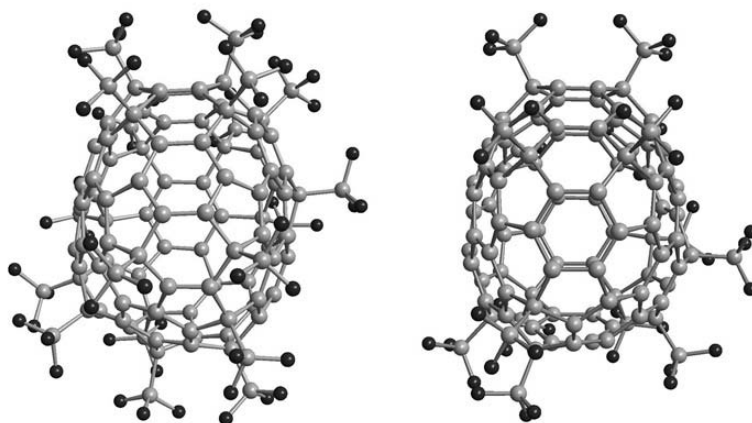


FIG. 3. Projections of the $C_{90}(30)(CF_3)_{18}$ (left) and $C_{90}(35)(CF_3)_{14}$ (right) molecules.

An analysis of the carbon cage connectivities in two molecules reveals that they contain different C_{90} cages, $C_s\text{-}C_{90}(35)$ and $C_1\text{-}C_{90}(30)$, respectively, i.e., the C_{90} isomers, which have been already confirmed previously either in a pristine form (disordered C_{90} (30) cage in co-crystals with $Ni^{II}(\text{OEP})$ [18]) or as chlorinated derivatives (both 30 and 35 isomers [21]). The description of molecular structures, their addition patterns, and comparison with corresponding chloro derivatives are convenient to perform using Schlegel diagrams (figs. 4 and 5).

In the $C_1\text{-}C_{90}(30)(CF_3)_{18}$ molecule, 18 CF_3 groups are attached to a $C_1\text{-}C_{90}$ cage exclusively in positions of double hexagon junctions (DHJs), whereas positions of triple hexagon junctions (THJs) remain unoccupied (fig. 4). All cage pentagons contain one or two attached CF_3 groups. The stabilization of the addition pattern is achieved due to the formation of five isolated or partially isolated $C=C$ bonds (av. bond length 1.33 Å) and one partially isolated benzenoid ring (av. C-C bond length 1.39 Å).

The previous X-ray crystallographic characterization of $C_{90}(30)$ fullerene derivative has been performed on the crystal, which contained both $C_{90}(30)Cl_{22}$ and $C_{90}(28)Cl_{24}$ molecules in the unit cell [20,21]. A comparison of the addition patterns of $C_{90}(30)(CF_3)_{18}$

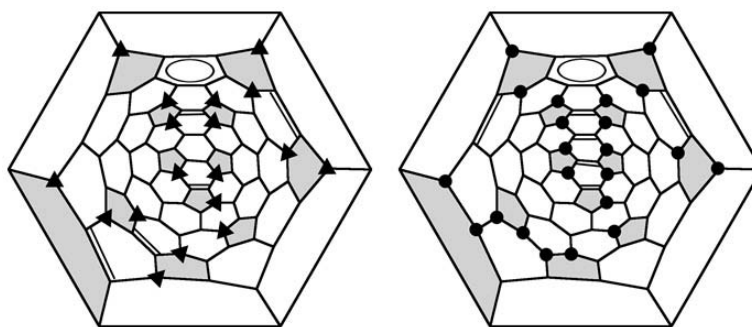


FIG. 4. Schlegel diagrams of $C_{90}(30)(CF_3)_{18}$ (left) and $C_{90}(30)Cl_{22}$ (right). Cage pentagons are highlighted with gray. Black triangles and circles denote attached CF_3 groups and Cl atoms, respectively. The isolated or partially isolated C=C bonds and benzenoid rings are also indicated.

and $C_{90}(30)Cl_{22}$ shows their rather close similarity because of 16 of 18 attachment positions in the former molecule are also occupied in the chlorinated molecule. This results in the same location of three C=C bonds and the benzenoid ring on the $C_{90}(30)$ carbon cage. The differences in the addition patterns concern the attachment of some Cl atoms in adjacent (*ortho*) positions, which are less favourable for bulkier CF_3 groups. For the same reason, the maximum number of CF_3 groups attached to fullerene cages is only 20 (structurally confirmed for C_{70} , C_{84} , C_{88} , and C_{94}) [23-26], whereas several fullerene chlorides with 32-34 Cl atoms are known [27,28].

The addition pattern of $C_{90}(35)(CF_3)_{14}$ of both crystallographically independent (but chemically identical) molecules is characterized by CF_3 attachment exclusively in positions of DHJs and the occupation of all twelve pentagons with CF_3 groups, while two additional CF_3 groups contribute to the formation of an isolated C=C bond (av. bond length 1.32 Å in two independent molecules) on the fullerene C_s - $C_{90}(35)$ cage (fig. 5). Three partially isolated benzenoid rings are also present on the cage (av. C-C bond length 1.40 Å).

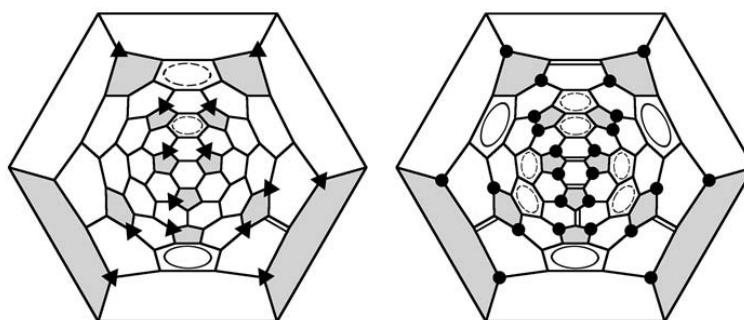


FIG. 5. Schlegel diagrams of $C_{90}(35)(CF_3)_{14}$ (left) and $C_{90}(35)Cl_{24}$ (right). Cage pentagons are highlighted with gray. Black triangles and circles denote attached CF_3 groups and Cl atoms, respectively. The isolated or partially isolated C=C bonds and aromatic substructures are also indicated.

The first crystallographic confirmation of the cage connectivity of $C_{90}(35)$ was reported for $C_{90}(35)Cl_{24}$ and $C_{90}(35)Cl_{28}$, which possess rather similar chlorination patterns [20,21]. A comparison of the addition patterns in $C_{1-}C_{90}(35)(CF_3)_{14}$ and C_s - $C_{90}(35)Cl_{24}$ demonstrates their similarity due to 12 common attachment positions. However, due to a large number of attached Cl atoms, several additions in *ortho* positions are present in the

$C_{90}(35)Cl_{24}$ molecule. Furthermore, all unoccupied carbon atoms on the C_{90} cage are involved into isolated aromatic substructures or isolated C=C bonds. Usually, CF_3 and chloro derivatives of fullerenes show rather different addition patterns as can be exemplified by the comparison in pairs of $C_{70}(CF_3)_{16}$ [29] and $C_{70}Cl_{16}$ [30] or $C_{76}(CF_3)_{18}$ [31] and $C_{76}Cl_{18}$ [5].

4. Conclusions

Trifluoromethylation of a higher fullerenes mixture followed by HPLC separation, crystallization, and X-ray crystallographic structure determination resulted in the first molecular structures of CF_3 derivatives of C_{90} fullerene, $C_{90}(30)(CF_3)_{18}$ and $C_{90}(35)(CF_3)_{14}$. The comparison of the addition patterns with those of the chlorides of the corresponding C_{90} isomers revealed their close similarities, whereas some differences can be attributed to different sizes of CF_3 group and Cl atom as well as to different numbers of attached groups/atoms. It should be noted that C_{90} isomers 30 and 35 belong to the energetically rather stable isomers according to theoretical calculations [16,32,33]. However, the cage connectivity of the most stable C_2-C_{90} (45) still remains unconfirmed in any experimental report.

Acknowledgments

This work was supported in part by the Russian Foundation for Basic Research (grants 12-03-00324 and 13-03-91332).

References

- [1] P.W. Fowler, D.E. Manolopoulos. *An Atlas of Fullerenes*, Clarendon, Oxford, 392 p. (1995).
- [2] T.J.S. Dennis, T. Kai, K. Asato, T. Tomiyama, H. Shinohara, T. Yoshida, Y. Kobayashi, H. Ishiwatari, Y. Miyake, K. Kikuchi, Y. Achiba. Isolation and characterization by ^{13}C NMR spectroscopy of [84]fullerene minor isomers. *J. Phys. Chem. A*, **103**, P. 8747–8752 (1999).
- [3] Y. Miyake, T. Minami, K. Kikuchi, M. Kainosho, Y. Achiba. Trends in structure and growth of higher fullerenes isomer structure of C_{86} and C_{88} . *Mol. Cryst. Liq. Cryst.*, **340**, P. 553–558 (2000).
- [4] N.B. Shustova, B.N. Newell, S.M. Miller, O.P. Anderson, R.D. Bolskar, K. Seppelt, A.A. Popov, O.V. Boltalina, S.H. Strauss. Discovering and verifying elusive fullerene cage isomers: structures of $C_2-p^{11}-(C_{74}-D_{3h})(CF_3)_{12}$ and $C_2-p^{11}-(C_{78}-D_{3h}(5))(CF_3)_{12}$. *Angew. Chem. Int. Ed.*, **46**, P. 4111–4114 (2007).
- [5] K.S. Simeonov, K.Yu. Amsharov, M. Jansen. Connectivity of the chiral D_2 -symmetric isomer of C_{76} through a crystal structure determination of $C_{76}Cl_{18} \cdot TiCl_4$. *Angew. Chem. Int. Ed.*, **46**, P. 8419–8421 (2007).
- [6] E. Kemnitz, S.I. Troyanov. Chlorides of isomeric C_{78} fullerenes: $C_{78}(1)Cl_{30}$, $C_{78}(2)Cl_{30}$, and $C_{78}(2)Cl_{18}$. *Mendeleev Commun.*, **20**, P. 74–76 (2010).
- [7] K.S. Simeonov, K.Yu. Amsharov, M. Jansen. $C_{80}Cl_{12}$ — a chlorinated derivative of the chiral D_2-C_{80} isomer: empirical rationale of halogen atoms addition pattern. *Chem.–Eur. J.*, **15**, P. 1812–1815 (2009).
- [8] S.I. Troyanov, N.B. Tamm. Crystal and molecular structures of trifluoromethyl derivatives of C_{82} fullerene: $C_{82}(CF_3)_{12}$ and $C_{82}(CF_3)_{18}$. *Crystallogr. Rep.*, **55**, P. 432–435 (2010).
- [9] N.B. Tamm, L.N. Sidorov, E. Kemnitz, S.I. Troyanov. Isolation and structural X-ray investigation of perfluoroalkyl derivatives of six cage isomers of C_{84} . *Chem.–Eur. J.*, **15**, P. 10486–10492 (2009).
- [10] S.I. Troyanov, N.B. Tamm. Crystal and molecular structures of trifluoromethyl derivatives of fullerene C_{86} , $C_{86}(CF_3)_{16}$ and $C_{86}(CF_3)_{18}$. *Crystallogr. Rep.*, **54**, P. 598–602 (2009).
- [11] S.I. Troyanov, N.B. Tamm. Cage connectivities of C_{88} (33) and C_{92} (82) fullerenes captured as trifluoromethyl derivatives, $C_{88}(CF_3)_{18}$ and $C_{92}(CF_3)_{16}$. *Chem. Commun.*, P. 6035–6037 (2009).
- [12] S. Yang, T. Wei, E. Kemnitz, S.I. Troyanov. Four isomers of C_{96} fullerene structurally proven as $C_{96}Cl_{22}$ and $C_{96}Cl_{24}$. *Angew. Chem. Int. Ed.*, **51**, P. 8239–8242 (2012).
- [13] M. Yoshida, J. Aihara. Validity of the weighted HOMO–LUMO energy separation as an index of kinetic stability for fullerenes with up to 120 carbon atoms. *Phys. Chem. Chem. Phys.*, **1**, P. 227–230 (1999).

- [14] Y. Achiba, K. Kikuchi, Y. Aihara, T. Wakabayashi, Y. Miyake, M. Kainosho. Higher Fullerenes: Structure and Properties. *Proceedings of "Science and Technology of Fullerene Materials" MRS Symposia*, Pittsburgh, P. Bernier, et al. (Eds.), **359**, P. 3–9 (1995).
- [15] Y. Achiba, K. Kikuchi, Y. Aihara, T. Wakabayashi, Y. Miyake, M. Kainosho. Trends in Large Fullerenes: Are They Balls or Tubes. *The Chemical Physics of Fullerenes 10 (and 5) Years Later*. Proceedings of the NATO Advanced Research Workshop, Varenna, Italy, June 12–16, 1995. Andreoni, W., Ed., Kluwer Academic Publishers: Dordrecht, Netherlands, P. 139–147 (1996).
- [16] G. Sun. Theoretical ^{13}C NMR chemical shifts of the stable isomers of fullerene C_{90} . *Chem. Phys.*, **289**, P. 371–380 (2003).
- [17] H. Yang, C.M. Beavers, Z. Wang, A. Jiang, Z. Liu, H. Jin, B.Q. Mercado, M.M. Olmstead, A.L. Balch. Isolation of a small carbon nanotube: the surprising appearance of $D_{5h}(1)-C_{90}$. *Angew. Chem. Int. Ed.*, **49**, P. 886–890 (2010).
- [18] H. Yang, B.Q. Mercado, H. Jin, Z. Wang, A. Jiang, Z. Liu, C.M. Beavers, M.M. Olmstead, A.L. Balch. Isolation and crystallographic identification of four isomers of $Sm@C_{90}$. *Chem. Commun.*, **47**, P. 2068–2070 (2011).
- [19] I.E. Kareev, A.A. Popov, I.V. Kuvychko, N.B. Shustova, S.F. Lebedkin, V.P. Bubnov, O.P. Anderson, K. Seppelt, S.H. Strauss, O.V. Boltalina. Synthesis and X-ray or NMR/DFT structure elucidation of twenty-one new trifluoromethyl derivatives of soluble cage isomers of C_{76} , C_{78} , C_{84} , and C_{90} . *J. Am. Chem. Soc.*, **130**, P. 13471–13489 (2008).
- [20] E. Kemnitz, S.I. Troyanov. Connectivity patterns of two C_{90} isomers provided by the structure elucidation of $C_{90}Cl_{32}$. *Angew. Chem. Int. Ed.*, **48**, P. 2584–2587 (2009).
- [21] S.I. Troyanov, S. Yang, C. Chen, E. Kemnitz. Six IPR isomers of C_{90} fullerene captured as chlorides: Carbon cage connectivities and chlorination patterns. *Chem.–Eur. J.*, **17**, P. 10622–10669 (2011).
- [22] www.mercorp.com
- [23] K. Chang, M.A. Fritz, N.B. Tamm, A.A. Goryunkov, L.N. Sidorov, C. Chen, S. Yang, E. Kemnitz, S.I. Troyanov. Synthesis, structure, and theoretical study of trifluoromethyl derivatives of $C_{84}(22)$ fullerene. *Chem.–Eur. J.*, **19**, P. 578–587 (2013).
- [24] D.V. Ignat'eva, A.A. Goryunkov, N.B. Tamm, I.N. Ioffe, L.N. Sidorov, S.I. Troyanov. Isolation and structural characterization of the most highly trifluoromethylated C_{70} fullerenes: $C_{70}(CF_3)_{18}$ and $C_{70}(CF_3)_{20}$. *New J. Chem.*, **37**, P. 299–302 (2013).
- [25] M.A. Lansikh, K. Chang, N.B. Tamm, E. Kemnitz, S.I. Troyanov. Trifluoromethyl derivatives of $C_{88}(33)$ fullerene. *Mendeleev Commun.*, **22**, P. 136–137 (2012).
- [26] N.B. Tamm, L.N. Sidorov, E. Kemnitz, S.I. Troyanov. Crystal structures of $C_{94}(CF_3)_{20}$ and $C_{96}(C_2F_5)_{12}$ reveal the cage connectivities in C_{94} (61) and C_{96} (145) fullerenes. *Angew. Chem. Int. Ed.*, **48**, P. 9102–9104 (2009).
- [27] H. Liang, Y.-Z. Tan, T. Zhou, Z.-L. Chen, S.-Y. Xie, R.-B. Huang, L.-S. Zheng. $C_{76}Cl_{34}$: High chlorination of the inherent chiral fullerene with a helical configuration. *Inorg. Chem.*, **49**, P. 3089–3091 (2010).
- [28] I.N. Ioffe, O.N. Mazaleva, C. Chen, S.-F. Yang, E. Kemnitz, S.I. Troyanov. C_{76} fullerene chlorides and cage transformations. Structural and theoretical study. *Dalton Trans.*, **40**, P. 11005–11011 (2011).
- [29] S.M. Avdoshenko, A.A. Goryunkov, I.N. Ioffe, D.V. Ignat'eva, L.N. Sidorov, P. Pattison, E. Kemnitz, S.I. Troyanov. Preparation, crystallographic characterization and theoretical study of $C_{70}(CF_3)_{16}$ and $C_{70}(CF_3)_{18}$. *Chem. Commun.*, P. 2463–2465 (2006).
- [30] S.I. Troyanov, A.A. Popov. A [70]fullerene chloride, $C_{70}Cl_{16}$, obtained by the attempted bromination of C_{70} in $TiCl_4$. *Angew. Chem. Int. Ed.*, **44**, P. 4215–4218 (2005).
- [31] N.B. Tamm, S.I. Troyanov. Trifluoromethyl derivatives of fullerene C_{76} , $C_{76}(CF_3)_{14-18}$. *Mendeleev Commun.*, **20**, P. 229–230 (2010).
- [32] Z. Slanina, X. Zhao, S.-L. Lee, E. Ōsawa. Computations on the IPR isomers of C_{88} and C_{90} . *Scr. Mater.* **43**, P. 733–741 (2000).
- [33] M. Watanabe, D. Ishimaru, N. Mizorogi, M. Kiuchi, J. Aihara. Thermodynamically and kinetically stable isomers of the C_{88} and C_{90} fullerenes. *J. Mol. Struct.*, - THEOCHEM, **726**, P. 11–16 (2005).

PREPARATION AND CHARACTERIZATION OF A NEW CLUSTERED $\{C_{70}\}_n$ FULLERENE MATERIAL

I.V. Mikheev¹, D.S. Volkov¹, M.A. Proskurnin¹, N.V. Avramenko¹, M.V. Korobov¹

¹Lomonosov Moscow State University, Chemistry Department, Moscow, 119991, Russia
mikheev.ivan@gmail.com

PACS 61.48.-c

A new clustered fullerene material $\{C_{70}\}_n$ has been prepared and studied using UV/vis spectroscopy, dynamic light scattering and liquid-liquid extraction. The material was prepared from aqueous fullerene dispersions of C_{70} by ultracentrifugation. The dispersions were obtained via an ordinary solvent-exchange procedure. Liquid-liquid extraction of $\{C_{70}\}_n$ from water to the organic phase without any extra reagents was observed for the first time. $\{C_{70}\}_n$ fullerene solid material was made and characterized with transmission electron microscopy and differential scanning calorimetry.

Keywords: fullerenes, solid material, extraction properties, DSC.

1. Introduction

Currently, technologies exist for the production of new fullerene materials [1]. Unique properties of fullerenes find a number of applications in various branches of science and technology. Of much importance are their use for the immobilization and transport of medicines [2-4]. At both cellular and macro levels, their aqueous solutions (aqueous fullerene dispersions, AFDs) are powerful antioxidants that adsorb free radicals and prevent aging and various pathologies like cancer, cardiovascular diseases etc. [2, 5, 6]. Fullerene clusters of certain sizes may create an antiviral cell barrier as well [7, 8]. Preparation of hydrophilic fullerene-based nanomaterials is on demand. Such materials may be prepared from C_{70} and higher fullerenes rather than from C_{60} only. An approach to this is to make AFDs from the corresponding fullerene followed by the treatment of the resulting colloidal solution. However, the methods of characterization and analytical control over the properties of such novel AFD-based materials are not well-developed yet. Thus, the preparation and physicochemical studies of the materials based on C_{60} , C_{70} or higher fullerenes seems rather appropriate.

Thus, the aim of this study is to (i) improve the general procedure for preparing aqueous fullerene dispersions; (ii) to work out an approach for preparing a solid powdered material from fullerene C_{70} ; and (iii) to carry out the physicochemical characterization of the prepared clustered material.

2. Materials and Methods

Commercially available fullerene C_{70} 99%+ (LLC “Neo Tech Production”, Russia) was used throughout. Chemically pure benzene and toluene (“Reachim”, Russia) and water (18.2 M Ω ×cm) from a Milli-Q purification system (Millipore, France) were used. The investigations of dynamic light scattering (DLS) were made using a Malvern “Zetasizer nano ZS” instrument. Spectrophotometric measurements were made using a Varian Cary 50 spectrophotometer. Ultrasonic treatment was performed with a piezoceramic emitter without

a concentrator immersed in the solution. The resonance frequency was 35 kHz, power up to 0.3 kW, volume 1–1.5 L. A DSC-30 TA Mettler Toledo differential scanning calorimeter was used to capture heating traces from 243 up to 313 K with a scanning rate of 5 K/min. High-resolution transmission electron microscopy (HRTEM) imaging was carried out using a JEM 2100F transmission electron microscope with accelerating voltage 200 kV.

AFD C_{70} was produced as reported elsewhere [9] with increased power of the sonication system, thus when increasing the quantity of fullerenes, the sonication duration is two weeks. The absorption spectra of AFD C_{70} completely matched the spectra described in [10, 11]. Aqueous solutions of fullerenes (Fig. 1) were prepared by the following procedure. A weighed portion of fullerene (0.5–0.6 g) was placed into a 200-mL volumetric flask, dissolved in 100 mL of toluene and sonicated for 2 h at 353 K; next, the solution was diluted to mark with toluene. Next, the prepared toluene solution was placed into a conic flask and 1 L of Milli-Q water was added, and the solution was sonicated for 14 days (12 h per day) at the maximum power setting of 0.3 kW at 353 K until complete evaporation of toluene (checked with LC/MS). Next, the solution was heated up for 30 min, and boiled for 15 min and filtered through a Shott filter followed by a $0.45\text{-}\mu\text{m}$ microporous membrane filter. The concentration of fullerene (130 ± 1 ppm, $n = 3$, $P = 0.95$) was measured by performing the total organic carbon analysis (TOC). The TOC analyzer was calibrated with a series of potassium hydrogen phthalate (KHP) samples with the 1-200 ppm range for carbon. The least square fit of TOC versus peak area gave c , ppm = $(10.2 \pm 0.1)S_{area}$, a.u., $P = 0.95$, $n = 7$, $r = 0.99863$.

2.1. General procedure for preparing $\{C_{70}\}_n$ fullerene material

Solid powered $\{C_{70}\}_n$ materials were produced as follows. AFDs of C_{70} were concentrated by ultracentrifugation. The solution was centrifuged for 25 min at 30000 rpm (298 K). Next, mother liquor was decanted by injection syringe and concentrated quantity of AFD was heated up to fully evaporation at 378 K. The resulting absorption spectrum of AFD C_{70} is shown in Fig. 1.

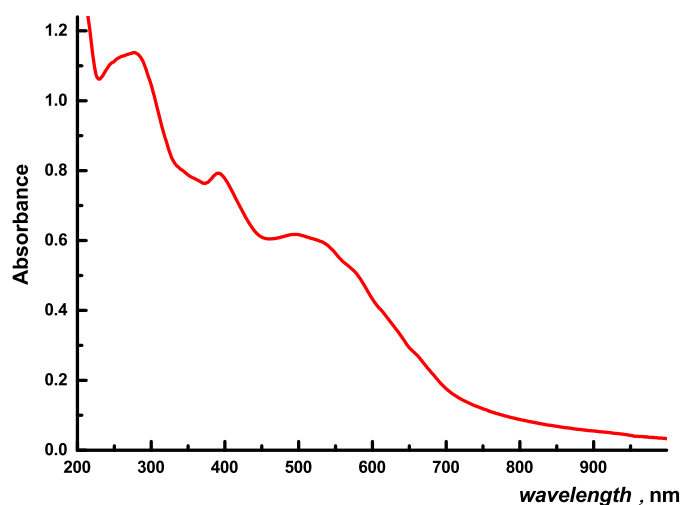


FIG. 1. Absorption spectrum of prepared aqueous dispersions of fullerenes C_{70}

2.2. Liquid-liquid extraction AFD C to toluene

Toluene without any extra reagents was added to AFD C₇₀ at a volume ratio of 1 to 1. Next, we performed the ultrasonic treatment at the maximum power setting of 0.3 kW and 378 K for 2 h in a closed test tube to prevent toluene evaporation. Then, we centrifuged the suspension at 4000 rpm for 15 min. Finally, the absorbance spectra of aqueous and organic phases were registered and compared to a toluene solution of pristine C₇₀ fullerenes and original AFD C₇₀ (see Figs. 2 and 3).

2.3. Differential scanning calorimetry (DSC) traces

The samples studied were mechanical mixtures ($\sim 1 : 3$ by weight) of the solid $\{C_{70}\}_n$ and the solvent (water or benzene), respectively. A sample of the tested substance was placed into a standard aluminum container and sealed. Calorimetric measurements were carried out at a heating rate of 5 K/min. A Ni-Au thermocouple was used as a detector of the heat flux. The temperature of the sample was measured by a platinum resistance thermometer. Pre-calibration was performed on the basis of data for the enthalpies of melting for indium, lead, and zinc. The calibration of the heat flux was carried out based on data for the enthalpy of melting of an indium standard sample. The enthalpy of melting of the samples studied was calculated from the squares of the corresponding peaks in the DSC trace. The temperature was measured with an accuracy of ± 0.2 K.

2.4. DLS analysis and HRTEM

DLS particle size distributions and ζ -potentials in AFD were measured with a 100 averages of 15 s scans to gain a histogram with the accuracy *ca.* 5%. The TEM specimens were prepared by dispersing the particle suspensions in ethyl alcohol onto TEM carbon-copper grids and by exsiccation in vacuum at 10^{-2} mm Hg.

3. Results and Discussion

3.1. Liquid-liquid extraction

For the first time, we observed the extraction of fullerenes from aqueous solutions to toluene with considerable distribution constant. This extraction distinguishes these experiments from previous reports for AFD C₆₀, where direct extraction was not observed, and AFD C₆₀ has been transferred to the organic phase only after addition of an inorganic salt [12]. We compared the absorption spectra of C₇₀ extracted into toluene from AFD C₇₀ and that of pristine C₇₀ dissolved in toluene (Fig. 2) and those for the aqueous phase of AFD C₇₀ before and after a sonication treatment during the extraction (Fig. 3). The shapes of spectra in Fig. 2 fully match, and we did not observe any red or blue shifts between the pristine toluene solutions and that from the extraction procedure using $dA/d\lambda$ and $d^2A/d\lambda^2$ derivative spectrophotometry in the UV/vis range.

Next, we calculated the recovery of the fullerene from AFD using the absorption spectra of AFD before and after the extraction (Fig. 3), which averaged *ca.* $97 \pm 2\%$, ($n = 3$, $P = 0.95$). Based on these results, one may assume that the C₇₀ recovered from AFD is a monomer, not subjected to any chemical modification and C₇₀ clusters in AFD are weakly bonded associates of C₇₀ monomers covered by a hydrophilic shell.

3.2. DLS and HRTEM experiments

The size of AFD C₇₀ was found to be *ca.* 105, 140, and 160 nm respectively for number, volume and intensity size distributions (Fig. 4). Moreover, we carried out the

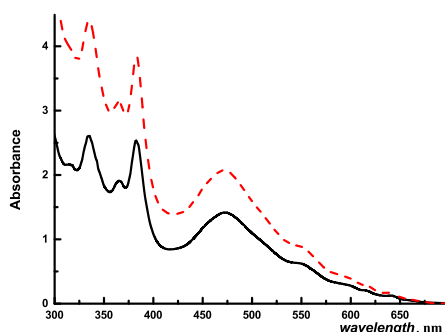


FIG. 2. Absorption spectra of fullerenes C_{70} extracted from AFD (black solid line) and pristine fullerenes C_{70} dissolved in toluene (red dash line)

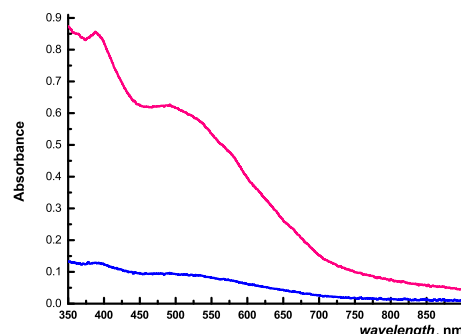


FIG. 3. Absorption spectra of AFD C_{70} before and after sonication treatment for 2 hours

measurements of ζ -potential for AFD C_{70} , which was estimated to be -40.8 ± 0.9 mV, and a rather low polydispersity index (PDI) of 0.08 was calculated for a AFD concentration of $14.6 \mu\text{M}$.

HRTEM data of the fullerene nanoparticles shows that the material is in fact clustered and shows spherical particles. HRTEM data for the target solid material (see Fig. 5) correlates well with above-discussed DLS data. Thus, we suggest that AFDs are not clumped together into large particles during the evaporation of the residual water. The particle size within the solid clustered material was found to be *ca.* 134 nm. The average number of C_{70} molecules in the cluster in terms of the spherical model was estimated at *ca.* 5×10^5 . The density of the cluster was assumed to be 1.7 g/cm^3 as in the C_{70} crystal.

3.3. DSC experiments

Finally, we recorded thermal effects related to the melting of water or, in another case, of benzene in the samples studied (see 2.3). In both cases, two peaks were observed (Figs. 6 and 7) that we believe corresponded to the melting of water (benzene) in the bulk solvent and in the pores within the clustered $\{C_{70}\}_n$ fullerene material. We assume that $\{C_{70}\}_n$ is a powder consisting of nanoclusters similar to nanodiamond powders [13]. Such powders show reproducible porous structures that disperse the solvent. Nanoparticles have solvent-filled pores in the secondary structure, and the extra peak in the DSC trace from the low temperature side corresponds to the solvent melting in the pores. For comparison, DSC experiments were carried out for pristine fullerene C_{70} mixed with water or benzene. Pristine C_{70} does not form nanoclusters and the corresponding secondary structure. As expected, in both cases the single peak of melting of the bulk solvent was observed only (Figs. 8 and 9). The differences between two peaks of melting in Figs. 6 and 7, ΔT_m , are 1.0 ± 0.4 K and 3.9 ± 0.4 K for water and benzene, respectively. For a similar $\{C_{60}\}_m$ material with water ΔT_m was previously reported as equal to 2 K [1].

The Gibbs-Kelvin equation was used to calculate the diameters of the nanophase in pores. We obtained diameters of *ca.* 40 ± 5 nm and *ca.* 30 ± 5 nm for water and benzene, respectively. These values are in agreement, which suggests that two solvents occupy the

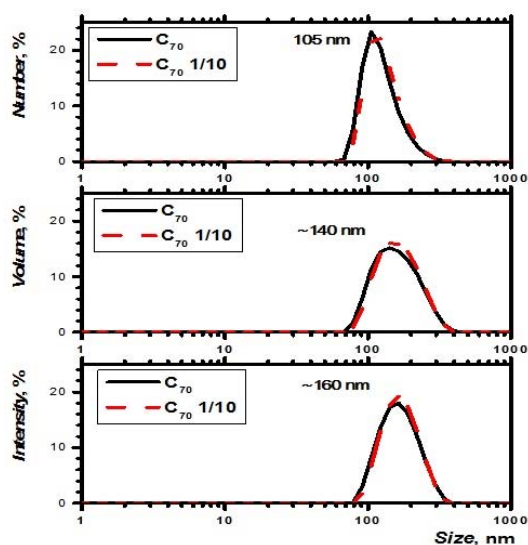


FIG. 4. Number, volume, and intensity size distributions for the AFD C_{70} (black solid line) and dispersion diluted by a factor of 10 (red dashed line)

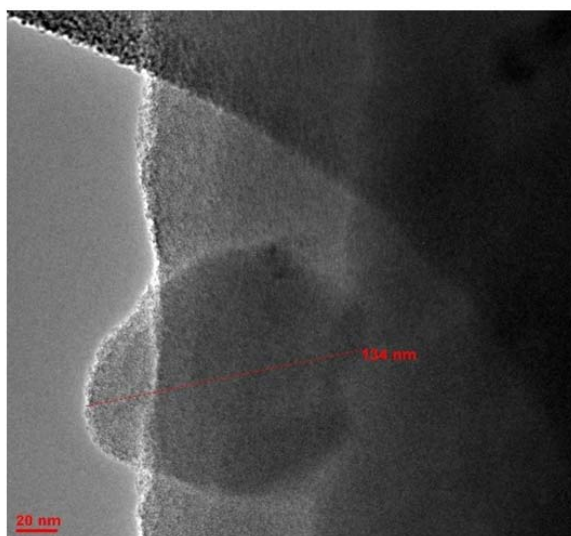


FIG. 5. TEM image of an AFD sample prepared by ultracentrifugation technique

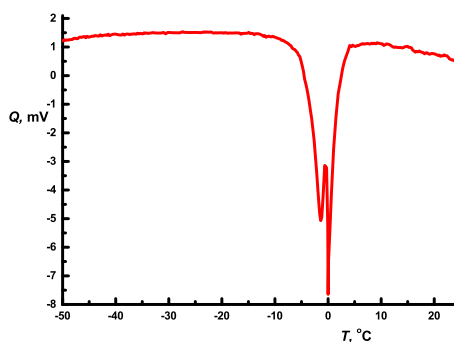


FIG. 6. Typical DSC trace of $\{C_{70}\}_n$ material with two endothermic effects for melting of water

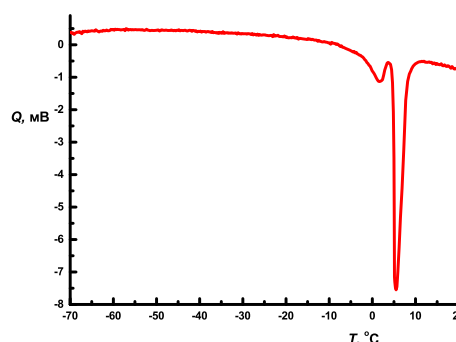


FIG. 7. Typical DSC trace of $\{C_{70}\}_n$ material with two endothermic effects for melting of benzene

same voids within the secondary structure formed by C_{70} aggregates. It is worth noting that solvents with different properties — water and benzene — interact with $\{C_{70}\}_n$ material in the same manner. Both solvents are dispersed onto the $\{C_{70}\}_n$ secondary structure. It is also noteworthy that benzene neither dissolves nor distracts C_{70} aggregates formed in an AFD.

4. Conclusions

The study clearly demonstrated evidence for the formation of a new C_{70} based material with unique properties. The material was produced in the form of aqueous fullerene

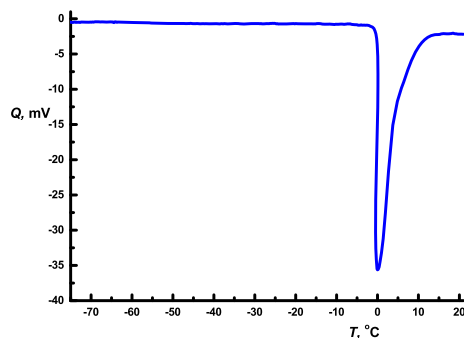


FIG. 8. Typical DSC trace of pristine C_{70} with water. A single endothermic effect observed corresponded to the melting of bulk water

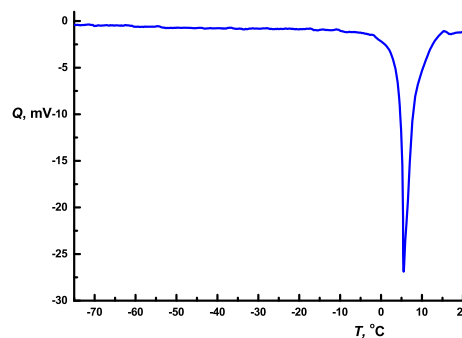


FIG. 9. Typical DSC trace of pristine C_{70} with benzene. A single endothermic effect observed corresponded to the melting of bulk water

dispersions and as a dry powder. In the first case, it was characterized using UV-vis spectra, dynamic light scattering and liquid-liquid extraction while in the second by means of differential scanning calorimetry and transmission electron microscopy. We observed liquid-liquid extraction of C_{70} from aqueous fullerene dispersions to monomeric solution in toluene with admissible recovery characteristics. The data obtained allows one to put forward a qualitative schematic structure for the C_{70} clusters in aqueous fullerene dispersions and in the powder. The developed procedure may be used to prepare clustered materials and aqueous fullerene dispersions for other members of the fullerene family.

Acknowledgments

This work was supported by the Russian Foundation for Basic Research, grants nos. 12-03-00653-a and 12-03-31569-mol_a and the Ministry of Science and Technology of Russian Federation, contract no. 16.740.11.0471 and by the grant for Leading Scientific Schools in Russia. We thank Dr. S. Savilov and his group at the scientific center of NanoChemistry and Chemistry of Atmosphere at the Department of Chemistry of MSU for HRTEM images. We thank P.I. Semenyuk at the A.N. Belozersky Institute of Physicochemical Biology of MSU for providing the DLS data.

References

- [1] M.V. Korobov, N.I. Ivanova, N.V. Avramenko, G.V. Andrievsky. In: Fullerenes, v.12: The Exciting World of Nanocages and Nanotubes, ed. by Kamat P., Guldi D., Kadish K.. Electrochemical Society, 2002.
- [2] M.D. Tzirakis, M. Orfanopoulos. Radical Reactions of Fullerenes: From Synthetic Organic Chemistry to Materials Science and Biology. *Chem. Rev.*, **113**(7), P. 5262–5321 (2013).
- [3] B. Pycke, T. Chao, P. Herckes, P. Westerhoff, R. Halden. Beyond nC_{60} : strategies for identification of transformation products of fullerene oxidation in aquatic and biological samples. *Analyt. Bioanalyt. Chem.*, **404**(9), P. 2583–2595 (2012).
- [4] S. Niu, D. Mauzerall. Fast and Efficient Charge Transport across a Lipid Bilayer Is Electronically Mediated by C_{70} Fullerene Aggregates. *J. Am. Chem. Soc.*, **118**(24), P 5791–5795 (1996).
- [5] E. Nakamura, H. Isobe. Functionalized Fullerenes in Water. The First 10 Years of Their Chemistry, Biology, and Nanoscience. *Accounts of Chemical Research*, **36**(11), P 807–815 (2003).

- [6] L. Xiao, H. Takada, K. Maeda, M. Haramoto, N. Miwa. Antioxidant effects of water-soluble fullerene derivatives against ultraviolet ray or peroxy lipid through their action of scavenging the reactive oxygen species in human skin keratinocytes. *Biomedicine & Pharmacotherapy*, **59**(7), P 351–358 (2005).
- [7] E. Hilburn, S. Murdianti, D. Maples, S. Williams, T. Damron, I. Kuriyavar, D. Ausman. Synthesizing aqueous fullerene colloidal suspensions by new solvent-exchange methods. *Colloids and Surfaces A: Physicochemical and Engineering Aspects*, **401**(0), P 48–53 (2012).
- [8] Y. Lyon, K. Adams, C. Falkner, J. Alvarez. Antibacterial Activity of Fullerene Water Suspensions: Effects of Preparation Method and Particle Size. *Environmental Sci. & Technol.*, **40**(14), P 4360–4366 (2006).
- [9] V. Andrievsky, V. Kosevich, M. Vovk, S. Shelkovsky, A. Vashchenko. On the production of an aqueous colloidal solution of fullerenes. *J. Chem. Soc., Chem. Communications*, **12**, P 1281–1282 (1995).
- [10] S. Deguchi, D. Alargova, K. Tsujii. Stable Dispersions of Fullerenes, C₆₀ and C₇₀, in Water. Preparation and Characterization. *Langmuir*, **17**(19), P 6013–6017 (2001).
- [11] N. Aich, J.V. Flora, N.B. Saleh. Preparation and characterization of stable aqueous higher-order fullerenes. *Nanotechnology*, **23**(5), P 055705(9p.) (2012).
- [12] G.V. Andrievsky, V.K. Klochkov, A.B. Bordyuh, G.I. Dovbeshko. Comparative analysis of two aqueous-colloidal solutions of C₆₀ fullerene with help of FTIR reflectance and UV–Vis spectroscopy. *Chem. Phys. Lett.*, **364**(1–2), P 8–17 (2002).
- [13] M.V. Korobov, N.V. Avramenko, A.G. Bogachev, N.N. Rozhkova, E. Osawa. Nanophase of water in nano-diamond gel. *J. Phys. Chem. C*, **111**(20), P 7330–7334 (2007).

FULLERENE FILMS WITH SUPPRESSED POLYMERIZING ABILITY

M. Yesilbas^{1*}, T. L. Makarova^{1,2}, I. Zakharova³

¹Umeå University, 90187 Umeå, Sweden

²Ioffe Physico-technical Institute, 194021 St. Petersburg, Russia

³State Technical University, 195251 St. Petersburg, Russia

*merveyesilbas.my@gmail.com

PACS 61.48.+c

Illumination of fullerene with visible light in the presence of oxygen leads to a transition of oxygen from triplet (ground) to singlet (excited) state where singlet oxygen is a long-lived reactive oxygen species. The effectiveness of fullerene as a singlet oxygen generator drastically decreases when fullerenes are condensed into a bulk material, mainly due to the polymerization ability. The ability of fullerene films to polymerize was studied for the C₆₀ fullerene films intercalated with tetraphenylporphyrine (TPP), CdS, CdTe, HNO₃ as well as the hydrogen plasma treated films. Raman spectroscopy was used for monitoring the polymerization process. The ability to polymerize was found to be tightly connected to the formation of charge-transfer (Wannier-Mott) excitons which are revealed in the absorption spectra and measured with the help of spectroscopic ellipsometry.

Keywords: Fullerene, CdS, CdTe, HNO₃, tetraphenylporphyrine, hydrogen plasma, Raman spectroscopy, spectroscopic ellipsometry, polymerization.

1. Introduction

Molecular oxygen also known as dioxygen (O₂) is a powerful oxidant which can destroy organic compounds quickly. Dioxygen in its ground state is present in triplet form (³O₂) which has a total spin of unity (S=1). Singlet oxygen (¹O₂) is a long-lived reactive oxygen species resulting from spin-forbidden transition from the ground state to the excited state of O₂ where the total spin is zero (S=0), thus and providing its very reactive behavior [1, 2]. Highly efficient production of ¹O₂ proceeds in the presence of a photosensitizer dye by low-energy illumination. In the liquid phase, there have been many applications of singlet oxygen, however, in the gas phase the utilization of ¹O₂ has been unexplored due to technical problems with the light stability of the photosensitizers. In particular, fullerenes promote the transition of molecular oxygen from a triplet to a singlet state in case of irradiation with visible light [1, 3] and this compound is then used to inactivate the viruses and bacteria [4-6], especially common in photodynamic therapy (PDT) [7, 8]. The effectiveness of fullerene molecules as photosensitizers is limited by their ability to form polymeric structures.

Fullerene (C₆₀) presents the f.c.c. structure with weak Van der Waals intermolecular bonds and can be transformed into different polymeric structures. The polymerization leads to a change in the structural, mechanical and electrical properties of pristine form of the C₆₀ [9]. Fullerenes can be polymerized in three different ways: photopolymerization, pressure polymerization and intercalation of C₆₀ structure with a guest compound [10]. In this work, the photopolymerization method was used, irradiating the thin C₆₀ films with visible light. In the so-called [2+2] cycloaddition, some of the double bonds on the molecule break up and linked to an adjacent molecule forming a ‘cyclobutane ring’ that consists four carbon atoms

[9]. In the cycloaddition process, double bonds of adjacent molecules are oriented parallel and complete polymerization then leads to a decrease in the distance between the molecules to 9.1–9.2 Å from the value of 10 Å in the case of unpolymerized state [11, 12]. The creation of intermolecular bonds stops the rotation of molecule and lowers the symmetry, which can be detected in Raman spectroscopy. The high icosahedral (I_h) symmetry with a high Raman scattering cross section of C_{60} enables Raman spectroscopy to be a very efficient tool for monitoring the polymerization. The formation of new bonds changes the mode positions of molecular vibrations, especially in $A_g(2)$ also called ‘pentagonal pinch mode’ [9, 13]. There are several factors affecting the position of the $A_g(2)$ mode, including polymerization and charge transfer. The calculations of *Porezag et.al.* [14] show that the $A_g(2)$ mode, which is situated at 1469 cm^{-1} in pristine C_{60} , should be linearly downshifted due to the number of polymer bonds, which was confirmed experimentally [15]. The calculated $A_g(2)$ mode position for the different phases of C_{60} due to calculation is shown in table 1.

TABLE 1. Shifted positions of the $A_g(2)$ - derived mode for different phases of C_{60}^1

Phase	Number of polymer bonds	$A_g(2)$ mode position (cm^{-1})
Pristine	0	1469
Dimers	1	1464
Orthorhombic	2	1459
Branched chains	3	1454
Tetragonal	4	1448
Rhombohedral	6	1407

¹Reference [9]

In the bulk form of C_{60} , an inter-molecular type of exciton exists which is also called the charge-transfer (CT) exciton. The formation of CT-excitons is a precursor to photopolymerization. The probability of exciton formation decreases when the guest molecules are intercalated in the voids of crystalline lattice in fullerene solids. Another way of preventing polymerization is the functionalization of fullerene molecules. The polymerization process on C_{60} is illustrated in figure 1 where two hexagon bonds of the fullerene are presented as ‘active sites (6=6)’. In the figure 1, the polymerization of pristine C_{60} in upper and hydrogen plasma treatment C_{60} in lower part is presented. The figure 1 shows that hydrogen plasma treatment of C_{60} protects the active sites (6=6) and thus prevents polymerization.

In this work, the polymerization process was monitored by Raman spectroscopy. Simultaneously, the formation of the CT- excitons in the C_{60} was extracted from the absorption spectra measured by the spectroscopic ellipsometry.

2. Experimental Part

2.1. Methods of Production of Films

C_{60} films were produced by using a quasi-closed volume vacuum evaporation technique. Films were prepared by discrete evaporation in a quasi-closed volume under a vacuum chamber pressure of 10^{-7} Torr. The semiconducting fullerene films were grown on glass substrates/ITO and silicon substrate. Then, the films were coevaporated with cadmium sulfide (CdS), cadmium telluride (CdTe), nitric acid (HNO_3) and tetraphenylporphyrin (TPP or H_2TPP) or treated in the hydrogen plasma discharge ($C_{60}:\text{H}$). The synthetic parameters for the films are given in table 2.

Active sites (6=6)

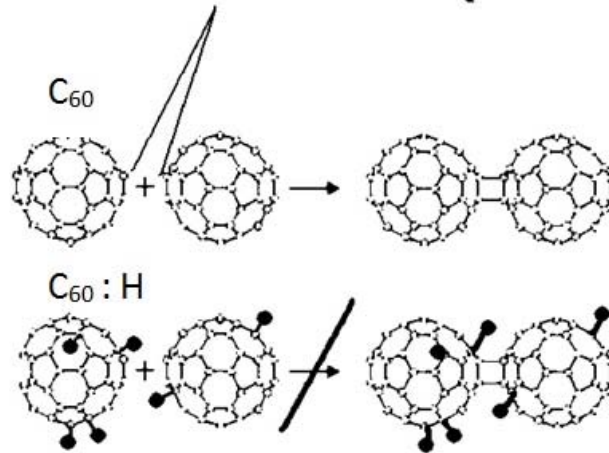


FIG. 1. Polymerization ability for C₆₀ (upper) and hydrogenated C₆₀ (lower)

TABLE 2. The synthetic parameters for C₆₀ films

Film #	Content	Composition ratio	T _{evaporator} , C	T _{substrate} , C	Deposition time, min
111	C ₆₀ HNO ₃	-	500	130	10
113	C ₆₀ HNO ₃	-	500	130	5
114 ²	C ₆₀	-	510	200	12
149	C ₆₀ :CdS	1:1	560	240	4
151	C ₆₀ :CdS	1:3	520	210	3
154	C ₆₀ :CdS	1:10	520	215	4
02_69	H ₂ TPP	-	320	150	5

² The sample was exposed to hydrogen plasma after the coevaporation

In hydrogen plasma treatment, the plasma chemical reactor, which is formed by a d.c. diode system with tungsten electrodes, was used operating a current density of less than 0.3 A/cm². The treatment was done at very low H pressure ($p = 3\text{--}10$ kP) and the films were on the periphery of the plasma discharge. The aim of producing hydrogen plasma treatment films in this experiment is to produce samples with very low concentration of hydrogen which means the hydrogen amount on attached fullerene is as small as possible and reducing pressure any more could lead to a quenching of the discharge.

2.2. Characterization of Films

A single grating Raman spectrometer (Renishaw 1000 Raman system) equipped with the three different lasers (514, 633 and 875 nm) and a CCD-detector was used for probing the polymerization. Measurements were performed at a wavelength of 514 nm with output power 1.8 mW. Scanning was done using an Olympus microscope attachment with 50x objective and the diameter of the focal spot approx 5 μm . Filters were used to reduce the performance to 10% and 1%, and the spectral data were independent of the laser power. The device collects the information from the central spot of 1 micrometer diameter. Taking into account that the laser operates on a fundamental transverse mode and emits a beam

that approximates a Gaussian profile, we estimate the power density in the central 1- μm spot at 10% laser intensity as 0.3 mW/mm². As a general rule, dimer formation requires the absorption of one photon in photo-induced polymerization of C₆₀ and a preferred range of fluences is 1 mW/mm² to 1000 mW/mm². A similar range of fluences can also be used for photo-assisted oxygen doping [16,17]. The spectral range for the films was determined from 200–1800 cm⁻¹ for 1st order, while the 2nd order spectra of the hydrogen plasma-treated films were probed from 2000–4000 cm⁻¹. The spectroscopic data for CT-excitons were obtained by rotating analyzer ellipsometer (J. A. Woollam Co., Inc. Ellipsometry Solutions, α -SETM) which provided the spectral range between 380 nm to 900 nm. Ellipsometry presents an indirect technique which requires an evaluated fix optical modeling with the experimental data. In our case, the semiconductor films presents the four-layer thickness where a layer of fullerene lies on the silicon substrate which has a native oxide and surface roughness. In turn, fullerene also has a surface layer with a certain roughness which effects the light reflection. The surface roughness value was measured by an Atomic Force Microscope and a value between 15–20 nm was obtained for several samples. Our films were modeled as a 3-layer thickness using EMA (Bruggeman Effective Medium Approximation) model.

3. Results and Discussions

3.1. Raman Spectroscopy

The A_g(2) mode presents a fingerprint property for the polymerization process and is downshifted due to the number of polymer bonds occurring, as was previously mentioned in [17]. The peaks in the A_g(2) mode region were fitted by Voigt lineshape using a program named (PeakFitTM program, Version 4 for Win32). The A_g(2) mode is a non-degenerate peak that cannot split. The appearance of the satellite presents the A_g(2) derived modes which means the film polymerizes (Fig.2).

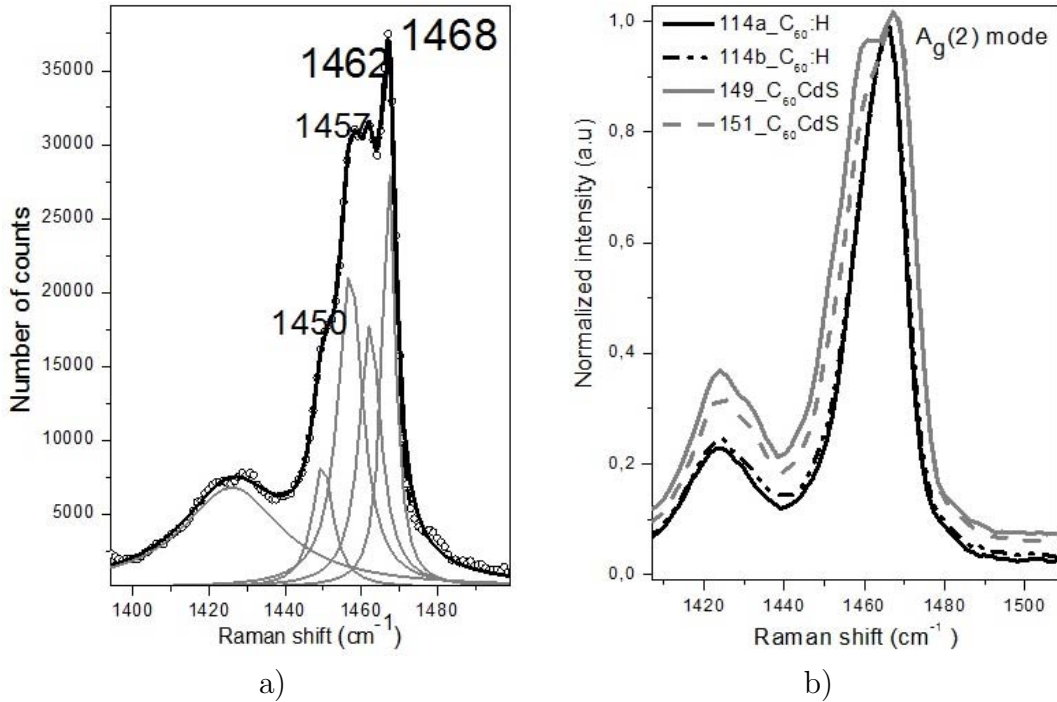


FIG. 2. A_g(2) modes (a) pristine C₆₀, (b) hydrogen treatment and CdS intercalated films

In panel 1, comparison of $A_g(2)$ modes for pristine C_{60} in (a), hydrogen-treated and CdS intercalated films in (b) are presented.

Pristine C_{60} presents a peak at 1468 cm^{-1} , as well as A_g -derived modes at the positions of 1462 , 1457 cm^{-1} and 1450 cm^{-1} , corresponding to dimers and linear chains, and even the signs of two-dimensional polymerization respectively. The spectra in Fig. 2 (a) show that pristine C_{60} strongly polymerizes under the laser light. In Fig.2 (b), CdS intercalated and hydrogen treatment films presents less polymerized structure. Especially, hydrogen plasma treatment films serve the narrowest peaks in the vicinity of $A_g(2)$ mode. It can be concluded that hydrogen plasma treatment films provides the best results for preventing polymerization.

In our experiments, TPP and HNO_3 intercalated films showed the most split structure in the vicinity of the $A_g(2)$ mode region (Fig. 3). We believe, that in this case, the splitting is related to charge transfer processes between the fullerene matrix and the guest molecules.

Having found that hydrogenated films are the most resistant to polymerization, we further studied the aging effects and compared the spectra of freshly prepared hydrogenated films with the ones kept over 4 years under ambient conditions.

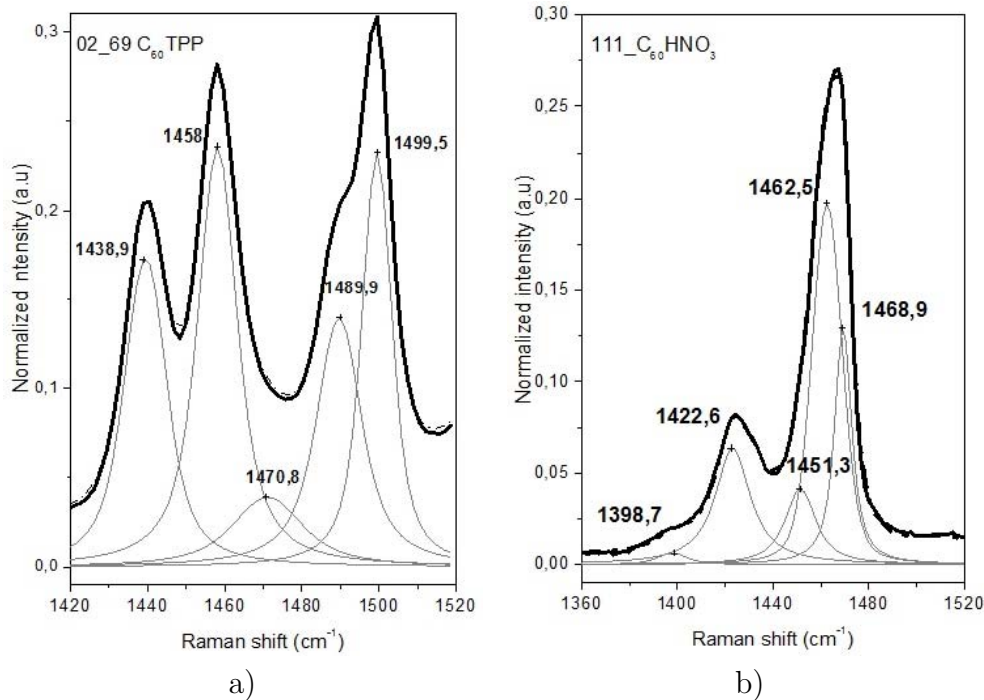


FIG. 3. $A_g(2)$ mode positions of TPP and HNO_3 intercalated films

The aging effects on the hydrogenated films in the 1^{st} and 2^{nd} order spectra were monitored by Raman spectroscopy. In the 1^{st} order spectra shown in figure 4, the pristine C_{60} film presents an unpolymerized peak at 1469 cm^{-1} and a derived mode at 1461 cm^{-1} . The freshly hydrogenated plasma treated film shows one unpolymerized peak at 1469 cm^{-1} but the aged hydrogenated film (2012) shows two peaks at 1463 and 1469 cm^{-1} mode positions where the area of first peak is twice as large as the second one. It can be concluded that the ability to polymerize has been restored.

To further analyze the aging effects, the 2^{nd} order spectra of the hydrogenated plasma treated films were probed. Although pristine C_{60} has no spectral features in the $1800\text{--}4000\text{ cm}^{-1}$ region, hydrogen plasma treatment of C_{60} reveals its sleeping modes and enables

a rich spectrum. The observation of the second order spectra of the fullerene films is a phenomenon which requires the absence of a polymerized phase and can be reached by either cooling below the glass transition temperature or heating above 450 K; also strong laser intensity is required [18].

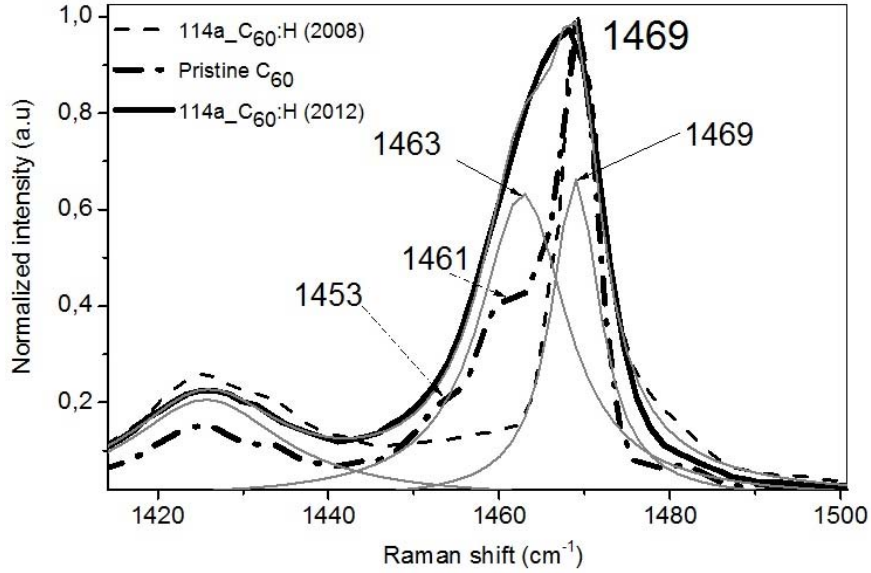


FIG. 4. Ageing effect on hydrogenated films³ in the vicinity of Ag (2) mode position

We were especially interested in the 2800–3000 cm^{-1} spectral region, which is where C-H stretching vibrations are found, is also where the second order peaks interfere. We used a very low intensity laser (1.8 mW) at room temperature in our experiments. Figure 5 demonstrates that the spectral features in the 2800–3000 cm^{-1} region are much stronger than in other regions depending on C-H stretching vibrations.

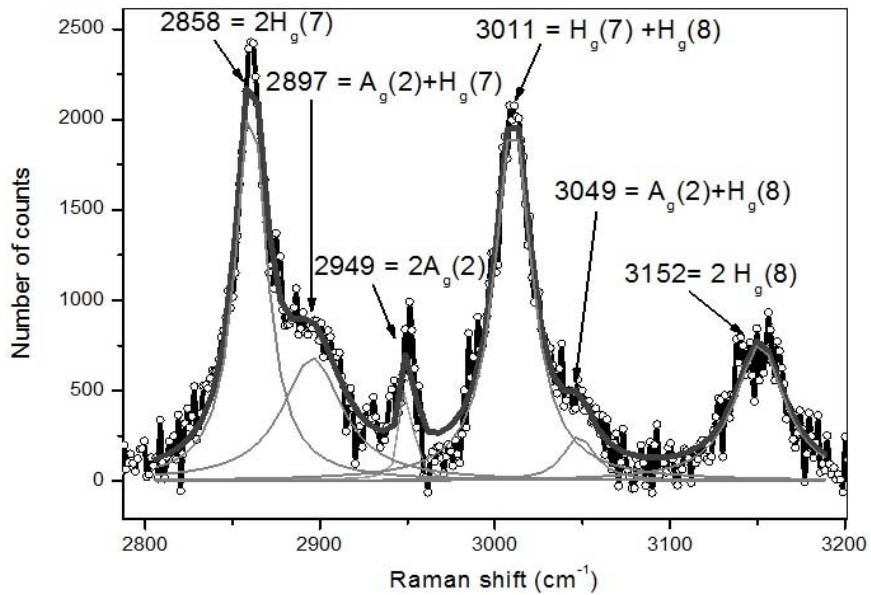


FIG. 5. The spectral region in 2800–3000 cm^{-1} for C_{60}H (2008) film. This region is also reported as C-H stretching vibrations for $\text{C}_{60}\text{H}_{36}$ [16]

Additionally, spectral features have been preserved in samples aged for four years in this region only. As a final discussion, plasma treated samples presented the best results for suppression of the ability to polymerize when hydrogen was attached to the active sites of fullerene, the so-called 6=6 bonds. The absence of polymerization leads to the generation of a large number of second order peaks in the Raman spectra, which was confirmed and expressed in detail by Dong [18]. The plasma treated films were unstable, except in the C-H stretching region from 2800–3000 cm^{-1} .

3.2. Spectroscopic Ellipsometry

CT- excitons revealed in absorption spectra were measured with ellipsometry. The spectral features of the films were probed by comparison of the experimental and theoretical data. In the ellipsometry analysis, the films were modeled as a trilayer including a surface roughness of 200 Å. The ellipsometric model was constructed using both experimental and calculated data from the program and the spectra from which the film's absorption coefficients were determined. Using the measured Ψ and Δ ellipsometric parameters, an extinction coefficient was obtained and then the absorption coefficient was calculated by equation (1):

$$\alpha = \frac{4\pi k}{\lambda} \quad , \quad (1)$$

where k is the extinction coefficient of the films. The results for the absorption coefficients are given in Figure 6.

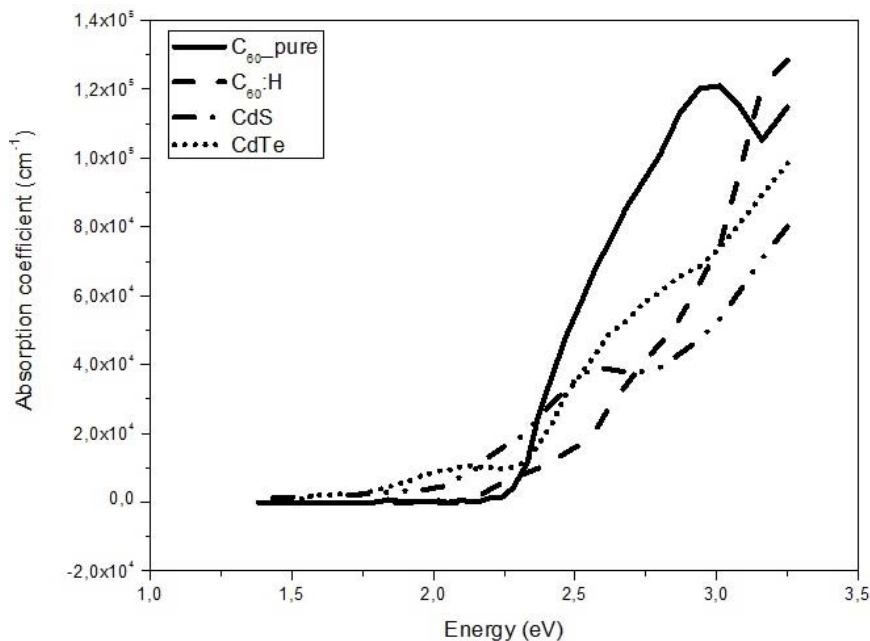


FIG. 6. The absorption coefficients of the films

According to Figure 6, the pristine C_{60} film presents high transparency until 2.2 eV. Above 2.2 eV, a very strong absorption increase was observed, which is probably showing the absorption of excitons. The peak in 2.8 eV can be related to a CT- electron. The CdTe intercalated films gave weak absorbing properties in the 1.5–2 eV region, which may be a result of CdTe itself having an optical threshold at 1.5 eV. There is also one additional mechanism of absorption switch which is present at about 2.2 eV. However, CdS intercalated films displayed more transparency than CdTe films. The optical absorption of CdS films start

approximately at 2.74 eV (4500 Å). Additionally, C₆₀CdS films already begin to absorb at 2 eV, which may possibly be related to the created impurity levels in the molecular C₆₀ solids. The hydrogen plasma-treated film doesn't provide any prominent absorption features in the investigated spectral range. The absorption features on the film likely depend on the Frenkel excitons and there are no signals related to CT-excitons. As a final result, it is noted that pristine C₆₀ film presents the highest absorption in the 2.5–3.5 eV region. The intercalated and plasma treatment films present more transparency. This phenomenon can be explained by the CT-exciton being formed in a pristine C₆₀ film, whereas it is suppressed in the intercalated films.

4. Summary and Conclusions

In this project, the CdS, CdTe, HNO₃, TPP-intercalated and hydrogen plasma-treated fullerene films were studied to determine their ability to generate singlet oxygen. As both polymerization and the generation of singlet oxygen require the triplet state of fullerene, we anticipated that mechanical isolation by the molecules such as weak charge transfer properties or dilute hydrogen functionalization can suppress the polymerization. Raman spectroscopy was used to monitor the polymerization process on the films. The A_g(2) mode was found to split in all cases, except for freshly hydrogen plasma-treated films. The splitting in the A_g(2) mode was very strong in HNO₃- and TPP- intercalated films. CdS and CdTe films also presented the features of A_g(2) - derived modes, which were weaker than the pristine C₆₀ film. The absorption spectra for pristine C₆₀ film had a prominent spectral band linked to CT-excitons. The absorption in the CT-exciton band was much smaller for CdS and CdTe films, whereas it was totally absent in the investigated spectral range for plasma-treated films.

Acknowledgements

The work is supported by the EU FP7 Marie Curie IRSES Project 269138 “Nano-Guard”.

References

- [1] D. Guldi, M. Prato. Excited-state properties of C₆₀ fullerene derivatives. *Accounts of Chemical Research*, **33**, P. 695–703 (2000).
- [2] D. M. McCluskey, T. N. Smith, P. K. Madasu, C. E. Coumbe, M. A. Mackey, P. A. Fulmer, J. H. Wynne, S. Stevenson, J. P. Phillips. Evidence for Singlet Oxygen Generation and Biocidal Activity in Photoresponsive Metallic Nitride Fullerene-Polymer Adhesive Films. *ACS Appl. Mater. & Interfaces*, **1**, P. 882–887 (2009).
- [3] C. S. Foote. Photophysical and photochemical properties of fullerenes. In: *Electron Transfer I*, ed. J. Mattay, Springer Berlin, Heidelberg, (1994) p. 1-17.
- [4] V. V. Zarubaev, I. M. Belousova, O. I. Kiselev, L. B. Piotrovsky, P. M. Anfimov, T. C. Krisko, T. D. Muraviova, V. V. Rylkov, A. M. Starodubzev, A. C. Sirotkin. Photodynamic inactivation of influenza virus with fullerene C₆₀ suspension in allantoic fluid. *Photodiagnosis and Photodynamic Therapy*, **4**, P. 31-35 (2007).
- [5] F. Käsermann, C. Kempf. Photodynamic inactivation of enveloped viruses by buckminsterfullerene. *Antiviral Research*, **34**, P. 65–70 (1997).
- [6] Y. Kai, Y. Komazawa, A. Miyajima, N. Miyata, Y. Yamakoshi. [60] Fullerene as a Novel Photoinduced Antibiotic. In: *Fullerenes, Nanotubes and Carbon Nanostructures*, Taylor & Francis, New York (2003), pp. 79-87.
- [7] S. Wang, R. Gao, F. Zhou, M. Selke. Nanomaterials and singlet oxygen photosensitizers: potential applications in photodynamic therapy. *J. Mater. Chem.*, **14**, P. 487–493 (2004).

- [8] P. Mroz, G. P. Tegos, H. Gali, T. Wharton, T. Sarna, M. R. Hamblin. Fullerenes as Photosensitizers in Photodynamic Therapy. In: *Medicinal Chemistry and Pharmacological Potential of Fullerenes and Carbon Nanotubes*, ed. by F. Cataldo and T. D. Ros, Springer (2008), pp. 79-106.
- [9] T. Wågberg. Studies of polymeric and intercalated phases of C₆₀, Umeå University, Umeå (2001).
- [10] T. Wågberg, P. Jacobsson, B. Sundqvist. Comparative Raman study of photopolymerized and pressure-polymerized C₆₀ films. *Phys. Rev. B*, **60**, P. 4535–4538 (1999).
- [11] A. N. Andriotis, M. Menon, R. M. Sheetz, E. Richter. McConnell Model for the Magnetism of C₆₀-based Polymers. In: *Carbon-Based Magnetism: An Overview of the Magnetism of Metal Free Carbon-Based Compounds and Materials*, ed. by T. L. Makarova and F. Palacio. B. V. Elsevier, Amsterdam (2006), pp. 483–500.
- [12] A. V. Okotrub, V. V. Belavin, L. G. Bulusheva, V. A. Davydov, T. L. Makarova, D. Tomanek. Electronic structure and properties of rhombohedrally polymerized C₆₀. *J. Chem. Phys.*, **115**, P. 5637–5641 (2001).
- [13] M. Yesilbas. *Evaluation of fullerene-based films ability to suppress spontaneous polymerization*, Umeå University, Umeå (2012).
- [14] D. Porezag, M. R. Pederson, T. Frauenheim, T. Khler. Structure, stability, and vibrational properties of polymerized C₆₀. *Phys. Rev. B*, **52**, P. 14963–14970 (1995).
- [15] T. Wågberg, P.-A. Persson, B. Sundqvist. Structural evolution of low-pressure polymerised C₆₀ with polymerisation conditions. *J. Phys. Chem. Solids*, **60**, P. 1989–1994 (1999).
- [16] P.C. Elkund. Phototransformation of fullerenes. Patent US5453413 (1993).
- [17] A. M. Rao, Zhou Ping, Wang Kai-An et. al. Photoinduced Polymerization of Solid C₆₀ Films. *Science*, **259**(5097), P. 955–957 (1993).
- [18] Z.-H. Dong, P. Zhou, J. M. Holden, P. C. Eklund, M. S. Dresselhaus, G. Dresselhaus. Observation of higher-order Raman modes in C₆₀ films. *Phys. Rev. B*, **48**, P. 2862–2865 (1993).

UV–Vis DIAGNOSTICS OF THE PMMA–C₆₀ COMPOSITE SYSTEM AND THE KINETICS OF ITS THERMAL DECOMPOSITION

A. A. Bogdanov¹, A. P. Voznyakovskii², A. O. Pozdnyakov^{1,3}

¹A. F. Ioffe Physico-Technical Institute, Saint Petersburg, Russia

²Federal State Unitary Enterprise Scientific Research Institute for Synthetic Rubber, Saint Petersburg, Russia

³Institute of the Problems of Mechanical Engineering, Russia

a.bogdanov@mail.ioffe.ru, shotputter@yandex.ru, ao.pozd@mail.ioffe.ru

PACS 78.40.Ri, 78.40.Me, 82.80.Rt, 68.60.Dv, 87.15.nr

The influence of polymer-fullerene interactions and fullerene aggregation on the thermal stability of polymethylmethacrylate-fullerene C₆₀ nanocomposite has been studied by means of thermal desorption mass-spectrometry and the UV-Vis absorption spectroscopy.

Keywords: fullerene, polymer, mass-spectrometry, UV-Vis electronic absorption, thermal stability.

1. Introduction

The properties of composite polymer-fullerene systems are influenced by the matrix-filler interactions and the extent of fullerene aggregation. Formation of the composites is implemented by co-dissolution of the components with subsequent film casting and solvent removal from the film. The introduction of the fullerene into the matrix is expected to change the properties of the material. In the majority of works devoted to nanocomposites, the main attention was paid to the influence of the highly dispersed filler on the strength of the material. In previous works (see, e.g., [1, 2] and references therein) the thermal stabilities of various polymer-fullerene systems were studied by means of thermal desorption mass-spectrometry (TDMS). TDMS permits to compare the thermal desorption (TD) spectra of the decomposition products of the neat polymer and the spectra of the composite. It was shown that the thermal desorption (TD) spectra of polymethylmethacrylate (PMMA)-C₆₀ nanocomposite can differ from those of neat PMMA. In the current work, we compare the TD spectra of well-characterized neat PMMA with the TD spectra of a PMMA-C₆₀ nanocomposite and with the character of thermally induced changes in the UV-Vis electronic absorption spectra of the composite.

2. Results and discussion

We used the radically polymerized PMMA (trade mark ACRYPET, Diapolyacrylate Co., Ltd, Japan) with molecular weight parameters of $M_n = 3.5 \cdot 10^4$, $M_w/M_n = 7.67$ as determined via gel permeation chromatography (Waters, USA, UV detector, Breeze software), fullerene C₆₀ (“Fullerene Technologies”, St.-Petersburg, purity – 99,5 %) and highly pure toluene without further purification. PMMA-C₆₀ blends were prepared by means of the co-dissolution of separately prepared C₆₀ and PMMA toluene solutions. The rated concentration of the components was 5.81 g (toluene)/8.9 mg (C₆₀)/29 mg (PMMA). The dissolution resulted in the formation

of a sediment. The real concentration of the components in the solution was, therefore, different from the initial one.

The solutions were cast onto the surface of a stainless steel foil-heater. Details of the TDMS experiments performed with the aid of the reflectron type MS are described elsewhere [1]. UV-Vis spectra were registered with a UV-1800 spectrophotometer in the 190–800 nm wavelength range, the slit thickness used was 1 nm. The films for UV-Vis measurements were prepared by casting PMMA or PMMA-C₆₀ solutions onto a quartz glass plate. Annealing of the samples was carried out at ~ 4 mbar in a Kendro Lab Products (Germany) vacuum oven.

The inset to Fig. 1 shows the full TD spectrum of MMA and the TD spectrum of toluene measured in TD experiments with the neat PMMA films cast from solution. It is seen that along with the main decomposition stage C, the decomposition pattern of PMMA contains two resolved low temperature stages (A and B) of MMA formation. Toluene removal from the film was almost completed at the onset of decomposition stage A. Stage C is interpreted to result from the dissociation of C-C bonds at random sites along the macromolecule. The low temperature stages (A and B) are usually interpreted to result from the decomposition of macromolecules initiated at defect sites along the chain [3]. The formation of the monomer in the low temperature range A can also be related to the depolymerization initiated at macroradicals, formed e.g. upon mechanical treatment or UV irradiation of the polymer [1,4].

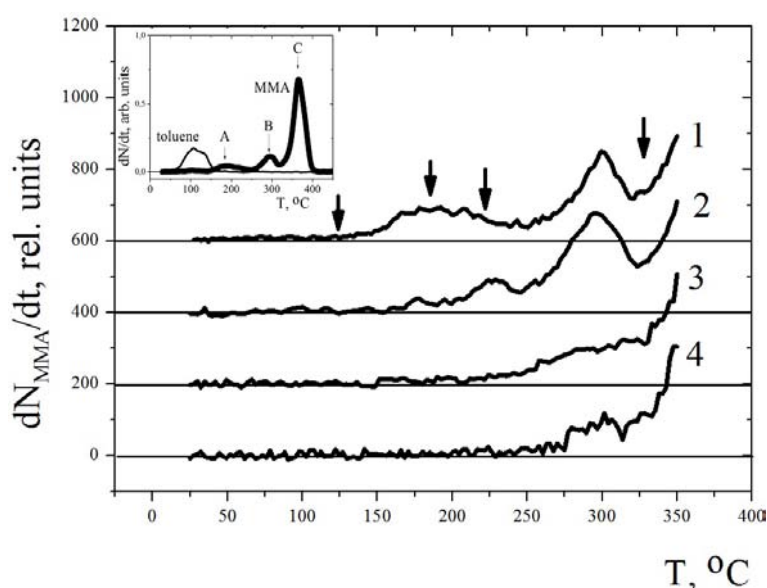


FIG. 1. Low temperature range of the TD spectra of MMA for neat PMMA (curve 1), composite system PMMA-C₆₀ after short, around 1 hour, (curve 2) and prolonged, around 24 hours, PMMA-C₆₀ co-dissolution (curve 3). Curve 4 is the TD spectrum of the sediment of PMMA-C₆₀ solution. The inset shows the full TD spectra of MMA for neat PMMA (thick line) and toluene (thin line). Arrows A, B and C show the characteristic features of TD spectrum of MMA (see text for details). Heating rate $\sim 2 \text{ K}\cdot\text{sec}^{-1}$

Stage C for the composite does not differ from that of neat PMMA. As is seen from Fig. 1, the shape of TD stages A and B for the composite (curves 2, 3) differs strongly compared to that of the neat PMMA (curve 1). The shape of the spectra is determined by the preparation details of the composite film, e.g. by the duration of the initial solution preparation and the conditions of the drying of the films. Nonetheless, we can outline the characteristic features

of the TD spectral shape changes. The intensity of stage A tends to decrease in the case of the composite (curves 2 and 3) compared to neat PMMA (curve 1). Stage B tends to decrease and tail to lower temperatures nonmonotonically with regards to time of dissolution. In order to clarify the question regarding the thermally induced changes in the composite, we have registered UV-Vis spectra of the composite for different annealing regimes. The characteristic temperatures shown by thick vertical lines in Fig. 1 have been chosen. These temperatures are related to the conditions of partial and complete removal (see inset to Fig. 1) of the solvent from the films as well as to the temperatures related to decomposition processes initiated at different defect sites of the PMMA (stages A and B).

Figure 2 shows the electronic absorption spectrum of the as-prepared PMMA-C₆₀ composite film (curve 3). The spectra of C₆₀ in toluene (curve 1) and hexane [6] (curve 2) are given for reference. As is seen, the spectrum of the film resembles the spectrum of the neat C₆₀ in solution (quantity and the position of the band's maxima, their line widths). The strong maxima in the hexane solution are attributed to the allowed transitions at wavelengths 211 nm (transition $8^1T_{1u} - 1^1A_g$), 256.6 nm ($6^1T_{1u} - 1^1A_g$), 328.4 nm ($3^1T_{1u} - 1^1A_g$) and more weak at 408.3 nm ($1^1T_{1u} - 1^1A_g$) with the vibronic structure at 404 nm and the broad weak band at 450–650 nm (vibronic structure of S₀ – S₁ transition) [5, 6].

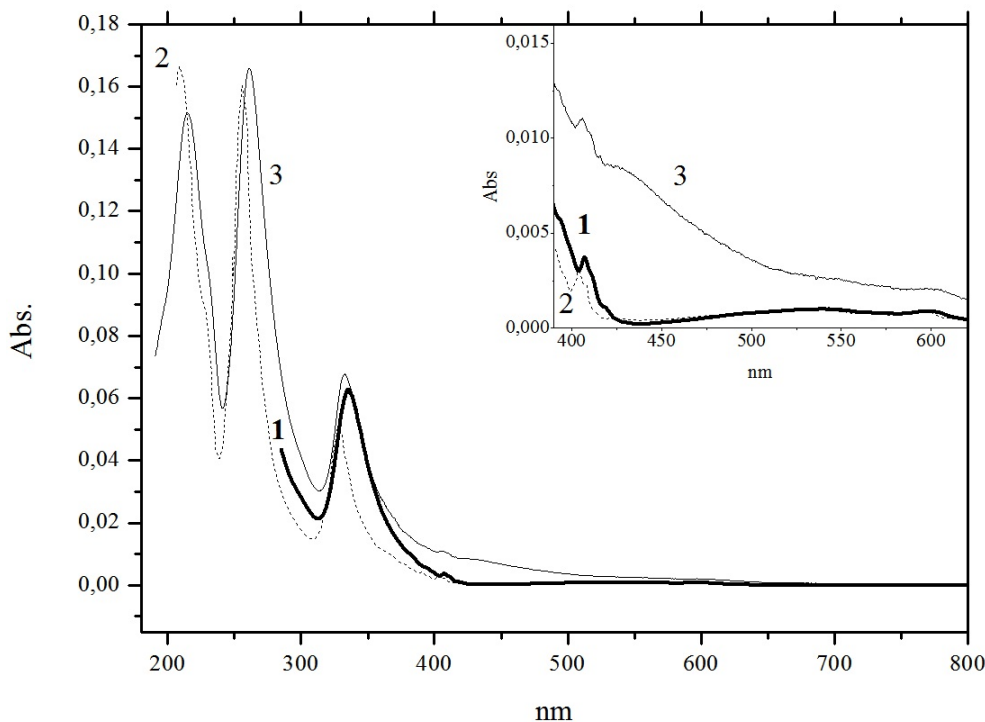


FIG. 2. Electronic absorption spectra of C₆₀ in toluene (curve 1) and in n-hexane (curve 2) (taken from [6]). The absorption spectrum of the initial composite PMMA-C₆₀ (curve 3). The inset shows the blowed-up spectral range 380–620 nm

One can note only a slight red shift of the bands (~ 4 nm for three strong bands) and their broadening. The only spectral change of qualitative character is the additional absorption in the 350–500 nm range. It is worth noting that the absorption maximum around 407 nm remains. From the above, we can conclude that no strong PMMA-C₆₀ bonds are formed of the type discussed, e.g. in [7] and the highly dispersed state of fullerene is preserved. Only

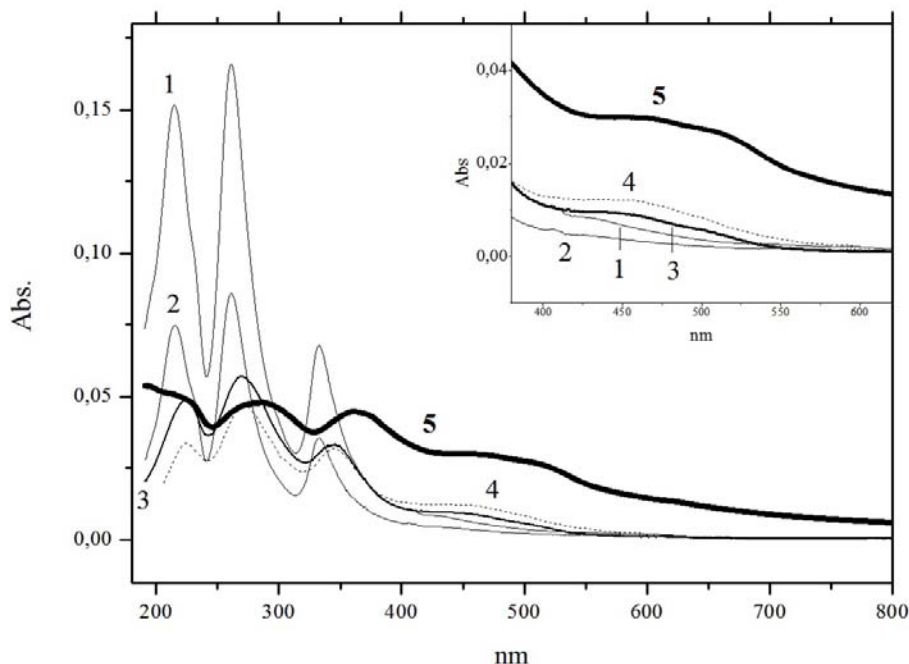


FIG. 3. Absorption spectra of the initial PMMA-C₆₀ film (curve 1), PMMA-C₆₀ composite film after heating up to 120 °C for 40 minutes (curve 2), after heating at 220 °C for 20 minutes (curve 3), after heating at 330 °C for 10 minutes (curve 5). Absorption spectrum of C₆₀ film (taken from [8]) at Al₂O₃ surface (curve 4). The inset shows the blowed-up spectral range 380–620 nm

additional absorbance in the 350–500 nm range can reflect the slight fullerene aggregation in the initial composite.

Figure 3 shows the absorption spectra of the initial PMMA-C₆₀ composite film (curve 1) prior to annealing, as well as the same film after annealing at 120 °C for 40 minutes (curve 2) and at 220 °C for 20 minutes (3). The absorbance spectrum (curve 4) of a neat fullerene C₆₀ film on a clean Al₂O₃ surface (taken from Ref. [8]) is additionally presented for comparison. Comparison of spectra 1 and 2 shows that they are similar. The decrease in the absorption in spectrum 2 is related to the changes in the film's thickness at different sites over the substrate surface. Such similarity of the spectra remained upon heating to 180 °C. The similarity of the spectra enables us to conclude that heating does not result in the formation of strong bonds between fullerene and the polymer, thus the fullerene dispersion state is not altered upon heating up to 180 °C. Note that the absence of strong PMMA-C₆₀ interactions is in good agreement with the results of Near-edge X-ray absorption fine structure spectroscopy [2]. Therefore, the decrease in monomer formation intensity at stage A for the composite may not be related to the formation of the strong interactions between the components and can be explained by the changes in the macromolecular dynamics in the presence of well dispersed fullerene molecules [9].

After annealing at 220 °C (curve 3), the spectrum of the film is radically changed: a significant broadening and red shift of the absorption bands is seen. The absorption band at 407 nm disappeared, while a broad band in the 380–550 nm appeared. The spectrum of the film became similar to the spectrum of a neat C₆₀ film. From these observations, one can suggest that heating of the composite results in the aggregation of almost total amount of the fullerene molecules present in the film. Such strong aggregation of the fullerenes in the narrow temperature range may indicate the growth of the mobility of the fullerene molecules

in the matrix. Upon further heating to 330°C (curve 5), additional strong changes were noted in the spectra: the maxima were strongly broadened and red shifted, while the band at 400–550 nm grew strongly and a strong absorption appeared in the 550–800 nm region. These high temperature changes in the spectra for PMMA decomposition at random sites (stage C in the inset to Fig. 1) requires further detailed studies.

We have therefore given evidence for the absence of strong polymer-fullerene interactions and an increase in the aggregation of fullerene molecules upon thermal annealing of PMMA-fullerene nanocomposites over a broad range of temperatures. These observations suggest that the thermal decomposition pattern of the PMMA matrix may be related to the changes in the macromolecular mobility in the presence of fullerene molecules.

Acknowledgements

A.O.P. thanks the Program of Fundamental Research of the RAS “Fundamentals of technologies of nanostructures and nanomaterials” for partial financial support.

References

- [1] Pozdnyakov A.O. Thermal Decomposition Mass-Spectra of Polymer-Fullerene C₆₀ Systems. *J. Macromolecular Sci., Pt B: Physics*, **52** (12), P. 1681–1696 (2013).
- [2] Pozdnyakov A.O., Brzhezinskaya M.M., Vinogradov A.S., Friedrich K. NEXAFS spectra of polymer-nanocarbon composites. *Fullerenes, Nanotubes, and Carbon Nanostructures*, **16** (5–6), P. 471–474 (2008).
- [3] Kashiwagi T., Inaba A., et al. Effects of Weak Linkages on the Thermal and Oxidative Degradation of Poly(methyl methacrylates). *Macromolecules*, **19** (8), P. 2160–2168 (1986).
- [4] Pozdnyakov O.F., Popov E.O., Pozdnyakov A.O. UV Photostability of PMMA-C₆₀ Fullerene Composition. *Techn. Phys. Lett.*, **38** (12), P. 1053–1055 (2012).
- [5] Leach S., Vervloet M., et al. Electronic spectra and transitions of the fullerene C₆₀. *Chem. Phys.*, **160** (3), P. 451–466 (1992).
- [6] Pavlovich V.S., Shpilevsky E.M. Absorption and fluorescence spectra of C₆₀ fullerene concentrated solutions in hexane and polystyrene at 77–300 K. *J. Appl. Spectroscopy*, **77** (3), P. 335–342 (2010).
- [7] Kurmaz S.V., Ozhiganov V.V. Fullerene Containing Branched Polymethacrylates and Polymer Networks: Synthesis, Structure, and Properties. *Polymer Science, Ser. A*, **53** (3), P. 232–245 (2011).
- [8] Tokmakoff A., Haynes D.R., George S.M. Desorption kinetics of C₆₀ multilayers from Al₂O₃ (0001). *Chem. Phys. Lett.*, **186** (4–5), P. 450–455 (1991).
- [9] Kropka J.M., Sakai V.G., Green P.F. Local Polymer Dynamics in Polymer-C₆₀ Mixtures. *Nano Lett.*, **8** (4), P. 1061–1065 (2008).

TOWARD PACLITAXEL–[60]FULLERENE IMMUNOCONJUGATES AS A TARGETED PRODRUG AGAINST CANCER

Y. Mackeyev¹, M. Raoof², B. Cisneros^{1,2}, N. Koshkina²,
C. S. Berger¹, L. J. Wilson¹, S. A. Curley³

¹Department of Chemistry and The Smalley Institute for Nanoscale Science & Technology,
Rice University, Houston, TX

²Department of Surgical Oncology, The University of Texas M. D. Anderson Cancer Center,
Houston, TX

³Baylor College of Medicine, One Baylor Plaza, MS390, Houston, TX 77030

mackeyev@rice.edu, mustafaraoof@yahoo.com, brandon.cisneros@gmail.com,
nvkoshki@mdanderson.org, csberger@rice.edu, durango@rice.edu, steven.curley@bcm.edu

PACS 81.20.Ka; 81.05.ub; 87.19.xj; 87.85.Qr, 87.85.Rs

Two newly synthesized water-soluble conjugates of Paclitaxel with malonodiserinolamide-derivatized [60]fullerene (C₆₀-ser) undergo hydrolysis and release their medical payload under biological conditions. *In vivo* testing of one of these compounds in a murine model showed tumor volume reduction similar to the FDA-approved drug Abraxane, but without the associated weight-loss, indicating better tolerance of this new formulation.

Keywords: Fullerene, Paclitaxel, Cancer, Immunoconjugate.

1. Introduction

Paclitaxel is a clinically used anticancer drug, which acts by binding stoichiometrically and specifically to the β -tubulin subunit in the microtubules in cell nuclei, thus preventing cell division [1]. Paclitaxel dissolved in Cremophor EL, polyethoxylated castor oil, (Taxol[®]) is widely used to treat various types of cancer, including breast cancer and non-small cell lung cancer (NSCLC) [2]. Abraxane is a water-soluble formulation of Paclitaxel, bonded to albumin as a delivery vehicle; it received US FDA approval in 2005 for medical use, including the treatment of NSCLC [3].

Paclitaxel's clinical use is primarily limited by its high non-specific cytotoxicity and its poor water solubility. Since there are many reports indicating that prolonged administration of higher Paclitaxel doses is poorly tolerated by patients because of myalgia and neurotoxicity [4–6], it is important to choose the right delivery vehicle for Paclitaxel which can mitigate these undesirable properties. [60]Fullerene, due to its antioxidant properties, was recently shown to serve as a possible prevention and treatment of various neurological diseases such as Parkinson's disease, Alzheimer's disease, senility, and schizophrenia, in which the role of free radical production has recently come into focus [7–9]. Thus, combining the water-soluble fullerene with Paclitaxel is a new strategy using the fullerene as a non-toxic transfection agent vector to deliver a chemotherapeutic prodrug to cancer cell nuclei.

Recently, we have shown that a fluorescently-labeled, biocompatible malonodiserinolamide-derivatized [60]fullerene (C₆₀-ser) is internalized within living cancer cells in association with serum proteins through multiple energy-dependent pathways. The labeled C₆₀-ser escapes endocytotic vesicles to eventually localize and accumulate in the nucleus of the cell through

the nuclear pore complex [10, 11]. *In vitro* studies indicate a very low cytotoxicity for C₆₀-ser in cells. Together, these findings suggest that C₆₀-ser can serve as a potential delivery vehicle for therapeutic agents with intranuclear activity (DNA plasmids, drugs such as paclitaxel, gemcitabine, camptothecin, cisplatin, siRNA, transcription factors, epigenetic agents, etc) to treat cancer. Targeted delivery of these vehicles can be achieved by their binding with tumor-specific antibodies, due to the known affinity of water-soluble fullerenes for antibodies to form immunoconjugates [12].

As part of our efforts to treat cancer with carbon nanostructure-mediated RF hyperthermia (including [60]fullerene) [13], here we report the syntheses of two new water-soluble conjugates of Paclitaxel with C₆₀-ser, **3** and **7**, which are expected to undergo hydrolysis and release Paclitaxel under controlled conditions. The rationale behind this approach is 1) to facilitate the membrane transfer, both cellular and nuclear, of Paclitaxel due to the properties of the [60]fullerene moiety as a transfection agent [14], 2) to achieve selective delivery of Paclitaxel from a prodrug by esterase hydrolysis inside cancer cells, and 3) to achieve high water solubility of the Paclitaxel prodrug in comparison to Paclitaxel itself.

Cell culture and *in vivo* testing of these [60]fullerene-Paclitaxel conjugates have shown that both **3** and **7** have equal or superior efficacy to current Cremophor EL and Abraxane[®] Paclitaxel formulations, though they both will require further refinement to become clinically viable.

2. Results and Discussion

2.1. Synthesis and characterization of C₆₀-Paclitaxel conjugates

C₆₀-Paclitaxel conjugates **3** and **7** have been synthesized and purified according to the procedure briefly described below. The reaction scheme is shown in Fig. 1.

Proton nuclear magnetic resonance spectra were measured with a *Bruker 400 MHz NMR spectrometer* with tetramethylsilane as an internal standard. MS spectra for water-insoluble compounds were collected using a *MS Reflex IV MALDI-TOF mass spectrometer* and for water-soluble fullerene derivatives, by *MS electrospray ionization time-of-flight (ESI-TOF) mass spectrometer*, both instruments from Bruker Daltonics Inc (Fremont, CA).

1 (Paclitaxel-2'-poly(ethylene glycol) ester) was synthesized generally following the scheme outlined in [15]. In a typical experiment, 1 g (1.171 mmol) of vacuum-dried Paclitaxel was put into a 100 ml flask with 50 ml of dry trichloroethene (1,1,2-trichloroethene) with 0.54 g (8.955·10⁻⁴ mol) of PEG600 carboxylic acid and 4-dimethylaminopyridine (DMAP, 0.3 g, 2.4 mmol) dissolved. The stirred solution was cooled with ice, and a solution of diisopropylcarbodiimide (*i*PrN=C=N*i*Pr, 0.15 g, 1.171 mmol) in 1 ml of trichloroethene was added. Reaction progress at RT was monitored by the dissolving of Paclitaxel. Flash purification on silica using a CH₂Cl₂-MeOH eluent system yielded 0.58 g of **1** (white solid, .041 mmol, 46%). MS Autoflex MALDI-TOF (positive ion mode): calculated masses = 1321.55 (n=8), 1365.58 (n=9), 1409.60 (n=10), 1453.63 (n=11), 1497.66 (n=12), 1541.68 (n=13), 1585.71 (n=14) Da; observed masses = 1322.736, 1366.754, 1410.789, 1454.808, 1498.844, 1542.902 Da [M+H⁺], 1388.827, 1432.827, 1476.859, 1520.893, 1564.968, 1608.990 Da [M+Na⁺]. NMR (CDCl₃, TMS reference): ¹H δ(ppm) = 1.109 (d), 1.177 (s), 1.223 (d), 1.643 (s), 1.671 (d), 1.808 (t), 1.931 (d), 2.043 (dd), 2.213 (d), 2.333 (s), 2.471 (t), 3.489-3.697 (m), 3.721 (dd), 3.746 (s), 4.013 (bs), 4.162 (dd), 4.262 (t), 4.244(s), 4.262 (t), 4.272-4.333 (m), 4.367 (dd), 4.433 (dd), 4.904 (d), 4.934 (d), 5.542 (q), 5.596 (s), 5.610 (s), 5.625 (s), 5.954 (d), 6.085 (t), 6.230 (s), 6.291 (s), 7.155 (t), 7.301-7.556 (m), 7.631 (q), 7.754 (d), 7.903 (d), 8.071 (d), 8.137 (d).

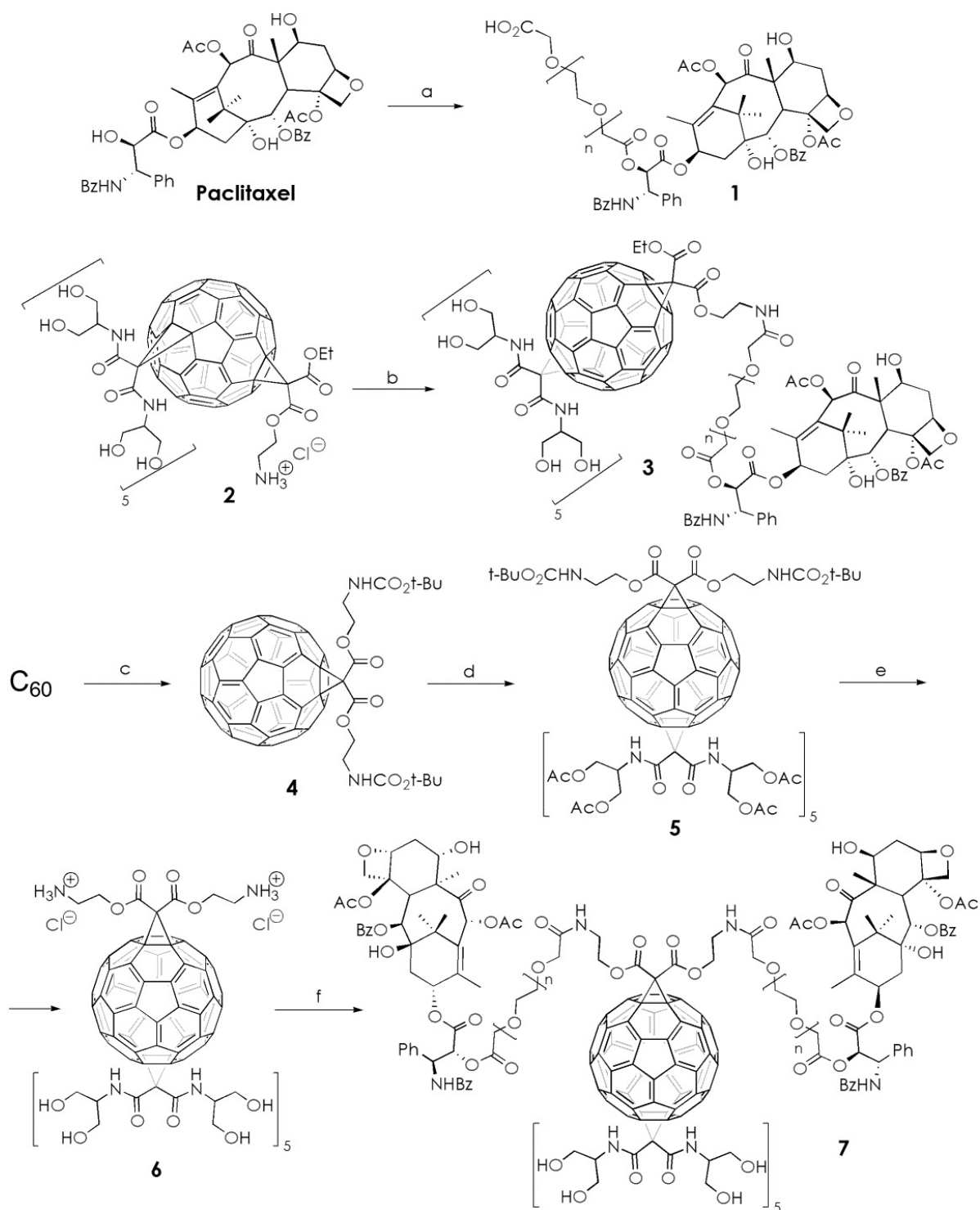


FIG. 1. The synthesis of C₆₀-Paclitaxel conjugates **3** and **7** ($n \approx 10$). Reagents and conditions: (a) PEG-600 dicarboxylic acid, in CHCl₂=CCl₂, iPrN=C=NiPr, 4-dimethylaminopyridine, 36 h; (b) **1**, EDC, MES hemisodium salt buffer (pH = 6.5), 15–30 min; (c) bis-(β-tert-butoxycarbonylaminoethyl) ester of malonic acid, CBr₄, DBU, 3 h; (d) N,N'-bis[2-(acetyloxy)-1-[(acetyloxy)methyl]ethyl]-malonamide, CBr₄, DBU, overnight; (e) 1 M HCl in dioxane: H₂O (99:1), 24 °C, 48 h; (f) **1**, EDC, MES buffer (pH = 6.5), 4 h

3 (C_{60} -ser-Paclitaxel-2'-poly(ethylene glycol) ester) was synthesized by dropwise addition of 10.8 mg (0.005 mmol) of **2** in 400 ml of water (prepared and purified according to procedure given in [10]) to 7.9 mg (0.0055 mmol) of **1**, with 1-ethyl-3-(3-dimethylaminopropyl)carbodiimide (EDC, 1 mg, 0.006 mmol), and hydroxybenzotriazole (HOBt, 0.5 mg, 0.004 mmol, catalytic amount) in 10 ml of 1M MES hemisodium salt buffer (pH = 6.5), stirring for 30 min at RT. Then the product was extracted with 3×10 ml of chloroform, dried *in vacuo*, purified by HPLC (MeOH – water, Atlantis T3 column, 4 ml/min flow rate, Waters LC Module 1Plus) to afford 5.1 mg of product (29% yield). MicroTOF ESI (positive-ion mode): calculated masses = 3437.11 (n=8), 3481.14 (n=9), 3525.17 (n=10), 3569.19 (n=11), 3613.22 Da (n=12); observed mass = 3440.0, 3483.4, 3528.1, 3572.1 Da [M⁺], 3461.6, 3505.5, 3550.3 Da [M+Na⁺], 3566.9 Da [M+K⁺].

4 (1',1'-dicarboxylic acid di-(2-*tert*-butoxycarbonylamino-ethyl ester) 1,2-methano[60]fullerene) was synthesized in accordance with a known literature procedure [16]. 727 mg of C_{60} (1 mmol) was dissolved in dry toluene (500 ml) with 500 mg of CBr_4 (1.5 mmol), with 585 mg (1.5 mmol) of malonic acid bis-(b-*tert*-butoxycarbonylaminoethyl) ester, prepared as described in [17]. The solution of 230 mg of DBU (1.5 mmol) in toluene was added within 30 min at RT, after which the reaction proceeded for 3 hours. The product was isolated via flash column chromatography using a toluene – ethyl acetate (9:1) eluent system. Yield was 455 mg (46%). MALDI-TOF MS (pos. ion mode): calculated mass = 1109.1, observed mass = [M+H⁺] 1110.0. ¹H NMR ($CDCl_3$, TMS ref.) ¹H δ (ppm) = 1.58 (s, 18H, C(CH₃)₃), 3.61 (t, 4H, CH₂NH), 4.59 (t, 4H, CH₂O), 5.11 (s, 2H, NH).

5 (3',3'-di-((2-((*tert*-butoxycarbonyl)amino)ethoxy)carbonyl)-3'', 3'', 3''', 3''', 3''''', 3''''', 3''''', 3''''''-deca-(2-acetoxy-1-acetoxymethylethylcarbonyl)-3'H, 3''H, 3'''H, 3''''H, 3'''''H, 3''''''H-hexacyclopropa [1, 9 : 16, 17 : 21, 40 : 30, 31 : 44, 45 : 52, 60] (C_{60-I_h}) [5,6] fullerene). 111 mg (0.1 mmol) of **4** dissolved in 300 ml of toluene, with 332 mg of CBr_4 (1 mmol), and 837 mg (2 mmol) of acetic acid 3-acetoxy-2-[2-(2-acetoxy-1-acetoxymethylethylcarbonyl)-acetylamino]-propyl ester (2 mmol) (“serinol malonate”, prepared according to [18], to which a solution of 141 mg of *tert*-butylimino-tris(dimethylamino)phosphorane (0.6 mmol) in 100 ml of dry methylene chloride was added in 3 hours. After 18 hours, the product was isolated via flash column chromatography with a chloroform - ethanol eluent (19:1). Yield 153 mg (48%). MALDI-TOF MS (pos. ion mode): calculated mass = 3190.95, observed mass = [M+H⁺] 3191.91. ¹H NMR (400 MHz, $CDCl_3$, TMS reference) δ (ppm) = 1.48 (s, 18H, C(CH₃)₃), 2.08 (s, 60H, acetate CH₃), 3.55 (t, 2H, CH₂NH), 4.38 (t, CH₂O), 4.58 (m, 10H, in serinol), 4.27 (m, 40H, in serinol), 4.9 (s, 12H, NH).

6 (3',3'-di-((2-aminiumethoxy)carbonyl)-3'', 3'', 3''', 3''', 3''''', 3''''', 3''''', 3''''''-deca-(2-hydroxy-1-(hydroxymethyl)ethylcarbonyl)-3'H, 3''H, 3'''H, 3''''H, 3'''''H, 3''''''H-hexacyclopropa [1, 9 : 16, 17 : 21, 40 : 30, 31 : 44, 45 : 52, 60] (C_{60-I_h})[5,6]fullerene dihydro-chloride) was obtained by hydrolysis of **5** (153 mg, 0.05 mmol), dissolved in 10 ml of dioxane-water (99:1) and saturated with HCl gas at RT up to a 1M concentration. The mixture was kept closed for 48 hours at RT, then the solvents was removed *in vacuo*, and the product was purified using a cellulose ester dialysis membrane (Thermo Scientific, 2000 MWCO) for 7 days using DI water with pH=4.0, adjusted by HCl_(aq.). Yield 107 mg (98%). ESI-TOF MS (pos. ion mode): calculated mass (cation) = 2152.0, observed masses = [M⁺+2H₂O] 2188.1. ¹H NMR (400 MHz, DMF-D₇, 2.75 peak used for ref.) δ (ppm) = 2.96 (t, 4H, CH₂NH₃⁺), 3.84 (t, 4H), 3.96 (m, 40H, CH₂OH), 3.55 (m, 10H, CH₂NH).

7 (C_{60} -ser-*bis*-Paclitaxel-2'-poly(ethylene glycol) ester) was synthesized by dropwise addition of 5.5 mg (0.0025 mmol) of **6** in 400 μ l of water to a solution of 7.9 mg (0.0055 mmol) of **1**, 1 mg (0.006 mmol) of EDC, 1 mg (0.008 mmol) of HOBt in 10 ml of 1M MES

TABLE 1. Hydrolysis half-lives in hours of 1, 3 and 7 at 23.5 °C

	1	3	7
0.1% CF ₃ CO ₂ H _(aq.) (pH ≈ 2)	1.68 ± 0.30	1.22 ± 0.21	n/a
1M MES buffer (pH = 5.6)	75.6 ± 13.0	64.5 ± 12.0	49.5 ± 12.0
1x PBS buffer (pH = 7.4)	47.4 ± 12.0	38.5 ± 11.0	35.5 ± 11.0

buffer (pH = 6.5), stirred for 4 h at RT. The product was extracted with 3 × 10 ml of chloroform, dried *in vacuo*, purified by HPLC (MeOH – water, 5PYE column, 4 ml/min flow rate, Waters LC Module 1Plus) to afford 5.0 mg of product (40% yield). MicroTOF ESI (positive-ion mode): calculated masses = 4890.91 (n+n=19), 4934.97 (n+n=20), 4979.02 (n+n=21) Da; observed mass = 4891.3, 4935.4 [M+H⁺], 5002.6, 4958.3 [M+Na⁺].

2.2. Aqueous solutions of the C₆₀-Paclitaxel conjugates

Dissolution of **1**, **3** and **7** in acidic or buffered solutions at pH=2.0 through physiological pH=7.4 resulted in the release of Paclitaxel, as expected. Half-lives, $t_{1/2}$, were calculated assuming that hydrolysis reactions follow Michaelis–Menten kinetics, are shown in Table 1.

Solubilities in water were estimated using standard filtration at RT and the freeze-drying method: 15 ± 3 mg/ml (**1**); 380 ± 80 mg/ml (**3**); ≥ 250 mg/ml (**7**).

Water-soluble fullerenes tend to form aggregates in aqueous solution [19,20]. Fig. 2 shows dynamic light scattering (DLS) data of a solution of **3** at 100 μg/mL, using a Malvern Zetasizer, Model Zen 3600 (He-Ne laser, 4.0 mW, 632.8 nm; Malvern Instruments Ltd, Malvern, Worcestershire, United Kingdom). As shown in the Figure, under these conditions the average hydrodynamic diameter of aggregated Compound **3** is ca. 240 nm.

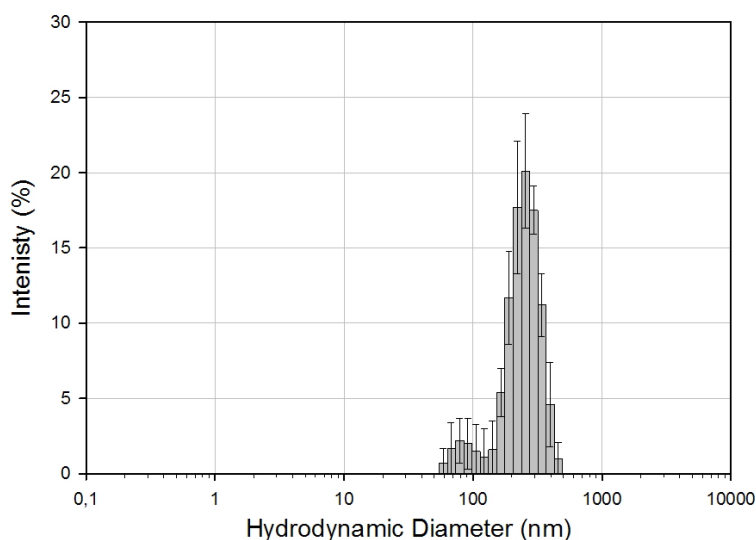


FIG. 2. Aggregate size distribution in solution of **3** (Concentration: 100 μg/mL, average $D_h = 244.5$ nm, solution filtered using 0.45 μM PES membrane)

2.3. Materials, cell cultures and cell lines

Normal human pancreatic ductal epithelial (HPDE) cells and pancreatic adenocarcinoma cells Panc-1 and AsPC-1 were seeded in 96-well plate. After overnight incubation, the cells were treated for 72 h with 1 mM Paclitaxel alone or **7**. C₆₀-ser, a similar unlabeled compound known

TABLE 2. In vitro timed pulse cytotoxicity assay of Abraxane, Paclitaxel, and Compound 3 in Hep3B cells

	IC ₅₀ Values of Paclitaxel and its Derivatives	
	24 h. exposure timepoint	72 h. exposure timepoint
Paclitaxel	7.94	10.31
Abraxane	21.5	5.40
3	3.58	1.02

to be a transfection agent [14], and untreated cells were used as controls. The cytostatic effect of treatment was determined by adding MTT (3-(4,5-dimethylthiazol-2-yl)-2,5-diphenyltetrazolium bromide) salt solution in PBS, which is reduced to purple formazan crystals in living cells.

Results support the assumption that C₆₀-ser showed no cytotoxic effect on normal and cancer cells and can therefore be used as a delivery vehicle for Paclitaxel. A dose of 1 μ M of Paclitaxel was toxic to all cells. Conjugate **7** is less cytotoxic toward cancer cells than Paclitaxel itself, as shown in Fig. 3. However, functionalization of C₆₀-ser with Paclitaxel to form **7** produced a Paclitaxel derivative that was more cytotoxic for normal HPDE cells than free Paclitaxel.

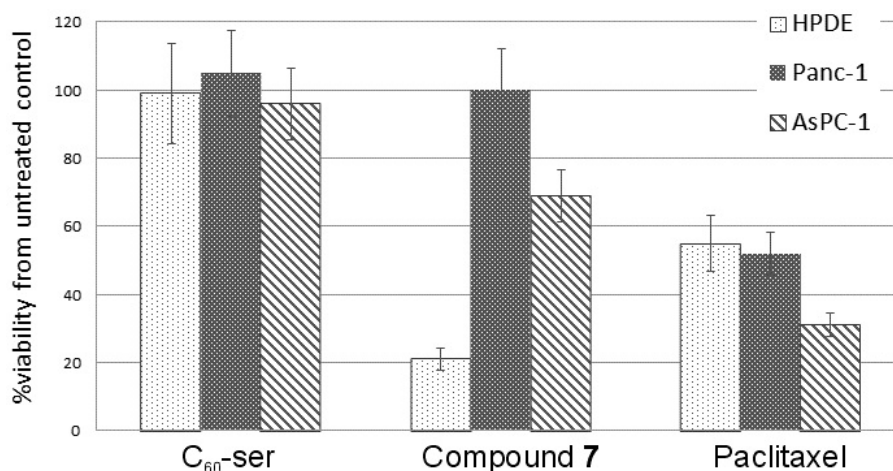


FIG. 3. Cytotoxic effect of Paclitaxel and Compound 7 for normal human ductal epithelial cells (HPDE) and malignant pancreatic cells (Panc-1 and AsPC-1). All cells received PTX at 0.2 M for 72 h. Cell viability was determined as a ratio to the untreated cells that were used as control

Cytotoxicity studies of **3** performed on hepatocellular carcinoma cell line HEP 3B showed that efficacy increased significantly when compared with Paclitaxel alone or when the drug was conjugated with albumin (Abraxane) (Table 2).

2.4. *In vivo* cytotoxic activity of **3**

Cells from the liver cancer cell line Hep3B which had been transfected with luciferase plasmid and green fluorescent protein were cultured according to the American Type Culture Collection (ATCC) guidelines for this cell line. Approximately 1.6 million cells in 10 μ L of PBS were injected into mice orthotopically under the liver capsule for 29 female C.B-17 SCID mice (Taconic, Hudson, NY). After four weeks, tumor development was verified using luminescence imaging. The mice were injected with 25 mg/kg firefly D-luciferin in 100 μ L saline and then

subjected to non-invasive bioluminescence imaging. After bioluminescence imaging confirmed tumor progression of hepatocellular carcinoma in all mice, animals were randomized in five groups of mice (6 mice/group): the first group received Paclitaxel (in Cremaphor EL), the second group received Abraxane, and the third group received Paclitaxel as Compound **3**. The other two groups received either C_{60} -ser alone or injections of saline and were used as controls. The C_{60} -ser group had five mice instead of six.

All groups were weighed daily and given an IP injection of the appropriate dose of drug in a 100 μ L sterile PBS dilution for five consecutive days. The Taxol group received 12.5 mg Paclitaxel/kg/day. The Abraxane and the Compound **3** groups received 30 mg Paclitaxel(equivalent)/kg/day. The dose administered for the Compound **3** group was calculated using the approximation that the prepared conjugate was 90% pure. The reason the Abraxane and Taxol groups received different doses of Paclitaxel was to achieve equal toxicity rather than equal molar doses, as Paclitaxel is more potent per quantity [21]. Based on the behavior of Abraxane, we assumed that the water-soluble conjugate would have a similar toxicity profile. The C_{60} -ser group received 78 mg/kg/day. This dosage represents the molar equivalent of C_{60} -ser for the Compound **3** group. Solutions of Taxol and Abraxane were prepared fresh daily. Compound **3** is susceptible to hydrolysis of the ester linkage so the solutions were prepared in advance, flash frozen, and thawed as necessary immediately prior to use.

At the end of the experiment, animals were euthanized and tumors were resected, weighed and preserved in formalin along with vital organs (kidney, liver and intestine). Results from this experiment are shown in Fig. 4. Compound **3** was equipotent to Abraxane. We noticed that the animals in the group receiving Abraxane tolerated the treatment less well than those receiving Compound **3**. The average body weight of mice in this group decreased $>10\%$ (Fig. 5). Two mice from this group had to be euthanized due to morbidity signs. In this way, the length of the study could be maximized, while still allowing for statistical analysis. In contrast, mice that received Compound **3** showed no evidence of toxicity and did not lose body weight until the end of the study.

3. Conclusions

Currently, the development of the Paclitaxel- C_{60} conjugates included in this work (Compounds **3** and **7**) serve as a contribution to the growing library of research utilizing fullerenes as therapeutic modalities. Compared to Paclitaxel and FDA-approved Abraxane, *in vitro* testing of Compound **3** yielded excellent results, showing $10\times$ and $5\times$ greater cytotoxicity than Paclitaxel and Abraxane, respectively. *In vivo* testing of Compound **3** in a murine model with orthotopic hepatocellular carcinoma showed tumor volume reduction similar to FDA-approved Abraxane, but without the weight-loss associated with present clinically approved formulations of Paclitaxel. This indicates the need for further studies of Compound **3** as a stand alone, water-soluble agent for the delivery of hydrophobic Paclitaxel. Good tolerance of Compound **3** in our studies implies that higher doses of it may be better tolerated than current clinical agents.

For Compound **7**, with twice the amount of Paclitaxel, *in vitro* testing demonstrated promising cytotoxicity values, but lack of specificity prevented it from being tested *in vivo*.

Our results support previous findings that C_{60} -ser is not toxic to cells and animals and is capable of altering the cytotoxic properties of a chemotherapeutic agent. We plan to investigate C_{60} -ser conjugated to other anticancer agents to find out which class of prodrugs is most suitable for delivery via the C_{60} -ser carrier vector.

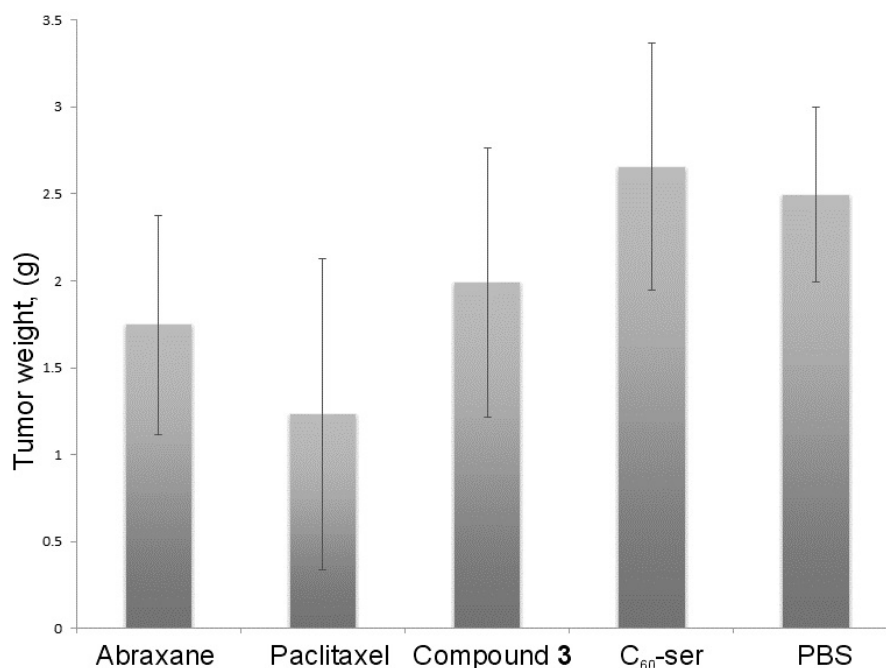


FIG. 4. Average tumor weights in murine subjects after treatment (average with standard dev.)

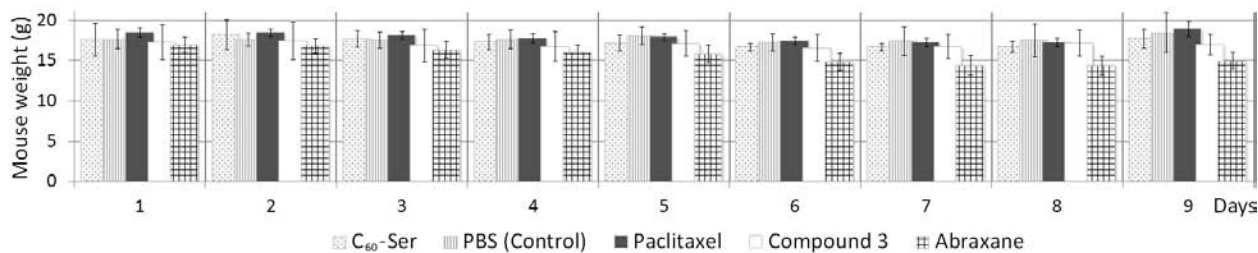


FIG. 5. The change in average body weight of mice during treatment (average with standard dev.)

Acknowledgments

We gratefully acknowledge the Welch Foundation (grant C-0627) and the Kanzius Research Foundation for support of this work.

References

- [1] Schiff P.B., Fant J., Horwitz S.B. Promotion of microtubule assembly in vitro by taxol. *Nature*, **277**, P. 665–667 (1979).
- [2] Sparreboom A., Van Tellingen O., Nuijten W.J., Beijnen J.H. Nonlinear Pharmacokinetics of Paclitaxel in Mice Results from the Pharmaceutical Vehicle Cremophor EL. *Cancer Res.*, **56**, P. 2112–2115 (1996).
- [3] Gradishar W.J. Albumin-bound Paclitaxel: a next-generation taxane. *Expert Opinion on Pharmacotherapy*, **7** (8), P. 1041–1053 (2006).
- [4] Cascinu S., Ficarelli R., et al. A phase I study of Paclitaxel and 5-fluorouracil in advanced gastric cancer. *European J. Cancer*, **33** (10), P. 1699–1702 (1997).
- [5] Postma T.J., Vermorken J.B., et al. Paclitaxel-induced neuropathy. *Annals of Oncology*, **5**, P. 489–494 (1995).
- [6] Schiller J.H., Storer B., et al. Phase I trial of 3-hour Paclitaxel with or without granulocyte colony-stimulating factor in patients with advanced cancer. *J. Clinical Oncology*, **12**, P. 241–248 (1994).

- [7] Dugan L.L., Turetsky D.M., et al. Carboxyfullerenes as neuroprotective agents. *Proc. Natl. Acad. Sci. USA*, **94**, P. 9434–9439 (1997).
- [8] Dugan L.L., Lovett E., et al. Carboxyfullerenes as neuroprotective agents. *Proc. Electrochem. Soc.*, **98**, P. 1236–1245 (1998).
- [9] Quick K.L., Ali S.S., et al. A carboxyfullerene SOD mimetic improves cognition and extends the lifespan of mice. *Neurobiology of Aging*, **29**, P. 117–128 (2008).
- [10] Raouf M., Mackeyev Y., et al. Internalization of C₆₀ fullerenes into cancer cells with accumulation in the nucleus via the nuclear pore complex. *Biomaterials*, **33**, P. 2952–2960 (2012).
- [11] Huang F., Mackeyev Y., et al. Evidence for nuclear internalisation of biocompatible [60]fullerene. *European Journal of Nanomedicine*, **5** (1), P. 51–55 (2013).
- [12] Ashcroft J.M., Tsybolski D.A., et al. Fullerene (C₆₀) immunoconjugates: interaction of water-soluble C₆₀ derivatives with the murine anti-gp240 melanoma antibody. *Chem. Commun.*, **28**, P. 3004–3006 (2006).
- [13] Gannon C.J., Cherukuri P., et al. Carbon nanotube-enhanced thermal destruction of cancer cells in a noninvasive radiofrequency field. *Cancer*, **110**, P. 2654–2665 (2007).
- [14] Sitharaman B., Zakharian T.Y., et al. Water-soluble fullerene (C₆₀) derivatives as nonviral gene-delivery vectors. *Molecular Pharmaceutics*, **5** (4), P. 567–578 (2008).
- [15] Greenwald R.B., Pendri A., Bolikal D., Gilbert C.W. Highly water soluble taxol derivatives: 2 polyethylene glycol esters as potential prodrugs. *Bioorg. Med. Chem. Lett.*, **4**, P. 2465–2470 (1994).
- [16] Camps X., Hirsch A., Efficient cyclopropanation of C₆₀ starting from malonates. *J. Chem. Soc. Perkin Trans.*, **1**, P. 1595 (1997).
- [17] Cho M., Lee J., et al. Visible light sensitized inactivation of MS-2 bacteriophage by a cationic amine-functionalized C₆₀ derivative. *Environmental Sci. & Technol.*, **44** (17), P. 6685–6691 (2010).
- [18] Wharton T., Wilson L.J. Highly-iodinated fullerene as a contrast agent for X-ray imaging. *Bioorganic & Medicinal Chem.*, **10** (11), P. 3545–3554 (2002).
- [19] Zakharian T.Y., Seryshev A., et al. A Fullerene-Paclitaxel Chemotherapeutic: Synthesis, Characterization, and Study of Biological Activity in Tissue Culture. *J. Am. Chem. Soc.*, **127**, P. 12508–12509 (2005).
- [20] Laus S., Sitharaman B., et al. Destroying Gadofullerene Aggregates by Salt Addition in Aqueous Solution of Gd@C₆₀(OH)_x and Gd@C₆₀[C(COOH₂)]₁₀. *J. Am. Chem. Soc.*, **127**, P. 9368–1969 (2005).
- [21] Desai N., Trieu V., et al. Increased antitumor activity, intratumor Paclitaxel concentrations, and endothelial cell transport of cremophor-free, albumin-bound Paclitaxel, ABI-007, compared with cremophor-based Paclitaxel. *Clinical Cancer Research*, **12**, P. 1317–1324 (2006).

CHARACTERIZATION OF FULLERENE DERIVATIVES BY MALDI LIFT-TOF/TOF MASS SPECTROMETRY

L. B. Piotrovsky¹, B. L. Milman¹, D. N. Nikolaev¹,
N. V. Lugovkina², E. V. Litasova¹, M. A. Dumpis¹

¹Institute of experimental medicine, Saint-Petersburg, Russia

²Institute of toxicology, Saint-Petersburg, Russia

levon-piotrovsky@yandex.ru, bormilman@yandex.ru

PACS 61.48.-c

MALDI LIFT-TOF/TOF mass spectra of fullerene C₆₀ and six of its derivatives, methano[60]fullerene carboxylic acid, its ethyl ester, diethyl methano[60]fullerene dicarboxylate, and three isomeric tetraethyl bis-methano[60]fullerene tetracarboxylates (compounds **I–VII**, respectively) as model analytes were recorded and discussed. This technique used in mass spectrometry for the first time is proposed for the characterization, structure elucidation, and non-target screening of fullerenes.

Keywords: Mass spectrometry, MALDI, LIFT-TOF/TOF mass spectra, fullerene derivative, reference mass spectra.

1. Introduction

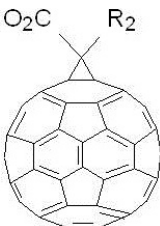
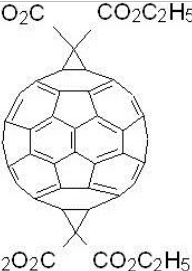
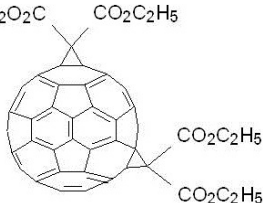
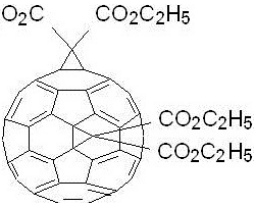
Fullerene derivatives have clear theoretical and applied relevance [1] and, correspondingly, call for new developments in their analysis. These compounds have been routinely characterized by matrix-assisted laser desorption-ionization time-of-flight mass spectrometry (MALDI-TOF MS) [2–6]. However, the corresponding mass spectra may be rather complicated and may contain a number of analyte- and matrix-associated ion peaks, as well as ionized adducts and products of their decomposition. So, the identification of molecular ions or protonated analyte molecules may be hindered. There may also be cases of simple MALDI spectra, where only intense peaks of molecular ions present. Those are certainly insufficient for both substructure elucidation and identification of complex fullerene compounds. For this reason, characteristic fragment ions are also needed.

There have been two generation techniques of characteristic MALDI mass spectra of fullerenes. First, the instruments combining MALDI ion sources, CID cells, and different mass analyzers were used [3, 5, 7]. Second, the technique of post-source decay (PSD) was introduced having such disadvantages as long acquisition times for spectra and rather low fragmentation efficiency [8]. The PSD spectra were recorded for some fullerene compounds [6].

In this research, we propose to use the commercial technique of MALDI LIFT-TOF/TOF MS [8] as one choice to obtain clean product-ion spectra for a reliable characterization/identification of fullerene derivatives. The LIFT process (a) selects a ‘family’ of precursor and its product ions generated from laser-induced ionization and succeeding fragmentation and (b) additionally accelerates these ions to detect them. To the best of our knowledge, this is the first time that this mass spectrometry technique has been used for fullerenes.

In the report, MALDI LIFT-TOF/TOF mass spectra acquired for six fullerene derivatives: methano[60]fullerene carboxylic acid **II**, its ethyl ester **III**, diethyl methano[60]fullerene dicarboxylate (**IV**), three isomeric tetraethyl bis-methano[60]fullerene tetracarboxylates (**V–VII**), and also fullerene itself **I** as model analytes (see Table 1), will be briefly described and discussed.

TABLE 1. Fullere derivatives

				
I	II: $R_1=R_2=H$ III: $R_1=C_2H_5,$ $R_2=H$ IV: $R_1=C_2H_5,$ $R_2=CO_2C_2H_5$	V	VI	VII

2. Experimental

The fullerene **I**, purity of 99.7–99.8%, was obtained from NeoTechProduct (Saint-Petersburg, Russia). Compounds **II–VII** were prepared and purified by known methods described in the literature.

A 10 μ l aliquot of the 0.02% and 0.002% w/v solution of every fullerene compound in toluene was mixed with a 10 μ l 0.1 % w/v solution of 2-[(2E)-3-(4-tert-butylphenyl)-2-methylprop-2-enylidene]malononitrile (DCTB, Sigma-Aldrich) in acetone. A 0.5 μ l volume of the mixture was deposited onto an AnchorChip MALDI plate (Bruker Daltonics) for analysis.

MALDI MS and LIFT MS/MS spectra were obtained by means of UltrafleXtreme MALDI TOF/TOF mass spectrometer (Bruker Daltonics). MALDI-ToF spectra were acquired by 300–4000 shots in the positive and negative ion reflector mode at 1000 Hz UV laser frequency and 10–40 % its power in a mass range from 400 to 1200–5000 Da. MALDI TOF/TOF spectra were composed from precursor ion peaks recorded at the above conditions to which were added product ion spectra acquired by 500–2500 shots in the corresponding ion mode at the same laser frequency and 14–35 % power in a mass range from 40 Da to a parent ion mass.

This matrix [2] (common ones such as α -cyano-4-hydroxycinnamic acid and 2,5-dihydroxybenzoic acid were also tested) and this MALDI plate, with special patches in the centers of spots, were of critical value to obtain ToF mass spectra with abundant molecular ion peaks.

3. Results and discussion

Mass spectra of compounds under consideration are given in Fig. 1 and in Table 2.

The ToF spectra were of a varied complexity. In most spectra, molecular ion peaks were the principal ones, with the rest of a few other peaks (Fig. 1c). The exclusion were mass spectra of the acid **II**, especially in positive mode, which consisted of a lot of peaks comparable in intensity to each other (Fig. 1a).

All our LIFT ToF/ToF spectra were of the same type, with molecular ions and series of product ions terminating mainly in C_{60} itself (Fig. 1b and d, Table 2). Fragmentation of the fullerene core was only observed in the case of **I**. Far lower mass fragments were very rare excluding the isomeric molecules **V–VII** (Table 2).

The LIFT spectra (Table 2) characterize all structural details of compounds **II–VII**, i.e. structure of addends bonded to the C_{60} core. Ester groups are eliminated as neutral species of $CO_2C_2H_5$ and $HCO_2C_2H_5$. There is no strong evidence to suggest that these are one-step

TABLE 2. MALDI LIFT-TOF/TOF spectra. Principal ions

Compound	m/z (composition), %	
	Positive mode	Negative mode
I	720 (M^+) 696 ($[M-C_2]^+$), 100% 672 ($[M-C_4]^+$), 6%	720 (M^-) ¹ 696 ($[M-C_2]^-$), low peak
II	778 (M^+) 733 ($[M-CO_2H]^+$) ² , 100% 720 ($[M-CHCO_2H]^+$) ³ , 6%	778 (M^-) 733 ($[M-CO_2H]^-$) ² , 100%
III	806 (M^+) 778 ($[M-C_2H_4]^+$), 100% 734 ($[M-C_2H_4-CO_2]^+$) ⁴ , 30% 733 ($[M-CO_2C_2H_5]^+$) ² , 30% 720 ($[M-CHCO_2C_2H_5]^+$) ³ , 5%	806 (M^-) 762 ($[M-CO_2]^+$), 9% 733 ($[M-CO_2C_2H_5]^-$) ² , 100% 720 ($[M-CHCO_2C_2H_5]^-$) ³ , 5%
IV	878 (M^+) 804 ($[M-HCO_2C_2H_5]^+$), 70% 778 ($[M-2C_2H_4-CO_2]^+$), 5% 764 (?), 17% 760 ($[M-HCO_2C_2H_5-CO_2]^+$), 42% 734 ($[M-2C_2H_4-2CO_2]^+$) ⁴ , 8% 733 ($[M-C_2H_4-CO_2-CO_2C_2H_5]^+$) ^{2,4} , 9% 732 ($[M-2CO_2C_2H_5]^+$), 12% 720 ($[M-C(CO_2C_2H_5)_2]^+$) ³ , 100%	878 (M^-) 834 ($[M-CO_2]^+$), 2% 805 ($[M-CO_2C_2H_5]^-$), 30% 765 (?), 9% 761 ($[M-CO_2C_2H_5-CO_2]^-$) ⁴ , 22% 760 ($[M-HCO_2C_2H_5-CO_2]^-$), 17% 733 ($[M-C_2H_4-CO_2-CO_2C_2H_5]^-$) ² , 13% 720 ($[M-C(CO_2C_2H_5)_2]^-$) ³ , 100%
V-VII	1036 (M^+) 991 ($[M-CO_2H]^+$), 10–21% 962 ($[M-HCO_2C_2H_5]^+$), 70–72% 935 ($[M-C_2H_4-CO_2C_2H_5]^+$), 4–6% 918 ($[M-CO_2-HCO_2C_2H_5]^+$), 5% 891 ($[M-C_2H_4-CO_2-CO_2C_2H_5]^+$), 7–9% 888 ($[M-2HCO_2C_2H_5]^+$), 5% 878 ($[M-C(CO_2C_2H_5)_2]^+$), 100% 804 ($[M-C(CO_2C_2H_5)_2-HCO_2C_2H_5]^+$), 7–8% 748 ($[M-4C_2H_4-4CO_2]^+$), 8–10% 733 ($[M-C(CO_2C_2H_5)_2-C_2H_4-CO_2-CO_2C_2H_5]^+$) ² , 4% 720 ($[M-2C(CO_2C_2H_5)_2]^+$) ³ , 77–80%	1036 (M^-) 963 ($[M-CO_2C_2H_5]^-$), 5–9% 919 ($[M-CO_2-CO_2C_2H_5]^-$), 2–3% 878 ($[M-C(CO_2C_2H_5)_2]^-$), 23–38% 758 (?), 10–16% 720 ($[M-2C(CO_2C_2H_5)_2]^-$) ³ , 100% 112 ($[C_6H_8O_2]^-$), 5–6%

¹Insignificant fragmentation at the set experimental conditions. ² $C_{60}CH^\pm$. ³ C_{60}^\pm . ⁴Intensity of the isotope peak of the ion with one less mass unit is subtracted.

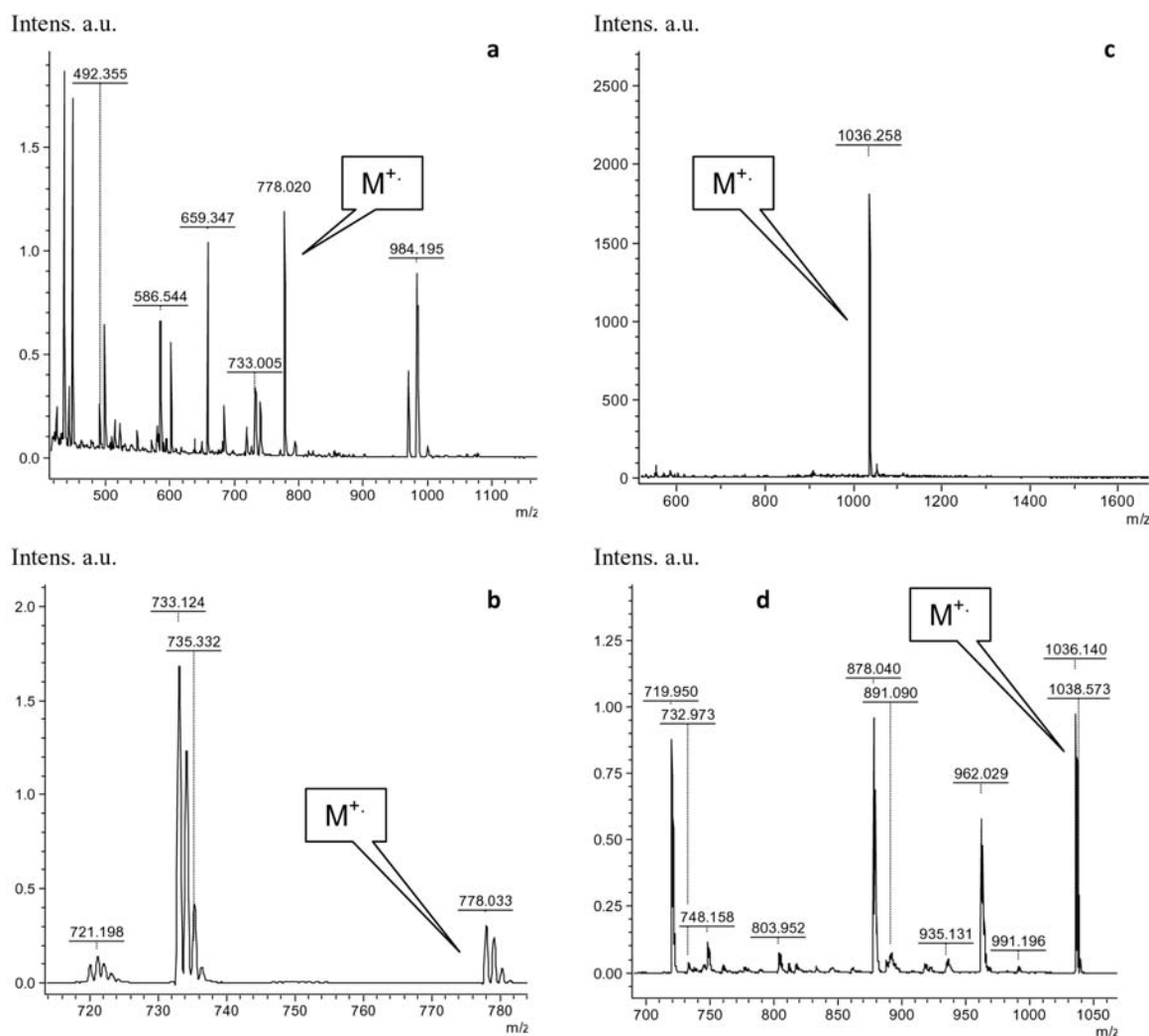


FIG. 1. ToF spectra of the compounds II (a) and V (c) in the positive mode. ToF/ToF spectra of the compounds II (b) and V (d) in the positive mode

processes. In concurrent reactions, carboxylate and ethyl groups were removed individually in the form of CO_2 and C_2H_4 , respectively. The presence of geminal carboxy ethyl groups in compounds **IV–VII** was correlated with the formation of $[\text{M}-\text{C}(\text{CO}_2\text{C}_2\text{H}_5)_2]^\pm$ fragments. The fullerene core of the molecules was observed as the ion with m/z 720 (C_{60}^\pm).

We did not find any significant difference between the spectra of regioisomers **V–VII**. Probably, a common intermediate is formed in the course of fragmentation of these compounds, which leads to the same product ions. Mass spectral discrimination between these fullerene derivatives calls for a special search for appropriate technique/method.

There are the distinct differences between the spectra of positive and negative ions (see Table 2). First, positive spectra contain more abundant peaks of different ion compositions. Second, some negative ion types are not available in positive spectra and *vice versa*. For example, peaks of fragments formed by means of elimination of ethylene molecules are more intensive in positive than negative spectra (see Table 2). Then, even- and odd-electron ions are present in spectra. The odd-electron ions dominate, especially in the case of positive ions: they account for an average of 3/4 of the peak intensity sum.

4. Conclusion

The MALDI LIFT-TOF/TOF technique known for its efficiency in proteomics, has been shown to provide single-type product-ion spectra of fullerene derivatives, enabling their characterization, structure elucidation, and non-target screening. This mass spectrometry technique used for fullerenes for the first time is suitable for building reference libraries of product-ion mass spectra [9] in the cases of these and other fullerene compounds.

Acknowledgments

The financial support from EC, Seventh framework programme (FP7), subprogramme: International research staff exchange scheme, project: Fullerene-based systems for oxidative inactivation of airborne microbial pathogens (RN 269138), is gratefully acknowledged.

References

- [1] Piotrovsky L.B., Kiselev O.I. *Fullerenes in biology* [in Russian]. Rostok, Saint-Petersburg, 2006, 336 p.
- [2] Brown T., Clipston N.L., et al. Matrix-assisted laser desorption/ionization of amphiphilic fullerene derivatives. *Int. J. Mass Spectrom.*, **210–211**, P. 249–263 (2001).
- [3] Frankevich V.E., Dashtiev M., et al. MALDI-Fourier transform mass spectrometric and theoretical studies of donor-acceptor and donor-bridge-acceptor fullerenes. *Phys. Chem. Chem. Phys.*, **7** (5), P. 1036–1042 (2005).
- [4] Zhou L., Deng H., et al. Analysis of three different types of fullerene derivatives by laser desorption/ionization time-of-flight mass spectrometry with new matrices. *Rapid Commun. Mass Spectrom.*, **19** (23), P. 3523–3530 (2005).
- [5] Rechthaler J., Pelzing M., et al. LDI and ESI MS as well as low energy CID of a self-assembling nanorod-forming fullerene derivative. *J. Mass Spectrom.*, **46** (11), P. 1108–1114 (2011).
- [6] Markov V.Y., Borschevsky A.Y., Sidorov L.N. MALDI mass spectrometry of fullerene derivatives. *Int. J. Mass Spectrom.*, **325–327**, P. 100–112 (2012).
- [7] Cordero M.M., Cornish T.J., Cotter R.J. Matrix-assisted laser desorption/ionization tandem reflectron time-of-flight mass spectrometry of fullerenes. *J. Am. Soc. Mass Spectrom.*, **7** (6), P. 590–597 (1996).
- [8] Suckau D., Resemann A., et al. A novel MALDI LIFT-TOF/TOF mass spectrometer for proteomics. *Anal. Bioanal. Chem.*, **376** (7), P. 952–965 (2003).
- [9] Milman B.L. *Chemical identification and its quality assurance*. Springer, Berlin, 2011, 281p.

SIMULATION OF SECONDARY ELECTRON TRANSPORT IN THIN METAL AND FULLERITE FILMS

E. O. Petrenko¹, M. V. Makarets², V. M. Mikoushkin³, V. M. Pugach¹

¹Kiev institute for Nuclear research NAS of Ukraine. Nauky av., 47, Kiev, Ukraine

²Taras Shevchenko National University of Kyiv, Phys. Dep. Akad. Glushkov av. 4, Kiev, 03022, Ukraine

³Ioffe Institute, 194021, St. Petersburg, Russia

ievgeniip@gmail.com

PACS 61.48.-c; 85.40.Hp; 61.80.Fe

Excitation processes and transport of recoiled and secondary electrons generated in fullerite and metal films under photons and electron irradiation were studied by computer simulation. Studied processes resulting in polymerization of fullerite were considered as the basic ones in formation of a pixel in electron nanolithography with fullerite film as an electron-beam resist. Reliability of the computer model and the important role of secondary electrons in the process of pixel formation were confirmed by comparison of the sizes of the calculated secondary electron swarm and the experimental cluster-pixel obtained previously. The photoelectron yield dependence on the incident photon's energy was also obtained with the same computer model for metal foils which can be used as a radiation strip-detector.

Keywords: Fullerite, Films, Electron beams, Electronic properties.

1. Introduction

Studying primary and secondary electron transport in metal films and in fullerites is important both for improving the efficiency of strip detectors [1] and for better understanding the mechanisms of fullerite modification and pixel formation by electron nanoprobe in high resolution electron beam lithography with fullerite as an electron beam resist [2–6]. Computer simulation of the transport for all electrons generated in fullerite C₆₀ under irradiation of primary electrons in the keV-energy range has been developed in the framework of the Monte-Carlo model [4,5]. A possible important role for secondary electrons in the formation of lithographic images is assumed to be in the process of formation of the minimal image in the form of a point (pixel) by the electron nanoprobe in a fullerite C₆₀ film [5]. The developed computer model was also applied to describe the charge accumulation in metal strip detectors [1]. In this paper, the developed computer model was applied in two cases: first, to obtain information about photoelectron yield and charge accumulation needed for strip detector design and second, to clarify the role of secondary electrons in pixel formation in a fullerite C₆₀ film by comparing the model results with experimental data.

2. Model and experimental details

According to [4,5], the computer model included the Monte-Carlo method for both electron transport description using the cross-sections for electron-atom elastic collisions with carbon (or nickel) atoms as well as for impact ionization. To describe photo-ionization, we have translated Penn's model [7] for electrons with full energy loss and have taken into account surface plasmons. All simulations were managed by the developed program packages. The program works as follows: electrons generated by ionization of atoms, in turn, trigger a number

of collisions, which can also lead to the emergence of the next generation of electrons, etc. Once the particle has passed the distance l , distributed by the law $e^{-l/\lambda}/\lambda$, where λ is the mean free path length, it dissipates via one of the interaction processes. The probability of the i -th process by which scattering a particle in a given state is equal σ_i/σ_{tot} , where σ_i is the corresponding cross section and σ_{tot} is the sum of those cross sections. In the evolution cascades, a crucial role is played by the collision's probability, thus only the largest cross sections in the above energy range were considered.

Modeling the irradiation processes by photons with 0.1–15 keV energy showed that photons also generate a swarm of secondary electrons. The number of these electrons is proportional to the number of photons and their energy satisfies the photoeffect law. The probability of photoelectron generation decreases exponentially in the target depth, and their further transport is determined only by interaction with the target. The principal distinction between photon and electron collisions with the targets atoms was well traced in the simulation. One photon is absorbed only once, creating a high-energy electron, and then it no longer interacts with the target. An electron with the same energy undergoes a huge number of collisions with the target atoms, and can transfer energy in a wide range, hence it can modify the target properties in the large volume. Numerous inelastic collisions between secondary electrons and carbon atoms in fullerite lead to creation of chemical bonds between fullerenes and finally to fullerite polymerization [5]. Secondary electrons near the foil surface can escape and thereby enhance the sensitivity of a metal-strip detector.

Modeling the electron transport in fullerite C_{60} has been performed using previously described experimental conditions [6] to compare the calculated and experimental data. A film with a thickness of 200–400 nm was grown by evaporation of high-purity soot onto the Si-substrates. Then, the film was irradiated by an electron nanoprobe with diameter less than 10 nm in a set of points to create a hidden image in the form of point clusters due to polymerization of irradiated areas. The energy of the irradiating electrons was 15 keV. Then, the irradiated film with a latent image was developed in chloroform. Irradiation and visualization of samples after development were made by a Scanning Electron Microscope [6].

Modeling the photo-irradiation processes was oriented to the experiments performed with a new kind of X-ray sensor that can potentially be used as an X-ray beam position monitor. It has been developed at the Kiev Institute for Nuclear Research and has been tested on the B16 beamline [8]. The sensitive part of this device is a nickel foil divided into four quadrants which are independently measured using four channels of a 4-channel low current monitor. Measurements have been performed to characterize the performance of the device as an X-ray Beam Position Monitor (XBPM) by reading the photocurrent emitted from the foils.

3. Results and discussion

The computer model was first applied to the relatively simple problem of photoionization yield description. Fig. 1 demonstrates the energy dependence of photoionization yield for a 50 μm nickel foil obtained in [8] (dashed curve) and in our simulation (solid curve). The low yield scale (of about 10^{-3}) is a result of high target density which reduces the secondary electron mean free path. Therefore, the calculated maximal radial deviation of secondary electrons was as low as 60–80 nm, which restricts the number of electrons leaving the nickel film. The minimum in the $h\nu = 8 - 10$ keV photon energy range is conditioned by the 8.3 keV nickel atomic level. Its excitation results in essential photon loss. Therefore, the number of electron-hole pairs, generated mainly by photons in conductivity zone, decreases along with the photoionization yield. Comparison of simulation and experimental data [8] shows satisfactory agreement of calculated and experimental data and the validity of the proposed model.

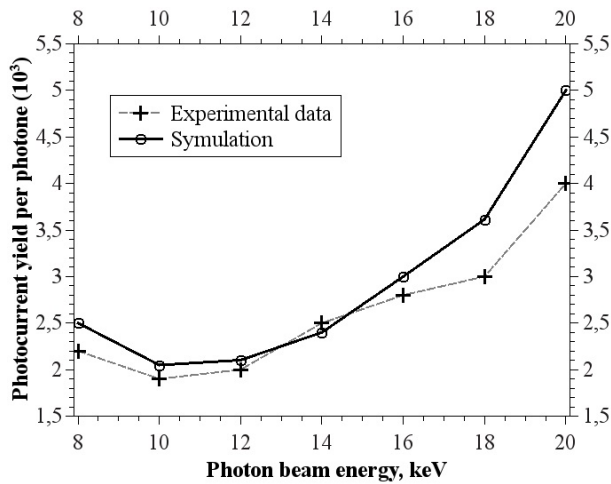


FIG. 1. Photoionization yield of nickel foil of $50 \mu\text{m}$ thickness obtained in experiment [8] (dashed curve), and in simulation (solid curve)

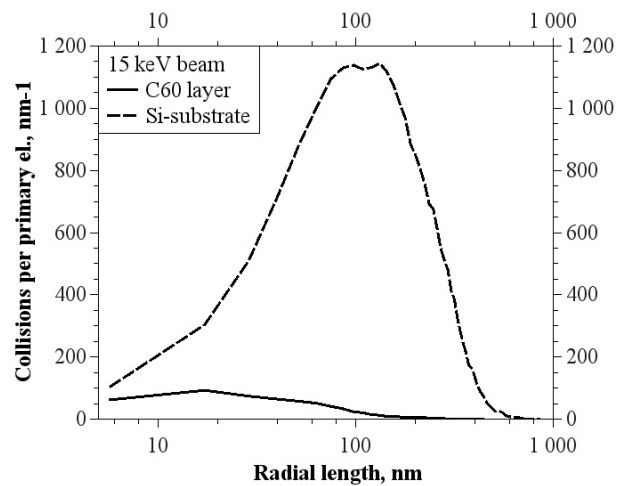


FIG. 2. Radial distributions of the inelastic collisions density between primary 15 keV electrons and atoms in 300 nm layer fullerite and in the Si-substrate

The fullerite film used in the experiment [6] was not thick enough to absorb irradiating (primary) 15 keV electrons. Therefore, the majority of primary electron-atom collisions followed by secondary electron generation and collisions takes place in the Si-substrate, which is confirmed by Fig. 2. This figure shows the calculated radial distribution of the density of all inelastic electron-atom collisions induced by 15 keV primary electrons in fullerite film and Si-substrate. We assume that every inelastic electron collision which transfers more than 2 eV to the fullerene electron system can excite it, and therefore, with some probability, create a chemical bond between two neighboring fullerenes. Therefore, the inelastic collision density can be considered a measure of the polymerization rate. In inelastic collisions, electrons with sufficient energy (more than about 8 eV) can also generate new secondary electrons. The energies of the majority of secondary electrons do not exceed several eV. Therefore, their inelastic cross section is very small and lifetime is very large. By this reasoning, the low-energy secondary electrons penetrate from silicon substrate back into the fullerite film. One should consider the substrate as an intensive source of low-energy electrons which can essentially enhance the polymerization of a fullerite film and enlarge the size of lithographic pixel in it. Note, that the radial distribution of inelastic secondary electron-atom collisions in the above-mentioned nickel foil, induced by the 15 keV photons, is similar to the one shown in Fig. 2, but the number of collisions is nearly three orders of magnitude less.

Figure 3 shows the radial distribution of the fullerite film-based inelastic electron-atom collision density for two groups of electrons: the low-energy group (2–10 eV) and the high-energy group (10 eV $-E$), where the energy of primary electrons E was 15 keV and 10 keV, respectively. One can see that the collision density for low-energy electrons does not radically exceed that for high energy ones near the beam axes (in several times only). But away from the primary beam area, collisions associated with low-energy electrons qualitatively dominate by many orders of magnitude, due to their huge numbers. Modeling showed that the effect of secondary electron generation by the substrate is smaller for the 10 keV beam, and it diminishes in energy due to a shortening of the penetration depth of the primary electrons. At the low

beam's energy, the secondary electrons are generated near the surface and can thus leave it immediately.

The role of secondary electrons and the substrate is more important in the case of photo-irradiation. The fullerite film is considered to be transparent for 15 keV photons. Therefore, practically all secondary electrons are formed in deeper layers of the Si-substrate. However, as is shown by our calculations, the electrons penetrate into fullerite film from the substrate. In addition, the collision density induced by photons is much smaller in fullerite film because secondary electrons are generated in deeper substrate layers.

The results of computer simulation for electron transport under irradiation of a 15 keV electron nanoprobe represented in Fig. 2 and 3 allow qualitative explanation of the corresponding experiment [6] – see Fig. 4. In this experiment, compound carbon clusters, consisting of a large disk-shaped cluster with small point-cluster superimposed on the top in the center, were formed.

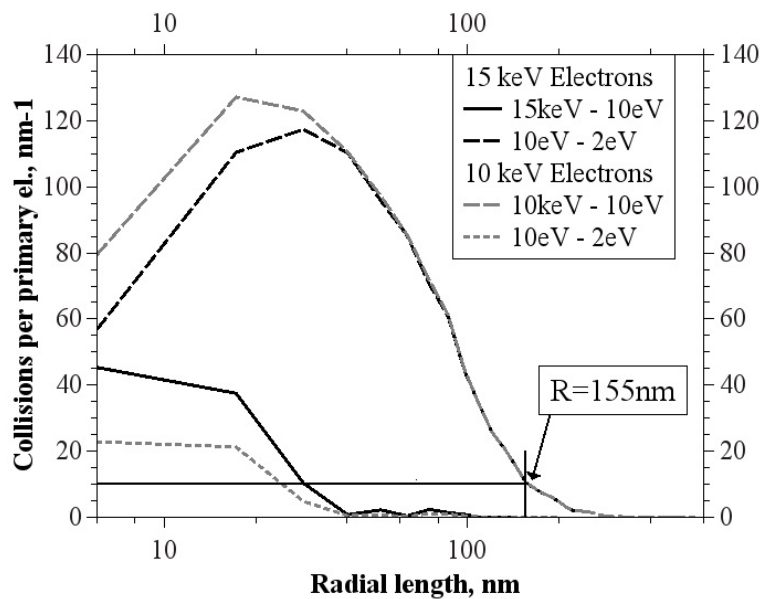


FIG. 3. Radial distributions of the inelastic collisions of all electrons with energy > 10 eV and energy < 10 eV with atoms. Primary electron energy is 10 and 15 keV



FIG. 4. Carbon clusters formed in the 300 nm fullerite film on the Si-substrate by a nanoprobe with energy 15 keV [6]. Cluster radius is about 1.5 microns

The simulation data qualitatively confirms the assumption that small clusters in the center are formed mainly by the high-energy electrons, while the large disk cluster is originated due to the polymerization under a swarm of low-energy secondary electrons. However, the radius of the disk-shaped cluster (~ 1500 nm) is much larger when compared to the secondary electron radial distribution obtained in the simulation ($\sim 350 - 400$ nm). While this result may seem incongruous, there is an explanation. One more effect should be taken into consideration to explain the larger size for the experimental pixel. It is a modification of fullerite properties (polymerization) during irradiation. Creation of new chemical bonds in a completely polymerized area is impossible. This fact can be considered by gradually reducing the inelastic electron collisions cross section and by correspondingly increasing the electron mean free-path during irradiation. Then, more of the secondary electrons from the cluster area may be transported to the cluster periphery, resulting in a radical increase of the polymerization rate there and thus enlargement of the cluster radius. This effect has been simulated and it was determined that the maximal and average spreads of low-energy electrons increase in dependence on the reduction of the relative inelastic cross section. It was shown that electron spread can reach the experimental radius value $R = 1500$ nm at one third of the initial cross section which corresponds to the creation of a majority part of the possible polymeric bonds.

4. Conclusions

Simulation using the developed computer model confirms the assumption [3, 6] that low-energy secondary electrons play an important role in fullerite polymerization and pixel formation in electron lithography with fullerite as an electron beam resist. The total contribution of secondary electrons to this modification can exceed 90%, and their radial deviation (the pixel radius) can be one to two orders of magnitude larger than the radius of the primary electron beam. A new mechanism for the radical increase of the pixel radius is suggested. This implies a long distance spread of the low-energy secondary electrons with reduced energy losses due to gradual polymerization of the irradiated area. The photoionization yield of metal foils is also caused due to secondary electron transport. A dependence of the nonmonotonous yield upon photon energy was observed and properly described by the modeling.

References

- [1] Makarets M.V., Petrenko E.O., Pugatch V.M. Accumulation of charge on metal strip detector under ion beam: experiment and simulation. *J. Nuclear Physics and Atomic Energy*, **13**, P. 146–152 (2012).
- [2] Mikoushkin V.M., Shnitov V.V. Electron beam-induced fullerite structure transformation, *Phys. Solid State*, **39** (1), P. 164–167 (1997).
- [3] Snitov V.V., Mikoushkin V.M., Gordeev Yu.S. Fullerite C_{60} as electron-beam resist for "dry" nanolithography. *Microelectron. Engin.*, **69** (2–4), P. 429–435 (2003).
- [4] Makarets N.V., Prylutsky Yu.I., et al. Simulation of fullerite C_{60} polymerisation under particle beams irradiation. *Mol. Cryst. & Liquid Cryst.*, **426**, P. 171–178 (2005).
- [5] Petrenko E.O., Makarets N.V., Mikoushkin V.M. Simulation of fast electron transport in thin fullerite C_{60} films. *Fullerenes, Nanotubes and Carbon Nanostructures*, **20** (4–7), P. 378–381 (2012).
- [6] Nevedomsky V.N., Mikoushkin V.M., et al. The role of secondary electrons in forming the image of electron nanoprobe. *Fullerenes, Nanotubes and Carbon nanostructures*, **16** (5–6), P. 682–686 (2008).
- [7] Penn D. Electron mean-free-paths calculation using a model dielectric function. *Phys. Rev. B*, **35**, P. 482–486 (1987).
- [8] Thomas C., Rehm G. Short Report on New XBPM tested on B16. Doc No: TDI-DIA-OPT-0011, July 1, 2011.

CVD GROWTH OF CARBON NANOTUBES WITH A Ni CATALYST IN A POLYIMIDE TRENCH

Kerstin Schneider¹, Boris Stamm², Katja Gutöhrlein²,
Claus Burkhardt², Alfred Stett² and Dieter P. Kern¹

¹Institute for Applied Physics and LISA⁺, Auf der Morgenstelle 10, 72076 Tübingen, Germany

²NMI Natural and Medical Sciences Institute at the University of Tübingen,
Markwiesenstraße 55, 72770 Reutlingen, Germany

kerstin.schneider@uni-tuebingen.de, Boris.Stamm@nmi.de, Katja.Gutoehrlein@nmi.de,
Claus.Burkhardt@nmi.de, Stett@nmi.de, dieter.kern@uni-tuebingen.de

PACS 81.15.Gh, 81.05.ub

Carbon nanotubes (CNTs) are ideal candidates as electrode materials for neuronal stimulation and monitoring devices such as microelectrode arrays (MEA). They provide a high charge injection limit without significant Faradic reactions and carbon nanotube electrodes have a high surface area to volume ratio. Flexible MEAs typically consist of thin conductors buried in a flexible insulator such as polyimide, where the actual contact areas have been opened by dry etching of the polyimide. CNTs are positioned in these contact areas by a low temperature (350 °C) chemical vapour deposition process from a catalyst which was deposited on the contact in the polyimide recess. To overcome poisoning of the catalyst by outgassing from the sidewalls of the polyimide trenches even at such low temperatures, a pre-treatment of the catalyst in an ammonia atmosphere for 15 min at 40 mbar and 350 °C was introduced. CNT growth on identical structures made from polyimide and silicon is compared in order to identify the relevant issues affecting growth.

Keywords: Carbon nanotube, Synthesis, CVD, polyimide.

1. Introduction

Since the first report on carbon nanotubes (CNTs) by Iijima in 1991, CNTs are becoming more and more important for applications, e.g. as electrode materials, in field emitter devices or in sensors. Carbon nanotubes (CNTs) are ideal candidates as electrode materials for neuronal stimulation and monitoring devices such as microelectrode arrays (MEA). They provide a high charge injection limit without significant Faradic reactions [1] and carbon nanotube electrodes have a high surface area to volume ratio. Flexible MEAs [2] typically consist of thin conductors buried in a flexible insulator such as polyimide, where the actual contact areas have been opened by dry etching of the polyimide. The objective in this work is to fabricate CNT-carpets on the surface of such contacts in a polyimide recess such that the CNTs form the actual interface to the living matter.

CNTs are often grown by chemical vapor deposition (CVD) or plasma enhanced CVD (PECVD) processes, which typically require temperatures around 700 °C. Such growth temperatures are too high for polymers like polyimide. We and others [3,4] have previously shown that it is possible to grow CNTs at temperatures below 400 °C on flat substrates, however, these processes failed when trying to grow CNTs in a polyimide recess. A prime candidate for the cause of this failure is the outgassing of carbonaceous gases [5–8] from the polyimide sidewalls of the recesses before and during growth, since in earlier experiments on flat substrates, it was already shown that this can poison the catalyst. Therefore, in experiments on nearly identical

recessed structures in polyimide and inert silicon we set out to identify the detrimental factors and to eliminate them.

2. Experiments

2.1. Sample preparation

Initially, a glass substrate was spin-coated for 30 s with an adhesion promoter (VM-652 or diluted VM-651 from HD Micro Systems). Afterwards the polyimide precursor (PI 2611, HD-Micro Systems) with a thickness of 5 μm was spin-coated (500 rpm for 5 s, then 4000 rpm for 30 s) onto it. The polyimide was then soft baked on a hot plate at 90 °C for 90 s, followed by 90 s at 150 °C. The final imidization process was performed under N₂ flow at a pressure of 0.4 MPa with a temperature ramp rate of 4 °C/min from room temperature to 330 °C – 350 °C. The final temperature between 330 °C and 350 °C was then held for 30 min. After that, the sample was gradually cooled to room temperature. These steps were performed twice in order to achieve a final polyimide thickness of 10 μm .

These polyimide substrates were cut into 1 cm \times 1 cm pieces and spin coated (2000 rpm/ramp 20/30s) with a photo-resist (ma-P 1275, Micro-Resist-Technology) with a total thickness of 11.1 μm . After a soft bake at 80 °C for 5 min, the sample was exposed for 150 s in a UV mask aligner (Karl Suss MJB3) and developed for 1 min (ma-D 331, Micro-Resist-Technology). As a pattern, an array of 30 μm diameter circular electrodes was used. Then, the polyimide was etched by reactive ion etching (RIE) with oxygen at 100 W plasma power and a pressure of 0.1 mbar. The resist could be used as an etching mask, because the etching rate of the resist was about 160 nm/min, while the etching rate of the polyimide was about 260 nm/min. The depth of these etched trenches was varied from 1 μm to 5 μm in 1 μm increments. Afterwards, the etching mask was removed with acetone in an ultrasonic bath for 1 min and rinsed with isopropanol.

In order to pattern the catalyst, a new layer of resist (ma-P 1215, Micro-Resist-Technology) with a thickness of 1.5 μm was spin-coated, soft baked at 90 °C for 90 s, exposed for 21 s and developed (ma-D 331) for 50 s. Afterwards, 10 nm Ti, 40 nm TiN as a diffusion barrier and 2 nm Ni as a catalyst were sputtered onto the sample and lift-off was performed in acetone. For this second exposure, the same electrode pattern was used, but it was aligned with an offset with respect to the first structure in order to produce catalyst areas inside the trenches as well as on the top of the polyimide surface. This was done in order to compare between the growth on the catalyst inside a trench and on the top surface.

In addition, nearly identical silicon structures were produced. To this end, ma-P 1275 with a thickness of 11.1 μm was again used as an etching mask. The silicon was etched in an RIE process with a gas mixture of 15 % O₂, 50 % SF₆ and 35 % Ar at 120 W plasma power with a pressure of 0.05 mbar. In this case, the etching rate of silicon amounted to about 230 nm/min. After removing the etch mask and cleaning the silicon samples in a 300 W oxygen plasma for 5 min, the catalyst dots were patterned the same way as on the polyimide structures.

2.2. Growth studies

In [4], we found that the optimum growing process had the following conditions: 5 mbar pressure, 5 min growing time, with a gas ratio of 1:1 (NH₃:C₂H₂). In addition, it was also found that the polyimide is outgassing carbon containing gases during the heating process, such as CO₂ and CH₄ [5–8]. This outgassing is poisoning the catalyst before CNT growth can start, so it is necessary to pre-treat the sample with NH₃ at 3.2 mbar as an etching gas [4]. Optimal pretreatment times were found to be 45 – 60 min at 450 °C and 75 – 90 min at 350 °C. In the

following experiments, growth on silicon samples was performed without any pretreatment, while the polyimide samples were pretreated according to the above-described procedure.

As presented in Fig. 1, no significant difference in the growth behavior on silicon was found, whether the CNTs grew on top of the surface or in the trench of the sample. The CNT height is shown as an average of 3 measurements with respective error bars.

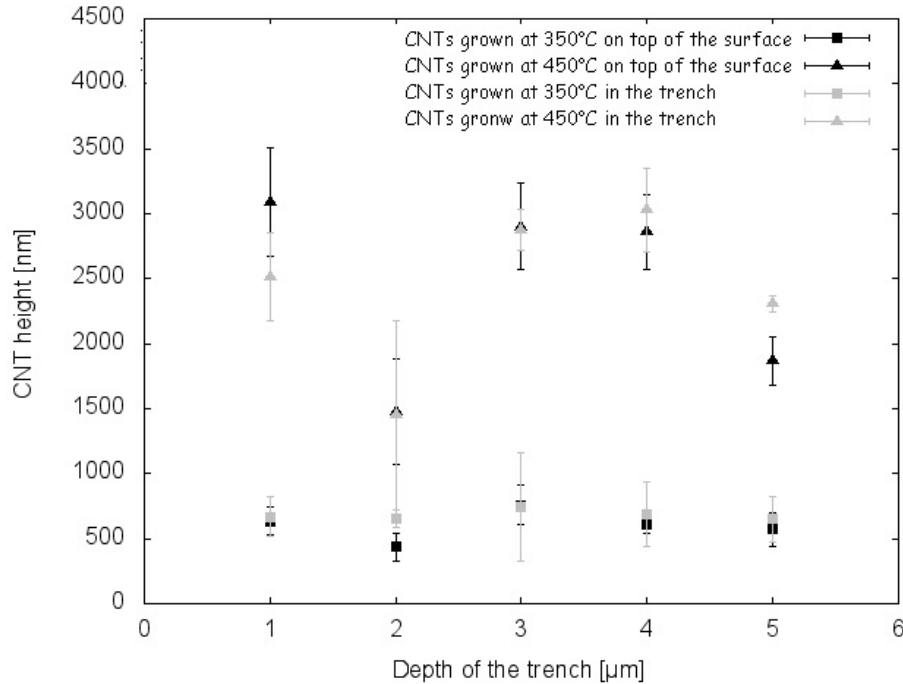


FIG. 1. CNT growth on Si. The grey dots are CNT heights in the trenches, the black dots are CNT heights on top of the surface of Si

CNTs grown on polyimide, however, showed a clear tendency to be shorter when growing inside a polyimide trench than when growing on the top surface (Fig. 2). No significant dependence of the CNT height on the depth of the trenches could be observed. It seems that the polyimide itself is influencing the growth process, as described in [4].

From this difference in growth behavior between Si and polyimide, we conclude that the sample geometry is not responsible for the low CNT growth inside the polyimide trenches. The mean free path of acetylene at 5 mbar at 350 °C is around 40 μm, which is nearly 10 times more than the depth of the trenches and since we are only dealing with height/width aspect ratios of less than 1/6, there should be no significant geometry effect on the precursor supply. In order to investigate whether the open sidewalls in the polyimide trenches were responsible for the reduced CNT growth, new samples were fabricated where the sidewalls were also covered with catalyst. This was achieved by sputter-coating the sample with the Ti/TiN/Ni catalyst stack immediately after the first lithography and reactive ion etching step. Lift-off was then performed with the first photo resist mask which was left after the etching. After pretreatment in NH₃ at 3.2 mbar for 45 min, CNTs were grown using the process developed in [4], namely 5 min at 450 °C and 5 mbar pressure at a gas ratio of 1:1 NH₃:C₂H₂. Fig. 3 shows the result of such a growth experiment exhibiting regular growth of CNTs on the bottom of the trench as well as on the sidewalls.

This result indicates that the open polyimide sidewalls could be responsible for reduced growth in a trench with uncovered walls. While on flat substrates, catalyst poisoning by

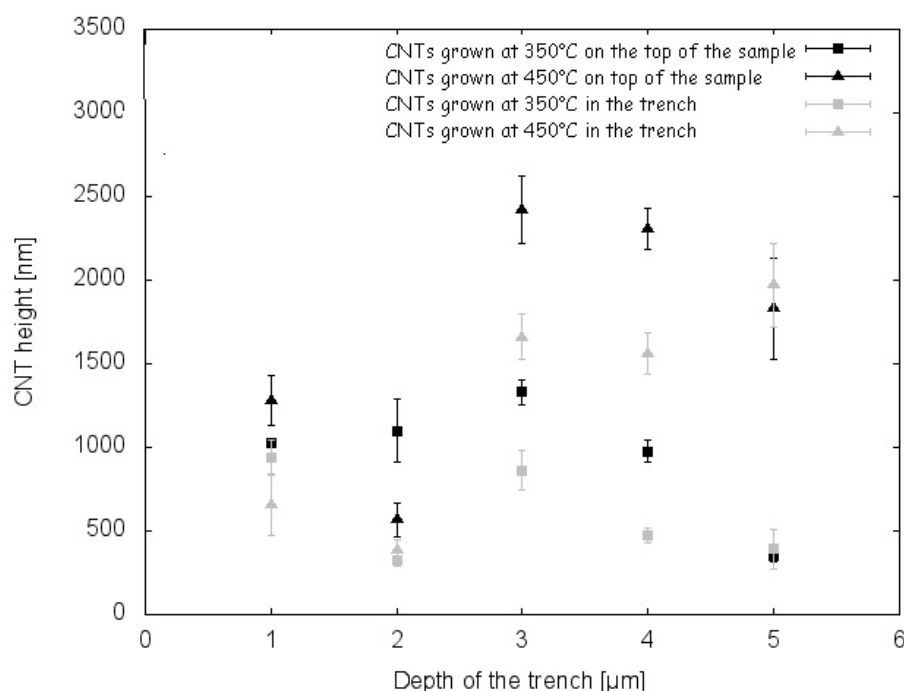


FIG. 2. CNT growth on Polyimide. The grey dots are CNT heights in the trenches, the black dots are CNT heights on top of the surface of Polyimide

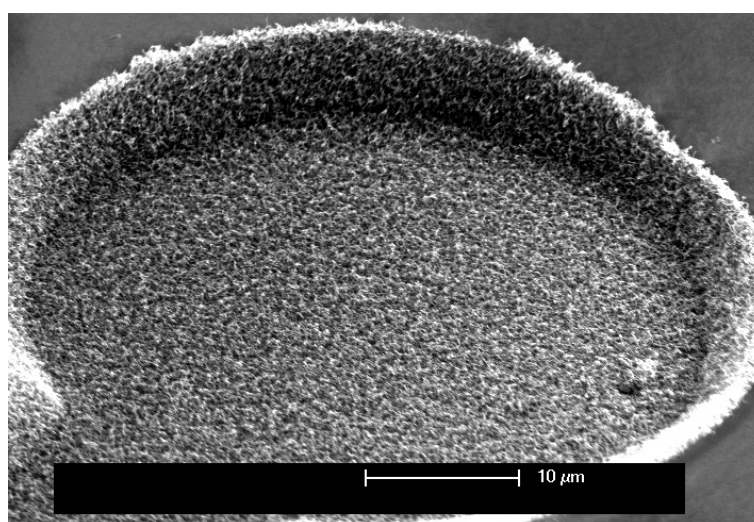


FIG. 3. A 3 μm deep trench in polyimide overgrown with CNTs

outgassing of carbonaceous gases such as CO_2 or CH_4 from the polyimide before growth was even started could be prevented by pretreatment in NH_3 for 45 min at a pressure of 3.2 mbar at reaction temperature. This procedure was obviously not sufficient in the case of polyimide trenches. Even increasing the pretreatment time to 2 h did not improve CNT growth. Therefore, the pretreatment pressure was increased to 20 mbar and 40 mbar. After a pretreatment at 20 mbar a slight improvement of CNT growth in the trenches was observed, but it was still significantly reduced compared to the top surface and rather long pretreatment times were necessary (see grey symbols in Fig. 4). At 40 mbar, the CNTs in the trenches have nearly the same height as the CNTs on the surface. In addition, at this higher pressure the pretreatment time could be

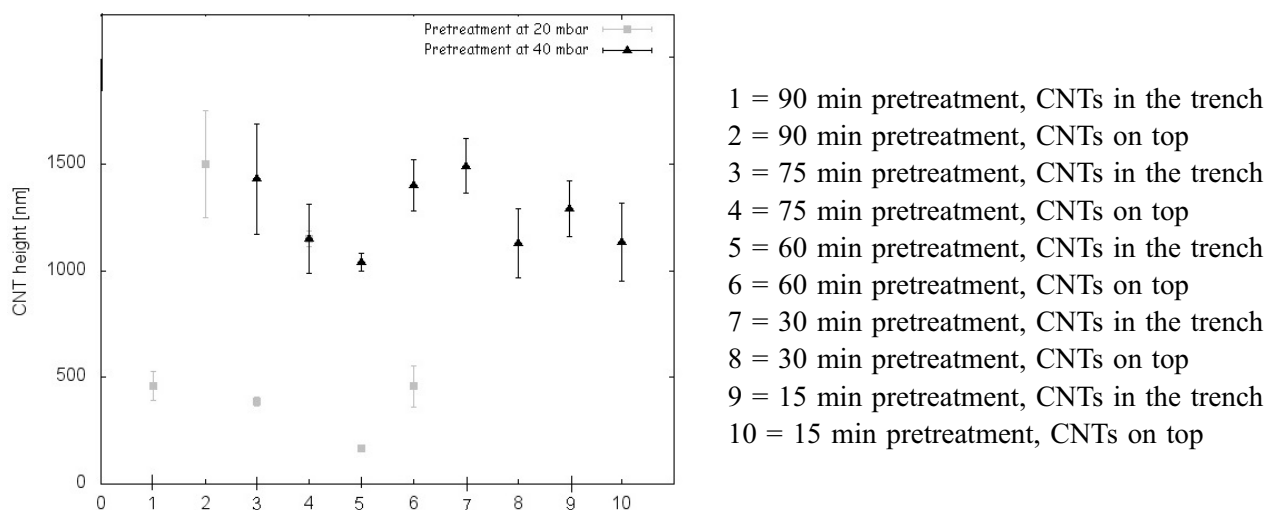


FIG. 4. CNT heights on Polyimide after different pretreatment times/pressures

reduced to 15 min at 350 °C. Obviously, a more efficient protection of the catalyst and possibly passivation of the sidewalls is achieved at this higher pressure.

2.3. Results

From the results of the growth experiments described above, we conclude that the difficulties in growing CNTs inside a polyimide trench were not caused by a too short mean free path of the acetylene molecules at 5 mbar, possibly resulting in a precursor depletion during the process, but rather by the behavior of the polyimide during the heating process itself, as described in [5–8]. The additional outgassing surface of the sidewalls can poison the catalyst in the trenches significantly more than on the surface. When the trench sidewalls were covered with the diffusion barrier and catalyst, no growth difference between the surface and the trenches was observed. Pretreatment for 15 min with NH_3 at an increased pressure of 40 mbar before CNT growth was sufficient to prevent catalyst poisoning at 350°C, also for open sidewalls, resulting in normal CNT growth.

References

- [1] Wang K., Fishman H.A., Dai H., Harris J.S. Neural Stimulation with a Carbon Nanotube Microelectrode Array. *Nano Lett.*, **6** (9), P. 2043–2048 (2006).
- [2] Molina-Luna K., Buitrago M.M., et al. Cortical stimulation mapping using epidurally implanted thin-film microelectrode arrays. *J. Neuroscience Methods*, **161** P. 118–125 (2007).
- [3] Hofmann S., Ducati C., Kleinsorge B., Robertson J. Direct growth of aligned carbon nanotube field emitter arrays onto plastic substrates. *Appl. Phys. Lett.*, **83** (2), P. 4661–4663 (2003).
- [4] Schneider K., Stamm B., et al. Carbon nanotubes grown on polyimide by chemical vapour deposition. *Nanotechnology (IEEE-NANO)*, 12th IEEE Conf. on Nanotechnology, P. 1–5 (2012).
- [5] Hu C.Z., Andrade J.D., Dryden P. Structural determination of pyrolyzed PI-2525 polyimide thin films. *J. Appl. Polymer Science*, **35**, P. 1149–1160 (1988).
- [6] Inagaki M., Ibuki T., Takeichi T. Carbonization behavior of polyimide films with various chemical structure. *J. Appl. Polymer Science*, **44**, P. 521–525 (1992).
- [7] Ortelli E.E., Geiger F., Lippert T., Wokaun A. Pyrolysis of kapton in air: an in situ DRIFT study. *Appl. Spectroscopy*, **55**, P. 412–419 (2001).
- [8] Hatori H., Yamada Y., et al. The mechanism of polyimide pyrolysis in the early stage. *Carbon*, **34** (2), P. 201–208 (1996).

PROPAGATION OF FEMTOSECOND PULSES IN CARBON NANOTUBES

N. N. Konobeeva¹, M. B. Belonenko²

¹Volgograd State University, Volgograd, Russia

²Volgograd Institute of Business, Volgograd, Russia

yana_nn@inbox.ru, mbelonenko@yandex.ru

PACS 73.63.Fg, 78.67.Ch

The generation of higher harmonics of carbon nanotubes interacting with femtosecond laser pulses was investigated. The analysis was conducted on the basis of quantum kinetic equation for the π -electrons involved in the inside of the band and inter-band transitions. The dynamics of the electromagnetic pulse, depending on the parameters of the problem, were studied.

Keywords: Carbon nanotube, femtosecond pulse, electromagnetic field.

1. Introduction

This paper investigates the dynamics of femtosecond pulses propagating in carbon nanotubes (CNTs). Significant progress in the synthesis of new mesoscopic structures and their great promise for use in nanoelectronics and optics has led to increased research in this area. The unusual manifestation of nonlinear optical properties of these materials when interacting with strong electromagnetic fields was expected. Theoretical and experimental studies predict that the strong nonlinear response is inherent in metal clusters [1–3], fullerenes [4–6], carbon nanotubes and composites based on them [7, 8]. In particular, the generation of higher harmonics, previously observed in noble gases [9, 10], has been predicted for mesoscopic structures. Moreover, a distinctive feature of the CNT is a strong selectivity of their high harmonic spectrum. A theoretical study of the nonlinear response of isolated nanotubes by intense laser radiation was studied in this work. A full quantum-theoretical approach to the one-electron approximation in the tight-binding model was used.

2. Statement of a problem

2.1. Kinetic equations

We consider an infinitely long single-walled carbon nanotube oriented along the z axis and irradiated normal to the axis of the ultra-short pulse with a natural frequency ω_0 , polarized to this axis: $\mathbf{E}(\mathbf{r}) = e_z E_z(x, y)$ (e_z is the unit vector along the z axis). CNTs are considered as a single-layer graphene sheet which is scrolled into a cylinder. We take into account only π -electrons, suggesting that their motion can be described in the tightly-bound approximation [11, 12]. CNT radius is much smaller than the wavelength of the field, which allows us to neglect the spatial inhomogeneity of the field in the tubes.

Following [13] in the one-electron approximation, the Schrödinger equation becomes:

$$i\hbar \frac{\partial \psi}{\partial t} = -\frac{\hbar^2}{2m_0} \Delta \psi + [W(\mathbf{r}) - e(\mathbf{E} \cdot \mathbf{r})] \psi. \quad (1)$$

Neglecting the harmonic solution of (1) can be written as:

$$\psi = \sum_{l, \mathbf{p}} C_l(\mathbf{p}) \psi_l(\mathbf{p}, \mathbf{r}), \quad (2)$$

where l is the set of quantum numbers characterizing the state of π -electrons with a given quasi-momentum. $\psi_l(\mathbf{p}, \mathbf{r}) = \hbar^{-0.5} \exp(i\mathbf{p}\mathbf{r}/\hbar) u_{l, \mathbf{p}}(\mathbf{r})$ are the Bloch functions with an amplitude $u_{l, \mathbf{p}}(\mathbf{r})$, which is periodical to an arbitrary vector lattice \mathbf{a} : $u_{l, \mathbf{p}}(\mathbf{r} + \mathbf{a}) = u_{l, \mathbf{p}}(\mathbf{r})$. Here $\mathbf{a} = n_1 \mathbf{a}_1 + n_2 \mathbf{a}_2$, n_1, n_2 are the integers, $\mathbf{a}_1, \mathbf{a}_2$ are the elementary vectors of the graphene hexagonal lattice.

The dispersion law for zig-zag CNTs can be written in the following form [14]:

$$\varepsilon_s(p) = \pm \gamma_0 \sqrt{1 + 4 \cos(ap) \cos(\pi s/m) + 4 \cos^2(\pi s/m)}, \quad (3)$$

where $s = 1, 2, \dots, m$, $(m, 0)$ is type of CNT, γ_0 is the hopping integral (2.7 eV), $a = 3b/2\hbar$, $b = 0.142$ nm is the distance between the adjacent carbon atoms.

From equations (1) and (2) with the spectrum of nanotubes:

$$\hat{H}_0 = \begin{pmatrix} 0 & H_{12}(\mathbf{p}) \\ H_{21}^*(\mathbf{p}) & 0 \end{pmatrix}, \quad (4)$$

which can be rewritten in the tightly-bound approximation as:

$$H_{12}(\mathbf{p}) = -\gamma_0 \sum_{j=1}^3 \exp\left(\frac{i\mathbf{p}\tau_j}{\hbar}\right), \quad (5)$$

where τ_j is the vector connecting the atom to its nearest neighbors. For density matrix elements taking into account $F = \Re(\rho_{cv})$; $\Phi = \Im(\rho_{cv})$; $\rho = \rho_{cc}$, ρ_{cv} is the density matrix, ω is the transition frequency, e is the electron charge, we can obtain the following expression:

$$\begin{aligned} \frac{\partial \rho}{\partial t} + eE_z \frac{\partial \rho}{\partial p_z} &= 2 \frac{e}{\hbar} E_z R_{ab} \Phi, \\ \frac{\partial F}{\partial t} + eE_z \frac{\partial F}{\partial p_z} &= \omega \Phi, \\ \frac{\partial \Phi}{\partial t} + eE_z \frac{\partial \Phi}{\partial p_z} &= \frac{e}{\hbar} E_z R_{ab} (2\rho - 1) - \omega F, \\ R_{ll, \mathbf{p}} &= \frac{i\hbar}{2} \int_{\Omega} \left(u_{l, \mathbf{p}}^* \frac{\partial u_{l, \mathbf{p}}}{\partial p_z} - \frac{\partial u_{l, \mathbf{p}}^*}{\partial p_z} u_{l, \mathbf{p}} \right) d^2 \mathbf{r}. \end{aligned} \quad (6)$$

The integration domain is the volume Ω of two-dimensional unit cell.

The initial conditions are following:

$$\rho_{t=0} = F_0(\varepsilon_c(p_z, s)); F|_{t=0} = \Phi|_{t=0} = 0. \quad (7)$$

This means that at room temperature, the electrons are distributed according to the equilibrium Fermi distribution with zero chemical potential ($\mu = 0$).

The boundary conditions reflect the periodicity of solutions in the space of quasi-momentum (similar for F and Φ):

$$\rho \left(t, \frac{\sqrt{3}\pi}{\omega_{cn}a} \right) = \rho \left(t, -\frac{\sqrt{3}\pi}{\omega_{cn}a} \right). \quad (8)$$

3. Electric current in nanotube

A quantum-mechanical operator of current density can be written in the following form [13]:

$$\hat{j}_z(r) = -\frac{ie\hbar}{2m_0} \left(\frac{\partial}{\partial z'} \delta(r-r') + \delta(r-r') \frac{\partial}{\partial z'} \right). \quad (9)$$

Total current density was decomposed into two components: $\hat{j}_z = j_z^{(1)} + j_z^{(2)}$, where intraband transitions is responsible for:

$$j_z^{(1)} = \frac{4e}{(2\pi\hbar)^2} \int_{1ZB} \frac{\partial \varepsilon_c(\mathbf{p})}{\partial p_z} \rho(t, \mathbf{p}) d^2\mathbf{p}, \quad (10)$$

and inter-band:

$$j_z^{(2)} = \frac{8e}{(2\pi\hbar)^2 \hbar} \int_{1ZB} \varepsilon_c(\mathbf{p}) R_{cv}(p_z, s) \Phi(t, \mathbf{p}) d^2\mathbf{p}. \quad (11)$$

We take into account that $\rho_{vv} + \rho_{cc} = 1$ and $\varepsilon_v = -\varepsilon_c$.

Choosing the gauge field, $\mathbf{E} = -\frac{1}{c} \frac{\partial \mathbf{A}}{\partial t}$, (where c is the light velocity in a vacuum). We need to change the momentum to a generalized momentum: $\mathbf{p} \rightarrow \mathbf{p} - e\mathbf{A}/c$, so:

$$\begin{Bmatrix} \Phi \\ F \\ \rho \end{Bmatrix} = \hat{x} \left(\mathbf{p} - \frac{e\mathbf{A}}{c} \right) \begin{Bmatrix} \Phi \\ F \\ \rho \end{Bmatrix}.$$

Then, equation (5) takes the following form with the replacement $\rho - 0.5 \rightarrow \rho$:

$$\begin{cases} \rho_t = -\frac{2}{c} A_t R \Phi, \\ F_t = \omega \Phi, \\ \Phi_t = -\frac{2}{c} A_t R \rho - \omega F. \end{cases} \quad (12)$$

The matrix of the system coefficients can be written as:

$$\hat{x} = \begin{bmatrix} 0 & 0 & A \\ 0 & 0 & \omega \\ A & -\omega & 0 \end{bmatrix}.$$

Where the notation: $A = -2c^{-1} A_t R$ and according to the approximation described in [15–19]:

$$e^{\hat{x}} = \hat{I} + \hat{x} \left(1 + \frac{(A^2 - \omega^2)}{3!} + \frac{(A^2 - \omega^2)^2}{5!} + \dots \right) + \hat{x}^2 \left(\frac{1}{2!} + \frac{(A^2 - \omega^2)}{4!} + \frac{(A^2 - \omega^2)^2}{6!} + \dots \right),$$

$$j_z^{(1)} = \frac{4e}{(2\pi\hbar)^2} \int_{1ZB} \frac{\partial \varepsilon_c(\mathbf{p} - e\mathbf{A}/c)}{\partial p_z} A(t)^2 \sum_{k=0}^{\infty} \frac{(A(t)^2 - \omega(\mathbf{p})^2)^k}{(2k+2)!} \frac{1}{(1 + \exp(-\varepsilon_c(\mathbf{p})/k_B T))} d^2\mathbf{p},$$

$$j_z^{(2)} = \frac{8e}{(2\pi\hbar)^2 \hbar} \int_{1ZB} \frac{-2A(t) \varepsilon_c(\mathbf{p} - e\mathbf{A}/c) R_{cv}(\mathbf{p})}{(1 + \exp(-\varepsilon_c(\mathbf{p})/k_B T))} \sum_{k=0}^{\infty} \frac{(A(t)^2 - \omega(\mathbf{p})^2)^k}{(2k+1)!} d^2\mathbf{p},$$

where k_B is the Boltzmann constant, T is the temperature.

The Maxwell equations for the dielectric non-magnetic medium can be written as following [16]:

$$\frac{\partial^2 \mathbf{A}}{\partial x^2} + \frac{2N_0}{c} a \frac{\partial^4 \mathbf{A}}{\partial t^4} - \frac{2N_0}{c} b \mathbf{A} + \frac{4\pi}{c} (j_1 + j_2) - \frac{1}{c^2} (1 + 4\pi\alpha) \frac{\partial^2 \mathbf{A}}{\partial t^2} - \frac{12\pi\eta}{c^4} \frac{\partial^2 \mathbf{A}}{\partial t^2} \left(\frac{\partial \mathbf{A}}{\partial t} \right)^2 = 0, \quad (13)$$

where \mathbf{A} is the vector-potential, $\mathbf{P}_L = \alpha \mathbf{E}$ is the polarization, $\mathbf{P}_{NL} = \eta |\mathbf{E}|^2 \mathbf{E}$ is the nonlinear part of polarization, t is the time. We consider a simple model, where the polarization vector is parallel to the vector \mathbf{E} is the electric field of light wave, $N_0, a, a_1, \dots, b, b_1, \dots$ are the empirical constants of medium dispersion [17].

4. Numerical analysis and results

Equation (13) was solved numerically [20]. Boundary conditions took on a Gaussian form with one field- (14a) and two field oscillations (14b):

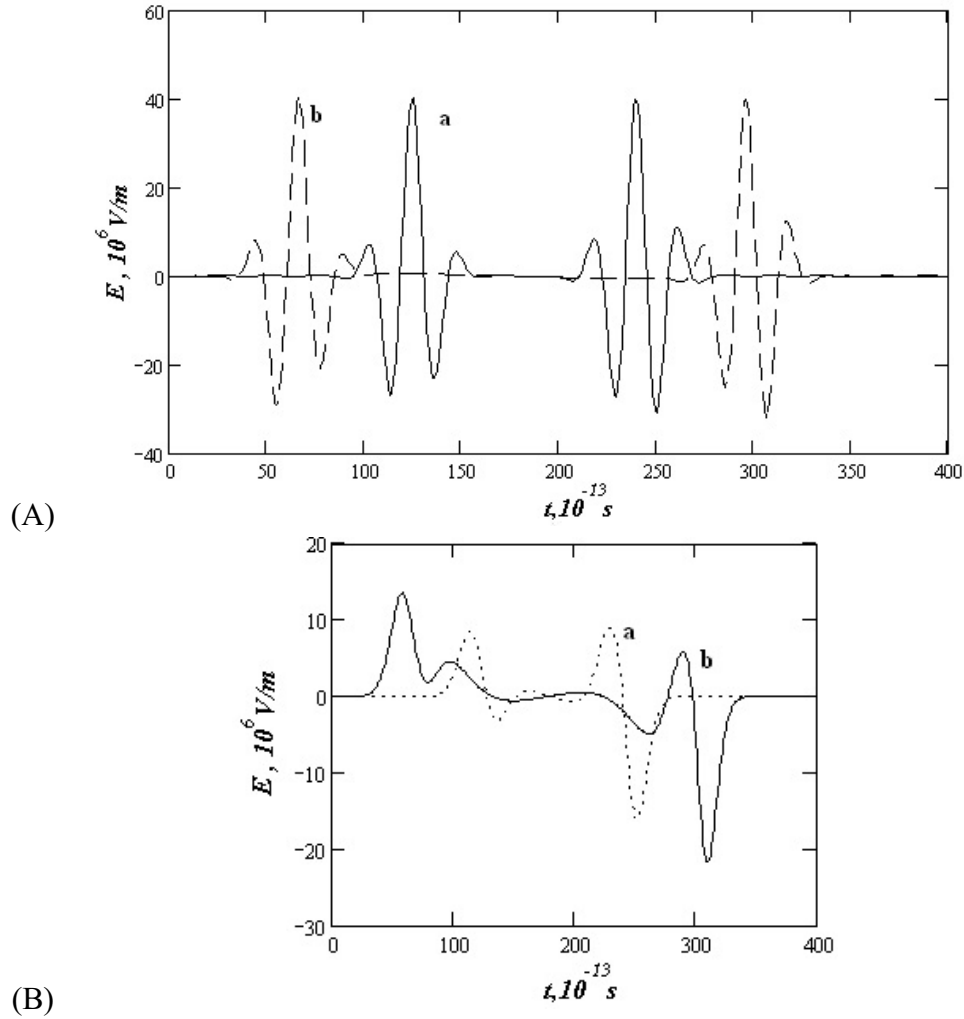


FIG. 1. Time dependence of the electric field at various space points a) $x = 0.1 \cdot 10^{-5}$ m; b) $x = 0.2 \cdot 10^{-5}$ m. (A) two field oscillations; (B) one field oscillation

$$A(0, t) = Q \cdot e^{-(ut)^2/\gamma},$$

$$\frac{dA(0, t)}{dx} = \frac{2Qut}{\gamma} e^{-(ut)^2/\gamma},$$

$$A(0, t) = Q \cdot e^{-(ut)^2/\gamma} \sin(ut),$$

$$\frac{dA(0, t)}{dx} = \frac{2Qut}{\gamma} e^{-(ut)^2/\gamma} \sin(-ut) + Q \cdot e^{-(ut)^2/\gamma} \cos(ut),$$

where Q is the pulse amplitude, u is the pulse velocity, $\gamma^2 = 1/(1 - u^2/A^2)$.

The evolution of the electric field during its propagation in the sample is shown in Fig. 1.

It can be seen from this dependence that when the propagation distance increases, pulses drift away from each other. Moreover, in the case of two field oscillations, the amplitude of the main peak is stable, and in the case of one oscillation there is a decrease in the main pulse amplitude and an increase in the trailing pulse. This can be attributed to the dispersion characteristics of the medium.

The dependence of the electric field on the initial pulse amplitude is shown in Fig. 2.

As expected, low-amplitude pulses propagate almost without distortion and exhibit only the dispersion spread. However, pulses with high amplitudes exhibit a larger distortion caused by both the interference of the edge pulse and the specific form of the medium's nonlinearity.

Figure 3 demonstrates that the dispersion constants have a great influence on the electric field (and the effect of the b constant is manifested much more strongly compared to the constant a). In our opinion, this effect is due to this type of dispersion reducing the linear response of the system to an external field.

Thus, based on the results of numerical calculations, one can draw the conclusion that the pulse propagation is determined primarily by the dispersion characteristics of the medium, as well as the process of establishing a balance between the dispersion and interference effects of the wave front.

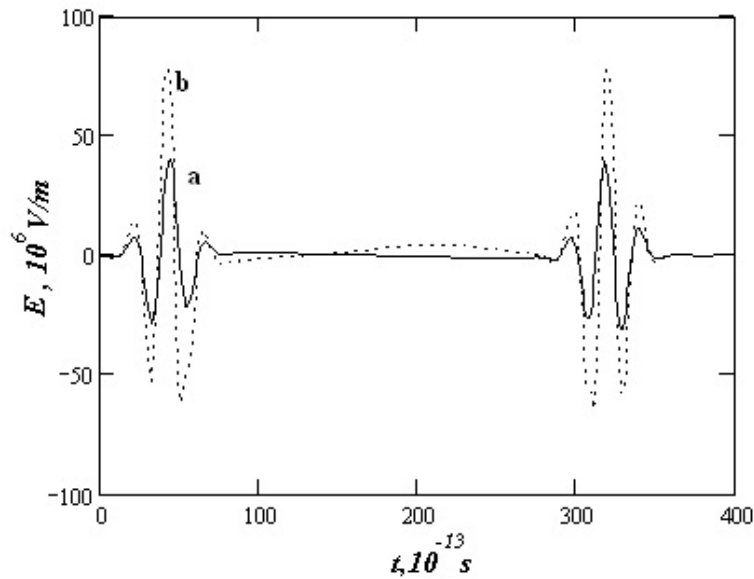


FIG. 2. Time dependence of the electric field at various initial amplitudes of the pulse ($x = 0.2 \cdot 10^{-5}$ m): a) $Q = 1$ a.u.; b) $Q = 2$ a.u. (the case of two field oscillations)

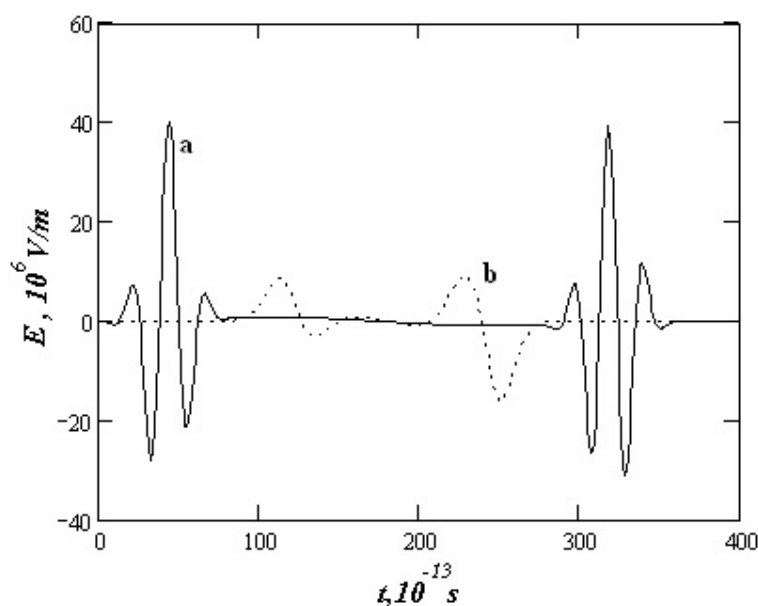


FIG. 3. Time dependence of the electric field at various dispersion constants ($x = 0.1 \cdot 10^{-5}$ m): a) $b = 0.001$ a.u.; b) $b = 0.005$ a.u. (the case of two field oscillations)

Acknowledgments

This study was supported by the Russian Foundation for Basic Research (project No. 12-02-31654).

References

- [1] Calvayrac F., Reinhard P.-G., Suraud E., Ullrich C.A. Nonlinear electric dynamics in metal clusters. *Phys. Rep.*, **337**, P. 493–578 (2000).
- [2] Veniard V., Taieb R., Maguet A. Atomic clusters submitted to an intense short laser pulse: A density-functional approach. *Phys. Rev. A*, **65**, P. 013202(1-7) (2001).
- [3] Daligault J., Guet C. Kinetic and Coulombic effects in the explosion dynamics of metal clusters in intense femtosecond laser fields. *Phys. Rev. A*, **64**, P. 043203(1-5) (2001).
- [4] Hertel I.V., Steger H., et al. Giant plasmon excitation in free C_{60} and C_{70} molecules studied by photoionization. *Phys. Rev. Lett.*, **68**, P. 784–787 (1992).
- [5] Hunsche S., Starczewski T., et al. Ionization and fragmentation of C_{60} via multiphoton-multiplasmon excitation. *Phys. Rev. Lett.*, **77**, P. 1966–1969 (1996).
- [6] Cambell E.E.B., Hansen K., et al. From above threshold ionization to statistical electron emission: The laser pulse-duration dependence of C_{60} photoelectron spectra. *Phys. Rev. Lett.*, **84**, P. 2128–2131 (2000).
- [7] Stanciu C., Ehlich R., et al. Experimental and theoretical study of third-order harmonic generation in carbon nanotubes. *Appl. Phys. Lett.*, **81**, P. 4064–4066 (2002).
- [8] Chen Y.-C., Ravavikar N.R., et al. Ultrafast optical switching properties of single-wall carbon nanotube polymer composites at 1.55 μm . *Appl. Phys. Lett.*, **81**, P. 975–977 (2002).
- [9] Ferray M., L’Huillier A., et al. Multiple-harmonic conversion of 1064 nm radiation in rare gases. *J. Phys. B: At. Mol. Opt. Phys.*, **21**, L31 (1988).
- [10] Chang Z., Rundquist A., et al. Generation of coherent soft X rays at 2.7 nm using high harmonics. *Phys. Rev. Lett.*, **79**, P. 2967–2970 (1997).
- [11] Il’inskii Yu.A., Keldysh L.V. *Electromagnetic Response of Material Media*. Plenum, New York, 1994, 304 p.
- [12] Davydov A.S. *Quantum Mechanics*. Pergamon, Oxford, 1976, 168 p.
- [13] Slepyan G.Ya., Khrutchinski A.A., Nimelentsau A.M., Maksimenko S.A. High-order optical harmonic generation on carbon nanotubes: quantum-mechanical approach. *Int. J. Nanoscience*, **3**, P. 343–354 (2004).
- [14] Wallace P.R. The Band Theory of Graphite. *Phys. Rev.*, **71**, P. 622–634 (1947).

- [15] Belonenko M.B., Glazov S.Yu., Meshcheryakova N.E. Dynamics of electromagnetic pulses with wide spectra in semiconductor superlattices. *J. Russian Laser Research*, **29** (2), P. 114–122 (2008).
- [16] Vongradova M.B., Rudenko O.V., Sukhorukov A.P. *Wave theory*. Nauka, Moscow, 1990, 432 p.
- [17] Yanyushkina N.N., Belonenko M.B. The influence of self-nonlinearity on the propagation of ultrashort optical pulses in carbon nanotubes in dispersive non-magnetic dielectric media. *Zh. Techn. Fiz.*, **83** (4), P. 155–158 (2013).
- [18] Sazonov S.V. The effect of resonance transparency anisotropic medium with a permanent dipole moment. *Zh. Eksp. Teor. Fiz.*, **124**, P. 803–819 (2003).
- [19] Sazonov S.V. Nonlinear propagation regimes of resonant pulses in multilevel quantum media. *Opt. Spektrosk.*, **95**, P. 666–674 (2003).
- [20] Kalitkin N.N. *Calculation methods*. Nauka, Moscow, 1978. 512 p.

THE SEMI-EMPIRICAL RESEARCH OF THE ADSORPTION OF BIOLOGICALLY ACTIVE MOLECULES ON THE OUTER SURFACE OF CARBON NANOTUBES

A. A. Kravchenko¹, T. A. Ermakova¹, O. A. Davletova¹, I. V. Zaporotskova¹,
T. K. Korchagina², U. V. Popov², G. A. Kalmikova²

¹Volgograd State University, Volgograd, Russia

²Volgograd State Technical University, Volgograd, Russia

Noroimush@gmail.com, taermakova09@mail.ru, olessya.08@mail.ru

PACS 68.43.-h

The object of this work is to research the interaction of carbon nanotubes with organic molecules containing the diphenyloxide fragment in order to identify new properties for the obtained compounds.

Keywords: Carbon nanotube, Adsorption, The semi-empirical research, MNDO, Diketones.

1. Introduction

Closed surface structure of carbon (fullerenes and nanotubes) shows a number of specific properties suitable for use it as a sort of materials and treat it as objects of interesting physical and chemical systems [1]. At the present time, nanotubes (or tubulenes) have changed from exotic objects to become the subject of large-scale physical and chemical research. Their unusual properties have become the basis of many challenging technical solutions. Now, nanotubes are the materials with a wide array of practical applications, the subject of commercial production, marketing and research. The outstanding feature of carbon nanotubes is their unique adsorption characteristics. The greatly curved surface of nanotubes (compared with a flat layer of graphite) can adsorb sufficiently large and heavy molecules including naturally-occurring organic molecules on its surface. Modern medicine development advances a need for new materials, one of which may be carbon tubulenes. Nanotubes with the drug substances deposited on their surface may be used to deliver drugs into infected human organs, followed by excretion of the tube from the human body. This should increase the effectiveness of existing drugs [2].

2. The conduct of the calculations

In this study, we will discuss the model of adsorption for organic molecules on the surface of carbon nanotubes. Many biologically active substances have heterocycles present in their structure. In these studies, a pair of model compounds were selected as biomolecule mimetics 1-(3-phenoxyphenyl)butane-1,3-dione and 2-(3-phenoxybenzoyl)cyclohexanone – both diketones containing the diphenylether fragment, which are new structures, characterized by high levels of similarity to known drugs, the absence of toxic properties in the model compounds, and a wide range of pharmacological properties which should be of practical and research interest to those in the medical field [3]. Software package Gaussian was used to build the model and calculations were performed using the MNDO scheme. Selection of this scheme was made for the following reasons: the method has worked well for calculations of molecules and solids; the error of the method is small compared to all previously known semi-empirical

schemes; low cost of computer computation time; the method is most effective for today's personal computers. Particular spatial configuration of molecules and their basic geometric characteristics were identified as a result of this research. The calculations were performed using the molecular cluster. To do this, the model of a single-walled zigzag type nanotube (0,5) diameter $r = 4.5 \text{ \AA}$ was used. The molecular tubulene clusters contained 96 carbon atoms; the dangling bonds at the boundaries were closed by pseudoatoms (these were selected as hydrogen atoms). Several connection options have been considered for adsorbed biologically active molecules:

- for the 2-(3-phenoxybenzoyl)cyclohexanone molecule, a single-center connection to the CNT surface was considered (Fig. 1);
- for the 1-(3-phenoxyphenyl)butane-1,3-dione molecule, a multicenter interconnection of two centers was considered (Fig. 2).

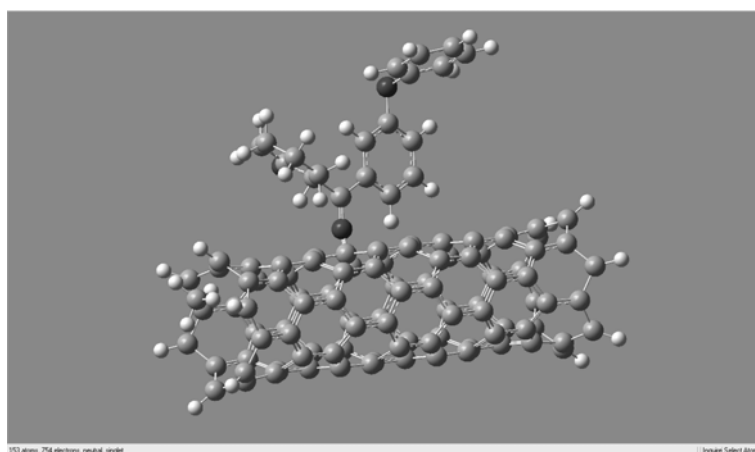


FIG. 1. The interaction of the molecule 2-(3-phenoxybenzene)-cyclohexanone with a carbon nanotube

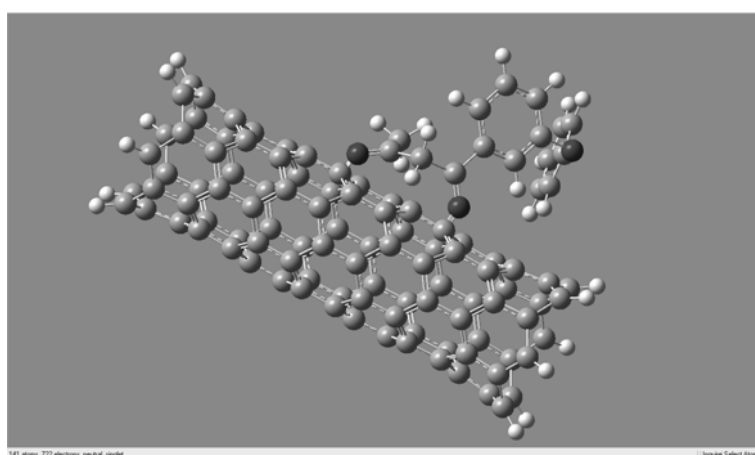


FIG. 2. The interaction of the molecule of 1-(3-phenoxyphenyl)-butan-1,3-dione with a carbon nanotube

The calculations were conducted in the medium of toluene as a solvent. The process was modeled as follows: a molecule was brought nearer to the outer surface of the carbon nanotubes in a stepwise fashion (0, 5) along a perpendicular drawn to the surface of the carbon

atom of the selected molecular cluster selected handset (in increments of 0.1 Å). The maximum convergence was chosen on the distance of 0.85 Å.

3. Inference

The calculations allowed us to construct profiles for the potential energy surface adsorption processes for the case of a single-site interaction mentioned above. The graph (Fig. 3) shows that there is an energy minimum on the distance between atomic systems at 2.3 Å, which corresponds to the Van-der-Waals force between tubulenes and the molecule, i.e. the so-called physical adsorption. The adsorption energy is $E = -10.42$ eV in this case. However, it is clear that being in this state, the molecule can also move into a more stable position, having overcome the potential barrier equal to 0.79 eV, i.e. a molecule of 2-(3-phenoxybenzoyl)cyclohexanone ceases to interact with the surface of the carbon nanotube.

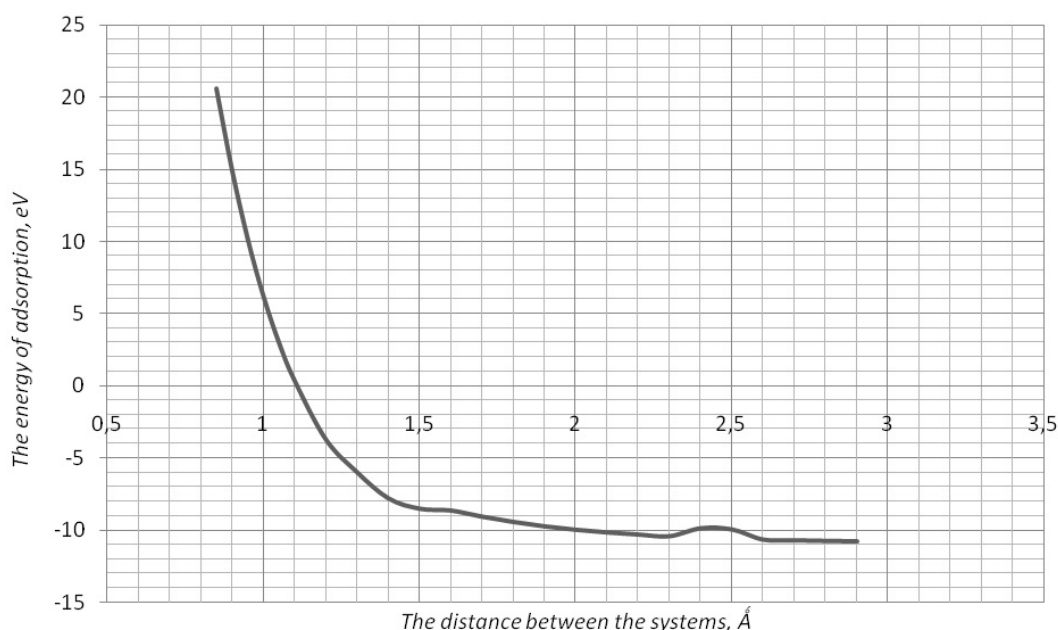


FIG. 3. The surface profile of the potential energy of interaction between molecules of 2-(3-fenoksibenzoil)-cyclohexanone with the surface of the carbon nanotube 'zig-zag' (0.5)

Theoretical calculations show that under these conditions (chosen sorption center, design scheme, etc.) the physical adsorption of a biologically active molecule on the surface of the tube was considered. It will be necessary to carry out future calculations with varying conditions and to conduct experiments to determine the means by which the chemical adsorption of organic molecules containing diphenylether fragment occurs on the external surface of the carbon nanotubes.

References

- [1] Sidorov L.N., Yurovskaya M.A., et al. *Fullerenes*. Publishing house 'Exam', Moscow, 2005, 688p. (In Russian).
- [2] Piotrowski L.B., Kiselev O.I. In: *Fullerenes in biology*. Publishing house 'Sprout', Saint Petersburg, 2006, p. 246–251.
- [3] Popov U.V., Korchagina T.K., Kalmykova G.V., Shinkarenko E.A. Synthesis of 2-(3-fenoksibenzoil)cyclohexanone. *Russian J. General Chem.*, **82** (7), P. 1220–1221 (2012).

SENSOR PROPERTIES OF CARBOXYL-MODIFIED CARBON NANOTUBES

N. P. Polikarpova¹, I. V. Zaporotskova¹, D. E. Vilkeeva¹, D. I. Polikarpov¹

¹Volgograd State University, Volgograd, Russia

nz.1103@mailru, irinazaporotskova@gmailru, vidinara@mailru, dimas700@mailru

PACS 00.30.91

This paper studies the sensor activity of carboxyl-modified single-walled carbon nanotubes (zig-zag, arm-chair type) to atoms and ions of alkali metals Na, Li, K. The mechanism of the carboxyl binding to the open border of the semi-infinite carbon nanotube is investigated. Calculations of the interaction processes between the sensor and sample alkali atoms and alkaline ions are performed. The process of scanning a sample surface site with atoms of metals under consideration is modeled and the functional carboxyl group chemical activity is defined. The research is performed by the MNDO method within the framework of the molecular cluster model and DFT method.

Keywords: sensor properties, carbon nanotube, sensory activity, functional carboxyl group, alkali metals, chemical active sensor, semi-empirical scheme MNDO, DFT method.

1. Introduction

In recent years carbon nanotubes have been regarded as a material of wide potential application, a commercial product and a subject of marketing research [1-7]. Their unique quasi-1D structure and extended curved π -bonding configuration define the nanotubes' remarkable structural, electronic and mechanical properties. Besides the above described characteristics, nanotubes possess high sorption activity [8], and owing to this valuable feature they can act as an effective adsorbent of various particles and, consequently, have a great potential for the development of chemical and biological sensors based on their sensitivity to their chemical environment [9,10]. It has been reported that devices with boundary modified carbon nanotubes can be successfully used as sensors. For example, an atomic force microscope with a specially selected functional group located at the end of the cantilever tip [11] can function as a sensor and is suitable to investigate the chemical composition of a sample surface. S.S. Wong, E. Josevlevich et. al. [11] report that carboxyl-modified carbon nanotubes have been fabricated experimentally. Theoretical simulations [12-14] demonstrate that carboxyl-modified carbon nanotubes are sensitive to ethanol, and the gases NO, and NO₂.

We assume that the potential of modified nanotubes' application as sensors is not limited to gases and can be suitable to detect other elements, for example, metals. Before [15] we investigated the mechanism of the carboxyl group binding to the open border of the semi-infinite carbon nanotube. In the present paper we performed calculations to study its sensitivity to atoms and ions of some alkali metals. Finally, we simulated the scanning process of a sample surface site and studied the functional group sensor activity to atoms of alkali metals.

2. The interaction mechanism between single-walled carboxyl-modified carbon nanotubes and atoms of alkali metals

We investigated the mechanism of interaction between some alkali atoms (potassium, sodium, lithium) and the boundary oxygen and hydrogen atoms of the carboxyl group – COOH on the border of carbon nanotube of (6, 0)-type (Fig. 1a) or (6, 6)-type. The process was simulated by an incremental approach when sample atoms moved to the O or H atoms of the functional group (Fig. 1b). The energy curves of the “nanotube + COOH - metal atom” system are presented in Fig. 2, 3, where each curve shows a minimum corresponding to the formation of bonds at certain distances. Analysis of the binding energies revealed that all the curves are characterized by barrier-free nature. Table 1 shows the main characteristics of Li, Na, K binding process to the boundary atoms (oxygen and hydrogen) of the carboxyl group that modifies the open border of the (6, 0) or (6, 6) carbon nanotubes. The obtained results allowed us to draw the following conclusion: since the interaction distances corresponding to the minimum on the interaction energy curves are long, there exists a weak van der Waals interaction between the atoms of the functional group and metal atoms. This is a very important result confirming that the designed sensor can undergo multiple uses without being destroyed.

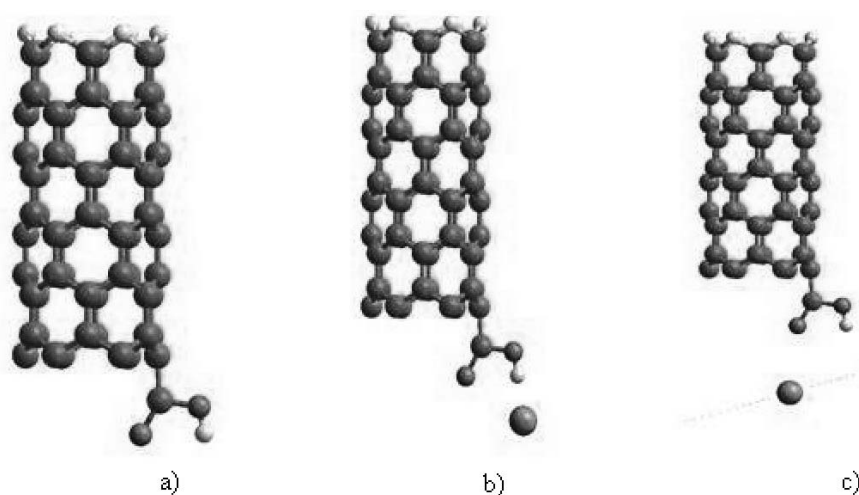


FIG. 1. The model of a sensor based on the modified (6,0) carbon nanotube: (a) the model of semi-infinite carbon nanotube (6,0) with the functional carboxyl group (-COOH) on the open border; (b) the model of incremental approach of a Na atom to the H atom of carboxyl group; (c) modeling of the scanning process of a random surface site with a Na atom, the dots indicate Na atom migration with respect to the modified nanotube

Thus, the obtained results proved the possibility of interaction between the boundary atoms of the carboxyl group and atoms of sample alkali metals.

3. Sensor properties of the carboxyl-modified carbon nanotube

We investigated the sensor properties of (6, 0) and (6, 6) carbon nanotubes modified by carboxyl group to sodium, potassium, lithium atoms and their ions Na^+ , K^+ , Li^+ . We studied the process of scanning the surface with an atom (or ions) to be initialized, and defined the functional group activity to the sample element. The process was simulated by incremental approach of a metal atom (or ion) to the functional group. The atom followed

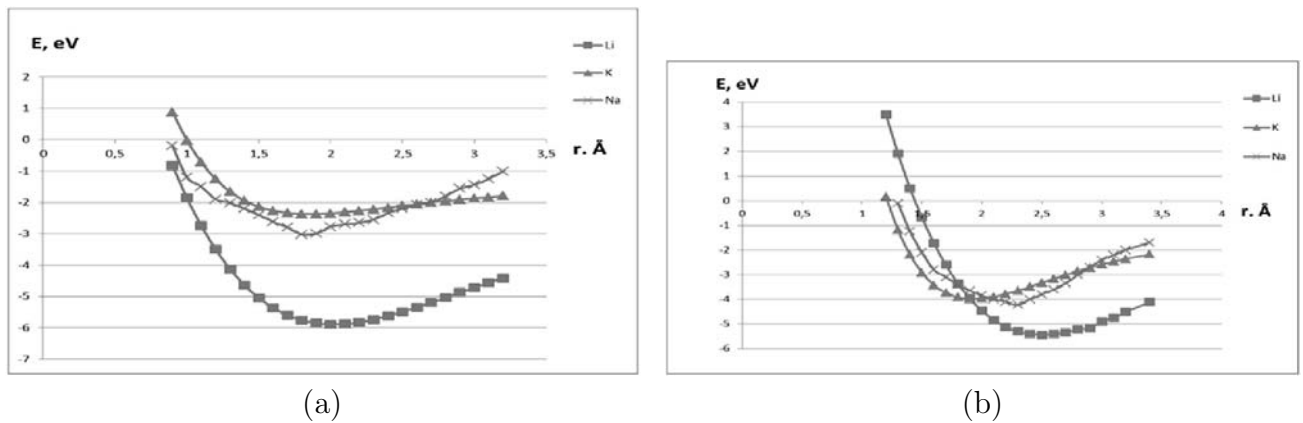


FIG. 2. The energy curves of interaction between the nanotube (6,0) modified by carboxyl group (-COOH) and atoms of alkali metals: (a) between atoms of metals and the hydrogen atom in the group; (b) between atoms of metals and the oxygen atom in the group

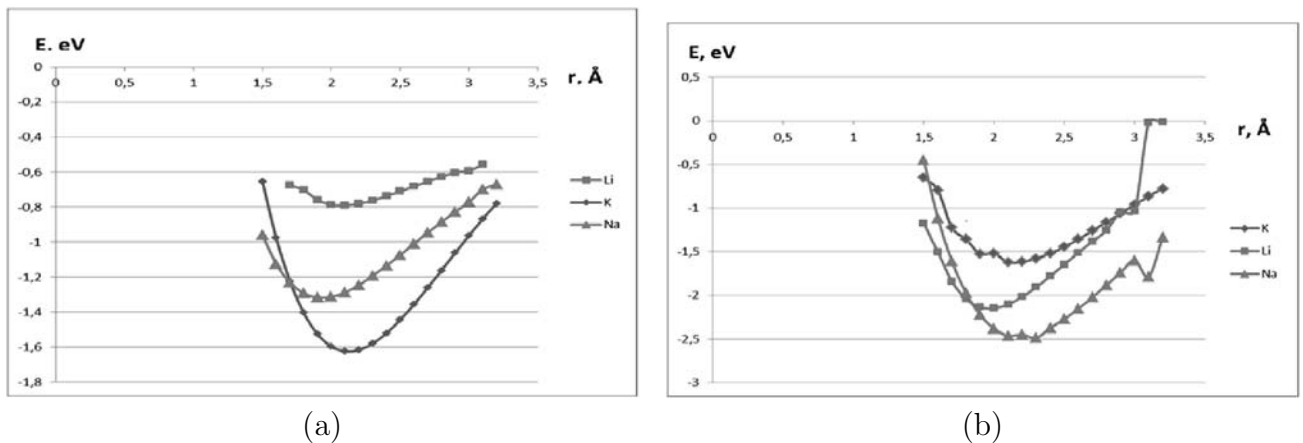


FIG. 3. The energy curves of interaction between the nanotube (6,6) modified by carboxyl group (-COOH) and atoms of alkali metals: (a) between atoms of metals and the hydrogen atom in the group; (b) between atoms of metals and the oxygen atom in the group

the path parallel to the modified border of the nanotube (Fig. 1c). The interaction energy curves (Fig. 4, 5) showed that the nanotube with the functional group is chemically sensitive to atoms and ions of sample metals: each curve has a characteristic minimum that indicates the formation of interaction between an atom (or an ion) of metal and the carboxyl group (co-called sensor interaction). It has to be pointed out that the minimum on each curve is located nearly beyond the boundary oxygen atom of the carboxyl group (-COOH). The sensor interaction distances and sensor interaction energies are shown in Table 2. The results obtained from the calculations demonstrate that modified carbon nanotubes can be used as sensors for specific elements and radicals that can be experimentally detected by the change in the potential of the sensor system based on the nanotube with the functional group.

TABLE 1. The main characteristics of Na, Na⁺, K, K⁺, Li, Li⁺ binding process to the boundary O and H atoms of carboxyl-modified carbon nanotube (6, 0) and (6, 6), where r_{int} — interaction distance between a metal atom and the O (or H) atoms of carboxyl group, E_{int} — interaction energy (MNDO and DFT methods)

Atomic bonds	r_{int} , Å	E_{int} , eV (MNDO)	E_{int} , eV (DFT)
Carbon nanotube (6, 0)-type			
K – O	1,9	-3,98	-4,30
K – H	2,1	-2,70	-1,04
Li – O	2,5	-5,44	-4,39
Li – H	2,0	-5,89	-4,62
Na – O	2,2	-4,23	-3,21
Na – H	1,8	-3,03	-1,77
Carbon nanotube (6, 6)-type			
K – O	2,1	-1,62	-1,83
K – H	2,1	-1,62	-1,45
Li – O	1,9	-2,14	-2,53
Li – H	2,1	-0,79	-1,96
Na – O	2,3	-2,48	-1,68
Na – H	1,9	-1,32	-1,33

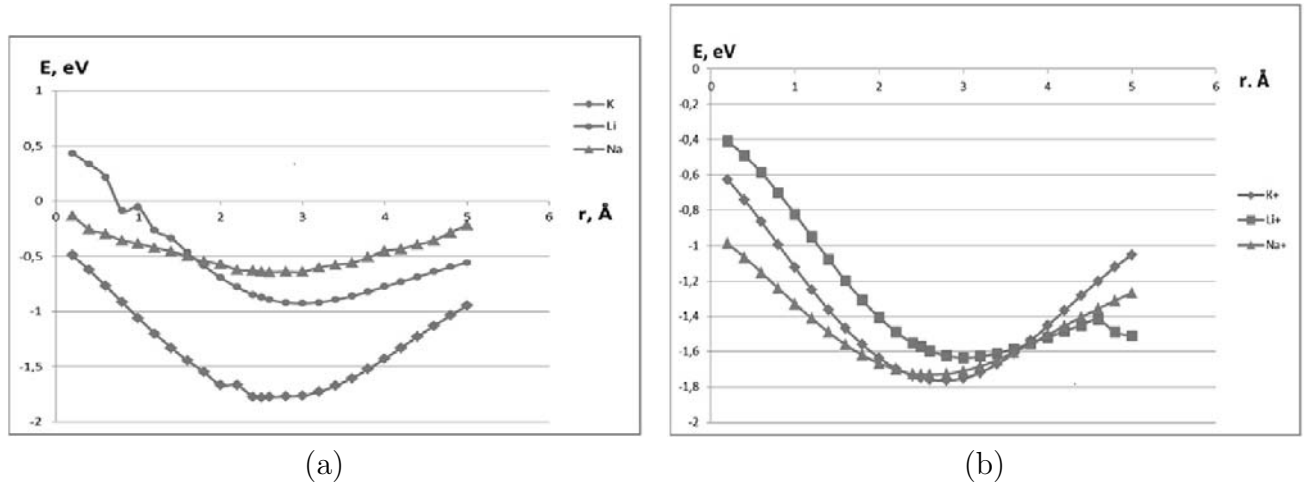


FIG. 4. The energy curves of interaction between atoms (ions) of metal and boundary atoms of the functional carboxyl group of (6,0) carbon nanotube obtained by modeling the scanning process, a distance of 0 Å corresponds to a point beyond the hydrogen atom: (a) for metal atoms K, Li, Na, (b) for metal ions K⁺, Li⁺, Na⁺

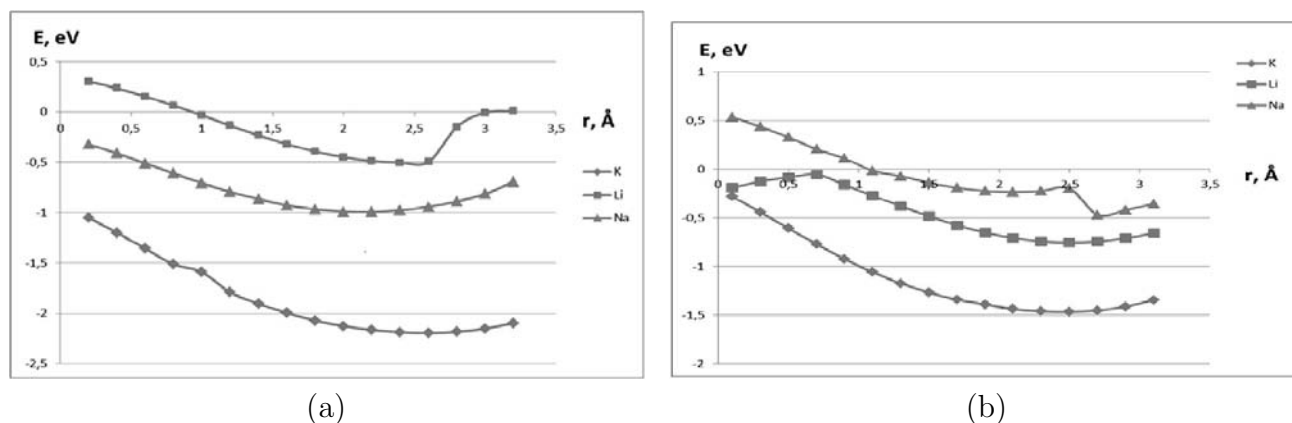


FIG. 5. The energy curves of interaction between atoms (ions) of metal and boundary atoms of the functional carboxyl group of (6,6) carbon nanotube obtained by modeling the scanning process, a distance of 0 Å corresponds to a point beyond the hydrogen atom: (a) for metal atoms K, Li, Na, (b) for metal ions K^+ , Li^+ , Na^+

TABLE 2. The main characteristics of the interaction process between the carboxyl-modified nanotube (6, 0) and (6, 6) and Na, Na^+ , K, K^+ , Li, Li^+ obtained from scanning the surface, where r_{s-int} - sensor interaction distance, E_{s-int} - sensor interaction energy, MNDO method

Atom/ion	r_{s-int} , Å	E_{s-int} , eV
Carbon nanotube (6, 0)-type		
K	2,5	-1,77
K^+	2,8	-1,76
Li	3,0	-0,93
Li^+	3,0	-1,63
Na	3,0	-0,64
Na^+	2,6	-1,73
Carbon nanotube (6, 6)-type		
K	2,5	-2,20
K^+	2,5	-1,47
Li	2,5	-0,50
Li^+	2,5	-0,76
Na	2,2	-0,99
Na^+	2,2	-0,23

4. Conclusion

This paper studies sensor properties of carboxyl-modified single-walled “zig-zag” and “arm-chair” carbon nanotubes to atoms and ions of alkali metals Na, Li, K. Calculations of the interaction processes between the sensor and sample alkali atoms and alkaline ions are performed. The research is performed by the MNDO method within the framework of the molecular cluster model and DFT method. The interaction energy curves showed that the nanotube with the carboxylate functional group is chemically sensitive to atoms and ions of sample metals: each curve has a characteristic minimum that indicates the formation of

interaction between an atom (or an ion) of metal and the carboxyl group (co-called sensor interaction). The performed theoretical studies prove the possibility of developing a sensor that responds to the presence of ultra-low quantities of materials and has a big potential for its application in chemistry, biology, medicine, etc.

Acknowledgements

The research has been supported by grant from the Ministry of Education and Science of the Russian Federation, project 14.B37.21.0080.

References

- [1] R. Saito, M.S. Dresselhaus, G. Dresselhaus. *Physical properties of carbon nanotube*, Imperial College Press, London UK, 251 p. (1999).
- [2] P. J. F. Harris, *arbon nanotubes and related structures. New Materials for the Twenty-first Century*, Cambridge University Press, New York USA, 336 p. (1999).
- [3] I.V. Zaporotskova. *Carbon and non-carbon nanomaterials and composite structures on its base: morphology and electron properties*, Volgograd Russia, Volgograd University Press, 456 p. (2009).
- [4] M.S. Dresselhaus, G. Dresselhaus, P. Avouris. *Carbon nanotubes: synthesis, structure, properties, and application*, Springer-Verlag, Berlin Germany, 464 p. (2000).
- [5] P.N. D'yachkov. *Electron properties and application of carbon nanotube*, Moscow Russia, BINOM, 488 p. (2010).
- [6] S. Chopra, A. Pham, J. Gaillard, A. Parker, A.M. Rao. Carbon nanotube based resonant circuit sensor for ammonia. *Appl. Phys.Lett.* **80**, P. 4632–4634 (2002).
- [7] S. Ghosh, A.K. Sood, N. Kumar. Carbon nanotube flow sensors Science, **299**, P. 1042–1044 (2003).
- [8] A. V. Eletskiy. Sorption properties of carbon nanostructure. *Uspehi Fizicheskikh Nauk*, **174**, P. 1191–1231 (2004).
- [9] S. N. Kim, J. F. Rusling, F. Papadimitrakopoulos. Carbon nanotubes fir electronic and electrochemical detection of biomolecules. *Adv. Mater.*, **19**, P. 3214–3228 (2007).
- [10] W.-D. Zhang, W.-H. Zhang. Carbon nanotubes as active components for gas sensors. *Journal of Sensors* (2009). doi:10.1155/2009/160698. 16, 2009.
- [11] S.S. Wong, E. Josevlevich, A.T. Wooley, C.L. Cheung, C.M. Lieber. Covalently functionalized nanotubes as nanometer sized probes in chemistry and biology. *Nature*. **394**, P. 52 (1998).
- [12] H.-L. Hsu, J.-M. Jehng, Y. Sung, L.-C. Wang, S.-R. Yang. The synthesis, characterization of oxidized multi-walled carbon nanotubes, and application to surface acoustic wave quartz crystal gas sensor. *Materials Chemistry and Physics*, **109**(1), P. 148–155 (2008).
- [13] J. Maklin, T. Mustonen, K. Kordas, S. Saukko, G. Toth, J. Vahakangas. Nitric oxide gas sensors with functionalized carbon nanotubes. *Physica Status Solidi B*, **244**(11), P. 4298–4302 (2007).
- [14] D. Fu, H. Lim, Y. Shi, et al. Differentiation of gas molecules using flexible and all-carbon nanotube devices. *Journal of Physical Chemistry C*, **112**(3), P. 650–653 (2008).
- [15] I.V. Zaporotskova, N.P. Polikarpova, D.E. Vil'keeva, P.A. Zaporotskov. Carboxylated carbon nanotubes as an active components of sensor devices. *Nanotechnics*, **1**(33), P. 46–52 (2013).

MIGRATION PROCESSES ON THE SURFACE OF CARBON NANOTUBES WITH SUBSTITUTE BORON ATOMS

S. Boroznin¹, E. Boroznina¹, I. V. Zaporotskova¹, P. A. Zaporotskov¹, O. A. Davletova¹

¹Volgograd State University, Volgograd, Russia

sboroznin@mail.ru, irinazaporotskova@gmail.com, sefm@volsu.ru

PACS 31.15.bu

The paper presents theoretical research into vacancy formation in two types of boron-carbon nanotubes BC_n, where $n = 3$. The research was performed using the MNDO method within the framework of an ionic-embedded covalent-cyclic cluster model, molecular cluster model and DFT method. We found that when a V-defect (vacancy) is introduced in a boron-carbon nanotube, the band gap of the defective tubules increases. This means that physical properties of materials can be purposefully changed by introducing defects. Vacancy migration along the atomic bonds in the tubule was simulated and vacancy transport properties were studied. It was found that the defect migration along different bonds actually represents the process of carbon or boron ions hopping between their stable states on the nanotube surface.

Keywords: Boron-carbon nanotubes, Vacancy, Activation energy, Vacancy migration, Semi-empirical methods of investigation.

1. Introduction

Liquid conductors commonly used in batteries and accumulators possess obvious drawbacks, namely short cycle life, low energy capacity and besides they are prone to leakage and spillage [1]. Structures with ionic conductivity can substantially extend cycle life of batteries since they can function both as electrolytes and electrodes simultaneously.

However, one of the main challenges we face when implementing the ionic conduction mechanism is that the size of an ion is often comparable to a distance between the sites of the crystal lattice, which explains why transport of charged ions similar to that one in metals almost never occurs in crystal structures. Therefore, to design a class of solid-state structures with ionic conductivity we need new materials with conduction properties that can be modified by using different methods. Recent studies have found that carbon nanotubes (CNTs), whose properties and conductive characteristics can be designed by applying different modification methods, can be successfully used as a material for ionic conduction. In [2] the results of research into the mechanism of ionic conductivity in single-walled CNTs with cylindrical symmetry are presented.

However, carbon cannot be regarded as the only element capable of forming nanotubular forms. Papers [3-7] theoretically predict and describe the formation of boron carbide nanotubes. The authors conclude that the calculated 1:3 ratio of boron and carbon in them is a clear sign that BC_n type tubular structures, where $n = 3$ are formed. This finding seems to be promising for research into electron and energy characteristics of boron carbon BC₃ tubules as well as ionic conductivity in them similar to that one displayed by carbon nanotubes. This paper presents the results of computer simulation of ionic conductivity in two types of BC₃ nanotubes (6, 0) by applying the MNDO method [8] within the framework of molecular and ionic-embedded covalent-cyclic cluster models.

2. Electronic structure of BC₃ nanotubes with a vacancy

In our previous work [9] we investigated geometric and electronic characteristics of monolayers in quasi-planar hexagonal boron carbide (BC₃ plane), the structure of which can be of two types that differ by mutual orientation of B and C atoms. We denote them as A and B to have an accurate identification in the text. Boron-carbon BC₃ nanotubes of small diameter (3 – 10 Å) were fabricated by rolling from the relevant segments of quasi-planar exagonal boron carbide. The extended unit cells (supercells) of A and B types BCNT (6, 0) are shown in Fig. 1. The calculations were performed using the semi-empirical MNDO method within the model of the ionic-embedded covalent-cyclic cluster [10] and ab initio DFT [11]. The studies found that these structures are stable with bond lengths between the atoms equal to 1.4 Å. We calculated the strain energy E_{str} values as the difference between specific energy values in quasi-planar boron carbide and those in the corresponding nanotubes. Dependence of strain energy values on the tubule diameter indicates that nanotube formation by rolling BC₃ plane is highly probable for boron carbide BC₃ of both types, since the strain energy values drop when the diameter of a tubule is increased (Fig. 2). For nanotubes of A-type tubule (n, 0) are most likely to form, where n = 6, 8 and 10. The band gap in the BCNT of the selected types allowed us to assign them to a class of narrow-gap semiconductors with conductivity independent of the diameter. This stability of conducting properties makes boron-carbon nanotubes very attractive for nanoelectronics.

We studied the electronic structure of A and B type BC₃ nanotubes (6, 0) (Fig. 1) with a vacancy (V-defect) using the MNDO method within the framework of the molecular cluster model. For the calculations we selected clusters in the form of a supercell consisting of four layers. The circumference of the system was geometrically closed. The distance between the nearest atoms was equal to 1.4 Å. The choice of the molecular cluster model was determined by the fact that the process under consideration is local. To eliminate the influence of boundary effects, the V-defect was located in the middle of the cluster. Two types of defects were considered: 1) V_B defect, when a boron atom is removed from the structure, 2) V_C defect, when a carbon atom is removed from the structure.

Our purpose was to study the process of vacancy formation on the BC₃ nanotubes surface and its influence on their geometric and electronic structure. To model this process, a boron or carbon atom was removed from the surface of the nanotube in 0.1 Å increments until its separation. We optimized geometric parameters for the atoms in the vicinity of the defect. The atoms in the vicinity of the vacancy had three degrees of freedom, which allowed them to move from their equilibrium positions in the process of simulation. Analysis of the tubule structure in the vicinity of defect showed that atoms on the surface do not change their positions and do not display any movement in the direction of vacancy location.

The results of calculations for the main electron energy characteristics of the selected boron-carbon nanotubes are presented in Table 1. The energy values for defect formation was calculated using the formula:

$$E_d = E_{BC_3} - (E_{str} + E_x), \quad (1)$$

where E_{BC_3} — the energy value of an ideal BCNT, E_{str} — the energy value of the structure with a vacancy E_x — the energy value of carbon or boron, respectively. It was found that in A-type of BC₃ nanotubes, the formation of a V-defect by breaking off a boron or carbon atom is possible, which may be proved by negative activation energy values on the curve. Positive activation energy values obtained from the calculations for B-type of BC₃ nanotubes show that the process of defect formation is unlikely to take place on this type of tubule surface. This fact can be explained by lower stability of BC₃ nanotubes of B-type compared

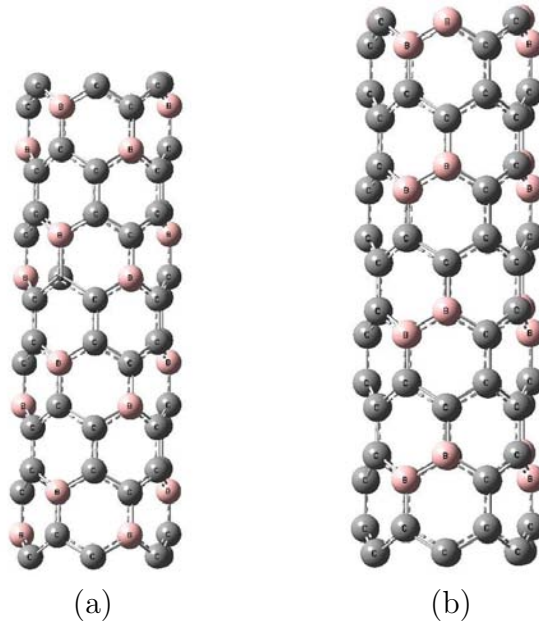


FIG. 1. The extended elementary cell of the BC_3 nanotube (6, 0): a) A - type of mutual orientation of C and B atoms; b) B - type of mutual orientation of C and B atoms

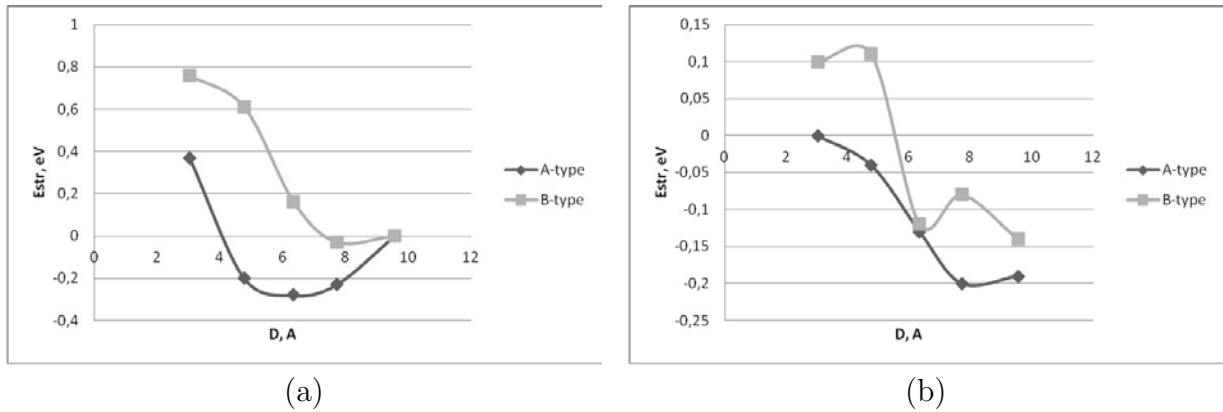


FIG. 2. Dependence of strain energy E_{str} on the diameter (d) of BC_3 tubule ($n, 0$) of A and B types calculated by the methods a) MNDO, b) DFT

with those of the A-type. Therefore, we shall further consider the A-type boron-carbon nanotube.

TABLE 1. Energetic characteristics of nanotubes with a vacancy

Type of a tubule	Type A with V_c defect	Type A with V_B defect	Type B with V_c defect	Type B with V_B defect	Flawless nanotube, type A	Flawless nanotube, type B
E_{homo}, eV	-7.21	-6.15	-8.03	-6.23	-7.37	-6.09
E_{lumo}, eV	-4.67	-3.84	-4.73	-4.52	-6.16	-6.02
E_d, eV	-0.83	-3.43	5.97	10.72	—	—
$\Delta E_g, eV$	2.54	2.31	3.30	1.71	1.21	0.07

Analysis of the electron and energy structure of tubules with vacancies and flawless tubules allowed us to come to the following conclusions. Introduction of V_B and V_C defects into a nanotube of A-type causes changes in the position of the highest occupied and lowest unoccupied molecular orbitals (E_{homo} and E_{lumo}). In both cases, a significant increase in the band gap in comparison with the value of ΔE_g 1.21 eV for flawless boron-carbon nanotubes (6, 0) is observed. We should point out that the values of the band gap obtained by applying the molecular cluster model turn out to be much larger than the ones obtained from calculations when using other more precise methods. However, we think that this model is convenient and efficient for the study of local processes, to which the formation of a single defect can be attributed. Single electron energy spectra (Fig. 3) show differences between nanotubes with V_B and V_C defects and a flawless nanotube.

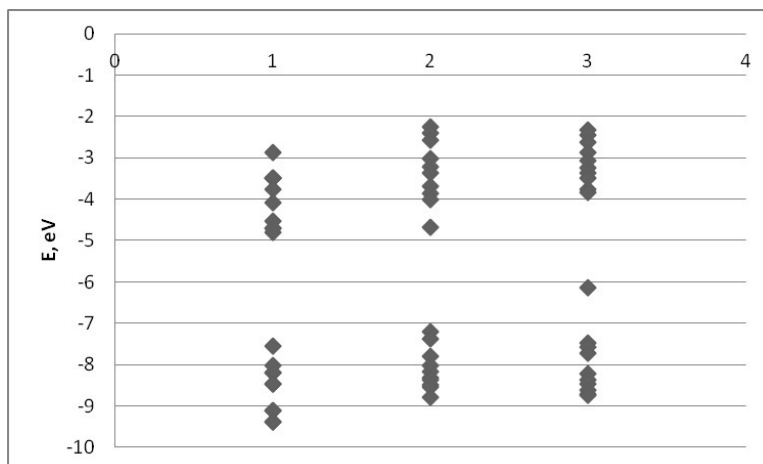


FIG. 3. Single electron energy spectra of BC_3 nanotube (6, 0) type A: 1 – flawless structure; 2 – structure with V_C defect; 3 – structure with V_B defect

3. Vacancy transport properties

Further, we investigated energy characteristics of defect migration on the surface of boron-carbon nanotubes. We considered two types of movement for two chemically inequivalent valence bonds between neighboring atoms that we denoted as I and II: I - when one bond lies on the fracture face of the nanotube, and the other two (II) lie symmetrically on either side of the fracture. They are not equivalent because of the tubule structural features that are discussed in detail in [2]. Vacancy transfer along the above described chemical bonds was modeled by using incremental approach of a neighboring carbon (or boron) atom along the virtual C-V or B-V bond to the site of vacancy location. Thus, the surface atom of the nanotube had two degrees of freedom, which allowed it to move within the surface and freely deviate from it. The geometrical parameters of the other two B and C atoms nearest to the vacancy were fully optimized during the calculation. Therefore, it seemed that the vacancy moved in a direction reverse to the atom migration.

Incremental method allowed us to build energy curves for vacancy transfer process and calculate activation energies (E_a) of the process. The curves (Fig. 4) are qualitatively similar: they have two energy minima corresponding to a stationary position of the vacancy on the tubule surface. The energy barrier between the minima have heights of 2.38 eV and 3.44 eV on migration paths I and II, respectively. We identify the barrier with activation energy of the defect. By comparing the activation energies for boron-carbon and carbon nanotubes

(6, 0) we found that the activation energy of the defect in BCNT of BC₃ type is 1 eV lower than that one in CNTs [2] for both migration paths. This means that the mechanism of ionic conductivity in the BC₃ nanotubes is energetically more favorable compared with that one in carbon nanotubes, so BCNTs with predicted conductivity might find application in nanoelectronics.

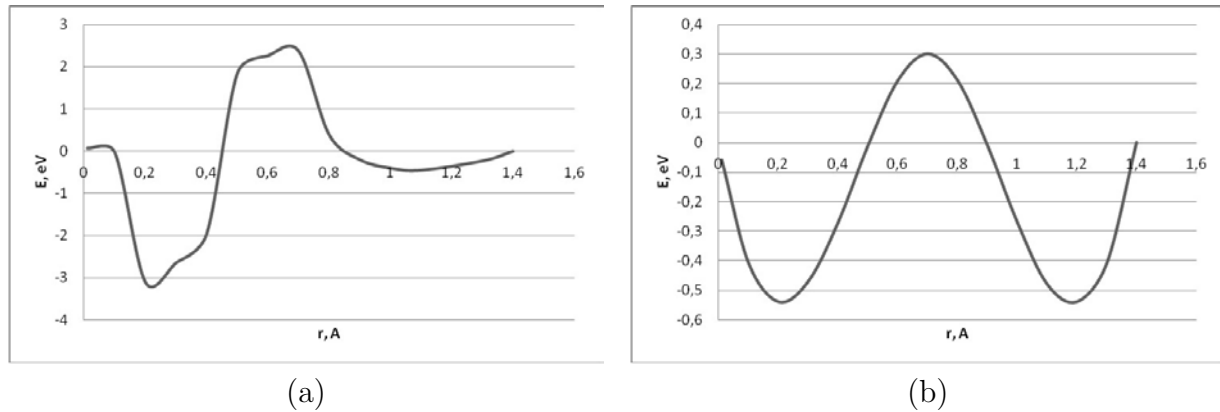


FIG. 4. The energy curves for defect transfer (vacancy transfer) in BC₃ nanotubes (6, 0) type: a) path I of defect transfer; b) path II of defect transfer

We investigated the vacancy formation mechanism in boron-carbon BC₃ nanotubes (6,0) of A and B types that differ by mutual orientation of boron and carbon atoms. The obtained activation energies showed that the formation of defects on the B-type BCNT surface was energetically unfavorable and, probably, can lead to the destruction of a tubular structure. We found that introduction of V-defects (vacancy) in the boron-carbon nanotube causes an increase in the band gap of the defective nanotubular structures. This means that physical properties of materials can be purposefully changed by introducing defects. Defect migration follows the paths along different bonds and actually represents the process of carbon or boron ions hopping between their stable states on the nanotube's surface.

Acknowledgment

The study was supported by The Ministry of education and science of Russian Federation, project 14.B37.21.0080.

References

- [1] H. Wang, J. Li, F. Gong, G. Zhou, Z.-S. Wang. Ionic Conductor with High Conductivity as Single-Component Electrolyte for Efficient Solid-State Dye-Sensitized Solar Cells. *J. Am. Chem. Soc.*, **135**(34), P. 12627–12633 (2013).
- [2] I.V. Zaporotskova. *Carbon and Uncarbon nanomaterials and composite structures on their base: structure and electronic properties*, Volgograd State University Publishing, Volgograd, 490 p. (2009).
- [3] G.G. Fuentes, E. Borowiak-Palen, M. Knupfer, T. Pichler, J. Fink, Wirtz L. and Rubio A. Formation and electronic properties of BC₃ single-wall nanotubes upon boron substitution of carbon nanotubes. *Phys. Rev. B*, **69**, P. 245403 (2004).
- [4] X.M. Liu, H.R. Gutiérrez, P.C. Eklund. Electrical properties and far infrared optical conductivity of boron-doped single-walled carbon nanotube films. *J Phys: Condens. Matter*, **22**, P. 334223 (2010).
- [5] J. Debnarayan, C.-L. Sun, L.-C. Chen, K.-H. Chen. Effect of chemical doping of boron and nitrogen on the electronic, optical, and electrochemical properties of carbon nanotubes. *Progr. Mater. Sci.*, **58**, P. 565–635 (2013).
- [6] P. Ayala, J. Reppert, M. Grobosch, M. Knupfer, T. Pichler, A.M. Rao Evidence for substitutional boron in doped single-walled carbon nanotubes. *Appl. Phys. Lett.*, **96**, P. 183110–183113 (2010).

- [7] L.S. Panchakarla, A. Govindaraj, C.N.R. Rao. Boron-and nitrogen-doped carbon nanotubes and graphene. *Inorg. Chim. Acta*, **363**, P. 4163–4174 (2010).
- [8] M. J. S. Dewar, W. Thiel. Ground states of molecules. The MNDO method. Approximations and Parameters. *J. Amer. Chem. Soc.*, **99**, P. 4899–4906 (1977).
- [9] I.V. Zaporotskova, S.V. Boroznin, E.V. Perevalova, D.I. Polikarpov Electronic structure and characteristics of certain types of boron containing nanotubes. *Vestnik VolGU. Seriya 10: Innovatsionnaya deyatelnost* **6**, P. 81–86 (2012), (in Russian).
- [10] A.O. Litinskii, N.G. Lebedev, I.V. Zaporotskova. The ionic-embedded covalent-cyclic cluster model in MNDO calculations of molecular interaction in heterogeneous systems. *Russ. J. of Physical Chemistry A*, **1(69)**, P. 189 (1995).
- [11] E.V. Butyrskaya. *Computer chemistry: theoretical basis and work with programs Gaussian and GaussView*, Solon-Press, Moscow, 224 p. (2011).

UTILIZING OF THE MEDIUM-ENERGY ION SCATTERING SPECTROMETRY FOR THE COMPOSITION INVESTIGATION OF GRAPHENE OXIDE FILMS ON SILICON SURFACE

V.V. Afrosimov, A. T. Dideykin, V. I. Sakharov, I. T. Serenkov, S. P. Vul

Ioffe Physical-Technical Institute of the Russian Academy of Sciences, Moscow, Russia
r.ilin@mail.ioffe.ru

PACS 68.65.Pq

The possibilities of Medium-Energy Ion Scattering (MEIS) spectrometry combined with ion channeling for the estimation of the composition of single layer graphene oxide films and produced graphene layers deposited on the surface of standard silicon substrates was investigated. It was found that the oxygen amount in the natural surface silicon oxide ranges from 2-8 times the possible oxygen content in a graphene oxide layer. This causes difficulties in the estimation of the oxygen concentration in graphene oxide deposited on such substrates. The proposed method of preliminary single hydrogen cathode surface processing in electroplating bath leads to the significant decrease of surface layer oxygen content which results in an increase in the accuracy of reduced graphene oxide composition estimation.

Keywords: graphene oxide, silicon oxide, Rutherford Backscattering Spectrometry.

The main obstacle in the creation of graphene-based field-effect transistors is the band gap absence in this material [1]. The latest studies showed the possibility of controlled bandgap width graphene layers production by means of thermal reduction of graphene oxide films on Si surface [2]. In this process, the evaluation of the graphene film composition, as well as the estimation of the bandgap width dependence and carrier mobility, on the remaining oxygen concentration becomes the experimental task of particular importance.

We investigated the possibilities of Medium-Energy Ion Scattering (MEIS) spectrometry combined with ion channeling in order to estimate the composition of near-surface layers of crystalline silicon as well as of graphene oxide films deposited on the surface of silicon substrates. MEIS, being a modification of Rutherford Back Scattering (RBS) spectrometry, differs from the latter by the possibility of achieving extremely high depth resolution in the elemental analysis of near-surface layers due to the utilization of high energy resolution electrostatic analyzers. For current work conditions (scattering of H^+ ions having the initial energy of 96 keV in silicon) the depth resolution was on the order of 1 nm. Using an aligned (channeling) spectra measurement regime, in which the probe ion beam direction was coincident with the low-index crystalline axis one (in our case it was $\langle 100 \rangle$ direction) made it possible to decrease dozens of times, relative to “random” regime, the signal of ions, back scattered from the bulk of single crystal silicon substrate, keeping the signal from amorphous layers. That resulted in a significant increase in the accuracy for the estimation of carbon and oxygen atom content and their depth distribution.

Oxygen content measurements were carried out for the natural oxide substrates, whereas for “substrate plus graphene oxide” structures, measurements were made to determine the carbon and oxygen contents and their depth distributions.

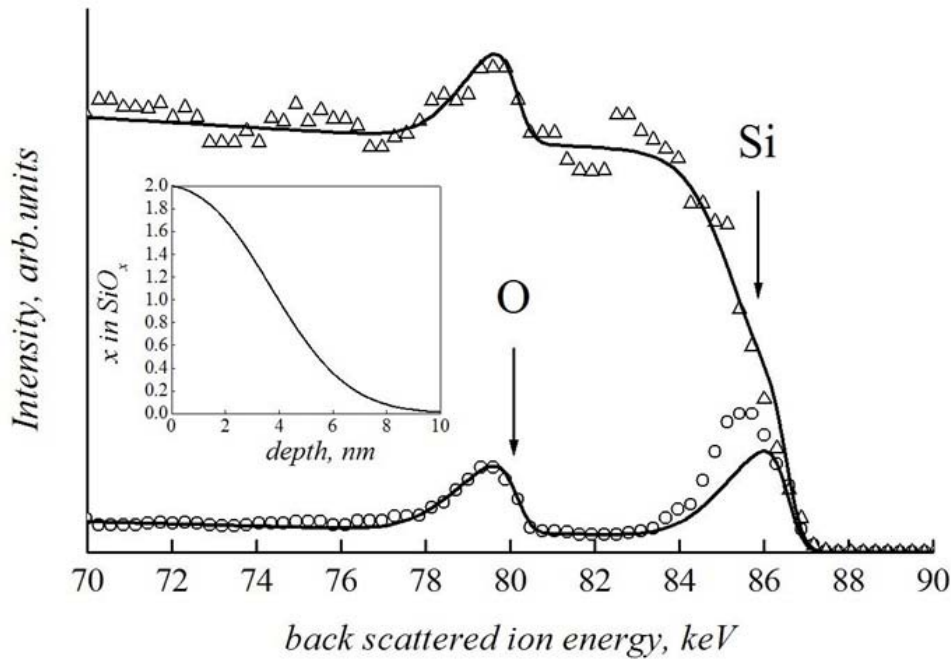


FIG. 1. The energy spectra of H^+ ions having the initial energy of 96 keV back scattered from pure silicon with natural surface oxide. Circles — aligned regime, triangles — “random” regime, solid curves — the result of computer simulation. Insert — the depth distribution of oxygen

Fig. 1 shows the energy spectra of H^+ ions, back scattered from the sample of a single silicon crystal with natural oxide. Arrows point to the energies of ions, back scattered from silicon (86 keV) and oxygen (80 keV) atoms of the sample surface. Solid lines are the result of computer simulation for “random” and aligned measurement regimes. Hereafter (e.g. Fig. 3), the aligned spectra simulation of near-surface layers took into account only the signal from silicon of the oxide layer, ignoring that of so called “surface peak” of ion scattering on pure silicon, and that is the reason for the discrepancy in the 84-86 keV region. Comparison of the spectra shows that the accuracy of the signal detection, corresponding to ion back scattering on oxygen in the aligned regime is significantly higher because the background bulk silicon signal is approximately suppressed nearly 20-fold. The computer simulation made it possible to determine the whole oxygen amount in natural oxide; in this particular case it was 16×10^{15} atoms/cm².

The “protacted” back (low energy) oxygen peak front (energies 77-80 keV) indicates a gradual oxygen concentration decrease from the surface to deeper layers. The depth dependence of oxygen concentration is shown in the insert in Fig 1. It is interesting to note, that the same phenomenon was observed in [3], devoted to MEIS investigation of artificially created oxide layers on silicon surface.

The oxygen content in the investigated substrates was found to range from 6×10^{15} to 19×10^{15} atoms/cm². For comparison, it should be noted that if the carbon atom content in the graphene oxide layer is 3.8×10^{15} atoms/cm² and each carbon atom accounts for a single oxygen atom (it corresponds to maximal oxidation rate), the tight to carbon oxygen monolayer must also contain 3.8×10^{15} atoms/cm². This means that the oxygen of the natural oxide significantly affects the accuracy when estimating the oxidation rate. In order to reduce the oxygen content, the single hydrogen cathode surface processing in electroplating bath

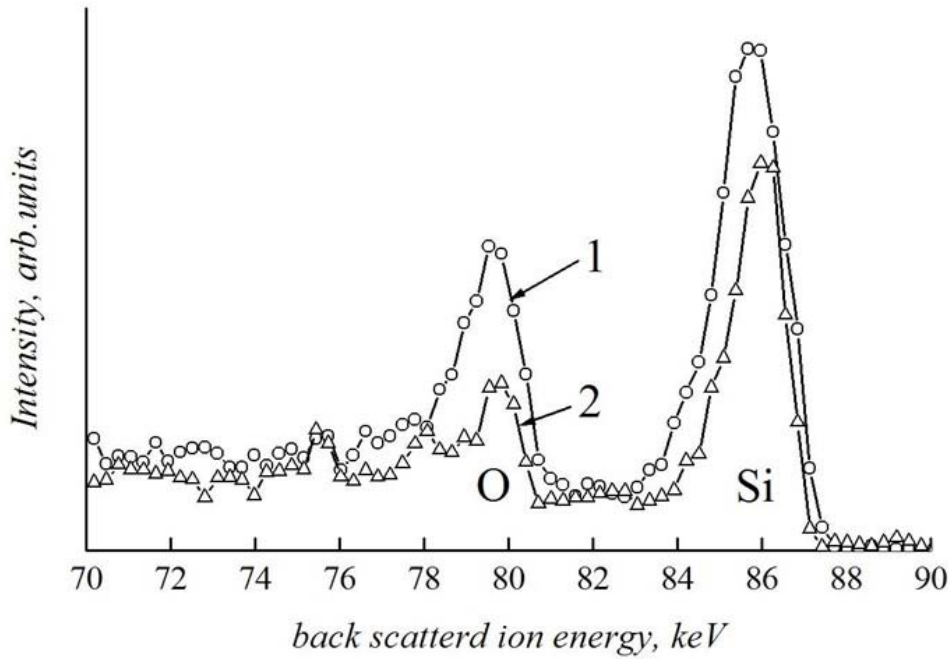


FIG. 2. The energy spectra of H^+ ions having the initial energy of 96 keV back scattered from silicon substrate before (1) and after (2) the processing in electroplating bath

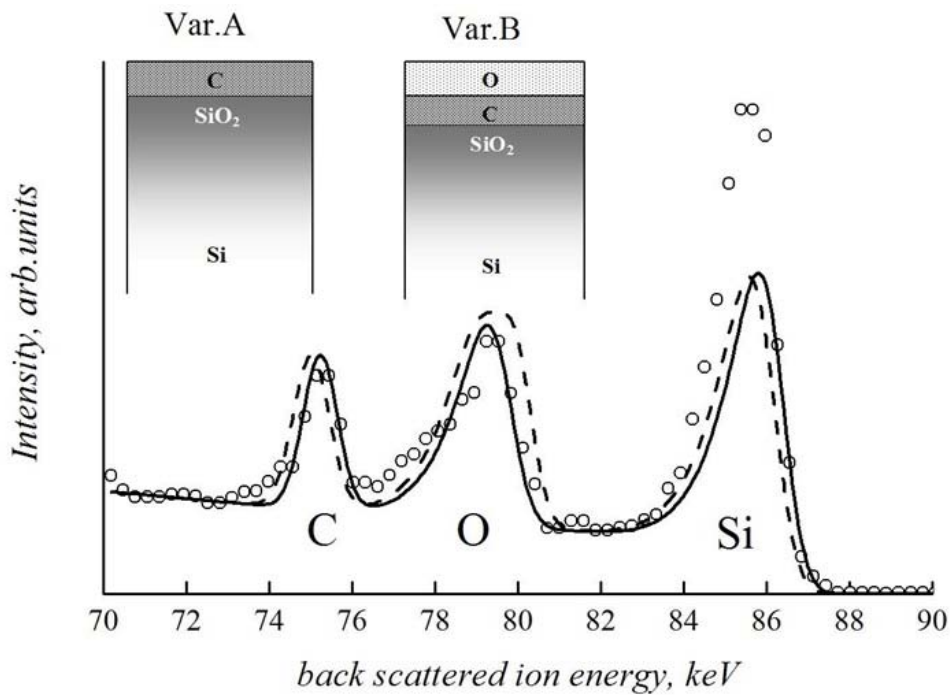


FIG. 3. The energy spectra of H^+ ions having the initial energy of 96 keV back scattered from graphene oxide layer, deposited on the silicon substrate. Circles — experiment, solid line — the MEIS computer simulation for the structure, schematically depicted in the insert Var.A, dashed line — the same for the structure depicted in Var.B insert

was applied. In Fig. 2 the MEIS substrate spectra before (1) and after (2) this processing are shown. The oxygen contents were found to be 16×10^{15} atoms/cm² and 8×10^{15} atoms/cm², respectively, i.e. the processing used halved the amount of oxygen in the surface oxide layer.

The MEIS aligned spectrum of sample having the structure “silicon substrate with the natural oxide plus graphene oxide layer” is shown in Fig. 3. Circles depict experimental results, while lines show the computer simulation for two modeling structures: solid — for one schematically depicted in Var.A insert and consisting of silicon, its oxide and graphene. With the help of computer simulation, the carbon and oxygen contents were found to be 7×10^{15} atoms/cm² and 10×10^{15} atoms/cm², respectively. It is important to note, that all three fore fronts (high energy) of silicon, oxygen and carbon calculated peaks coincided with experimental ones. Dashed curve shows the result of modeling of the structure, depicted in Var.B insert, where the oxygen monolayer of $\sim 4 \times 10^{15}$ atoms/cm² laying above the graphene film was added. In this variant, the essential discrepancy was observed for all fore fronts, leading one to conclude that there is no covering oxygen layer, at least of the amount, similar to that of the complete monolayer. Comparison of the simulated and experimental spectra demonstrated the high MEIS sensitivity to graphene’s oxidation rate.

Accordingly, the described investigations allow one to draw the conclusion that MEIS-based diagnostics, when applied to the solving of silicon-graphene structures synthetic problems, is rather promising and can give much pertinent information.

Authors appreciate Russian Federal Objective Program (agreement 21.09.2012 8683) for financial support.

References

- [1] D. Reddy, L.F. Register, G.D. Carpenter, S.K. Banerjee. Graphene field-effect transistors. *J. Phys. D: Appl. Phys.*, **44**, P. 313001 (20p.) (2011).
- [2] V.M. Mikoushkin, V.V. Shnitov, S.Yu Nikonov, A.T. Dideykin, S.P. Vul’, A.Ya. Vul’, D.A. Sakseev, D.V. Vyalikh, O.Yu. Vilkov. Controlling Graphite Oxide Bandgap Width by Reduction in Hydrogen. *Tech. Phys. Lett.*, **37**(10), P. 942–945 (2011).
- [3] E.P. Gusev, H.C. Lu, T. Gustaffson, E. Garfunkel. Growth mechanism of thin silicon oxide films on Si(100) studied by medium-energy ion scattering. *Phys. Rev.B*, **52**(3), P. 1759–1775 (1995).

INVESTIGATION OF STRUCTURE AND TRANSPORT PROPERTIES OF GRAPHENE GROWN BY LOW-PRESSURE NO FLOW CVD ON POLYCRYSTALLINE Ni FILMS

O. V. Kononenko^{1*}, V. N. Matveev¹, D. P. Field², D. V. Matveev³, S. I. Bozhko³,
D. V. Roshchupkin¹, E. E. Vdovin¹, A. N. Baranov⁴

¹Institute of Microelectronics Technology and High Purity Materials,
Russian Academy of Sciences, Chernogolovka, Russia

²School of Mechanical and Materials Engineering, Washington State University, Pullman, WA

³Institute of Solid State Physics, Russian Academy of Sciences, Chernogolovka, Russia

⁴Moscow State University, Moscow, Russia

*oleg@iptm.ru

PACS 68.65.Pq; 81.05.ue; 73.50.Jt

Graphene films were synthesized by the low-pressure no flow CVD on polycrystalline nickel catalyst films grown by the self-ion assisted deposition technique at different biases. Graphene films were transferred to a SiO₂/Si substrate using PMMA. The graphene grown on Ni films with bimodal grain size distribution and weaker (111) texture had higher thickness uniformity and a lower number of graphene layers. The graphene grown on Ni films with a monomodal grain size distribution and stronger (111) texture had lower thickness uniformity and a higher number of graphene layers. The transport properties of the graphene films were investigated with the aid of Hall measurements.

Keywords: Graphene, CVD Synthesis, Electronic properties.

1. Introduction

Among various carbon nanostructures, graphene as a single atom two-dimensional (2D) sp² hybrid carbon sheet shows unique properties for fundamental research [1–4] and promising applications in condensed-matter physics, electronics, and materials science. The interest in graphene-based structures has increased tremendously after the empirical discovery of graphene sheets in 2004 [5].

It is highly desirable to develop reliable synthesis techniques to fabricate graphene films. Recently we have developed a method to grow graphene films by low-pressure no flow CVD using thin Ni films deposited on SiO₂/Si substrates. As was shown earlier, the quality and uniformity of graphene films strongly depend on the structure of Ni films [6–9].

The graphene growth mechanism during CVD consists of several stages. The first is decomposition of a carbon containing precursor. The second is diffusion of carbon into bulk Ni, and the third is segregation and precipitation of carbon onto the Ni surface. If Ni films contain numerous defects, such as grain boundaries, triple junctions and dislocations which are good sinks for impurities, then carbon accumulates at these sites during the segregation stage leading to the formation of multilayer graphene [6–9].

As we showed in previous works [10, 11], the self-ion assisted deposition (SIAD) technique is a powerful method for control of microstructure of thin metal films. Due to the self-ion bombardment, high purity films are obtained during deposition.

2. Experimental

The Ni films were deposited by the self-ion assisted deposition technique on oxidized Si(100) substrates at 0 and -5 kV biases. High purity Ni (99.9999) was used as a source. The vacuum during deposition was about 10^{-6} torr. During deposition, the accelerating voltage was held at 0 or -5 kV. The thickness of the films was about $0.38 \mu\text{m}$. After Ni deposition substrates were placed in a quartz tube reactor, which was pumped down to a pressure about 10^{-6} torr and then inserted into a preheated to 950°C furnace. When the samples were heated to the reaction temperature, acetylene was admitted into the quartz tube up to a pressure of 0.4 torr for 5 s and then pumped out and the quartz tube reactor was extracted from the furnace.

X-ray diffraction (XRD) spectra were measured before and after graphene growth with a Bruker D8 DISCOVER diffractometer.

Crystallographic texture of the tested films was performed by orientation imaging microscopy [12, 13] using a field emission scanning electron microscope (FESEM). Electron backscatter diffraction (EBSD) technology was used for obtaining diffraction patterns over a regular array for each film examined. Inherent in the orientation imaging technique is complete crystallographic information that describes the spatial arrangement of texture and microtexture.

Transfer of the resulting graphene was done with the aid of poly(methyl methacrylate) (PMMA) that was spincoated on the surface of the graphene film to serve as a support. The PMMA/graphene layer was detached from the substrate by wet-etching of the Ni film with a 1 wt% aqueous solution of hydrochloric acid and then manually laid on the target substrate (SiO_2/Si). The PMMA was finally removed by exposure to acetone in vapor and then liquid form.

Raman spectra and mapping images of graphene films were measured with a Renishaw Raman microscope using a 633 nm excitation wavelength.

Hall measurements were performed to investigate transport properties of graphene films. Hall bar structures were fabricated using standard photo lithography and oxygen plasma etching.

3. Results and discussion

XRD spectra were collected from as-deposited Ni films and from Ni films after graphene synthesis (Fig. 1). The XRD spectra of as-deposited films showed strong Ni (111) peaks and weak Ni (200) peaks. Intensity of Ni (111) peak for the -5 kV film was stronger than that for the 0 kV film. Intensities of the Ni (111) and Ni (200) peaks increased in both films after graphene growth.

Figure 2 contains a representative orientation image of 0 and -5 kV Ni films after graphene synthesis. We observed that the Ni films deposited at -5 kV bias were strongly (111) textured. The average grain size was about $1 \mu\text{m}$. Ni films deposited at 0 kV bias had (111) oriented grains and a noticeable fraction of (100) oriented grains. A bimodal grain size distribution was observed in the films. In a matrix of rather small grains (about $1.5 \mu\text{m}$), a few larger grains ($4\text{--}6 \mu\text{m}$) were found.

Figure 3 shows back scattered electron images of the graphene films grown on Ni films deposited at 0 and -5 kV biases. Darker contrast corresponds to a thicker graphene films. It is seen that graphene film grown on the -5 kV Ni substrate consists of a larger number of layers.

In Raman spectroscopy graphene is typically characterized by a D-peak near $1300 - 1350 \text{ cm}^{-1}$, a G-peak near 1580 cm^{-1} and a 2D-peak near $2600 - 2700 \text{ cm}^{-1}$ [14]. The relative intensities and the widths of the G and 2D peaks give us possibilities to judge about the number of layers in graphene films. Raman spectra were collected from graphene films grown on 0 and -5 kV biased Ni films and transferred to $\text{SiO}_2/\text{Si}(100)$ substrates. The sharp peaks are

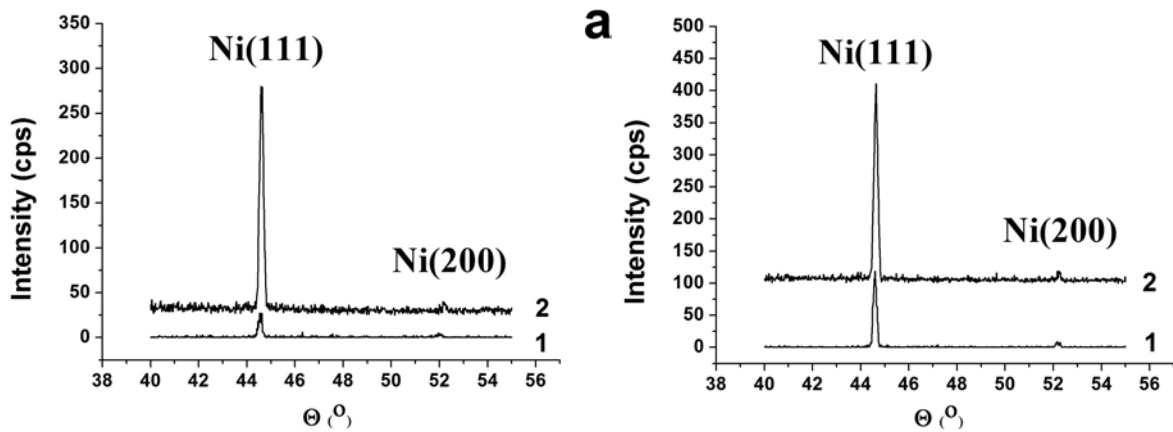


FIG. 1. a) XRD spectra collected from an as-deposited Ni film and b) from Ni films after graphene synthesis. Curves (1) correspond to films deposited at 0 kV bias and curves (2) correspond to films deposited at -5 kV bias

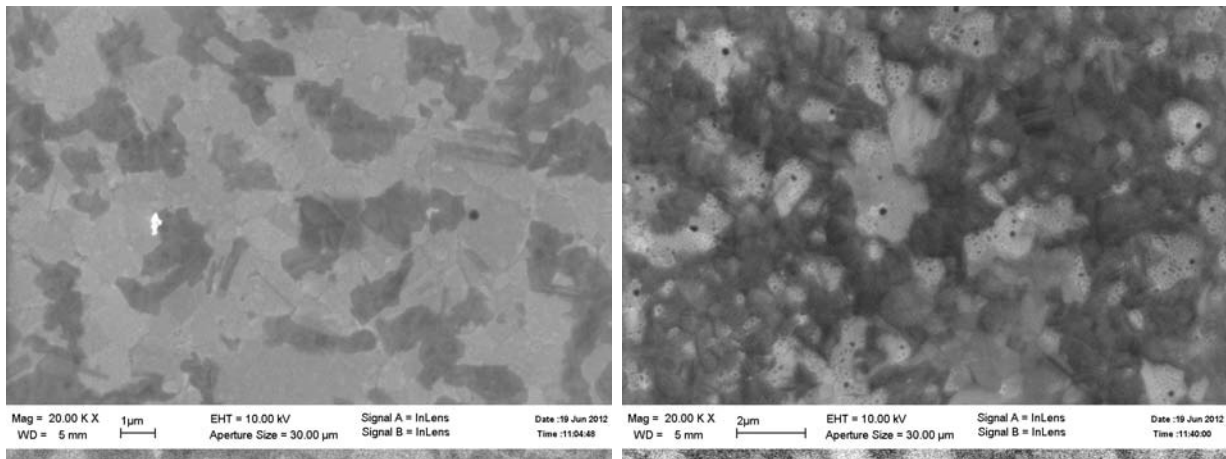


FIG. 2. Orientation images of the Ni films deposited at 0 (a) and -5 kV (b) bias obtained after graphene synthesis

indicative of the crystallinity of the films and the plot shows several distinct peaks, one at about $1582 - 1588 \text{ cm}^{-1}$ (G peak) and the other at about $2650 - 2670 \text{ cm}^{-1}$ (2D peak). The peak at around 1582 cm^{-1} is attributed to sp^2 phonon vibrations. The 2D peak is used to confirm the presence of graphene and it originates from a double resonance process that links phonons to the electronic band structure. A peak occurring at about $1320 - 1350 \text{ cm}^{-1}$ (D band) indicates phonon scattering at defect sites and impurities. Spectra collected from graphene films, for the most part, show single Lorentzian lineshape and narrow linewidth.

Figure 4 contains a representative Raman spectra of transferred graphene films grown on 0 and -5 kV Ni films. The spectrum from graphene grown on the 0 kV Ni film (Fig. 4a) presents typical features for monolayer graphene: the I_{2D}/I_G intensity ratio is ~ 1.85 , and the full width at half-maximum (FWHM) of the 2D band is $\sim 65 \text{ cm}^{-1}$. Small D and D' peaks (near 1620 cm^{-1}) indicates that some defects such as grain boundaries, vacancies and impurities are contained in the graphene film. The spectrum corresponding to graphene grown on the -5 kV Ni film (Fig. 4b) has a noticeable upshift of $\sim 15 \text{ cm}^{-1}$ in the 2D band, as well as a broadening of the 2D band line width ($\sim 30 \text{ cm}^{-1}$) that can be fit with four or more Lorentzian peaks. The I_{2D}/I_G intensity ratio is ~ 0.65 , and the FWHM of the 2D band is $\sim 95 \text{ cm}^{-1}$. It

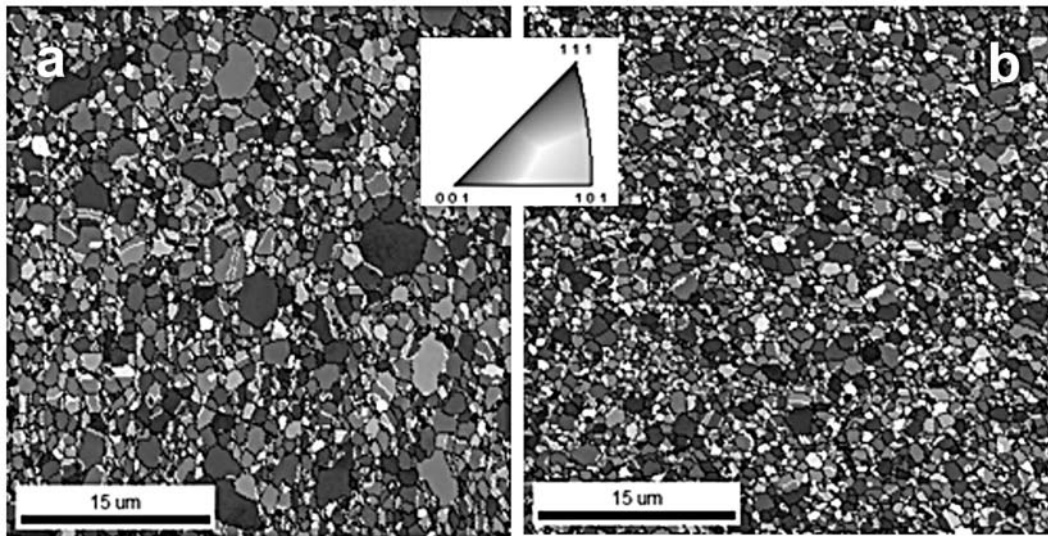


FIG. 3. Back scattered electron images obtained from Ni films deposited at 0 (a) and -5 kV (b) bias after graphene synthesis

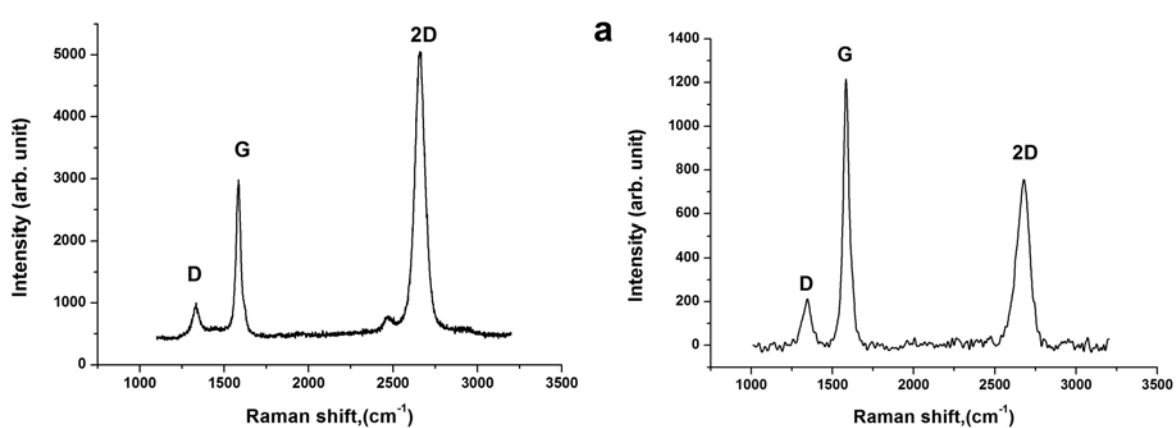


FIG. 4. Raman spectra collected from graphene films grown on 0 (a) and -5 kV (b) biased Ni films and transferred to $\text{SiO}_2/\text{Si}(100)$ substrates

is known that the 2D peak position exhibits an upshift with an increased number of graphene layers, and the fitting of the 2D peak with two or more Lorentzian peaks is a signature of multilayer graphene. The I_{2D}/I_G intensity ratio is smaller than one, which also is characteristic of multilayer graphene [15–17].

Raman spectra were collected from both types of graphene films over $2000 \mu\text{m}^2$ area. The I_{2D}/I_G values were then extracted from the spectra. Fig. 5 show the I_{2D}/I_G contour maps for graphene grown on 0 and -5 kV-biased Ni films (a and b, respectively), on an oxidized silicon substrate. Nearly 74% of Raman spectra collected from the graphene grown on 0 kV bias Ni films shows the hallmark of monolayer/bilayer graphene and about 25% indicates multi-layer graphene. Graphene films grown on -5 kV bias Ni films demonstrated only about 33% of monolayer/bilayer character, while 67% was multi-layer graphene. Thus, the graphene grown on Ni films with a bimodal grain size distribution and weaker (111) texture had higher thickness uniformity and lower number of graphene layers. Conversely, the graphene grown on Ni films with a monomodal grain size distribution and stronger (111) texture had lower thickness uniformity and a higher number of graphene layers.

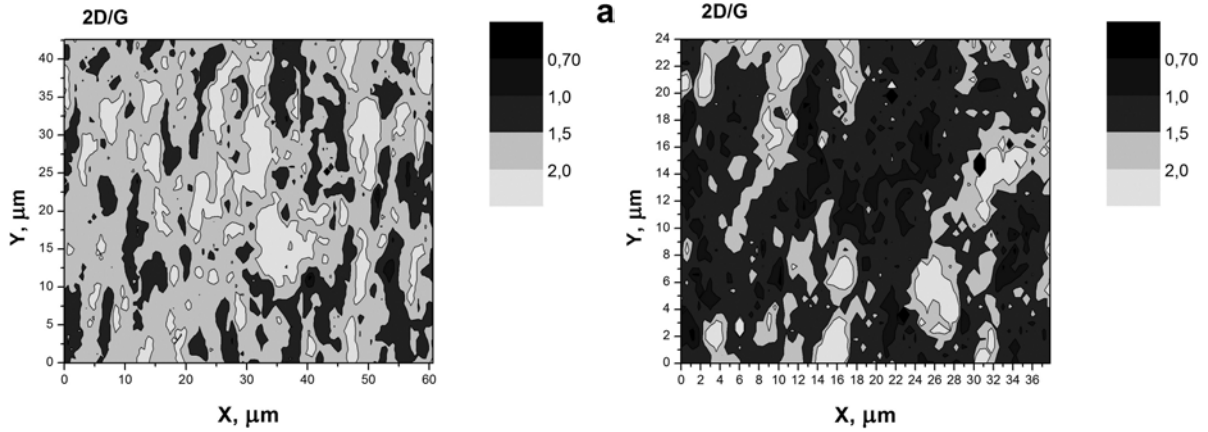


FIG. 5. I_{2D}/I_G contour maps of graphene grown on 0 (a) and -5 kV (b) biased Ni films and transferred to SiO_2/Si (100) substrates

The transport properties of Ni-supported graphene films deposited at 0 kV bias were investigated. The most direct and precise method to measure the mobility is the Hall measurement. The sheet resistance (R_s) of the graphene was measured at 900 Ohm/square from the four probe method. Subsequently, the Hall mobility is derived from:

$$\mu = \partial R_{xy} / \partial B / R_s, \quad (1)$$

where B is the magnetic field perpendicular to the Hall bar plane. The measurement was taken at 4.2 K and the Hall mobility was about $1200 \text{ cm}^2/\text{V}\cdot\text{s}$. Thus, the film had p-type conductivity. The carrier density was about $10^{13}/\text{cm}^2$, determined from:

$$n_{Hall} = 1/eR_{Hall}. \quad (2)$$

The relatively lower mobility of the graphene is attributed to the nonuniformity of the film quality and the poor adhesion with substrates, damages of the graphene during transfer to the target substrate, and the residual resist and impurities on the surface of the graphene.

4. Conclusion

Graphene films were synthesized by the low-pressure no flow CVD on polycrystalline nickel films. Ni films were deposited by the self-ion assisted deposition technique at 0 and -5 kV biases. 0 kV Ni films possessed bimodal grain size distribution and weaker (111) texture. The graphene grown on that films with a bi-modal grain size had higher thickness uniformity and predominately consisted of a mono- or bilayer film. Ni films deposited at -5 kV bias had smaller grain size and stronger (111) texture. The graphene grown on these films had lower thickness uniformity and a higher number of graphene layers.

References

- [1] Novoselov K.S., Geim A.K., et al. Two-dimensional gas of massless Dirac fermions in graphene. *Nature*, **438**, P. 197–200 (2005).
- [2] Katsnelson M.I., Novoselov K.S. Graphene: New bridge between condensed matter physics and quantum electrodynamics. *Solid State Commun.*, **143**, P. 3–13 (2007).
- [3] Meyer J.C., Geim A.K., et al. The structure of suspended graphene sheets. *Nature*, **446**, P. 60–63 (2007).
- [4] Schedin F., Geim A.K., et al. Detection of individual gas molecules adsorbed on graphene. *Nature Mater.*, **6**, P. 652–655 (2007).

- [5] Novoselov K. S., Geim A. K., et al. Electric Field Effect in Atomically Thin Carbon Films. *Science*, **306**, P. 666–669 (2004).
- [6] Zhang Y., Gomez L., et al. Comparison of Graphene Growth on Single-Crystalline and Polycrystalline Ni by Chemical Vapor Deposition. *J. Phys. Chem. Lett.*, **1**, P. 3101–3107 (2010).
- [7] Thiele S., Reina A., et al. Engineering polycrystalline Ni films to improve thickness uniformity of the chemical-vapor-deposition-grown graphene films. *Nanotechnology*, **21**, P. 015601 (2010).
- [8] Liu N., Fu L., et al. Universal Segregation Growth Approach to Wafer-Size Graphene from Non-Noble Metals. *Nano Lett.*, **11**, P. 297–303 (2011).
- [9] Reina A., Thiele S., et al. Growth of large-area single- and Bi-layer graphene by controlled carbon precipitation on polycrystalline Ni surfaces. *J. Nano Res.*, **2**, P. 509–516 (2009).
- [10] Kononenko O.V., Matveev V.N., et al. The effect of self-ion bombardment on the properties of thin metal films. *Vacuum*, **46**, P. 685–690 (1995).
- [11] Field D.P., Kononenko O.V., Matveev V.N. The microstructure of Cu films deposited by the self-ion assisted technique. *J. Electron. Mater.*, **31**, P. 40–44 (2002).
- [12] Adams B.L., Wright S.I., Kunze K. Orientation imaging: The emergence of a new microscopy. *Metall. Trans.*, **24A**, P. 819–831 (1993).
- [13] Krieger-Lassen N.C., Conradsen K., Juul-Jensen D. Image processing procedures for analysis of electron back scattering patterns. *Scanning Microscopy*, **6**, P. 115–121 (1992).
- [14] Ferrari A.C. Raman spectroscopy of graphene and graphite: Disorder, electron-phonon coupling, doping and nonadiabatic effects. *Solid State Commun.*, **143**, P. 47–57 (2007).
- [15] Gupta A., Chen G., et al. Raman Scattering from High-Frequency Phonons in Supported N-Graphene Layer Films. *Nano Lett.*, **6**, P. 2667–2673 (2006).
- [16] Ferrari A.C., Meyer J.C., et al. Raman Spectrum of Graphene and Graphene Layers. *Phys. Rev. Lett.*, **97**, P. 187401 (2006).
- [17] Cancado L.G., Reina A., Kong J., Dresselhaus M.S. Geometrical Approach for the Study of G' Band in the Raman Spectrum of Monolayer Graphene, Bilayer Graphene, and Bulk Graphite. *Phys. Rev. B*, **77**, P. 245408 (2008).

HIERARCHICALLY POROUS GRAPHENE IN NATURAL GRAPHITIC GLOBULES FROM SILICATE MAGMATIC ROCKS

V. A. Ponomarchuk^{1,2}, A. T. Titov^{1,2}, T. N. Moroz¹, A. N. Pyrayev¹, A. V. Ponomarchuk¹

¹Sobolev Institute of Geology and Mineralogy SB RAS, Novosibirsk, Russia

²Novosibirsk State University, Novosibirsk, Russia

ponomar@igm.nsc.ru, pyrayev@gmail.com

PACS 81.00.00 + 81.05.ue + 83.80.Nb

Naturally-occurring nanostructured graphites from silicate magmatic rocks, which are rare, were characterized using electron microscope and X-ray spectroscopy. This graphite consists of porous carbon, nanographite layers, micro- and nanotubes. The porous carbon is classified as macroporous matter with a small amount of mezopores. Evidence for the unusual properties of porous carbon are given: nanographite layers are created at the exposed surface of sample and the nanotubes occurs in the bulk of porous carbon.

Keywords: Porous carbon, Nature nanostructured graphite, Graphene, Microtubes, Nanotubes, Magmatic rock.

1. Introduction

Over the past 30 years the understanding about the properties of carbon has increased considerably, due to the study of fundamental physical and chemical properties of laboratory-produced synthetic nanomaterials. Thus, along with well-known allotropic forms of condensed carbon, allotropes with zero dimensionality (0-D) - fullerene [1], graphene (2-D-allotrope), micro- and nanotubes (1-D-allotrope) [2] have been discovered. It should be noted, relative to the last allotrope, that pioneer investigations of 1-D-structures were published in 1952 [3] by domestic (Russian) inventors. The publications mentioned above have attracted an enormous amount of attention from the scientific community, as expressed by an increased number of theoretical and experimental investigations, searching of nanotechnology-based solutions, synthetic methods for different carbon morphologies and organized assemblies of them. In addition, the emphasis for research of sp^2 -connected carbon nanostructures has changed direction over time, from fullerene followed by nanotubes to graphene and porous carbon. Porous carbon is used for battery electrodes, catalyst supports, supercapacitors, immobilization of biomolecules as well as adsorption agent of molecules in liquid phase, in water purification processes. The last usage is an old one, dating to 2000 B.C. in ancient Egypt at that [4]. However, the exclusive properties of porous carbon are not limited to the above-mentioned range of applications. In this paper, based on phenomenological data about natural graphite extracted from magmatic rock, we report here about porous carbon as a basic element that combines 1D and 2D nanostructures in 3D-superstructures.

The synthesis of sp^2 -hybridized carbon nano- and microstructures is carried out in both laboratory and industrial scale setups. Although numerous reviews [5, 6, 7, 8 et al.] display widely varying synthetic methods, all have a common conceptual design consisting of: heating (plasma, laser, microwaves, electric arc, thermal heating), carbon-bearing precursor

(methane, acetylene etc.), commonly presence of metal catalysts (Fe, Ni, Co etc.), relatively short experiment time (ranged between minutes and tens of hours) and severely controlled timing.

Generally, artificial synthesis of carbon nanostructures is carried out under low pressure conditions (less than atmospheric pressure). A few works [9] report details about high-pressure (500 MPa) synthesis of such carbon nanostructures. These facts indicate the wide range of acceptable pressures to form carbon nanostructures.

It is unlikely that all these “man-made” conditions are fulfilled in a natural environment. Single cases of sp^2 -hybridized carbon nano- and microstructures are detected in geological samples [10], thus confirming the partial appearance of the above-mentioned factors required for synthesis in combination with currently unknown “natural” nanotechnology specificities. Identifying of these specificities is a very important problem and a solution to this problem demanded primarily investigation of natural sp^2 -hybridized carbon structures (microtubes, porous carbon, graphene and nanographite layers) and combinations thereof.

2. Materials and methods

The exotic needle-shaped form of graphite was first discovered and described in the graphite-palagonit globular leukogabbro of Verhnetalnahskaya stratified trap intrusions in the Siberian platform [11]. The amount of graphite in leukogabbro reaches 3-5%. Graphite occurs in the form of globules in rock. The size of the globules varies from 0.5 mm to 1.5–2 cm. Under the microscope, small globules have the shape of a sphere or an ellipsoid, while large globules have an amoeba-shaped form. The morphology of globules is determined by the fringe of dense graphite on its periphery. The outer surface of each globule is smooth, while the interior has brush needle-like crystals of graphite. In the central parts of multi-layer graphite globules, needle accretions of graphite in the form of a sea urchin are found. Mesostasis in the graphite globules is presented by palagonite, amphibole, clinopyroxene, ilmenite and apatite. This paper presents data on the morphological features of natural carbon aggregation and micro- and nano-carbon structures.

In order to investigate in detail the morphology, texture and structure of graphite particles, they were separated from a silicate rock by numerous “soft” decomposition of samples in hydrofluoric acid followed by hand sampling and an additional chemical purification process. Initially, graphite particles remain in rocks until, under stressed conditions, they are removed by rock decomposition. The graphite materials under investigation, therefore, occur as individual fragments.

The obtained samples were characterized using the following: optical microscope, scanning electron microscopy TSCAN and X-ray microprobe analysis with the energy (EDX) and wave (WDX) dispersion (LEO1430VP equipped with EDX OXFORD and MEBAX-micro), Jobin Ivon Raman spectrometer T6400 (excitation radiation $\lambda = 514.5$ nm, Ar+laser) equipped with optical microscope and Finnigan MAT-253 mass spectrometer equipped with Elemental Analyser EA 1112 and GasBench II (the precision is $\pm 0.2\%$).

3. The structure and morphology of nanostructured assembly

The series of scan-images (figures below) make possible the detailed study of the structure, texture and morphology of the inner and outer parts of different graphite particle fragments of graphite particles. Graphite particles characterized by 3D-regularity are composites consisting of elementary nanostructures: nano- and microtubes (1D-regularity), nanographite layers (2D-regularity) and porous carbon. These structures have a certain order with regards to each other as shown in scan-image of globule (fig. 1A and 1B).

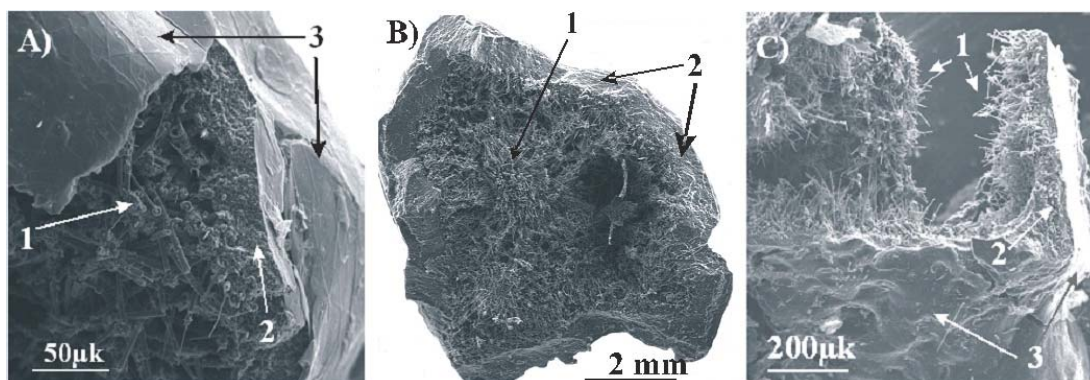


FIG. 1. Scan-image of nature nanostructured graphite fragments: A) – globule, B) – crust, C) fragment of nanostructured graphite. Symbolic notations: **1** – micro- and nanotubes; **2** – porous carbon; **3** – wrinkle nanographite layer

Outer surface (**3**), an organized nanographite layer, is the boundary surface between a rock and graphite particle. The surface morphologies of the graphite formations under investigation here are given in detail in [12]. Here, it should be noted that the cleavage (“wrinkle”) character of a particle surface is usually explained by a difference in the thermal expansion coefficients of nanographite and the carrier rock.

There is a contact between nanographite layer and porous carbon in the inner part (**2**). Micro- and nanotubes “grow out” of porous carbon, as shown in fig. 1A and 1B. This is a typical phenomenon in studied natural nanostructured graphites. The series of scan-images (figure 2) illustrate graphite particle portions- porous carbon - micro- and nanotubes and makes their relationship more clear. Figure 2A exhibits a scan-image of a planar graphite particle covered by a micro- and nanotubes “forest” on the one side (about 500 tubes per square mm) and nanographite layer on the other side (not shown in the figure). Porous carbon is situated between the microtube base and nanographite layer. The appearance of a secondary nanographite layer (**3**), situated over micro- and nanotubes, is a feature of this sample. On the basis of microscopic observations, it may be concluded that this layer was extended along the full surface of planar structure, but only a part of it remains after sample preparation procedures.

Radial structures **4** (fig. 2A), composed of small porous carbon round sectors and radially extended multilayer nano- and microtubes (fig. 2B) attract special interest. The existence of such structural combinations indicated a feature of “natural” nanotechnology not previously mentioned in the literature relating to the laboratory synthesis of nanostructures, as far as we know. Structural binding of porous carbon and nano- and microtubes is an important element of the natural nano- and microtube formation model.

There are cylindrical hollow tubes **5** (fig. 2B) in the central part of porous carbon round islands (**4**, fig. 2A). It should be mentioned that hollow tubes with diameters varying from units to tens of microns were observed in porous carbon layers of natural nanostructured graphite. This can be considered as fluid and solution conductors [12, 13]. The walls of the hollow tubes are nanographite layers **7** (fig. 3A). The formation of fluid-conducting tubes with nanographite incrustation in porous carbon is an unusual fact that undoubtedly attracts the attention of nanotechnology investigators because of the realization of a graphene synthetic method different from previously known techniques [14].

The data described above exhibit quite a constructive role for porous carbon, due to its properties in naturally nanostructured graphite formation process. The properties of

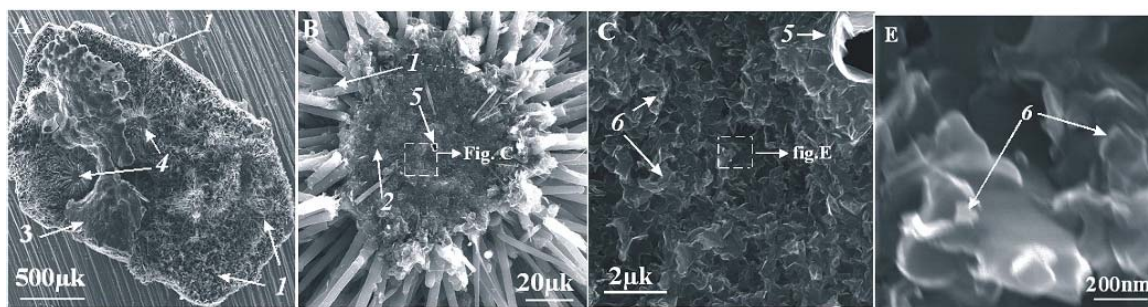


FIG. 2. Scan-image of flat nanostructured graphite fragment. A – overview; B – fluid-conducting canal within the frame of the porous graphite and radially expanded micro- and nanotubes; C – porous graphite surface - multiplied image of square dashed line sector of fig. 2B; E – porous graphite surface - multiplied image of square dashed line sector of fig. 2C. Symbolic notations: (1, 2, 3 - look at fig. 1), 4 – porous carbon round islands, 5 – fluid-conducting cylindrical hollow tube, 6 – fragments of nanographite layers

porous carbon can be partially revealed from the scan-images series shown in fig. 2B, 2C and 2E. It is obvious that porous carbon consists of numerous disorderly linked wrinkle fragments of nanographite layers. There is a strong linking between fragments of nanographite layers plane and nanographite sheet borders due to their chemical activity. It is impossible to estimate the pore size of samples under investigation quantitatively, but it is possible using visual evaluation of fig. 2C and 2E to distinguish sufficiently large pores (around 50 nm) that are attributed to the porous and macroporous (i.e. multimodal) materials, according to supposition of Dubinin [15], which was subsequently accepted by IUPAC [16].

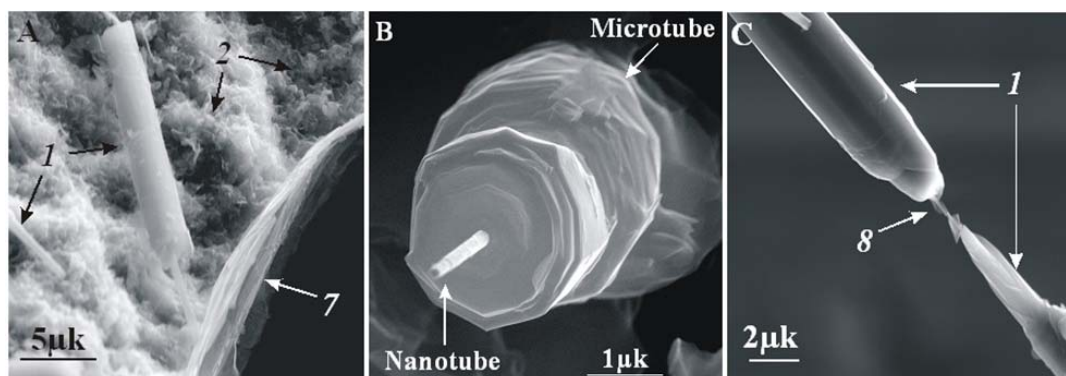


FIG. 3. A – scan-image of complex combination of the fluid-conducting canal, porous carbon, micro- and nanotube and wall of fluid-conducting canal composed of nanographite layer; B – nanotube wrapped in microtube; C – microtubes linked by nanotube. The microtube helix is due to chirality

Along with porous carbon, an easily-discernible nanotube with diameter of about 100 nm or less wrapped in a segment of microtube is shown in fig. 3A. The nanotube is located along the axis line of microtube. Such a complex combination of micro- and nanotubes is the most that natural specimens feature as may be seen in the numerous scan-images. There are three interesting features in this picture: 1 – microtubes (with the diameter more than 100 nm) were more subject to destruction than nanotubes. This point can be explained by the expanded linear size of nanotubes in comparison with microtubes

that are illustrated by fig. 3B and 3C. The stated interpretation is in accordance with the nano-physical data: strength increases with decreasing linear size; 2 – the 100 nm limit, in this case, is a natural border for the 1-dimensional carbon structure, mechanical properties exchange, as well as an amazing border that divides the nano-world from the micro-world [17]; 3 – there is a difference between the nano- and microtube interaction with porous carbon, as is clearly shown in fig. 2B. The base of the microtubes only contact the porous carbon, while nanotubes penetrate into the porous carbon. In spite of the morphological unity of micro- and nanotubes, the last point indicates that there are different formation mechanisms for each of these structures.

The formation of nanotubes is quite acceptably explained by a vapor–liquid–solid (VLS) mechanism [18]. The main points of VLS-mechanism are the decomposition of carbon-bearing phase in the raw material, diffusion of elemental carbon to metallic catalyst, saturation of the catalyst surface by carbon and structurization of nanotube. The component composition of nanostructured graphite was investigated using EDC and SR XRF [13]. It exhibits a relatively high content of Fe in carbon matrix, reaching 2 wt. %. The SR XRF data showed the presence of platinum (~ 10 ppm) in studied nanostructured graphites, as well as the Fe catalyst of the VLS-mechanism and is able to initiate nanotube formation. Subsequent increasing of the nanotube radius may be conceptually explained by another mechanism: carbon deposition according to vapor-grown carbon fibers (VGCF) model [19]. Many of the process details for this model must be specified. In order to understand the mechanism of porous carbon formation, additional investigations are necessary.

In addition to electron microscopy and elemental analysis, the natural nanostructured graphite was characterized by Raman spectroscopy. This widely-applicable method has been used recently to characterize graphite formations (including different nanostructures such as nanographite ribbons, carbon nanotubes and fullerenes [20]). It should be noted that since this is a non-destructive analysis, the same specimen may be used in subsequent analyses. Moreover, it is even possible to estimate the temperature of graphite formation in geological objects using Raman spectroscopy [21].

The recording of the signal was conducted using a multi-channel detector with backscattering geometry and an unconditioned orientation of the sample. Figure 4 shows examples of typical Raman spectra for observable nanostructured graphites. There are three significant peaks in these spectra. The Raman peak at 1580 cm^{-1} , referred to first order spectrum, is specified by a one-background process of Raman dispersion and is due to a doubly-degenerate symmetry component E_{2g} of the Brillouin zone. This band is always present in graphite spectra and marked as G . Simultaneously, it should be noted that this band is typical in all spectra of sp^2 -hybridized carbon compounds.

The Raman band at 1352 cm^{-1} , marked in fig. 4 as D_1 , is usually explained by the presence of defects in the sample, and in the case of grapheme, by boundary defects, such as ragged carbon bonds. While the D_1 peak is quite intense there is a low intensity peak D_2 , appearing at the long wavelength end of peak G . Substantially, peak D_2 should be considered as a “shoulder” of the G peak. The spectra of highly-oriented pyrolytic graphite (HOPG) exhibit a low intensity of peak D_1 in comparison with peak G . This is considered as a criterion of significant graphite crystallite grain size. The table demonstrates relations $R_1 = D_1/G$ of the investigated graphites. The R_1 values range from 0.02 to 0.2, seemingly indicating a high level of graphite crystallinity.

In order to quantitatively evaluate the degree of crystallinity for carbonaceous matter using Raman spectra data, the formalism depicted in [21] was used. Calculation were performed using the relation $R_2 = I_{D1}/(I_G + I_{D1} + I_{D2})$, where I_G , I_{D1} and I_{D2} — are squares

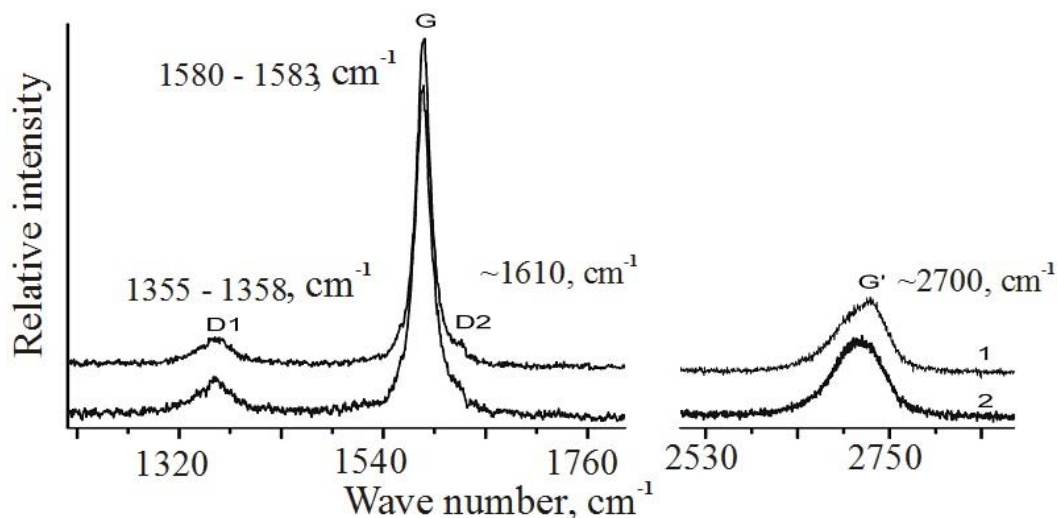


FIG. 4. Raman spectra of nature nanostructured graphites

TABLE 1. Raman spectra parameters of nanostructured graphites from magmatic rocks

	R_2	R_1	Peak position D_1 (cm^{-1})	Peak D_1 width (cm^{-1})	Peak position G (cm^{-1})	Peak G width (cm^{-1})	Crystallite size L_a (\AA)
nt1	0.0408	0.024	1359.8	26.9	1583.0	15.29	~ 2000
nt2	0.1916	0.08	1358.3	53.1	1583.1	17.77	~ 230
nt3	0.2385	0.107	1357.0	66.4	1582.3	20.32	129
nt4	0.3069	0.186	1355.6	64.9	1580.2	24.51	96

of G -, D_1 - and D_2 -peaks accordingly. The table presents that as R_2 increases, the full width at half-height for the D_1 and G peaks increase, as well as the in-plane crystallite size L_a . It is notable that the least defective sample with minimal R_1 value had a significant crystallite size that may be found in HOPG graphites [22]. There is a peak at 2700 cm^{-1} in the short-wave end of the Raman spectrum for the sample. In the case of Bernal's packing and low number of layers (less than 10), the parameters for this peak (position, intensity, peak form) are currently widely used in the characterization of nanostructured carbon as well as in the estimation for the number of graphene layers. This peak in the upper spectrum of fig. 4 is not symmetrical and it is similar in form to graphite. The bottom spectrum, on the basis of numerous publications, apparently demonstrates the occurrence of a significant number of nanographite layers in a sample (more than 10). The temperatures for graphite globules formation, calculated using a previously-reported method [21], indicated a range from 470 to 700°C . Moreover, geological data allows one to estimate the pressure of formation for graphite globules (about 100 – 200 MPa), which is less than the formation pressures for artificial carbon nanostructures [9].

4. Conclusion

The results presented in this paper demonstrate that 3D-graphite formation occurs under exclusive geological conditions. These unique structures consist of porous carbon and sp^2 -like hybridized carbon nanostructures (micro- and nanotubes). The porous carbon is the

key structure of nanostructured graphite because: 1 - nanographite layer formation occurs at the surface of the porous carbon; 2 - nanotube formation occurs within the porous carbon.

References

- [1] H.W. Kroto, J.R. Heath, S.C. O'Brien, R.F. Curl, R.E. Smalley. C60: Buckminsterfullerene. *Nature*, **318**, P. 162 (1985).
- [2] S. Iijima. Helical microtubules of graphitic carbon. *Nature*, **354**, P. 56–58 (1991).
- [3] L.V. Radushkevich, V.M. Lukyanovich. The structure of carbon formed by thermal decomposition of carbon oxide on an iron contact. *Journal of Physical Chemistry*, **26**, P. 88–95 (1952).
- [4] S.M. Manocha. Porous carbons. *Sadhana*, **28**, P. 335–348 (2003).
- [5] M. Paradise, T. Goswami. Carbon nanotubes – Production and industrial applications. *Materials and Design*, **28**, P. 1477–1489 (2007).
- [6] Yu.E. Lozovik, A.M. Popov. Formation and growth of carbon nanostructures: fullerenes, nanoparticles, nanotubes and cones. *Phys. Usp*, **40**, P. 717–737 (1997).
- [7] A.V. Eletskii. Carbon nanotubes. *Phys. Usp*, **40**, P. 899–924 (1997).
- [8] G.D. Nessim. Properties, synthesis, and growth mechanisms of carbon nanotubes with special focus on thermal chemical vapor deposition. *Nanoscale*, **2**, P. 1306–1323 (2010).
- [9] S.K. Simakov, A.A. Grafchikov, A.K. Sirotkin, I.A. Drozdova, E.A. Grebenshchikova, A.E. Lapshin. Synthesis of carbon nanotubes and fullerite structures at PT parameters corresponding to natural mineral formation. *Doklady Earth Sciences*, **376**, P. 87–89 (2001).
- [10] J.A. Jaszczak, S. Dimovski, S.A. Hackney. Micro- and nano-scale graphite cones and tubes from Hackman Valley, Kola Peninsula, Russia. *Canad. Mineralogist*, **45**, P. 379–389 (2007).
- [11] V.V. Ryabov, A.J. Shevko, M.P. Gore. *Magmatic formations of Norilsk region. Petrology of the traps. Atlas of igneous rocks*. Nonpareil, Novosibirsk, 408 p. (2000).
- [12] V.V. Ryabov, V.A. Ponomarchuk, A.T. Titov, D.V. Semenova. Micro- and Nanostructures of Carbon in Pt–Low-Sulfide Ores of the Talnakh Deposit (Siberian Platform). *Doklady Earth Sciences*, **446**(2), P. 1193–1196 (2012).
- [13] V.A. Ponomarchuk, Y.P. Kolmogorov, V.V. Ryabov, A.T. Titov, T.N. Moroz, D.V. Semenova, A.N. Pyryaev, A.V. Ponomarchuk. SR XRF Study of Natural Micro- and Nanostructured Carbon from Igneous Rocks. *Bulletin of the Russian Academy of Sciences. Physics*, **77**(2), P. 203–206 (2013).
- [14] M.J. Allen, V.C. Tung, R.B. Kaner. Honeycomb Carbon: A Review of Graphene. *Chem. Rev.*, **110**(1), P. 132–145 (2010).
- [15] M.M. Dubinin. The potential theory of adsorption of gases and vapors for adsorbents with energetically nonuniform surfaces. *Chem Rev.*, **60**, P. 235–241 (1960).
- [16] IUPAC Manual of Symbols and Terminology, Appendix 2, Pt. 1, Colloid and Surface Chemistry. *Pure Appl. Chem.*, **31**, P. 578 (1972).
- [17] H. Gleiter. Nanostructured materials: basic concepts and microstructure. *Acta Materialia*, **48**(1), P. 1–29 (2000).
- [18] R.T.K. Baker. Catalytic growth of carbon filaments. *Carbon*, **27**, P. 315–323 (1989).
- [19] V.Z. Mordkovich. Carbon Nanofibers: A New Ultrahigh-Strength Material for Chemical Technology. *Theoretical Foundations of Chemical Engineering*, **37**(5), P. 429–438 (2003).
- [20] M.A. Pimenta, G. Dresselhaus, M.S. Dresselhaus, L.G. Cancado, A. Jorio, R. Saito. Studying disorder in graphite-based systems by Raman spectroscopy. *Phys.Chem.Chem.Phys.*, **9**, P. 1276–1291 (2007).
- [21] O. Beyssac, B. Goffe, C. Chopin, J.N. Rouzaud. Raman spectra of carbonaceous material in metasediments: a new geothermometer. *J. metamorphic Geol.*, **20**, P. 859–871 (2002).
- [22] S.S. Bukalov, L.A. Mikhalecin, Ya.V. Zubavichus, L.A. Leytis, U.N. Novikov. Structure investigation of graphites and some another sp² carbonic materials using micro-, Raman spectroscopy and X-ray diffraction methods. *Ros. Chem. J.*, **L**(1), P. 83–91 (2006).

THE INFLUENCE OF THE AMBIENT CONDITIONS ON THE ELECTRICAL RESISTANCE OF GRAPHENE-LIKE FILMS

D. M. Sedlovets, A. N. Redkin

Institute of Microelectronics Technology and High-purity Materials,
Russian Academy of Science, Chernogolovka, Russia
sedlovets@iptm.ru, arcadii@iptm.ru

PACS 81.05.ue

Since the discovery of graphene, researchers are not only interested in monatomic layers of carbon, but also in multilayered graphene structures named graphene-like films, which can be used, for example, as sensors. An understanding of the relationship between the growth conditions and the ability of the films to respond to certain gases, the ability to obtain films with desired properties and the ability to operate their sensor properties at the synthesis stage – are all of utmost scientific interest. In our study, we considered these issues. Synthetic conditions are not the only factors that affect the properties of the graphene-like films. In this work, we show that the electrical resistance also depends upon ambient conditions. Depending on the gas present in the environment, the resistance of the films can be changed. It follows from these results that we obtained carbon films possessing a selective sensitivity to ethanol vapor.

Keywords: Carbon films, Gas sensors, Graphene, Synthesis, Electrical properties.

1. Introduction

Since the discovery of graphene, the attention of many scientists has been focused on the study of this unique material. However, researchers are not only interested in the monatomic layer of carbon, but also in multilayered graphene structures, named graphene-like films and used, for example, as sensors. Graphene-based sensors, described in the literature, work on various principles: like field-effect transistors [1,2], surface acoustic waves [3,4], quartz crystal microbalances [5], micro electromechanical systems [6,7], conventional semiconducting metal oxides combined with graphene [8,9]. However, most of the reported gas/vapor sensors mainly operate in the resistive mode [10–12]. This sort of sensor is easy to fabricate and provides the possibility of direct measurement. Because the method of fabrication is based on a change in the electrical conductivity of the material during the interactions with gases, to understand the effect of different factors on the electrical resistance of such films is of great practical value. However, to understand the relationship between the growth conditions and the ability of films to respond to certain gases, and thus to obtain means to fabricate films of desired properties and to control their sensor properties at the synthesis stage – are of utmost scientific interest. These issues were the object of our study.

Earlier, we reported the method of obtaining graphene-like films by pyrolysis of ethanol vapor. This is a simple, low-cost and scalable approach, which excludes the use of flammable gases. At high temperatures (900 – 1000 °C), the pyrolysis of ethanol allows one to obtain carbon films not only on a catalytic metal surface, but also on dielectric substrates. It was found that the final properties of samples can be controlled by changing the growth conditions: for example, the sheet resistance decreased with increasing reaction temperature, while an increase in the synthesis duration led to a reduction of the sheet resistance [13].

TABLE 1. Sensitivities to some gases of the samples obtained at various synthesis temperatures on different substrates

	CH₄	C₂H₄	H₂	C₂H₅OH	i-C₃H₇OH
1000 °C (Cu)	0.13 %	–	–	2.75 %	0.16 %
900 °C (Cu)	–	–	–	2.11 %	0.75 %
800 °C (Cu)	–	–	–	0.72 %	0.94 %
1000 °C (quartz)	0.01 %	0.06 %	-	3.25 %	0.05 %
900 °C (quartz)	0.03 %	0.08 %	1.3 %	13.7 %	2.1 %

Reaction conditions are not only the factors affecting the properties of the graphene-like films. In this work, we show that ambient conditions can influence a film's electrical resistance. Depending on the gas present in the environment, the resistance of the films can vary. This fact led us to test these films as sensors.

2. Experimental technique

The experimental setup consisted of an airtight quartz vessel connected to a controlled gas flow system, and a rigidly fixed sample coupled with a measuring device. The gases used were: hydrogen, carbon monoxide, methane, ethylene as well as ethanol and isopropanol vapors. In the last case, the airflow was bubbled through the liquid reagent so that the concentrations of ethanol and isopropanol vapors were about 2 and 1.5 percent by volume, respectively. The resistance was measured directly between two contacts positioned on top of the sensing graphene films. For this purpose, two copper strips were deposited by vacuum evaporation.

The procedure was as follows: previously the vessel was ventilated with a certain gas for 1 hour to establish stationary conditions. Thus, the concentration of gases, except ethanol and isopropanol vapors, was 100%. A sample was quickly placed in the vessel and a change in the sensor resistance with exposure to the interacting gas/vapor was studied (sensitivity and response time were measured directly). Then, the sample was quickly taken out in air and a recovery time was registered.

The samples used in the experiments as sensors were obtained by pyrolysis of ethanol under the following conditions: reaction temperature was varied from 800 – 1000 °C, quartz and metal foil were used as substrates.

3. Results and discussion

It was determined experimentally that there was no film response upon exposure to carbon monoxide. Sensitivities of the samples obtained at various reaction temperatures on different substrates to other gases are given in Table 1. These values were estimated as changes in the materials resistance upon interaction with different gases, using the equation (1).

$$\text{Sensitivity} = (R_{\max} - R_0)/R_0, \quad (1)$$

where R_{\max} and R_0 – maximum resistance of the response and initial resistance, respectively.

The sensitivity values were negligible (about 1% or much less) for all gases except ethanol vapor. So, we can assume that our sensors exhibit a high selectivity for ethanol vapor. The result is of great practical value, because a lot of sensors usually respond to a number of different gases. A better chemical affinity can be achieved by functionalization of

graphene [14,15]. Because films obtained by pyrolysis of ethanol vapor contain carboxyl groups on the surface [16], the good chemical selectivity of our sensors is evidently due to this fact.

The efficiency of graphene sensors was recently found to be improved by increasing their surface area [17]. In our case, this is easy to achieve, because the size of the films we obtained is only limited by the size of the reactor. Furthermore, with our technique, thin carbon films can be directly grown onto almost any dielectric substrate (as long as it can be heated up to the growth temperature and not subjected to strong thermal expansion). Generally, films formed on quartz substrates possess a higher sensitivity than structures obtained on copper foil. Perhaps this can be explained by the inevitable damage of the films during transfer.

Figure 1 shows changes in response for the last sample towards a mixture of C_2H_5OH vapor with air. The response time was determined to be 10 minutes. As follows from the insert in Fig. 1, the sensor possesses good recover ability.

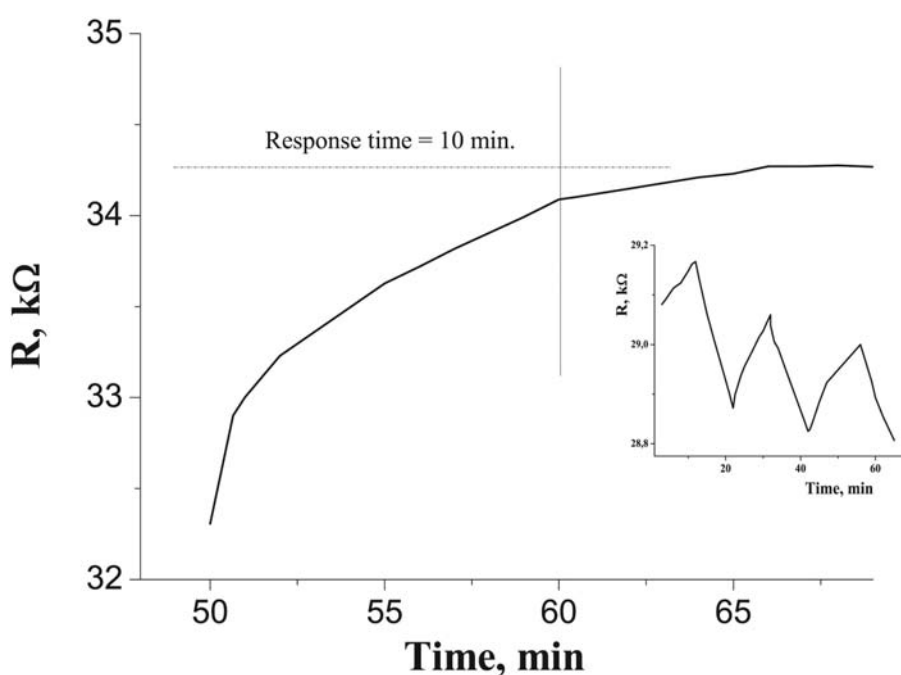


FIG. 1. The time response of the electrical resistance R to the exposure to ethanol vapor for the sample obtained at $900\text{ }^{\circ}\text{C}$ on a quartz substrate. Insert: dynamic changes in response of the sensor during an “in/out” cycle (one step of cycle = 10 min)

4. Conclusions

We show that a relationship exists between the growth conditions and the ability of films to respond to certain gases. But the synthetic conditions are not the only factor influencing the properties of graphene-like films. Their electrical resistance also depends on the ambient conditions. Selective sensitivity of different samples to some gases of various concentrations was studied. The obtained results suggest that the proposed method is highly promising for obtaining carbon films, which possess a selective sensitivity to ethanol vapor.

A more detailed study of the sensor characteristics (including a detection limit) of the films in relation with their synthesis conditions will be the subject of future investigations.

Acknowledgments

This work was supported by the Russian Foundation for Basic Research (project No. 11-02-00498a).

References

- [1] Kim C.H., Yoo S.W., et al. Effect of temperature and humidity on NO₂ and NH₃ gas sensitivity of bottom-gate graphene FETs prepared by ICP-CVD. *IEEE Electron Dev. Lett.*, **99**, P. 1–3 (2012).
- [2] Rumyantsev S., Liu G., et al. Selective gas sensing with a single pristine graphene transistor. *Nano Lett.*, **12**, P. 2294–2298 (2012).
- [3] Arsat R., Breedon M., et al. Graphene-like nano-sheets for surface acoustic wave gas sensor application. *Chem. Phys. Lett.*, **467**, P. 344–347 (2009).
- [4] Arash B., Wang Q., Duan W.H. Detection of gas atoms via vibration of graphenes. *Phys. Lett. A*, **375**, P. 2411–2415 (2011).
- [5] Yao Y., Chen X., Guo H., Wu Z. Graphene oxide thin film coated quartz crystal microbalance for humidity detection. *Appl. Surf. Sci.*, **257**, P. 7778–7782 (2011).
- [6] Micro-Hotplate by CMOS Technology with Applications for Sensors, In Situ Processing, and Process Monitoring, Nov. 7, 1995, US patent No. 5,464,966.
- [7] Semancik S., Cavicchi R.E., Gaitan M., Suehle J.S. Temperature-controlled, micromachined arrays for chemical sensor fabrication and operation. US Patent, US 5345213 A (1994).
- [8] Singh G., Choudhary A., et al. ZnO decorated luminescent graphene as a potential gas sensor at room temperature. *Carbon*, **50**, P. 385–394 (2012).
- [9] Yi J., Lee J.M., Park W. Vertically aligned ZnO nanorods and graphene hybrid architectures for high-sensitive flexible gas sensors. *Sensors and Actuators B*, **155**, P. 264–269 (2011).
- [10] Massera E., Ferrara V.L., et al. Gas sensors based on graphene. *Chemistry Today*, **29**, P. 39–41 (2011).
- [11] Schedin F., Geim A.K., et al. Detection of individual gas molecules adsorbed on graphene. *Nature Mater.*, **6**, P. 652–655 (2007).
- [12] Fowler J.D., Allen M.J., et al. Practical chemical sensors from chemically derived graphene. *ACS Nano*, **3**, P. 301–306 (2009).
- [13] Sedlovets D.M., Redkin A.N., Korepanov V.I., Trofimov O.V. Electrical Conductivity and Optical Properties of Thin Carbon Films Grown from Ethanol Vapor. *Inorg. Mater.*, **48** (1), P. 34–39 (2012).
- [14] Singh V., Joung D., et al. Graphene based materials: past, present and future. *Progr. Mater. Sci.*, **56**, P. 1178–1271 (2011).
- [15] Gomez De Arco L., Zhang Y., et al. Continuous, highly flexible, and transparent graphene films by chemical vapor deposition for organic photovoltaics. *ACS Nano*, **4**, P. 2865–2873 (2010).
- [16] Paul R.K., Badhulika S., et al. The Production of Oxygenated Polycrystalline Graphene by One-Step Ethanol Chemical Vapor Deposition. *Carbon*, **49**, P. 3789–3795 (2011).
- [17] Hill E.W., Vijayaraghavan A., Novoselov K. Graphene sensors. *IEEE Sensors J.*, **11**, P. 3161–3170 (2011).

TOPOLOGICAL MECHANOCHEMISTRY OF GRAPHENE

E. F. Sheka, V. A. Popova, N. A. Popova

Peoples' Friendship University of Russia,
117302 Moscow, Miklukho-Maklay str. 6, Russia

sheka@icp.ac.ru

PACS 31.1+z; 81.05.Uw; 81.40.Lm; 31.15.Ct; 82.20.Wt

The current paper describes the effects caused by uniaxial tension of a graphene molecule in the course of the mechanochemical reaction. Basing on the molecular theory of graphene, the effects are attributed to both mechanical loading and chemical modification of the edge atoms of the molecule. The mechanical behavior is shown to be not only highly anisotropic with respect to the direction of the load application, but greatly dependent on the chemical modification of the molecule edge atoms, thus revealing the topological character of the graphene deformation.

Keywords: graphene, molecular theory, electron correlation, mechanochemical reaction; chemical modification; strength characteristics, Young's moduli.

1. Introduction

Topochemical reactions have been studied since the nineteenth century (see [1] and references therein). The first stage of the study was completed in the late 1920's [2] and then, a renewed interest in them appeared after the 1970 publication of the Woodward and Hoffmann monograph devoted to the conservation of orbital symmetry [3]. Since then, topochemical reactions have become an inherent part of not only organic, but inorganic chemistry, as well. Readers interested in this topic are referred to a set of comprehensive reviews [1, 4-7]. The current state of the art in this field can be exemplified by the direct structural understanding of the topochemical solid state photopolymerization reaction [8].

Currently, we are witnessing the next pulse, stimulating investigations in the field, which should be attributed to the appearance of a new class of spatially extended molecular materials, such as sp^2 hybridized carbon nanostructures. Obviously, the main members of the class such as fullerenes, nanotubes, and numerous graphene-based species are absolutely different from a formal topology viewpoint. Thus, fullerenes exist in the form of a hollow sphere, ellipsoid, or tube consisting of differently packed benzenoid units. Carbon nanotubes are present predominantly in cylindrically packed units. In graphene, the benzenoid units form one-atom-thick planar honeycomb structure. If we address the common terms of the formal topology, namely, connectivity and adjacency, we have to intuitively accept their different amounts in the three species listed above. In turn, the connectivity and adjacency determine the 'quality' of the C-C bond structure of these species, thus, differentiating them by this mark. Since non-saturated C-C bonds are the main target for chemical reactions of any type, one must assume that identical reactions, involving the bonds, will occur differently for different sp^2 -hybridized carbon-based nanostructures. Therefore, one may conclude that the spatially extended sp^2 -hybridized carbon-based nanostructures present not only peculiar structural chemicals, but a class of species for which the formal and empirical topologies

overlap. For the first time, results, presented in [9, 10], have revealed this tight interconnection in terms of molecular quantum theory. Not only fullerenes, but carbon nanotubes and graphene (their fragments) have been considered at the molecular level. The obtained results are related to the computational study of the intermolecular interaction between fullerene C_{60} and one of the other addends, among which there are both sp^2 -hybridized carbon nanostructures and monoatomic species. The intermolecular interaction lays the foundation of any reaction so that its topological peculiarities may evidence a topochemical character of the reaction being studied. However, since the ‘quality’ of the C-C bonds is the most sensitive point of the inherent topology of the sp^2 -hybridized carbons, external actions, such as mechanical deformation, on the bonds should obviously result in particular topological effects that accompany the relevant intramolecular reactions. The current paper is devoted to the discussion of such reactions that are represented by the mechanochemical one related to the uniaxial tension of a graphene molecule.

2. Uniaxial tension of graphene as a mechanochemical reaction

Below we will consider a particular topological effect caused by the influence of both the loading direction and the graphene molecule edge termination on the inherited topology of the molecule. Graphene deformation, under external mechanical loading, is extremely sensitive to the state of the edge atoms and makes it possible to disclose the topological nature of this sensitivity.

Recently, a new approach has been suggested to describe graphene deformation, based on considering the failure and rupture process of graphene as the result of a mechanochemical reaction [11-14]. A similarity between the mechanically induced reaction and the initial chemical ones, first pointed out by Tobolski and Eyring seventy years ago [15], suggested the use of a well developed quantum-chemical approach of the reaction coordinate [16] in the study of atomic structure transformation under deformation. First applied to the deformation of poly(dimethylsiloxane) oligomers [17], the approach has revealed a high efficacy in exhibiting elastic, plastic, and superplastic regions of the oligomer uniaxial tension, disclosing the mechanism of its failure and rupture. This has been successfully applied recently for the description of the uniaxial tension of both graphene [11, 12] and graphane [13] molecules, thus positioning itself as a significant part of the molecular theory of graphene [18].

The main point of the approach concerns reaction coordinate definition. When dealing with chemical reactions, the coordinate is usually selected among internal ones (valence bond, bond angle or torsion angle) or is presented as a linear combination of the latter. Similarly, mechanochemical internal coordinates (MICs) are introduced as modified internal coordinates, defined in such a way as to be able to specify the considered deformational modes [17, 19]. Thus, uniaxial tension and contraction are described by linear MICs similar to valence bonds. In the case of tensile deformation, the benzenoid pattern of graphene sheets and a regular packing of the units predetermined the choice of either parallel or normal MICs orientation with respect to the chain of C-C bonds. In rectangular nanographene sheets and nanoribbons, the former orientation corresponds to tensile deformation applied to the zigzag edges (*zigzag* mode) while the latter is attributed to the armchair edges (*armchair* mode). The MIC configurations of the two tensile modes of the (5,5) nanographene (NGr) molecule are presented in Fig.1. The molecule lays the foundation for previously performed computational experiments [11-14] and presents a rectangular fragment of a graphene sheet that is cut along zigzag and armchair edges and contains 5 benzenoid units along each direction. The deformation proceeds as a stepwise elongation of the MICs with increments of $\delta L=0.1\text{\AA}$, so that the current MIC length constitutes $L = L_0 + n\delta L$, where L_0 is the initial

length of the MIC and n counts the number of the deformation steps. The right ends of all the MICs are fixed so that these dark colored atoms are immobilized while the atoms on the left ends of MICs move along the arrows providing the MIC successive elongation, once excluded from the optimization, as well. The relevant response force is calculated as the energy gradient along the MIC, while the atomic configuration is optimized over all of the other coordinates under the MIC constant-pitch elongation. The results presented in the paper were obtained in the framework of the Hartree-Fock unrestricted (UHF) version of the DYQUAMECH codes [20] exploiting advanced semiempirical QCh methods (PM3 version [21]).

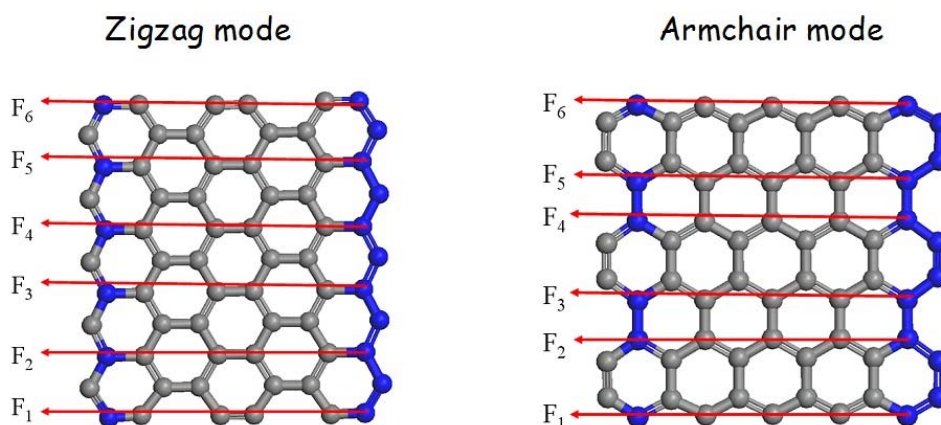


FIG. 1. Six mechanochemical internal coordinates of uniaxial tension of the (5,5) NGr molecule for two deformation modes. $F_1, F_2, F_3, F_4, F_5, F_6$ are forces of response along these coordinates. Dark atoms fix the coordinates ends

The corresponding forces of response F_i applied along the i^{th} MICs are the first derivatives of the total energy $E(R)$ over the Cartesian coordinates [17]. When the force calculation is completed, the gradients are re-determined in the system of internal coordinates in order to proceed further in seeking the total energy minimum by the atomic structure optimization. Forces F_i are used afterwards for determining all the required micro-macroscopic mechanical characteristics, which are relevant to the uniaxial tension, such as the total force of response $F = \sum_i F_i$, the stress $\sigma = F/S = \left(\sum_i F_i\right)/S$, where S is the loading area, the Young's modulus $E = \sigma/\varepsilon$, where both stress σ and the strain ε are determined within the elastic region of deformation.

3. Computational results

Thus arranged computations have revealed that a high stiffness of the graphene body is provided by that one of the benzenoid units. The anisotropy of the unit mechanical behavior in combination with different packing of the units either normally or parallel to the C-C bond chains lays the ground for the structure-sensitive mechanism of the mechanical behavior of the object that drastically depends on the deformation modes [11-13]. The elastic regions of tensile deformation for both (5, 5) NGr and nanographane (NGra) molecules are extremely narrow and correspond to the first few steps of the deformation. The deformation, as a whole, is predominantly plastic and dependent on many parameters, among which, the most important is the chemical composition of the molecule edge atoms [14].

The equilibrium structures of the (5, 5) NGr molecule before and after uniaxial tension, which was terminated by the rupture of the last C-C bond coupling two fragments of the molecule, are shown in Fig. 2. Looking at the picture, two main peculiarities of the molecule deformation should be notified. The first concerns the anisotropy of the deformation with respect to two deformational modes. The second exhibits a strong dependence of the deformation on the chemical composition of the molecule edge atoms. As mentioned above, the deformation anisotropy of graphene has been attributed to the mechanical anisotropy of the constituent benzenoid units [11, 12]. The dependence of the deformation on the chemical modification of the framing edge atoms has been revealed for the first time.

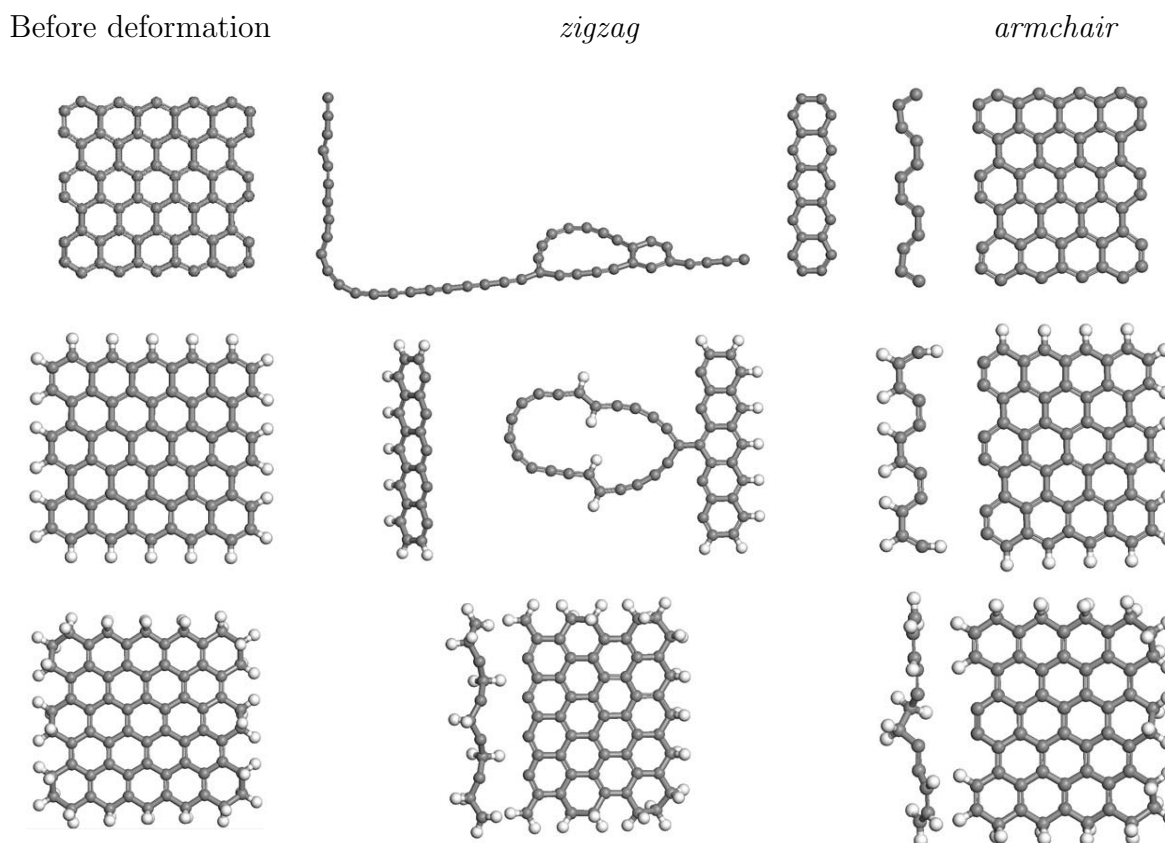


FIG. 2. Equilibrium structures of the (5,5) NGr with different chemical modification of edge atoms before and after completing tensile deformation in two modes of deformation. Bare edges (top); H₁-terminated edges (middle); H₂-terminated edges (bottom)

As seen in Fig. 2, the deformation behavior is the most complex for the naked molecule. The mechanical behavior of the (5, 5) NGr molecule is similar to that of a tricotage sheet when either the sheet rupture has both commenced and been completed by the rupture of a single stitch row (*armchair* mode) or the rupture of one stitch is ‘tugging at thread’ the other stitches that are replaced by still elongated one-atom chain of the carbon atoms (*zigzag* mode). In the former case, the deformation is one-stage and is terminated on the 17th step of the deformation. In contrast, the deformational mode *zigzag* is multi-stage and consists of 250 consecutive steps with an elongation of 0.1Å at each step [11, 12]. The formation of the one-atom chain under zigzag-mode tension of the naked graphene piece has been supported experimentally [22].

Quite unexpectedly, the character of the deformation seems to be strongly dependent upon the chemical substitution at the molecule edges. As seen in Fig. 2, the addition of one hydrogen atom to each of the molecule edge atoms does not change the general character of the deformation: it remains a tricotage-like one, so that there is still a large difference between the behavior of *zigzag* and *armchair* modes. At the same time, the number of the deformation steps of the *zigzag* mode reduces to 125.

Even more drastic changes for this mode are caused by the addition of a second hydrogen atom to the edge (Fig. 2). Still, the *armchair* mode is quite conservative while the *zigzag* one becomes practically identical to the former. The tricotage-like character of the deformation is completely lost and rupture occurs at the 20th step.

Figure 3 presents a set of the ‘stress-strain’ relations that fairly well highlight the differences in the mechanical behaviors of all the three molecules. Table 1 presents the Young’s moduli that were defined in the region of the elastic deformation. As seen from the table, the Young’s moduli depend on the character of the edge atom chemical modification. As shown in [13], elastic properties of extended molecules such as polymers [17, 23] and nanographenes [13] are determined by dynamic characteristics of the objects, namely, by force constants of the related internal vibrations. Since benzenoid units provide the determining resistance to any deformation of the graphene molecules, the dynamic parameters of the stretching C-C vibrations of the units are mainly responsible in the case of the uniaxial tension. Changes in the Young’s moduli mean that there are changes in the force constants (and, consequently, frequencies) for these vibrations. The latter are attributed to the G-band of graphene that lays the foundation of a mandatory testing of any graphenium system by the Raman spectroscopy. In numerous cases, the relevant band is quite wide which might indicate the chemical modification of the edge zone of the graphene objects under investigation.

Since the deformation-induced molecule distortion mainly concerns basal atoms, such drastic changes in the deformation behavior point to a significant influence of the chemical state of the edge atoms on the electronic properties in the basal plane. The observed phenomenon can be understood if it is suggested that: 1) both the deformation and rupture of the molecule is a collective event that involves the electron system of the molecule as a whole; 2) the electron system of the graphene molecule is highly delocalized due to valuable correlation of the odd electrons; and 3) the electrons correlation is topologically sensitive because the chemical termination of the edge atoms so strongly influences the behavior of the entire molecule. The latter has turned out to be the reality, indeed. The topography of the atomic chemical susceptibility transformation over the molecule’s atoms is presented elsewhere [25].

4. Topological character of the odd electron correlation in graphene

The performed computations have revealed that the correlation of the studied molecules’ odd electrons changes quite remarkably in the course of the deformation. This result can be illustrated by the evolution of the total number of effectively unpaired electrons N_D during the deformation. The N_D value is a direct characteristic of the extent of the electron correlation [18], on one hand, and the presents molecular chemical susceptibility [24], on the other. Changes in N_D reveal deformation-induced changes in the molecule chemical activity induced by deformation.

Figure 4 presents the evolution of N_D for the three studied molecules. Since breaking each C-C bond causes an abrupt change in N_D , a tooth-like character of the relevant dependences related to the *zigzag* mode of the molecule with the naked and H-terminated

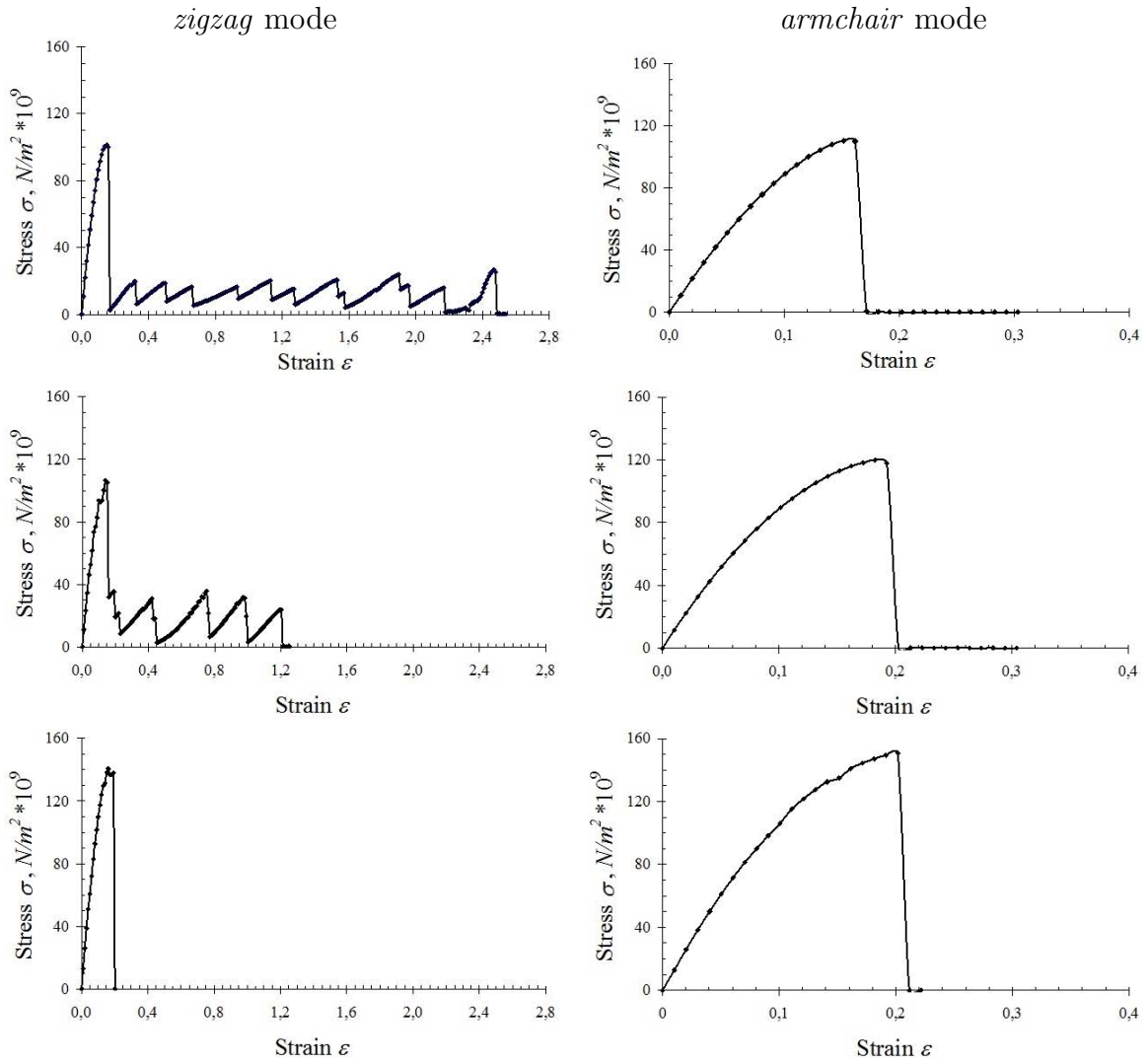


FIG. 3. Stress-versus-strain dependences of tensile deformation of the (5, 5) NGr molecule with different edge-atom chemical modification in two deformation modes. Naked molecule (top); H_1 -terminated edges (middle); H_2 -terminated edges (bottom)

edges is quite evident. One should draw attention to the N_D absolute values as well as to their dependence on both the chemical modification of the edge atoms and the deformational modes. Evidently, the chemical activity of the molecules drastically changes in the course of the mechanically induced transformation. This changing is provided by the redistribution of the C-C bond lengths caused by the mechanical action. This action combines the positions of both basal plane and edge atoms into the a single whole and is topologically sensitive. Therefore, the redistribution of the C-C bonds over their lengths causes changes in the topological ‘quality’ of individual bonds.

5. Conclusion

Data presented in the current paper undoubtedly show that chemical modification of the graphene molecule’s edge atoms has a great impact on its mechanical behavior. This feature results from the significant correlation of the molecule’s odd electrons followed by

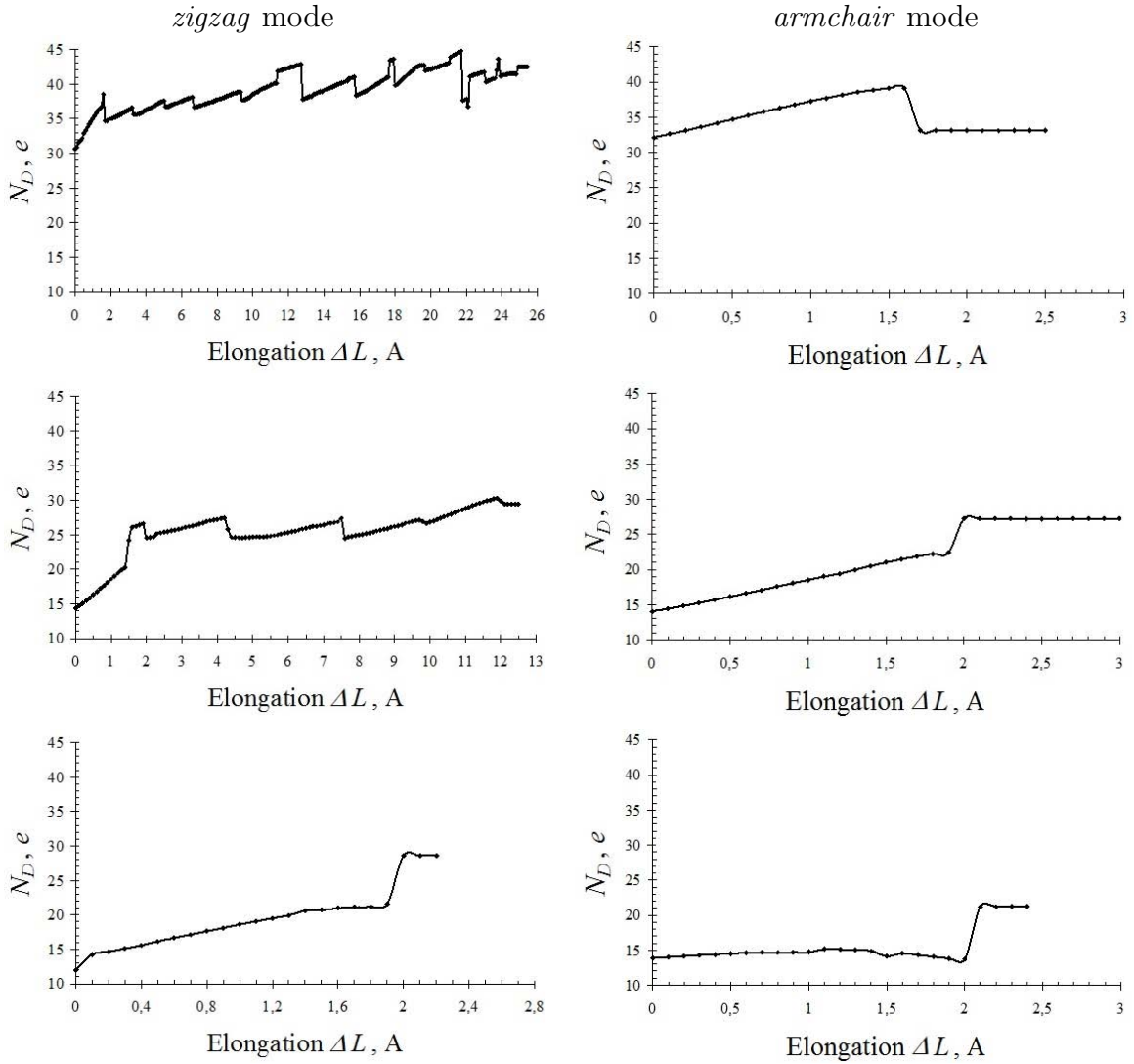


FIG. 4. Evolution of the odd electrons correlation in terms of the total numbers of effectively unpaired electrons under tensile deformation of the (5, 5) NGr at two deformation modes. Bare edges (top); H₁-terminated edges (middle); H₂-terminated edges (bottom)

their conjugation over the molecule. Thus, the transition from the naked molecule, characterized by the maximal correlation of the odd electrons, to the molecule with the single- and double-hydrogen-terminated edges is followed by a considerable suppression of the correlation related to the edge atoms in the former case and a complete zeroing of the latter in the second case. As it turns out, the changes are not local and strongly influence the electronic structure in the basal plane, where the main deformation process occurs, causing a redistribution of the C-C bonds over their lengths, thus, changing ‘the quality’ of the bonds and providing the topological character of the deformation processes in graphene.

Acknowledgments

Financial support provided by the Ministry of Science and High Education grant 2.8223.2013 is highly acknowledged.

References

- [1] G.M.J. Schmidt. Photodimerization in the solid state. *Pure Appl. Chem.*, **27**, P. 647–678 (1971).
- [2] A.W.K. de Jong. Über die Konstitution der Truxill – und Truxinsäuren und über die Entwicklung des Sonnenlichtes auf die Zimtsäuren und Zimtsäure –Salze. *Chem. Ber.*, **56B**, P. 818–832 (1923).
- [3] R.B. Woodward, R. Hoffmann. *The Conservation of Orbital Symmetry*. Verlag Chemie in Weinheim, Bergstr (1970).
- [4] V. Enkelmann. Polydiacetylenes. *Adv. Polym. Sci.*, **63**, P. 91–121 (1984).
- [5] M. Hasegawa. Topochemical photopolymerization of diolefin crystals. *Pure Appl. Chem.*, **58**, P. 1179–1188 (1986).
- [6] V.V. Boldyrev. Topochemistry and topochemical reactions. *Reactivity of Solids*, **8**, P. 231–246 (1990).
- [7] L.R. MacGillivray, G.S. Papaefstathiou. *Encyclopedia of Supramolecular Chemistry*. DOI: 10.1081/E-ESMC 120012761 Marcel Dekker, 1316 (2004).
- [8] F. Guo, J. Marti-Rujas, Z. Pan, et al. Direct structural understanding of a topochemical solid state photopolymerization reaction. *J. Phys. Chem. C*, **112**, P. 19793–19796 (2008).
- [9] E.F. Sheka, L.Kh. Shaymardanova. C₆₀-based composites in view of topochemical reactions. *J. Mat. Chem.*, **21**, P. 17128–17146 (2011).
- [10] E.F. Sheka. Topochemistry of spatially extended *sp*² nanocarbons: fullerenes, nanotubes, and graphene. In: Ashrafi A. R., Cataldo F., Iranmanesh A et al. (eds.) Topological Modelling of Nanostructures and Extended Systems. *Carbon Materials: Chemistry and Physics*, **7**, Springer, Heidelberg, P. 137–148 (2013).
- [11] E.F. Sheka, N.A. Popova, V.A. Popova, E.A. Nikitina, L.Kh. Shaymardanova. A tricotage-like failure of nanographene. *J. Mol. Mod.*, **17**, P. 1121–1131 (2011).
- [12] E.F. Sheka, N.A. Popova, V.A. Popova, E.A. Nikitina, L.Kh. Shaymardanova. Structure-sensitive mechanism of nanographene failure. *J. Exp. Theor. Phys.* **112**, P. 602–611 (2011).
- [13] N.A. Popova, E.F. Sheka. Mechanochemical reaction in graphane under uniaxial tension. *J. Phys. Chem. C*, **115**, P. 23745–23754 (2011).
- [14] V.A. Popova, N.A. Popova, E.F. Sheka. Effect of chemical modification of edge atoms of graphene sheets on their strength. arXiv:1301.0944 [cond-mat.mtrl-sci] (2013).
- [15] A. Tobolski, H. Eyring. Mechanical properties of polymeric materials. *J. Chem. Phys.*, **11**, P. 125–134 (1943).
- [16] M.J.S. Dewar. MO theory as a practical tool for studying chemical reactivity. *Fortschr. Chem. Forsch.*, **23**, P. 1–63 (1971).
- [17] E.A. Nikitina, V.D. Khavryutchenko, E.F. Sheka, H. Barthel, J. Weis. Deformation of poly (dimethylsiloxane) oligomers under uniaxial tension. Quantum-chemical view. *J. Phys. Chem. A*, **103**, P. 11355–11365 (1999).
- [18] E.F. Sheka. Computational strategy for graphene: Insight from odd electrons correlation. *Int. J. Quant. Chem.*, **112**, P. 3076–3090 (2012).
- [19] V.D. Khavryutchenko, E.A. Nikitina, A.L. Malkin, et al. Mechanics of nanoobjects. Computational mechanochemistry. *Phys. Low-Dim. Struct.*, **6**, P. 65–84 (1995).
- [20] V.D. Khavryutchenko, A.V. Khavryutchenko. Jr. DYQUAMECH dynamical-quantum modelling in mechanochemistry. Software for personal computers, Institute of Surface Chemistry, Nat. Acad. Sci. of the Ukraine, Kiev (1993).
- [21] J.J.P. Stewart. Optimization of parameters for semiempirical methods I. Method. *J. Comput. Chem.*, **10**, P. 209–220 (1989).
- [22] C. Jin, H. Lan, L. Peng, K. Suenaga, S. Iijima. Deriving carbon atomic chains from graphene. *Phys. Rev. Lett.*, **102**, P. 205501 (2009).
- [23] K. Tashiro, M. Kobayashi, H. Tadacoro. Theoretical evaluation of three-dimensional elastic constants of native and regenerated celluloses: role of hydrogen bonds. *Polymer Journ* **24**, P. 899–916 (1992).
- [24] E.F. Sheka. *Fullerenes: Nanochemistry, Nanomagnetism, Nanomedicine, Nanophotonics*. CRC Press, Taylor and Francis Group. Boca Raton (2011).
- [25] E.F. Sheka, V.A. Popova, N.A. Popova. Topological mechanochemistry of graphene. In: Advances in Quantum Methods and Applications in Chemistry, Physics, and Biology, ed. by Hotokka M. Braändas E.J., Maruani J. and Delgado-Barrío G. *Progress in Theoretical Chemistry and Physics*, Springer, Berlin, Heidelberg, **27**, P. 285–301 (2013).

THE ELECTRON-PHONON MATRIX ELEMENT IN THE DIRAC POINT OF GRAPHENE

^{1,2}S. V. Koniakhin, ^{1,2,3}E. D. Eidelman

¹ Ioffe Physical-Technical Institute of the Russian Academy of Sciences - 194021
St. Petersburg, Russia

² St. Petersburg Academic University - Nanotechnology Research and Education Centre
of the Russian Academy of Sciences - 194021 St. Petersburg, Russia

³ St. Petersburg Chemical Pharmaceutical Academy - 197022 St. Petersburg, Russia
kon@mail.ioffe.ru

PACS 63.22.Rc, 63.20.kd

The chief aim of this paper is to derive the matrix element of electron-phonon interaction in graphene as a function of phonon wave vector. The tight binding model, harmonic crystal approximation, and deformation potential approximation were employed for obtaining the matrix element. Required microscopic parameters are available in the current literature. This technique allows the most precise derivation of the electron-phonon matrix element in graphene based on the semiempirical models. Scattering of electrons from the Dirac point is considered as most important. The 2D plots of the e-ph matrix element absolute value as a function of the phonon wave vector for in-plane modes are given as a result. These plots show the high anisotropy of the e-ph matrix element and singularities in high symmetry points. The results are in agreement with the long-wavelength approximation.

Keywords: graphene, electron-phonon interaction.

1. Introduction

Electron-phonon interaction can affect transport properties of extremely pure graphene [1,2] and consequently its investigation is important for creating electronic devices based on graphene layers, particularly thermoelectric devices [3,4]. Raman spectroscopy is one of the most comprehensive techniques for studies of graphene [5,6] and double resonant Raman peaks are footprints of electronic and vibrational properties of the crystal. This encourages the research of electron-phonon interaction in graphene. The knowledge of vibrational properties, electron wave functions and deformation potential in total can lead to derivation of the electron-phonon matrix element.

2. Harmonic crystal approximation

Graphene is a two dimensional crystal with a honeycomb lattice of carbon atoms. One of the alternatives for the unitary cell is rhombic one. It contains two atoms in basis: A and B types. They have different directions of the chemical bonds, which causes their inequivalence. Reciprocal lattice for the two-dimensional hexagonal crystal is also hexagonal lattice, which is in addition rotated over 60 degrees. Brillouin zone carries symmetrical properties of the crystal and consequently it must be hexagon-shaped. To specify the position of each atom, one can write $\mathbf{R}(u, s) = \mathbf{R}_u + \mathbf{r}_s$, where \mathbf{R}_u is the position of unitary cell in crystal and \mathbf{r}_s is the position of atom of s type in the unitary cell.

The vibrational properties of graphene can be described on the basis of the harmonic crystal approximation [7]. This method starts from the Newton's second law for each atom in crystal:

$$m\ddot{x}_\alpha(u, s) = - \sum_{u' s' \beta} \Phi_{\alpha\beta}(u - u', s, s') x_\beta(u', s'), \quad (1)$$

where $x_\alpha(u, s)$ is α component of displacement of the s type atom in the u cell, and $\Phi_{\alpha\beta}$ are interatomic force constants. The infinite system of the classical motion equations after substitution are:

$$x_\alpha(\mathbf{q}, u, s) = \frac{1}{\sqrt{m}} w_\alpha(\mathbf{q}, s) \exp(i\mathbf{q}\mathbf{R}(u, s) - i\omega(\mathbf{q})t) \quad (2)$$

reduces to the eigenvector problem:

$$\omega^2(\mathbf{q}) w_\alpha(\mathbf{q}, s) = \sum_{s' \beta} C_{\alpha\beta} \begin{pmatrix} \mathbf{q} \\ s \ s' \end{pmatrix} w_\beta(\mathbf{q}, s'), \quad (3)$$

for the dynamical matrix $C_{\alpha\beta}$ that is defined as:

$$C_{\alpha\beta} \begin{pmatrix} \mathbf{q} \\ s \ s' \end{pmatrix} = \frac{1}{m} \sum_{u'} \Phi_{\alpha\beta}(u - u', s, s') \cdot \exp(i\mathbf{q} \cdot (\mathbf{R}(u, s) - \mathbf{R}(u', s'))). \quad (4)$$

It is useful to introduce the vector $\mathbf{W}_s(\mathbf{q}) = (w_x(\mathbf{q}, s), w_y(\mathbf{q}, s))^T$. Eigenvalues for the dynamical matrix give squared frequencies for phonons of different phonon modes and eigenvectors represent corresponding directions and phases of atomic displacements. For a crystal with 2 atoms in its basis, the dynamical matrix dimensions are 6 by 6. But out of plane modes can be separated, and therefore, the in-plane modes can be described by a 4 by 4 dynamical matrix. Interatomic force constants utilized to construct the dynamical matrix are available in current literature [8–12]. The density-functional theory (DFT) is used in [10] to obtain the interatomic force constants for neighbors, up to twentieth, and we use here these data as the most complete.

3. Derivation of electron-phonon matrix element

The wave functions of electron with wave vector \mathbf{k} in graphene can be written as

$$\psi_{\mathbf{k}}(\mathbf{r}) = \frac{1}{\sqrt{N}} \sum_{u, s} C_s(\mathbf{k}) \varphi(\mathbf{r} - \mathbf{R}_u - \mathbf{r}_s) \cdot \exp(i\mathbf{k}(\mathbf{R}_u + \mathbf{r}_s)). \quad (5)$$

Coefficients $C_s(\mathbf{k})$ define the true Hamiltonian eigenstates with wave vector \mathbf{k} , and $\varphi(\mathbf{r})$ is the atomic wave function. Most of important optical and electronic properties of graphene are defined by the bands that appear as a result of interaction between electrons from π orbitals of carbon atoms. Consequently, $\varphi(\mathbf{r})$ here is close to the π orbitals.

The phonon is a wave of atomic displacements from their equilibrium positions and consequently it causes a deviation potential from the potential of unperturbed crystal. It leads to the possibility of electron scattering on corresponding perturbation. For small atomic displacements, the perturbation potential is directly proportional to these displacements. Thereby, one can write the scalar product of atomic displacement and gradient of the certain potential in the following expression:

$$\delta V_{\mathbf{q}}(\mathbf{r}) = \sum_{u'',s''} (\mathbf{W}_{s''}(\mathbf{q}) \cdot \nabla V(\mathbf{r} - \mathbf{R}_{u''} - \mathbf{r}_{s''})) \cdot \exp(i\mathbf{q}(\mathbf{R}_{u''} + \mathbf{r}_{s''})). \quad (6)$$

In the hard ion approach the potential of an atom is assumed to be rigid and consequently in relation (6) V is directly the potential of the atom that is used to calculate band structure in the material, e.g. to construct tight-binding matrix elements in the tight binding model. Indeed, the form of atomic potential changes when the atom is displaced and it leads to the concept of deformation potential. In [13], the deformation potentials in nanotubes and graphene were studied on the basis of *ab initio* calculations.

The Electron-phonon matrix element defines the process of electron scattering with wavevector \mathbf{k} into the state with wavevector \mathbf{k}' on introduced potential:

$$M_{e-ph}(\mathbf{k} \rightarrow \mathbf{k}' = \mathbf{k} + \mathbf{q}) \equiv M_{e-ph}(\mathbf{k}, \mathbf{q}) = \int d\mathbf{r} \psi_{\mathbf{k}'}^\dagger(\mathbf{r}) \delta \hat{V}_{\mathbf{q}}(r) \psi_{\mathbf{k}}(\mathbf{r}). \quad (7)$$

Basic formulae for calculation of the electron-phonon matrix element are given in [13] in clear form, and where possible, designations from [13] are used. However, in [13], the authors mainly investigate nanotube transport properties and do not give the electron-phonon matrix element as a function of the wave vector or represent 2D plots of M_{e-ph} . For instance, the precise Raman spectra calculation requires such information.

After substitution of relations (2), (5), and (6) to (7) one obtains:

$$M_{e-ph}(\mathbf{k}, \mathbf{q}) = \sum_{u,s} \sum_{s'} \sum_{u'',s''} C_{s'}^\dagger(\mathbf{k}') C_s(\mathbf{k}) \times \exp(i\mathbf{k}(\mathbf{R}_{\Delta u} + \mathbf{r}_s) - i(\mathbf{k} + \mathbf{q})\mathbf{R}_{u''} + i\mathbf{q}(\mathbf{R}_{\Delta u''} + \mathbf{r}_{s''})) \cdot (\mathbf{W}_{s''}(\mathbf{q}) \cdot \mathbf{g}(s'; \Delta u, s; \Delta u'', s'')), \quad (8)$$

where

$$\mathbf{g}(u'; \Delta u, s; \Delta u'', s'') = \int d\mathbf{r} [\varphi^\dagger(\mathbf{r}) \nabla V(\mathbf{r} - (\mathbf{R}_{\Delta u''} + \mathbf{r}_{s''} - \mathbf{r}_{s'})) \varphi(\mathbf{r} - (\mathbf{R}_{\Delta u} + \mathbf{r}_s - \mathbf{R}_{s'}))]. \quad (9)$$

Fig. 1 represents relative positions of atoms that figures in the integral in relation (9).

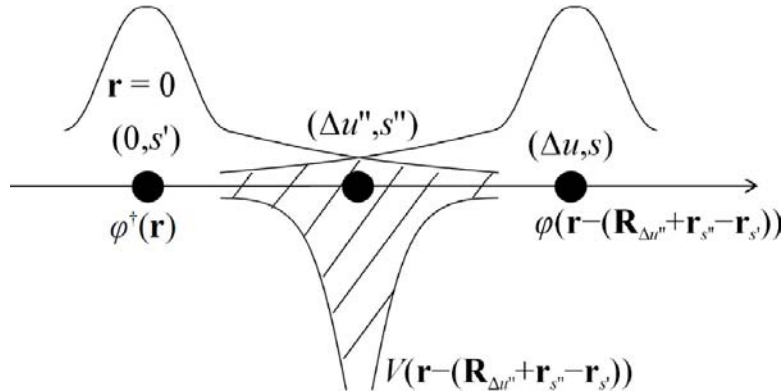


FIG. 1. Diagram illustrating the structure of terms in the expression for the deformation potential.

As was mentioned previously, the relevant electron states in graphene are the result of π orbital interactions. Due to the geometry of the π - π bond, the energy of interaction

between carbon atoms changes significantly only if atoms are displaced along the bond axis. Mathematically it means that the direction of the potential gradient lies along vectors between atom s' and its neighbors. Also, only interactions between nearest neighbors are dominant. Consequently, the two types of terms appear. The first one is so-called off-site term, where $\Delta u = 0$, $s = s'$:

$$\mathbf{g}(s'; 0, s'; \Delta u'', s'') = \frac{\mathbf{R}_{\Delta u''} + \mathbf{r}_{s''} - \mathbf{r}_{s'}}{|\mathbf{R}_{\Delta u''} + \mathbf{r}_{s''} - \mathbf{r}_{s'}|} \cdot \lambda(|\mathbf{R}_{\Delta u''} + \mathbf{r}_{s''} - \mathbf{r}_{s'}|), \quad (10)$$

This corresponds to perturbation of the diagonal terms of Hamiltonian. The second type are on-site terms, where $\Delta u'' = 0$, $s'' = s'$ or $\Delta u'' = \Delta u$, $s'' = s'$:

$$\begin{aligned} \mathbf{g}(s'; \Delta u, s; 0, s') &= \frac{\mathbf{R}_{\Delta u} + \mathbf{r}_s - \mathbf{r}_{s'}}{|\mathbf{R}_{\Delta u} + \mathbf{r}_s - \mathbf{r}_{s'}|} \cdot \alpha(|\mathbf{R}_{\Delta u} + \mathbf{r}_s - \mathbf{r}_{s'}|), \\ \mathbf{g}(s'; \Delta u, s; \Delta u, s) &= -\frac{\mathbf{R}_{\Delta u} + \mathbf{r}_s - \mathbf{r}_{s'}}{|\mathbf{R}_{\Delta u} + \mathbf{r}_s - \mathbf{r}_{s'}|} \cdot \alpha(|\mathbf{R}_{\Delta u} + \mathbf{r}_s - \mathbf{r}_{s'}|). \end{aligned} \quad (11)$$

They define the off-diagonal perturbation of the Hamiltonian. Numeric values of α and λ are given in [13].

4. Results and discussion

Electrons near the Fermi level make the main contribution to the transport phenomena in graphene. Due to the shape of electron dispersion, these electrons have a wave vector lying near the Dirac point (K point or conical point) of the Brillouin zone. Visible light can excite electron hole pairs also in the region of the Dirac point only. Consequently, scattering of electrons from the Dirac point of the Brillouin zone attracts most interest.

Fig 2. shows the absolute value of electron-phonon matrix element as a function of the phonon wave vector \mathbf{q} for TA,LA,TO and LO modes. Initial electron wave vector \mathbf{k} corresponds to the Dirac point ($\mathbf{k} = (4\pi/3a_0, 0)$). High anisotropy of the electron-phonon matrix element is detected. Patterns obey D_{3h} symmetry, which is strictly necessary for the Dirac point of Brillouin zone in graphene. The directions in Brillouin zone and segments of hexagonal Brillouin zone with high and low values of the electron-phonon matrix element tolerably match to the ones from [14]. In [14], the authors used density-functional perturbation theory (DFPT) to calculate the electron-phonon matrix element, but the details of their calculations are unfortunately very brief.

Next, there are estimations [15] of the matrix element of scattering of electron in Dirac point within the long wave length approximation. For small phonon wave vectors \mathbf{q} , the following behavior was indicated:

$$\begin{aligned} M_{e-ph}^{TA,LA} &\sim q, \\ M_{e-ph}^{TO,LO} &\sim const. \end{aligned} \quad (12)$$

It can be seen that the obtained results agree well with estimations from [15].

Introduced derivation of the electron-phonon matrix element is based on the most complete and full sets of microscopic material parameters, and thus, it provides the most precise semiempirical approach at this point. The results obtained can be used for improvement of Raman spectra calculation. Taking into account the high anisotropy of the electron-phonon matrix element is also important for investigation of the electron drag by phonons in graphene.

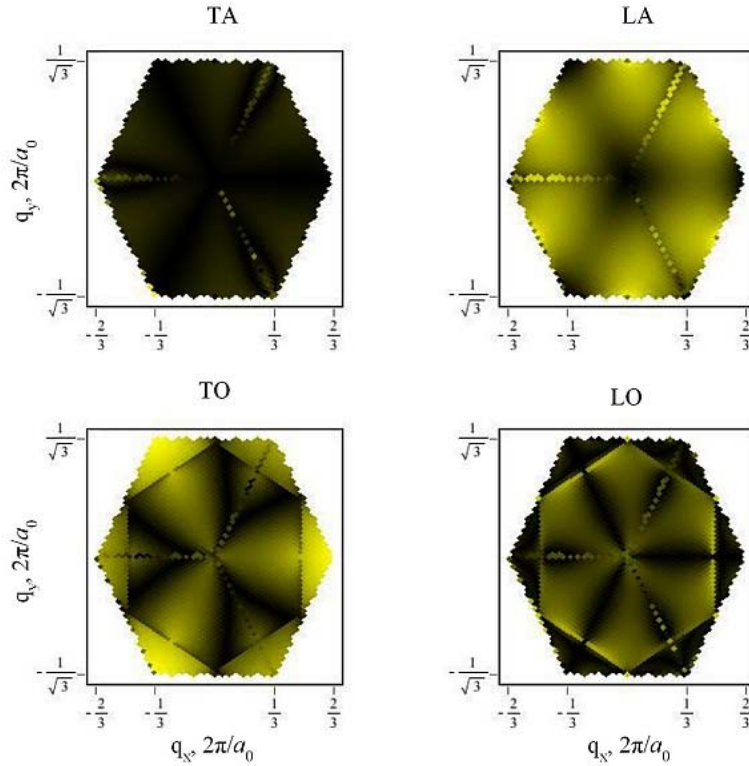


FIG. 2. Absolute value of electron-phonon matrix element for TA, LA, TO, and LO modes as a function of wave vector. The initial state of the electron corresponds to the Dirac point. Lighter areas correspond to larger values of matrix elements.

Acknowledgements

We would like to thank A. Ya. Vul' and A. T. Dideykin for their attention. This work was supported by the Dynasty foundation Grant for PhD students and by the St. Petersburg government grant for PhD students. The work was partly supported by programs of the Presidium of the Russian Academy of Sciences "Fundamental Foundations of the Technologies of Nanostructures and Nanomaterials" and "Quantum Mesoscopic and Unordered Systems".

References

- [1] Tse Wang-Kong, Das Sarma S. Energy relaxation of hot Dirac fermions in graphene. *Phys. Rev. B.*, **79**, P. 235406 (2009, Jun.).
- [2] Mariani Eros, von Oppen Felix. Temperature-dependent resistivity of suspended graphene. *Phys. Rev. B.*, **82**, P. 195403 (2010, Nov.).
- [3] Wang Deqi, Shi Jing. Effect of charged impurities on the thermoelectric power of graphene near the Dirac point. *Phys. Rev. B.*, **83**, P. 113403 (2011, Mar.).
- [4] Checkelsky Joseph G., Ong N. P. Thermopower and Nernst effect in graphene in a magnetic field. *Phys. Rev. B.*, **80**, P. 081413 (2009, Aug.).
- [5] A. C. Ferrari, J. C. Meyer, V. Scardaci et al. Raman Spectrum of Graphene and Graphene Layers. *Phys. Rev. Lett.*, **97**, P. 187401 (2006, Oct.).
- [6] Venezuela Pedro, Lazzeri Michele, Mauri Francesco. Theory of double-resonant Raman spectra in graphene: Intensity and line shape of defect-induced and two-phonon bands. *Phys. Rev. B.*, **84**, P. 035433 (2011, Jul.).

- [7] Born M., Huang K. *Dynamical Theory of Crystal Lattices. Oxford classic texts in the physical sciences.* Clarendon Press (1996).
- [8] Al-Jishi R., Dresselhaus G. Lattice-dynamical model for graphite. *Phys. Rev. B.*, **26**, P. 4514–4522 (1982, Oct.).
- [9] A. Grüneis, R. Saito, T. Kimura et al. Determination of two-dimensional phonon dispersion relation of graphite by Raman spectroscopy. *Phys. Rev. B.*, **65**, P. 155405 (2002, Mar.).
- [10] Dubay O., Kresse G. Accurate density functional calculations for the phonon dispersion relations of graphite layer and carbon nanotubes. *Phys. Rev. B.*, **67**, P. 035401 (2003, Jan.).
- [11] Wirtz Ludger, Rubio Angel. The phonon dispersion of graphite revisited. *Solid State Communications*, **131**(3-4), P. 141 (2004).
- [12] Hui Wang, Yufang Wang, Xuewei Cao et al. Vibrational properties of graphene and graphene layers. *Journal of Raman Spectroscopy*, **40**(12), P. 1791–1796 (2009).
- [13] J. Jiang, R. Saito, Ge. G. Samsonidze et al. Electron-phonon matrix elements in single-wall carbon nanotubes. *Phys. Rev. B.*, **72**, P. 235408 (2005, Dec.).
- [14] K. M. Borysenko, J. T. Mullen, E. A. Barry et al. First-principles analysis of electron-phonon interactions in graphene. *Phys. Rev. B.*, **81**, P. 121412 (2010, Mar.).
- [15] Mañes J. L. Symmetry-based approach to electron-phonon interactions in graphene. *Phys. Rev. B.*, **76**, P. 045430 (2007, Jul.).

THE ADSORPTION PROPERTIES OF POLYCRYSTALLINE GRAPHENE: QUANTUM-CHEMICAL SIMULATION

N. A. Lvova¹, O. Yu. Ananina²

¹Federal State Budgetary Institution “Technological Institute for Superhard and Novel Carbon Materials”, Moscow, Troitsk, Russia

²Zaporizhzhya National University, Zaporizhzhya

nlvova@tisnum.ru, ananyina@znu.edu.ua

PACS 68.43.-h, 81.05.ue, 03.67.Lx

This study presents the results of quantum-chemical simulation of H₂O, NH₃, PH₃, and CH₄ molecules and their fragments adsorption onto graphene nanoclusters with different types of grain boundaries. We describe the molecule adsorption states on graphene and estimate the adsorption energy characteristics. It is shown that the presence of grain boundaries changes the geometric and electronic parameters of graphene, and can lead to a physical adsorption and chemisorption of molecules without dissociation, unlike in ordered graphene. Dissociative chemisorption of molecules on the grain boundaries is accompanied by some significant changes in the geometric, electronic, and energy state of graphene. The features of the energy change differences for the HOMO-LUMO of graphene with the chemisorbed dissociation fragments can be used to identify the gas molecules on graphene by their electronic spectra.

Keywords: Polycrystalline graphene, Dislocation defect, Electronic properties, Adsorption properties.

1. Introduction

The discovery of graphene, the first truly two-dimensional crystal, and the study of the remarkable electronic properties of this promising nanoscale structure has caused a huge increase in the interest of carbon nanomaterials. Mostly, studies have focused on electronic transport phenomena in graphene and its applications in carbon-based electronics. There is also interest in the mechanism of interaction between the adsorbed particles and line defects on the graphene surface in connection with the possible use of polycrystalline graphene as a material for chemical sensors [1]. Dislocations, grain boundaries, and other topological defects in graphene are the subject of recent experimental and theoretical studies [2-5]. However, at present, their structure and properties remain poorly investigated.

2. Calculation Techniques

In this paper, we studied the adsorption of molecules and radicals on a graphene surface containing grain boundaries with different θ misorientation angles and concentration of dangling bonds. The modeling was performed using the MNDO semiempirical techniques included in the MOPAC 2009 software package [6], as well as ab initio Hartree-Fock methods of the PC GAMESS software package [7]. C₁₃₂H₂₈, C₁₄₃H₂₉, C₉₁H₂₃, C₇₃H₂₁, and C₁₁₉H₂₉ graphenes with a (1.0) intergranular boundary were constructed as a model, and C₉₇H₂₄, C₁₀₄H₂₆ containing more complex grain boundaries with misorientation angles $\theta=16^\circ$. The boundaries were formed by polygons located in the 7-5-6-6-7-8-5 and 4-7-5-8-4-10-5 sequence. Figures 1,2 illustrate the fragments of clusters with inter-granular boundaries. The boundaries, consisting of a set of various polygons, lead to a change in the graphene sheet topology:

it bends forming a ridge along the boundary. The α angle between the adjacent grains was about 30-35 and 40-45 degrees for the $C_{97}H_{24}$ and $C_{104}H_{26}$ clusters respectively. A similar graphene sheet curvature was obtained by the authors of [2] to simulate the grain boundaries using molecular dynamics. The misorientation angle θ in [2] was from 0 to 30 degrees, the α angle varied in a wide range of 0–85°, but values of α between 20° and 40° occurred most frequently.

In the adsorption simulation for each molecule, we considered various positions as adsorption centers: carbon atoms at the grain boundary; over the carbon polygons centers on the boundaries; and over the C-C bonds. The interaction of molecules and radicals with dislocation defects, graphene grain boundaries can lead to physical adsorption and chemisorption, and that may cause a change in the electrical, physical, and chemical properties of graphene. The binding energies (E_b) of the adsorbed molecules were calculated as the difference between the sum of the pure graphene total energy (E_g) and isolated molecule energy (E_{mol}), and the total energy of a “graphene - adsorbed molecule” system (E_{syst}):

$$E_b = (E_g + E_{mol}) - E_{syst} \quad (1)$$

3. Results and Discussion

3.1. The adsorption of molecules on graphene containing a (1.0) boundary

Such violations of the graphene crystal lattice as the occurrence of adjacent 5- and 7-gons can lead either to the appearance of point defects like the Stone-Wales -type defects [8], or to the formation of dislocations [5]. The (1.0) dislocation defect is characterized by a Burgers vector:

$$\vec{b} = m\vec{a}_1 + n\vec{a}_2, \quad m = 1, n = 0, \quad (2)$$

and an insert of a graphene material strip (the strip is limited by the dotted lines in Figure 1a). The sequence of (1.0) dislocation defects aligned along one axis describes a defect like a (1.0) grain boundary having a wedge-shaped graphene insert and the angle of:

$$\theta = \theta_1 + \theta_2 = 2 \arcsin \frac{|\vec{b}_{(1.0)}|}{2d_{(1.0)}}, \quad (3)$$

where $\vec{b}_{(1.0)}$ is Burgers vector, $d_{(1.0)}$ is the distance between the (1.0) dislocations cores.

The lengths of the C-C bonds at the (1.0) boundary take the values of 1.39-1.52 Å, which differ significantly from the lengths of C-C bonds for orderly graphene (1.42-1.44 Å). There were changes in the values of the bond angles. Changes in the bond geometry led to the distribution of charge between the carbon atoms, a positive charge is localized on the heptagon carbon atoms, while a negative charge is localized on the pentagon carbon atoms. Although the charge distribution is insignificant, it can affect the adsorption properties of graphene with linear defects. In ordered graphene, the charge on the carbon atoms is missing. For ordered graphene with a (1.0) boundary, the HOMO-LUMO width decreases, while for ordered graphene with the same number of carbon atoms, $\Delta E_{HL} \sim 5.49$ eV, for the $C_{132}H_{28}$ cluster with a (1.0) boundary $\Delta E_{HL} = 3.70$ eV.

Analysis of the H_2O , PH_3 , NH_3 and CH_4 adsorption calculation results proved that the physical adsorption states are almost identical to those of ordered graphene, the values of the binding energy of molecules to graphene being 51, 39, 41, and 16 meV. That is, the changes in the electronic state of the graphene with grain boundaries are insufficient for significant changes in the molecules' binding energy during the act of physical adsorption.

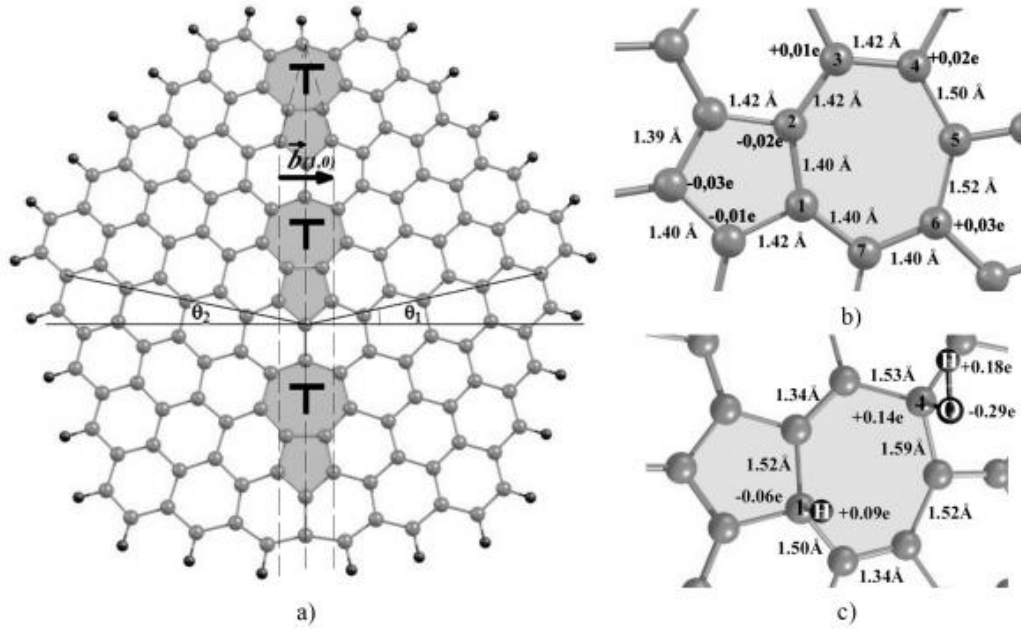


FIG. 1. (a) A $C_{132}H_{28}$ cluster containing (1.0) grain boundary; a fragment of the cluster before (b) and after (c) water molecule adsorption

Chemisorption on the (1.0) graphene grain boundary requires that the H_2O , PH_3 , NH_3 , and CH_4 molecules dissociate into fragments. The chemisorption induces significant changes in the geometric, electronic, and energy state of graphene. For example, the value of the energy difference between the HOMO-LUMO (ΔE_{HL}) increases, and there is a transfer of charge from graphene to the chemisorbed fragments of the dissociated molecule.

The adsorption sites selected for the water dissociation fragments affects the system parameters. The minimum energy is in the system where the -H and -OH groups are chemisorbed respectively on the carbon atoms of the pentagon and the heptagon on the boundary (Figure 1c). There is the second water molecule physically adsorbed on the (1.0) boundary. The second molecule is held at the surface, forming a hydrogen bond with the oxygen atom of the -OH fragment chemisorbed on the (1.0) boundary. The binding energy is 0.47 eV.

The charge transfer in the case of -OH and -NH₂ radical chemisorption is -0.115 and -0.085 e, these particles act as acceptors, while -PH₂ and -CH₃ fragment chemisorption does not result in the “particle-graphene” charge redistribution (Table 1). For all the chemisorbed molecules, the binding energy value for the fragments calculated using formula (1) is about 1 eV, which is significantly less than the sum of the heats of adsorption for -H and the -OH group on graphene. Thus, following the results obtained in [9], the heat of adsorption of hydrogen on the ordered graphene is ~ 5 eV. Obviously, the total energy of the “graphene-adsorbed fragments” system increases due to the formation of dangling bonds of some carbon atoms and the tension in the graphene lattice. It is noticed that the ΔE_{HL} value for the chemisorption of different fragments of the molecule dissociation take different values. This feature can be used to identify the molecules of gases on graphene in the electronic spectra.

TABLE 1. Geometric, electronic, and energy parameters of the $C_{132}H_{28}$ graphene cluster (Figure 1) containing the (1.0) boundary with adsorbed fragments of dissociation of water, phosphine, ammonia, and methane

Molecule, XH_n	Graphene atom bonded to (XH_{n-1})	Graphene atom bonded to (H)	${}^1R(C-X)$, Å	$Q(XH_{n-1})$, e	$Q(C)$, e	$\Delta(\Delta E_{HL})$, eV	E_b , eV
H_2O	C4	C1	1.46	-0.115	+0.139	+1.51	0.81
PH_3	C6	C4	1.98	+0.030	-0.013	+1.75	0.73
NH_3	C2	C1	1.51	-0.085	+0.101	+1.47	0.94
CH_4	C2	C5	1.58	+0.026	+0.023	+1.58	1.14

${}^1R(C-X)$ is C-X interatomic distance, X is O,P,N,C; $Q(X_{n-1})$ is charge on radicals, $Q(C)$ - charge on graphene atom bonded to (XH_{n-1}) , $\Delta(\Delta E_{HL}) = \Delta E_{HL(ads)} - \Delta E_{HL(clean)}$ is the difference between the energy values $\Delta E_{HL(ads)}$ for the cluster with an adsorbed molecule and $\Delta E_{HL(clean)}$ for the clean cluster.

3.2. Adsorption of molecules on graphene containing a boundary with a misorientation angle of $\theta = 16^\circ$

The ideal grain boundaries formed by pentagon-heptagon pairs have been observed in experiments [2]. However, the boundaries between the grains with random orientation are most common. These boundaries can be rough, corrugated or protruding, and have some dangling bonds and other active adsorption sites. Due to this, it is interesting to research the structure and properties of grain boundaries with an arbitrary crystallographic orientation via quantum chemistry techniques. The structure of grain boundaries has been studied in [3,4] using a transmission electron microscopy technique. Statistical analysis showed that the most frequent misorientation angles included were near 0 and 30° , and in the intermediate values of 13–17 degrees. In this study, we investigated the adsorption properties of the grain boundary separating the areas with a misorientation angle $\theta=16^\circ$. The corresponding crystallographic directions in different grains were positioned symmetrically relative to the boundary.

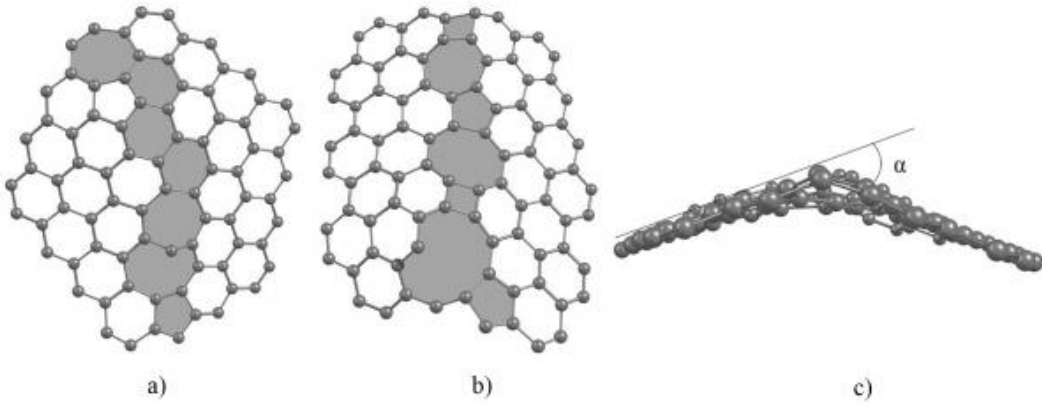


FIG. 2. Fragments of clusters containing grain boundaries for $\theta=16^\circ$: $C_{97}H_{24}$, a top view (a), $C_{104}H_{26}$, a top view (b) and a side view (c)

The calculations in this study showed that the C-C bond lengths at the boundary with $\theta=16^\circ$ vary from 1.34–1.58 Å, wider than at the (1.0) boundary. The charges on the atoms are distributed in a complex manner from -0.07 to +0.10 e, and for each of the clusters, the maximum positive charge is localized on the atoms with only two nearest neighbors. The authors of [2] discovered that the addition of hydrogen atoms to similar atoms leads to the maximized heat adsorption. In [10], to simulate water adsorption onto the diamond surface with a vacancy defect, the authors found a metastable state in which the molecule, without losing its integrity, is chemisorbed onto the surface. The oxygen atom thus forms a bond with the carbon atom initially having two nearest neighbors and a dangling bond. In this regard, it is of interest to find these bound states that do not require pre-dissociation at the grain boundaries of polycrystalline graphene.

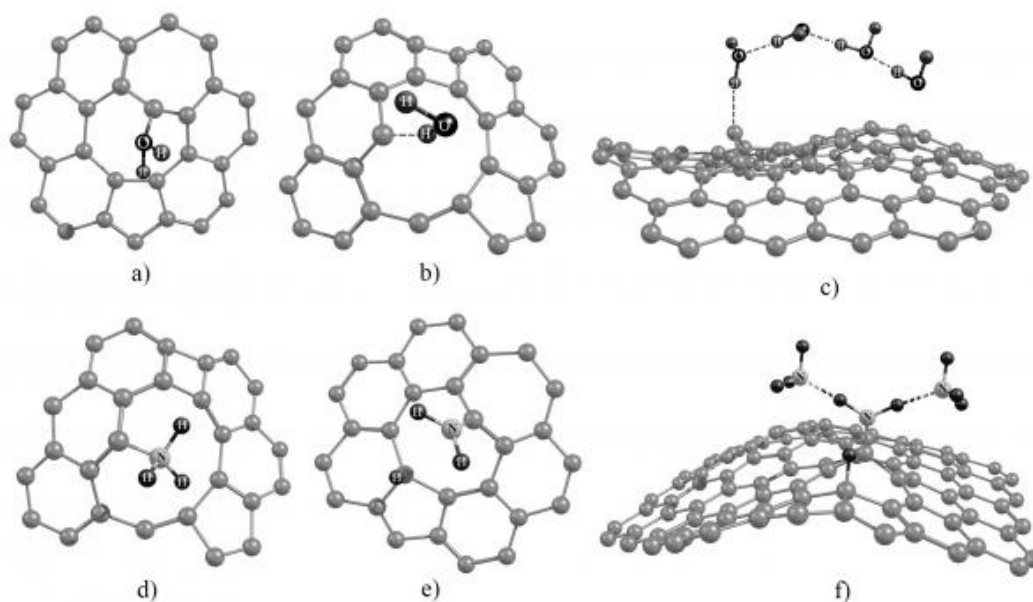


FIG. 3. Boundary molecules adsorption results: a water molecule is chemisorbed to form a covalent (a) and a hydrogen (b) surface-molecule bond; (c) - chain formation of four bound water molecules; the ammonia molecule adsorption result on the boundary to form a covalent bond (d), a dissociation on the surface of the $C_{97}H_{24}$ cluster (e); attaching three molecules (f)

In this study we found a bound state of a water molecule, which forms a C-O chemical bond (Figure 3a). However, the molecule can also join the cluster surface with the formation of a weak hydrogen bond (Figure 3b). Subsequent water molecules can be attached to the first molecule, thus forming chains along the graphene sheet surface (Figure 3c). The binding energy per molecule for such a chain is bigger than for the first molecule. The bound state was also found for an ammonia molecule (Figure 3d). We also observed a dissociation of the molecule as it approached the surface atoms, where a positive charge of +0.094 e was initially localized on the ($C_{97}H_{24}$ cluster) and +0.023 e on the ($C_{104}H_{26}$ cluster). The dissociation results are plotted in Figure 3e. Two molecules can join the adsorbed radical NH_2 to form the hydrogen bonds (Figure 3f). These calculation results are shown in Table 2.

A CH_2 radical is chemisorbed on the surface to form a double bond with one carbon atom (Figure 4a) and single bonds with two carbon atoms (Figure 4b). In the state shown in Figure 4b, a significant positive charge of $Q=+0.12$ e is localized on the attached radical, and the ΔE_{HL} value significantly decreases (by 0.46 eV).

TABLE 2. Calculation results of the geometric, electronic, and energy parameters for graphenes interacting with H₂O, NH₃ molecules and CH₂ radical (to Figure 3,4)

Molecule, XH _n	¹ P _{C-X}	R(C-X), Å	Q(XH _{n-1}), e	Q(C), e	Δ (ΔE _{HLL}), eV	E _b per molecule, eV
H ₂ O, covalent bond C-O	1.49	1.49	+0.335	-0.041	-0.37	0.41
H ₂ O, hydrogen bond C-H	0.05	2.04	-0.043	+0.006	-0.04	0.26
H ₂ O, four bound molecules	0.09	1.89	-0.064	-0.01	-0.12	0.36
NH ₃ , covalent bond C-N	0.83	1.50	+0.506	+0.011	-0.45	1.35
NH ₃ , a dissociation on the C ₉₇ H ₂₄ cluster	1.24	1.37	+0.068	+0.219	+0.24	2.50
NH ₃ , a dissociation on the C ₁₀₄ H ₂₆ cluster	0.95	1.49	-0.074	+0.111	+0.48	4.27
NH ₃ , three bound molecules	1.77	1.29	+0.328	+0.243	-0.16	1.44
CH ₂ , a double bond	1.92	1.31	-0.003	+0.014	+0.10	7.87
CH ₂ , two single bonds	0.99	1.48	+0.120	+0.194, -0.011	-0.46	3.63

¹P_{C-X} is bond order between the C and X atoms.

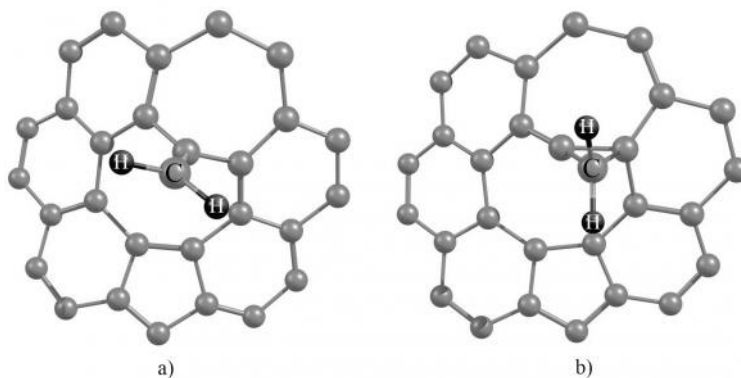


FIG. 4. CH₂ radical adsorption result, forming a double bond (a) and two single bonds (b)

4. Conclusion

These calculations enable one to conclude that H₂O, PH₃, NH₃ and CH₄ molecules are chemisorbed on the (1.0) grain boundary in graphene only in case of dissociation into fragments. The dissociation fragments' chemisorption increases the HOMO-LUMO energy difference values for (ΔE_{HL}) graphene. The ΔE_{HL} dependence on the type of adsorbed molecules can be used to create gas sensors.

For more complex grain boundaries, separating the areas with a misorientation angle of $\theta = 16^\circ$, with dangling bonds and other active adsorption sites, physical and chemical adsorption of molecules is possible without their dissociation into fragments. The activation energy of molecular and dissociative adsorption and the molecule-surface binding energy depend on the type of molecule, on the position of the adsorbing center, the number of adsorbed particles in the immediate vicinity, and the distance to the neighboring adsorbed particle. The simulation studies showed that molecules such as H₂O and NH₃ can form a chemical bond on the graphene surface containing a grain boundary with $\theta=16^\circ$ misorientation angles, without prior dissociation. In chemisorption states on graphene, the H₂O molecules show the acceptor properties, while the NH₃ molecules possess the donor properties. The CH₂ radical is chemisorbed on the surface to form some strong chemical bonds, wherein there can be a charge transfer of up to +0.12 e.

References

- [1] A. Salehi-Khojin, D. Estrada, K.Y. Lin, M.-H. Bae, F. Xiong, E. Pop, R.I. Masel. Polycrystalline graphene ribbons as chemiresistors. *Advanced Mater.*, **1**, P. 53–57 (2012).
- [2] S. Malola, H. Häkkinen, P. Koskinen. Structural, chemical, and dynamical trends in graphene grain boundaries. *Phys. Rev. B*, **81**, P. 165447(1-6) (2010).
- [3] P. Huang, C.S. Ruiz-Vargas, A.M. van der Zande, et al. Grains and grain boundaries in single-layer graphene atomic patchwork quilts. *Nature*, **469**, P. 389–392 (2011).
- [4] K. Kim, Z. Lee, W. Regan, C. Kisielowski, M.F. Crommie, A. Zettl. Grain boundary mapping in polycrystalline graphene. *ACS Nano*, **5**(3), P. 2142–2146 (2011).
- [5] O.V. Yazyev, S.G. Louie. Topological defects in graphene: dislocations and grain boundaries. *Phys. Rev. B*, **81**, P. 195420(1-7) (2010).
- [6] J.P. Stewart. MOPAC2009, Stewart Computational Chemistry, Vers. 11.039. W. (<http://OpenMOPAC.net>).
- [7] A.A. Granovsky, PC GAMESS. Firefly, Vers. 7.1. F, 8.0.0. (<http://classic.chem.msu.su/gran/gamess/index.html>).
- [8] Y.-H. Zhang, K.-G. Ge Zhou, K.-F. Xie, X.-C. Gou, J. Zeng, H.-L. Zhang, Y. Peng. Effects of Stone-Wales defect on the interactions between NH, NO and graphene. *J. Nanosci. Nanotechnol.*, **10**(11), P. 7347–7350 (2010).
- [9] P.A. Butrimov, O.Yu. Anan'ina, A.S. Yanovskii. Quantum-chemical study of interaction of hydrogen atoms with graphene. *J. Surface Investigation, X-Ray, Synchrotron and Neutron Tech.*, **4**(3), P. 476–479 (2010).
- [10] N.A. Lvova, O.Yu. Ananina. Quantum chemical simulations of water adsorption on a diamond (100) surface with vacancy defects. *Russian J. of Phys. Chem. A*, **87**(9), P. 1515–1519 (2013).

THE EVOLUTION OF FEW CYCLES OPTICAL PULSES IN A DOUBLE-LAYER GRAPHENE – BORON NITRIDE TAKING INTO ACCOUNT NONLINEARITY OF A MEDIUM

A. V. Pak¹, M. B. Belonenko²

¹Volgograd State University, Volgograd, Russia

²Volgograd Institute of Business, Volgograd, Russia

pak.anastasia@gmail.com, mbelonenko@yandex.ru

PACS 75.75 -, 73.20 Hb, 73.22 Pr

The propagation of ultra-short optical pulses in a thin film created by graphene grown on a boron nitride was considered, taking into account non-linear medium characteristics. Electron conduction in such a system described with a long-wave effective Hamiltonian for the low temperatures media. The electromagnetic field is taken in the framework of classical Maxwell equations. Dependence of the pulse shape on the initial pulse amplitude and the parameters of the linear and nonlinear polarization is shown.

Keywords: Graphene, Boron Nitride, Optical pulse, Nonlinearity.

1. Introduction

Recently, the number of studies on boron nitride-supported graphene has increased [1–8]. Primarily, this is due to graphene’s unusual properties [9]. Note that boron nitride has a similar hexagonal lattice to graphene, as well as the fact that the ionic character of interatomic bonds in the hexagonal boron nitride (h-BN) leads to the absence of surface-based ‘dangling’ covalent bonds and charge trapping [8]. As found in [8], the roughness of graphene on h-BN is much smaller than that of graphene on SiO₂, and charge fluctuations are two orders of magnitude weaker. In general, the electronic characteristics of graphene on h-BN are almost the same as that of free graphene. Thus, to explore graphene on a substrate is much easier and more convenient [8].

The evolution of an ultra-short optical pulse propagating in a double-layer structure of graphene – boron nitride in non-magnetic environments would be revealed taking into account the nonlinear polarization of the medium.

2. Basic equations

We considered a layer of graphene on a substrate of boron nitride. The Hamiltonian we have chosen, in a long-wave approximation, can be written in matrix form as:

$$H(k) = \begin{pmatrix} 0 & k^* & 0 & t \\ k & 0 & 0 & 0 \\ 0 & 0 & \Delta & f^* \\ t & 0 & f & -\Delta \end{pmatrix}, \quad (1)$$

where t is the electron overlap integral between the layers of graphene and boron nitride; Δ is the band gap for boron nitride; $k = v_{FG}(k_x + ik_y)$, v_{FG} – is the Fermi velocity for graphene;

k_x, k_y – are the electron pulse components: $f = v_{FBN} (k_x + ik_y)$; v_{FBN} – is the Fermi velocity for boron nitride.

The Hamiltonian (1) can be rewritten using a block matrix structure [10]:

$$H(k) = \begin{pmatrix} 0 & k^* & 0 & t \\ k & 0 & 0 & 0 \\ 0 & 0 & \Delta & f^* \\ t & 0 & f & -\Delta \end{pmatrix} \equiv \begin{pmatrix} H_{11} & H_{12} \\ H_{21} & H_{22} \end{pmatrix}.$$

In the case of a large band gap in boron nitride compared to the electron's energy, a long-wave approximation can be considered. This makes it possible to write the effective Hamiltonian analogously to bigraphene [10]:

$$H^{eff} \equiv H_{11} - H_{12}H_{22}^{-1}H_{21} = -\frac{1}{t} \begin{pmatrix} \Delta & -\frac{1}{t}f^*k^* \\ -\frac{1}{t}fk & -\frac{1}{t^2}|k|^2\Delta \end{pmatrix}. \quad (2)$$

The Hamiltonian (2) is easily diagonalized, which gives the electronic spectrum:

$$\varepsilon(k_x, k_y) = \frac{1}{2}\Delta \left(\left(1 - \frac{v_{fg}^2 (k_x^2 + k_y^2)}{t^2} \right) + \sqrt{\left(1 + \frac{v_{fg}^2 (k_x^2 + k_y^2)}{t^2} \right)^2 + \frac{4v_{fg}^2 v_{fnb}^2 (k_x^2 + k_y^2)^2}{\Delta^2 t^2}} \right), \quad (3)$$

where v_{FG}, v_{FBN} – the Fermi velocity of electrons for graphene and boron nitride, respectively.

According to quantum-mechanical laws, the presence of an external electric field E , directed along the X axis, the Coulomb gauge can be chosen in the following form: $E = -\frac{1}{c} \frac{\partial A}{\partial t}$.

It is necessary to replace the momentum with a generalized momentum: $p \rightarrow p - \frac{e}{c}A$ (e is the electron charge). In this case, the effective Hamiltonian (2) can be rewritten as:

$$H = \sum_{p\sigma} \varepsilon \left(p - \frac{e}{c}A(t) \right) a_{p\sigma}^+ a_{p\sigma}, \quad (4)$$

where $a_{p\sigma}^+, a_{p\sigma}$ – are the creation and annihilation operators of electrons with quasi-momentum p and spin σ . The vector-potential A is considered as $A = (0, 0, A(x, t))$.

Maxwell's equations for polarization of the medium can be written as [11]:

$$\frac{\partial^2 \mathbf{E}}{\partial x^2} - \frac{1}{c^2} \frac{\partial^2 \mathbf{E}}{\partial t^2} + \frac{4\pi}{c} \frac{\partial \mathbf{j}}{\partial t} = \frac{4\pi}{c^2} \frac{\partial^2 \mathbf{P}}{\partial t^2}. \quad (5)$$

Here, we neglect the laser beam diffraction in directions perpendicular to the beam propagation axes. In Eqn. (5), \mathbf{E} is an electric field of light wave, $\mathbf{P} = \alpha \mathbf{E} + \beta |\mathbf{E}|^2 \mathbf{E}$ – is a polarization of the medium, t is a time, c is a speed of light in a vacuum. There is a simple model for the medium nonlinearity when the polarization vector is considered to be parallel to \mathbf{E} .

We write the expression for the current density:

$$j_0 = e \sum_{ps} v_s \left(p - \frac{e}{c}A(t) \right) \langle a_{ps}^+ a_{ps} \rangle, \quad (6)$$

where $v_s(p) = \frac{\partial \varepsilon_s(p)}{\partial p}$, and brackets denote averaging with the nonequilibrium density matrix $\rho(t)$: $\langle B \rangle = \text{Sp}(B(0)\rho(t))$.

Further, we consider the case of low temperatures, when the sum (6) contributes only a small area in momentum space near the Fermi level. Therefore, we rewrite the expression for the current density in the form:

$$j = e \int_{-\Delta}^{\Delta} \int_{-\Delta}^{\Delta} dp_x dp_y v_y \left(p - \frac{e}{c} A(x, t) \right). \quad (7)$$

The range of pulses integrated in (7) was determined from the particles number equality:

$$\int_{-\Delta}^{\Delta} \int_{-\Delta}^{\Delta} dp_x dp_y = \int_{-\Delta}^{\Delta} \int_{-\Delta}^{\Delta} dp_x dp_y \langle a_{p_x, p_y}^+ a_{p_x, p_y} \rangle.$$

3. The results of numerical simulation

Equation (5) was solved numerically using a direct finite-difference cross-like scheme [12]. Steps by time and coordinates were determined using standard conditions of stability, strides of finite-difference scheme were halved serially, until the solution did not change in the eighth sign. The initial conditions were chosen as an ultra short optical pulse consisting of a single oscillation of the zero-width field, respectively, that can be specified by setting the potential \mathbf{A} as:

$$\begin{aligned} A(x, t) &= Q \exp(-(x - vt)^2/\gamma), \\ \gamma &= (1 - v^2)^{1/2}, \end{aligned} \quad (8)$$

where Q is the amplitude, v is the initial ultra-short pulse velocity on the sample input. This initial condition corresponds to the fact that the sample is fed an ultra-short pulse, consisting of a single oscillation of the electric field. The values of energy parameters are expressed in Δ units. The resulting evolution of the electromagnetic field propagating along the sample is shown in Fig. 1.

The amplitude of the pulse decreased when the linear polarization of the medium gradually increased. This fact can be interpreted as the pulse spending part of its energy on medium polarization.

The pulse behavior presented in Fig. 1 concerns the presence of dispersion, which leads to a broadening of the optical pulse, as well as non-linearity in the same equation, thus leading to a ‘narrowing’ of the pulse. The competition between these two terms leads to a deformation of the initial pulse shape and rise to its stable form.

More clearly, the effects associated with nonlinear pulse appear at the front and lead to the formation of additional peaks and the broadening of the pulse which can be explained by an imbalance between dispersion and nonlinearity in the system. This is clearly seen in Fig. 3. The dependence of the electric field pulse on the magnitude of the medium’s nonlinear polarization is shown in Fig. 3.

As can be seen in Fig. 3, involving non-linear polarization leads to the appearance of a wave front for the second maximum. As in the case of linear polarization, the initial pulse amplitude decreases, which is to be expected.

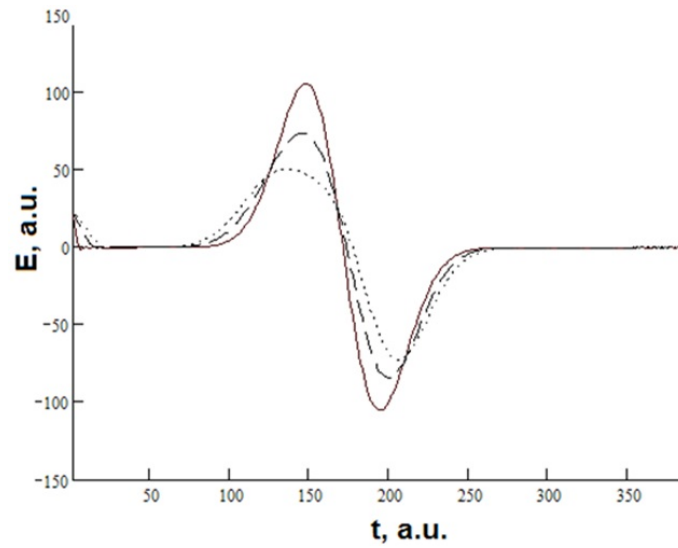


FIG. 1. Time dependence of the electric field: a) solid line – $\alpha = 0.0$; b) dotted line – $\alpha = 0.3$; c) dashed line – $\alpha = 0.5$, the nonlinear polarization is absent. Time, a.u. is time $3 \cdot 10^{-16}$ s.; electric field a.u. is 10^7 V/m

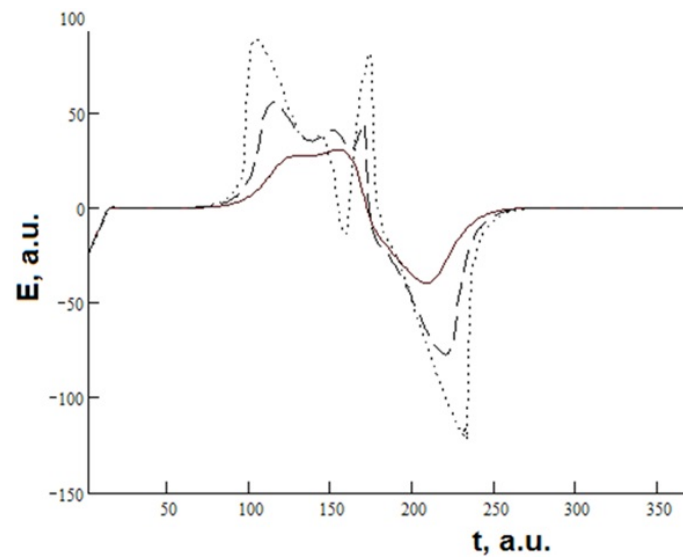


FIG. 2. Time dependence of the pulse form for different cases of pulse amplitude value: a) solid line – $Q = 2$; b) dotted line – $Q = 3$; c) dashed line – $Q = 5$. Time and electric field a.u. as in Fig. 1

4. Conclusion

As follows from the obtained results, the stable ultra-short optical pulses can undergo propagation in hexagonal boron nitride-supported graphene in a medium with nonlinear polarization.

By increasing the initial pulse amplitude, the wave front is broadened, and there is a second pulse of lower intensity. This effect may be useful in the development of hybrid devices based on the effect of light interaction with graphene electrons.

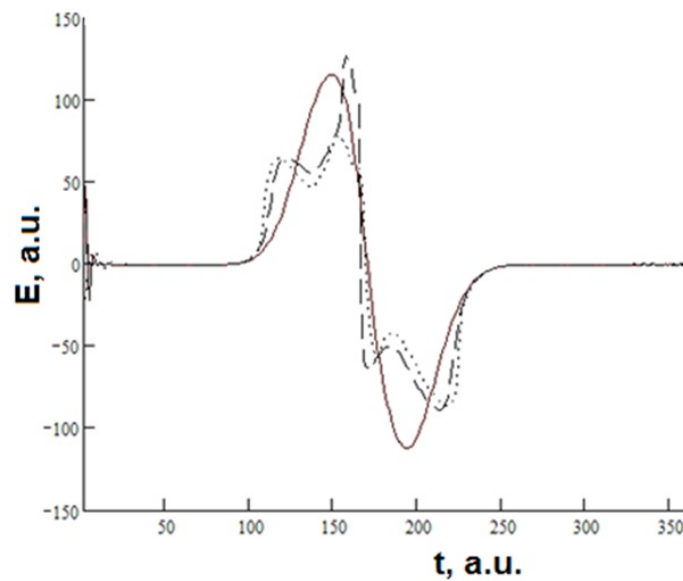


FIG. 3. Time dependence of the electric field on time taking into account the nonlinear polarization of the medium: a) solid line – $\beta = 0.03$; b) dotted line – $\beta = 0.4$; c) dashed line – $\beta = 0.6$ the dispersion is almost zero, $\alpha = 0.01$. Time and electric field a.u. as in Fig.1

Acknowledgments

This work was supported by Russian Foundation for Basic Research (grant No. 12-02-31654).

References

- [1] Giovannetti G., Khomyakov P.A., et al. Substrate-induced band gap in graphene on hexagonal boron nitride: Ab initio density functional calculations. *Phys. Rev. B*, **76**, P. 073103 (2007).
- [2] Greber T. Graphene and boron nitride single layers. In: *The Handbook of Nanophysics*, ed. by Sattler K., Taylor and Francis Books, Inc, Oxfordshire, 2010.
- [3] Avetisyan A.A., Partoens B., Peeters F.M. Stacking order dependent electric field tuning of the band gap in graphene multilayers. *Phys. Rev. B*, **79**, P. 035421 (2009).
- [4] Wakabayashi K., Takane Y., Sigrist M. Perfectly conducting channel and universality crossover in disordered graphene nanoribbons. *Phys. Rev. Lett.*, **99**, P. 036601 (2007).
- [5] Blase X., Rubio A., Louie S.G., Cohen M.L. Stability and band-gap constancy of boron-nitride nanotubes. *Europhys. Lett.*, **28** (5), P. 355–340 (1994).
- [6] Chen Y., Zou J., Campbell S.J., Le Caer G. Boron nitride nanotubes: Pronounced resistance to oxidation. *Appl. Phys. Lett.*, **84**, P. 2430–2432 (2004).
- [7] Breshenan M.S., Hollander M.J., et al. Integration of hexagonal boron nitride with quasi-freestanding epitaxial graphene: toward wafer-scale, high-performance devices. *ACS Nano*, **6** (6), P. 5234–5241 (2012).
- [8] Xue J., Sanchez-Yamagishi J., et al. Scanning tunneling microscopy and spectroscopy of ultra-flat graphene on hexagonal boron nitride. *Nature Mater.*, **10**, P. 282–285 (2011).
- [9] Rutter G.M., Jung S., et al. Microscopic polarization in bilayer graphene. *Nature*, **7**, P. 649–655 (2011).
- [10] Cortijo A., Guinea F., Vozmediano M.A.H., Geometrical and topological aspects of graphene and related materials. *arXiv*: 1112.2054v1 (2011).
- [11] Landau L.D., Lifshitz E.M. *Theoretical physics. II. Field theory*, Science, Moscow, 1988, 512 p.
- [12] Bakhvalov N.S. *Calculus of approximations (analysis, algebra, ordinary differential equations)*, Science, Moscow, 1975, 632 p.

NANODIAMOND-BASED OIL LUBRICANTS ON STEEL-STEEL AND STAINLESS STEEL – HARD ALLOY HIGH LOAD CONTACT: INVESTIGATION OF FRICTION SURFACES

M. Ivanov¹, Z. Mahbooba^{2,3}, D. Ivanov¹, S. Smirnov⁴,
S. Pavlyshko⁴, E. Osawa⁵, D. Brenner³, O. Shenderova²

¹Ural Federal University, Yekaterinburg, Russia

²International Technology Center, Raleigh, USA

³North Carolina State University, Raleigh, USA

⁴Institute of Engineering Science Ural Branch RAS, Yekaterinburg, Russia

⁵NanoCarbon Research Institute, Tokita, Japan

m.g.ivanov@ustu.ru, zmahbooba@itc-inc.org, d.m.ivanov@ustu.ru, svb@imach.uran.ru,
osawaeiji@aol.com, brenner@ncsu.edu, oshenderova@itc-inc.org

PACS : 81.40.Pq, 81.07.-b

In the current paper, synergistic compositions of detonation nanodiamond (DND) particles in the form of aggregates and fully deagglomerated 5nm particles were used as additives to 10W40 and 5W30 oils, correspondingly. Ring-on-disk and block-on-ring tribological tests were performed under high load conditions (300N and 980N) using friction pairs with different relative hardness. Significant reduction of wear was observed for the HRC25/25, HRC25/50 and HRC30/HRC60 steel/steel friction pairs, while for the HRC60/60 steel/steel and HRA86/HRC24 hard alloy/steel friction pairs increased wear took place. It was concluded that use of ND in lubricants under high load conditions should be approached cautiously taking into account absolute and relative hardnesses of the friction surfaces.

Keywords: Nanodiamond, Nanolubricants, Friction, Wear, Polishing.

1. Introduction

Over the last few years, interest in applications of nanoparticles as lubricant additives (nanolubricants) has steadily grown due to the demonstrated reduction of friction and wear with the use of nanoparticles-containing lubricant formulations [1]. Carbon-based ultrafine additives play a special role among nanomaterials due to their high biocompatibility [2] providing reduced environmental impact effect. Studies of lubricating compositions with detonation nanodiamond (DND) and detonation soot (a mixture of DND particles with different forms of sp²-bonded carbon) [3–5] as additives have demonstrated their positive impact on the performance of lubricant compositions, often superior to other nanoparticle fillers.

While the positive effect of DND additives on the lubrication properties of oils has been demonstrated [3–7] and a variety of hypotheses of DND tribological action are considered, in order to optimize additive composition and expand the range of applications of DND nanolubricants, mechanisms of DND action need to be further elucidated and clearly linked to the operational conditions of tribological tests (characteristics of friction surfaces, load, rotational speed, composition of lubricant, etc.). In the current work, we have focused on understanding of the role of friction surfaces properties, particularly relative hardness of the friction pairs. In the earlier work by Zhornic et al. [5], modification of Litol-24 lubricant with detonation soot

reduced wear of steel-steel friction pairs with hardness 20–25 HRC by approximately 30-fold and for the steel pairs with hardness 30–40 HRC by 5-fold, correspondingly. However, for the steel with hardness 62–65 HRC, the wear was increased ~ 1.14 times. The authors attributed the increased wear of the friction pairs with an initial hardness ≥ 60 HRC in the presence of detonation soot to the brittle fracture of the surface layer originating from increased stress concentration due to hard nanodiamond particles embedded on the surface. The [5] concentration of the detonation soot in the lubricant, though, was relatively high, ~ 1 wt%. Since the authors used *as is* detonation soot, it can be assumed that the average agglomerate size was typical for detonation soot, a few hundred nanometers.

In the current paper, synergistic compositions of detonation nanodiamond (DND) aggregates as well as deagglomerated 5nm particles [9] were used with molybdenum dialkyldithiophosphate and zinc dialkyldithiophosphate as additives to 5W30 and 10W40 oils. The DND concentration was varied between 0.01 and 0.05 wt%. Block-on-ring tribological tests were performed using steel\steel block and ring samples with HRC30/HRC60 and HRC60/HRC60 relative hardness, correspondingly. In the disk-on-ring test steel\steel friction pairs with hardness HRC25\25, HRC25\50 and a hard alloy (WC)\steel friction pairs with hardnesses HRA86\HRC24 were used. In the comparative tests with or without DND additives, a significant reduction of wear or, on the contrary, an increase in wear took place, depending on the hardnesses of the friction pairs. It can be concluded that use of ND in lubrication of friction pairs tested under high load conditions and in the presence of hard surfaces should be approached cautiously, even when using fully deagglomerated 5 nm detonation ND particles.

2. Experimental

In the current work, agglomerates of the detonation ND particles with 100 nm average particle size (DND synthesized by NPO Altai) as well as deagglomerated DND were used. Deagglomeration of DND was done using attrition bead milling [9], resulting in particles with 4.6 nm average volumetric size in DI water as measured via a dynamic light scattering technique using a Malvern Instruments tool. The trade name of this DND produced at NanoCarbon Research Institute is NanoAmando. Stable transparent colloidal dispersions of DND in PAO oil (PAO-6) have been formulated using a special polyfluorinated surfactant [10]. Dispersion of the DND in the oil was assisted by ultrasonic treatment. An example of stable colloidal suspension of 20 nm DND in PAO oil with excellent dispersivity was illustrated earlier [8]. DND-based additives were used in combination with other synergistic additives [8], such as organic molybdenum and zinc additives, molybdenum dialkyldithiophosphate (MoDDP) and zinc dialkyldithiophosphate (ZDDP). Additive compositions were prepared with same concentration of synergistic additives, either pure MoDDP (called ND/M) or MoDDP in combination with ZDDP (called ND/M/Z).

The commercial oils for testing were the 5W30 (Semi-Synthetic) – Mobil Super API SN engine oil and Lukoil Standard 10W40 API SF/CC mineral oil. Mixing of the DND-based additives with commercial oils was done in 1:30 and 1:60 proportions. Testing of the DND-based additive performance in 5W30 Mobil Super oil was done using a block on ring test apparatus, UMT-3, produced by CETR, USA. A block from SAE 01 tool steel with hardness HRC=30 or HRC=60 and flat friction surfaces with roughness $0.2 \mu\text{m rms}$ were used. The stainless steel ring had a hardness HRC=60 and roughness $0.3 \mu\text{m rms}$. The rotational velocity was 200 rpm and the load was 300 N. This set of experiments was done at an average temperature of 75–80 °F and 45–50% humidity. Samples were purified with IPA after the tribotests for further analysis. Scar profiles were measured using an Alpha-Step IQ stylus-based surface profiler. Roughness maps and roughness were measured using a Zygo NewView 5000

3D optical profiler. Roughness was measured at 5 points along a scar (ring surface) and averaged. At every point, the roughness was measured over a distance of 50 μm . Tribological experiments were performed using a special tribology tester (ring-on-disk module) with two carbon steels and stainless steel (austenite steel 12Kh18N10T) - hard alloy (WC, HRC= 74–76). The rotational velocity was 200 rpm and the load was 980 N, 5 hour test. Measurements of mass wear of the friction pairs were performed in this set of experiments.

3. Results and discussion

The 5 nm ND in 5W30 Mobil oil experiments were performed for 2 friction pairs of the stainless steel samples, which are designated below as H30/H60 ('soft on hard') and H60/H60 ('hard on hard') surfaces. The H30/H60 pair tests were performed for three ND-based additives (ND/M/Z at 1:30 and 1:60 dilutions in Mobil and ND/M at 1:60 dilution). The H60/H60 pair tests were performed for the composition that showed the best results in the test for the H30/H60 pair. All results were compared to the reference samples ran for pure Mobil oil without ND-based additives. For 100nm ND in 10W40 Lukoil oil, experiments were done for 1 composition of the ND-based additive, ND/M at 1:60 dilution. Details are provided below.

3.1. Tribological characteristics for the H30\H60 friction pair

Fig. 1a presents the friction coefficient as a function of time for H30 block over H60 ring for pure Mobil 5W30 oil and for the oil with DND-based additive (ND/M/Z at 1:60 dilution in Mobil). When using a ND-based additive, an improvement in the COF of 10% was observed in a 5 hour test. Modest reduction in the COF was accompanied by a significant reduction in wear. The scar area for the pure Mobil 5W30 samples was 1.777 μm^2 , while for the sample tested with DND additive, it was about half that value: 980 μm^2 . Scar profiles obtained with a stylus profilometer are presented in Fig. 1b. The scar profile was smoother for the sample treated with the DND additive, as compared with pure Mobil oil (Fig. 1b). Fig. 2 illustrates optical micrographs of the scars in the block samples as well as roughness maps of the scar in a block and ring surface after 5hr tests for tests run with pure Mobil oil and Mobil oil with ND-based additive. The 3-D topographical maps of the ring surfaces and the scars formed during tests using pure Mobil oil and Mobil oil with DND additive demonstrate a more pronounced topological uniformity for the surfaces of samples treated with the DND additive. Measurements averaged over 5 data points are also provided in Fig. 2, and clearly demonstrate that the presence of DND provides a significant polishing effect: the rms of the scars on the block and ring surfaces tested with the DND additive are about 28% and 37% lower, correspondingly, than the roughness of the scars and rings observed in experiments performed with pure oil.

Table 1 summarizes measurements of COF, wear and roughness for the samples tested with different type and concentration of the synergistic additives to ND. As can be seen from the table, a mixture of MoDDT and ZDDP in combination with 5 nm ND provides more pronounced resistance to wear than a combination of the ND and MoDDP. The combination of ND and ZDDP was not tested, since a residue appeared in the mixture a few days after preparation.

Combinations of ND and MoDDP and ND\MoDDP\ZDDP were transparent and colloidally stable for at least 1 month (time of observation).

3.2. Tribological characteristics for the H60\H60 friction pair

Figure 3a presents the friction coefficient as a function of time for H60 block over H60 ring for pure Mobil 5W30 oil and for the oil with DND-based additive (ND/M/Z at 1:60

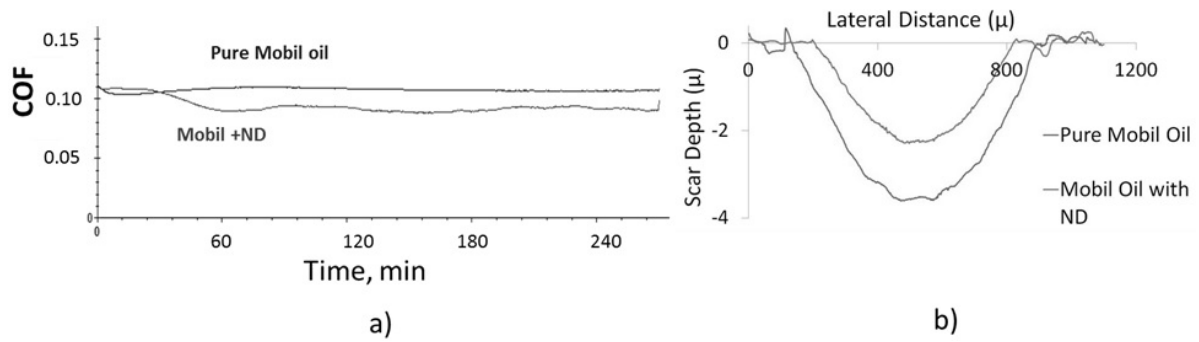


FIG. 1. Friction coefficient as a function of time (a) and scar profiles in the block (b) for H30 block obtained in the 200 rpm/30 kg 5 hrs block-on-ring tests for pure Mobil 5W30 oil and for the oil with DND additive.

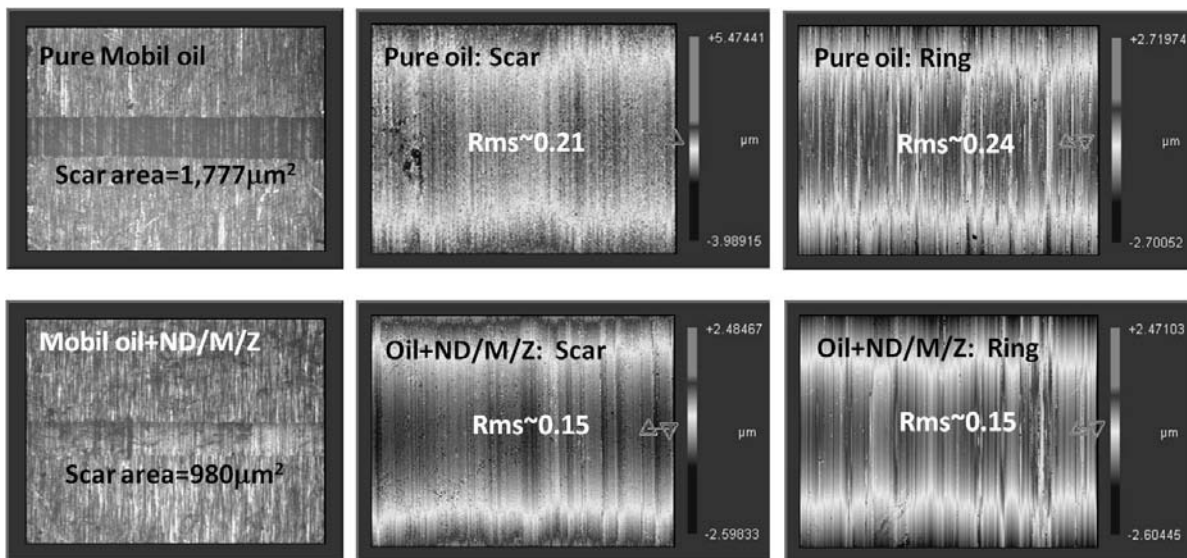


FIG. 2. Microscopy images ($10\times$ zoom) (left) and roughness maps of the scar in a block and a ring after 5hrs tests at 30 kg load and 200 rpm for pure Mobil 5W30 oil (top) and its dilution with ND/M/Z additives for the H30 block over H60 ring test ('soft on hard' surfaces). Dimensions of the roughness maps are $0.72\text{ mm} \times 0.54\text{ mm}$

dilution in Mobil). COF in a test with oil containing ND-based additive was by 4% higher in comparison with COF for pure oil. An increase in the COF was accompanied by a significant increase in wear. The scar area for the pure Mobil 5W30 samples was $525\ \mu\text{m}^2$, while the sample tested with the DND additive had a scar area about twice that level, $1190\ \mu\text{m}^2$. Scar profiles obtained with a stylus profilometer are presented in Fig. 3b; they were rough for both samples. Fig. 4 illustrates optical micrographs of the scars in the block samples as well as the roughness maps of the scar in a block and ring surface after 5 hrs for tests run with pure Mobil oil and Mobil oil with the ND-based additive. The 3-D topographical maps of the ring surfaces and the scars formed during tests using pure Mobil oil with the DND additive demonstrate that the presence of DND significantly increased the roughness when hard steel surfaces were sliding against each other at the high external load used in these experiments (300 N). This observation was also confirmed by the increased roughness values for both the ring and the scar in the block for the sample tested with a ND additive, as compared to the test using pure Mobil

TABLE 1. Samples composition, hardness of the friction pair (block/ring) and tribological characteristics of the tests (scar width and depth ($W \times D$), scar area, average COF (AvgCOF) and COF at the end of the 5 hrs test (End COF))

Sample	Composition	Scar $W \times D$ (scar area, μm^2)	AvgCOF & (End COF)	RMS Scar/Ring
H30/H60	Pure Mobil	722.78×3.68 (1777)	0.1086 ± 0.00266 (0.1065)	$0.214 \pm 0.040 /$ 0.240 ± 0.039
H30/H60	ND/M/Z 1:30	655.14×2.92 (1264)	0.1006 ± 0.01167 (0.092)	$0.165 \pm 0.031 /$ 0.141 ± 0.043
H30/H60	ND/M/Z 1:60	627.89×2.53 (980)	0.1005 ± 0.0117 0.090	$0.152 \pm 0.050 /$ 0.147 ± 0.031
H30/H60	ND/M 1:60	748.01×3.90 (1892)	0.09365 ± 0.0158 0.089	$0.150 \pm 0.017 /$ 0.222 ± 0.033
H60/H60	Pure Mobil	339.18×0.74 (525)	0.09674 ± 0.00205 0.0978	$0.120 \pm 0.030 /$ 0.236 ± 0.022
H60/H60	ND/M/Z 1:60	539.05×1.89 (1190)	0.1045 ± 0.00255 0.102	$0.381 \pm 0.034 /$ 0.272 ± 0.011

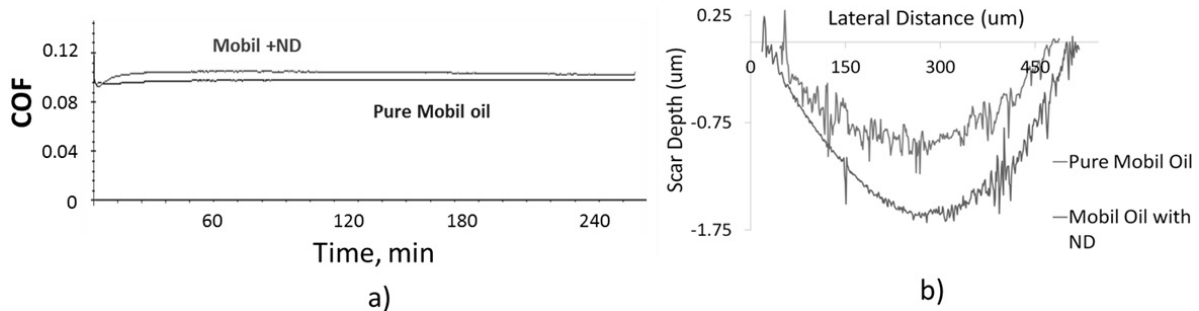


FIG. 3. Friction coefficient as a function of time (a) and scar profiles in the block (b) for H60 block obtained in the 200 rpm/30 kg 5 hrs block-on-ring tests for pure Mobil 5W30 oil and for the oil with ND/M/Z additive

oil (Table 1, Fig. 4). Especially high roughness was observed for a scar in the block, since its surface is under constant sliding load, while for the ring, sliding contact is distributed over its periphery.

3.3. Wear characteristics for the steel\steel and hard alloy\steel friction pairs

Table 2 illustrates results of the wear tests for the friction pairs composed of materials with different composition and hardness. The following friction pairs were tested: carbon steel St45 (normalized versus normalized) HRC 25/25; carbon steel St45 (normalized versus quenched) HRC25/50; stainless steel (austenite steel 121810) HRC24 versus hard alloy (WC, 15%Co), HRA86.

A significant increase in wear can be seen from the Table 2 for the hard alloy WC in the test with oil containing ND additive.

4. Conclusion

Nanodiamond-based additive for lubricants is now available as a commercial product. Current tests indicate that application of ND-based additives need to be used with caution when

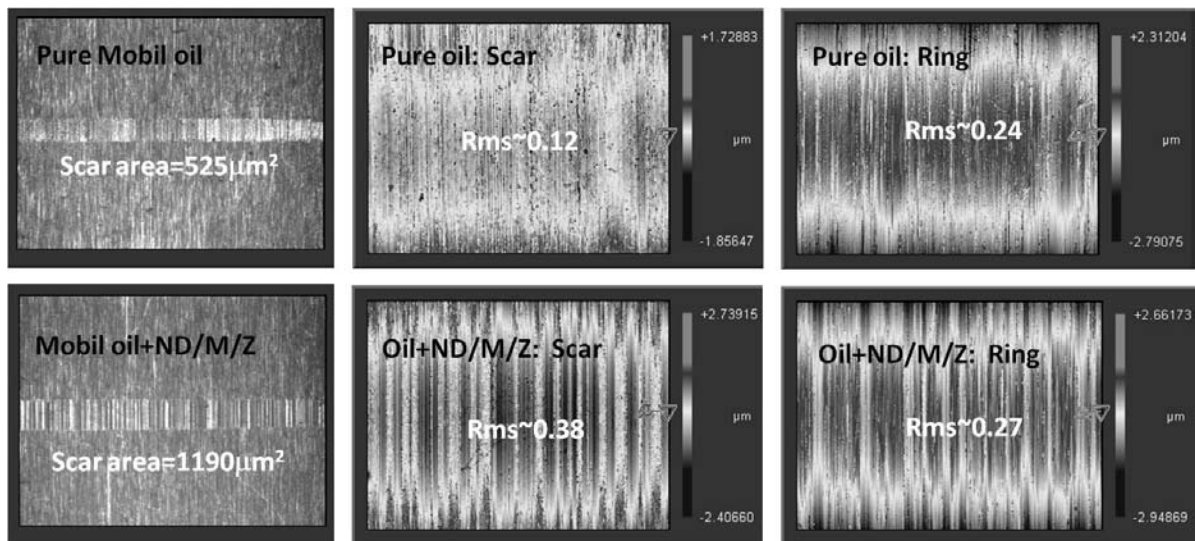


FIG. 4. Microscopy images ($13\times$ zoom) (left) and roughness maps of the scar in a block and a ring after 5 hrs tests at 30 kg load and 200 rpm for pure Mobil 5W30 oil (top) and its dilution with ND/M/Z additives for the H30 block over H60 ring test ('hard on hard' surfaces). Dimensions of the roughness maps are $0.53\text{ mm} \times 0.4\text{ mm}$

TABLE 2. Wear characteristics of rings and disks in the 5 hrs tests with and without ND additives in the 10W40 oil at 200 rpm and 980 N load in the disk-on-ring test.

Sample (ring/disk)	Ring pure oil, wear, mg	Ring oil+ND, wear, mg	Disk pure oil, wear, mg	Disk oil+ND, wear, mg
HRC 25/25	0.04	0.03	0.035	0.015
HRC 25/50	0.01	0.005	0.015	0.005
HRC24/HRA86	0.005	0.0	0.013	0.028

taking into consideration the hardness of the friction surfaces. While in the 'hard on soft' steel\steel friction pairs NDs provide significant reduction in wear and demonstrate a polishing effect, in the 'hard on hard' steel friction pair and in the hard WC alloy the abrasive nature of NDs plays a role and results in increased wear of the sliding surfaces. A possible mechanism can be incorporation of ND particles into the hard surface and playing a role of high stress concentrators [5]. However, a detailed mechanism for this phenomenon requires further studies.

Acknowledgments

Present work is supported by RFBR (grant 12-03-93937-G8.) and G8 Japan, USA: Nanodiamond-based Nanospacer Lubricants.

References

- [1] Neville A., Morina A., Haque T., Voong M. Compatibility between tribological surfaces and lubricant additives-how friction and wear reduction can be controlled by surface/lube synergies. *Tribology International*, **40**, P. 1680–1695 (2007); *Nanolubricants*, ed. By J.-M. Martin and N. Ohmae, Wiley, 2008, 246 p.

- [2] Schrand A. M. et al. Cytotoxicity and Genotoxicity of Carbon Nanomaterials. In: *Safety of Nanoparticles: From Manufacturing to Medical Applications*, ed. by Webster T.J. [Ser. Nanostructure Science and Technology], P. 159–187 (2009).
- [3] Ivanov M., Ivanov D. Nanodiamond nanoparticles as additives to lubricants. In: *Ultrananocrystalline Diamond*, 2nd edn, ed. by Shenderova O., Gruen D., Elsevier, 2012, ch. 8.
- [4] Dolmatov V. Yu. Detonation Nanodiamonds in Oils and Lubricants. *J. Superhard Materials*, **32**, P. 14–20 (2010).
- [5] Zhornik V.I., Kukareko V.A., Belotserkovsky M.A. *Tribomechanical Modification of Friction Surface by Running-In in Lubricants with Nano-Sized Diamonds*. Nova Science Publishers, 2011.
- [6] Ivanov M.G., Kharlamov V.V., et al. Tribological properties of the grease containing polytetrafluoroethylene and ultrafine diamond. *Friction and Wear*, **25** (1), P. 99–103 (2004).
- [7] Ivanov M.G., Pavlyshko S.V., et al. Nanodiamonds Particles as Additives in Lubricants. *Mater. Res. Soc. Symp. Proc.*, **1203**, 1203-J17-16 (2010).
- [8] Ivanov M.G., Pavlyshko S.V., et al. Synergistic Compositions of Colloidal Nanodiamond as Lubricant-additive. *JVST B*, **28** (4), P. 869–877 (2010).
- [9] Osawa E. Recent progress and perspectives in single-digit nanodiamond. *Diamond Relat. Mater.*, **16**, P. 2018–2022 (2007).
- [10] Ivanov M.G., Deev L.E., Shenderova O.A. Lubricant additive. WO/2011/011714. International Application, No.: PCT/US2010/043099. Publication Date: 27.01.2011.

SYNERGISTIC INFLUENCE OF FLUORINE AND HYDROGEN ON PROCESSES OF THERMAL TRANSFORMATIONS OF CARBON-CONTAINING SYSTEMS UNDER HIGH PRESSURES

V. A. Davydov¹, A. V. Rakhmanina¹, V. N. Agafonov², V. N. Khabashesku³

¹L.F.Vereshchagin Institute for High Pressure Physics of the RAS, Troitsk, Moscow

²GREMAN, UMR CNRS-CEA 6157, Université F. Rabelais, Tours

³Department of Chemical and Biomolecular Engineering, University of Houston

vdavydov@hppi.troitsk.ru, avrakhman@yandex.ru, agafonov@univ-tours.fr, valery@uh.edu

PACS 62.50.-p, 81.07.-b, 81.05.ug

Thermal transformations of naphthalene ($C_{10}H_8$), octafluoronaphthalene ($C_{10}F_8$) and their binary mixtures at 8.0 GPa have been investigated by X-ray diffraction, Raman spectroscopy, scanning and transmission microscopies. As a result, the pronounced synergistic effect of fluorine and hydrogen on mechanisms, p , T parameters and products of pressure-temperature-induced transformations of carbon-containing systems has been established. Simultaneous presence of fluorine and hydrogen gives rise to significant reduction of the temperature thresholds (TT) for carbonization, graphitization and diamond formation in $C_{10}H_8 - C_{10}F_8$ mixtures in comparison with the TT values for pure $C_{10}H_8$ and $C_{10}F_8$ at the same pressure. This synergistic effect manifests itself also in the simultaneous presence in the products of transformation of both nano- and micrometer-sized diamond fractions. The reasons of formation of different diamond fractions in the products of binary mixture treatment are discussed in this work.

Keywords: High pressure, High temperature, Transformations, Nanocarbon materials.

1. Introduction

Comparative studies of pressure-temperature-induced transformations of naphthalene ($C_{10}H_8$), fluorographite ($CF_{1.1}$), and their binary mixtures have led to the observation of a synergistic effect for fluorine and hydrogen on the mechanisms, p , T parameters and products of the transformations of binary mixtures of hydrocarbons and fluorocarbon compounds relatively to transformations of pure compounds [1]. Along with a significant decrease in the p , T parameters for the initiation of carbonization, graphitization and diamond formation in binary mixtures relatively to transformations of pure hydrocarbon and fluorocarbon compounds, a synergistic effect results in a considerable increase in the content of nanosize graphite and diamond phases in the products of binary mixture transformations. This finding is particularly attractive from an application standpoint, since it presents additional opportunities for the synthesis of pure and doped nanosize modifications of graphite and diamond with fine-tuned properties. However, the mechanistic nature of the nanosize carbon phase formation remains a subject for discussion. In the present work, we have attempted a more detailed investigation of the synergistic effect on processes of nanosize carbon phase formation in the products of reactions using hydrocarbon-fluorocarbon mixtures, which has been exemplified by two structural analogs, naphthalene and octafluoronaphthalene.

2. Experimental section

Naphthalene (Chemapol) and octafluoronaphthalene (Alfa Aesar) have been used as starting hydrocarbon and fluorocarbon materials, respectively. Homogeneous 1:1 mixtures of $C_{10}H_8 - C_{10}F_8$ were prepared by thorough grinding of weighed amounts of powdered starting materials in an agate mortar. Samples of heterogeneous $C_{10}H_8 - C_{10}F_8$ mixtures appeared as two-layer compacts made from two separately compacted pellets of pure naphthalene and octafluoronaphthalene.

Tablet-shaped samples (5 mm diameter, 4 mm height) of starting materials were placed into a graphite heater and then treated in the ‘Toroid’ high pressure apparatus under a pressure of 8.0 GPa and different temperatures up to 1500 °C. Isothermal exposure times were kept at 20 seconds. Samples of high pressure states were quenched under pressure and recovered at ambient conditions, and then characterized by X-Ray diffraction, Raman spectroscopy, scanning (SEM) and transmission (TEM) electron microscopies. X-ray diffraction patterns of powder samples were recorded on an INEL CPS 120 diffractometer using $Co K_{\alpha 1}$ radiation source. Microscopy characterization of the samples was carried out on SEM Ultra plus (Carl Zeiss) and TEM JEOL JEM-1230 microscopes.

3. Results and discussion

XRD patterns for the starting $C_{10}H_8$, $C_{10}F_8$ and products of their treatment under 8.0 GPa pressure and different temperatures are shown in Fig. 1. This figure also presents XRD patterns of the samples produced by pressure – temperature treatment of the homogeneous $C_{10}H_8 - C_{10}F_8$ binary mixture.

XRD data show that active stages of octafluoronaphthalene carbonization at 8.0 GPa proceeded at considerably lower temperatures than naphthalene, which maintained its thermal stability up to ~ 600 °C. According to Fig. 1, two broad peaks at 30.5 and 50.5 °, which

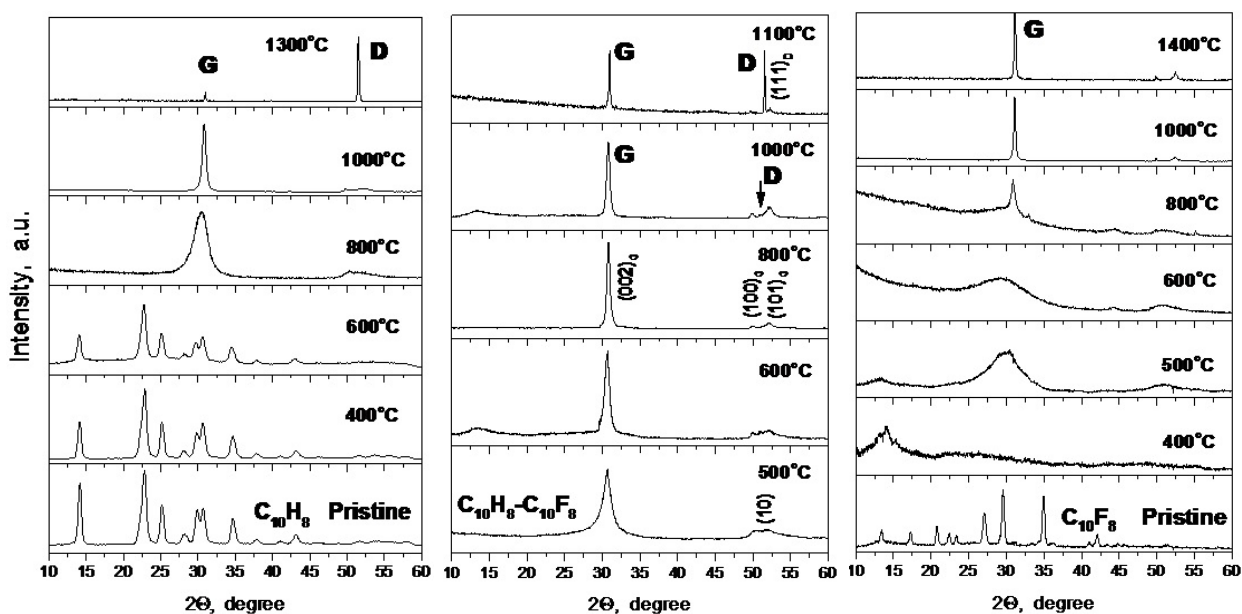


FIG. 1. XRD patterns of pristine $C_{10}H_8$, $C_{10}F_8$ and products of their treatment under pressure 8.0 GPa and different temperatures in the form of individual compounds (left and right panels) and homogeneous binary mixture (middle panel) (G – graphite, D – diamond)

are related to three-dimensional (002) and two-dimensional (10) reflexes of weakly-ordered graphite-like materials, already appeared in the diffractogram of the $C_{10}F_8$ transformation products at a temperature of 500 °C. These peaks indicate the formation of small fragment packings of graphene planes. In the case of naphthalene, similar states of carbon are formed at temperatures of 700 – 800 °C. Further increasing treatment temperature resulted in an acceleration of the graphitization processes, which caused growth in the linear sizes and the three-dimensional ordering of graphene layers. This was shown on the diffractogram by an intensity increase and narrowing of the (002) main reflex and splitting of the two-dimensional (10) reflex into two three-dimensional (100) and (101) graphite reflexes. In the case of $C_{10}F_8$, the formation of fairly crystalline graphite was noted at a temperature of ~ 900 °C, while for naphthalene, this occurred at ~ 1000 °C.

According to SEM data, graphite particles produced from $C_{10}H_8$ exhibit an oval shape, while those produced from $C_{10}F_8$ show a mostly polygonal form. Another special feature of the $C_{10}F_8$ -produced material, is that besides the micron size graphite particles, which are the main product of naphthalene treatment, some amount of weakly-ordered nanosize carbon phase, not observed in the products of $C_{10}H_8$ transformations, was present.

X-Ray data shown on Fig. 1 indicate that the temperature threshold for initial diamond formation in the pure naphthalene-based system is 1300 °C. For $C_{10}F_8$, the formation of diamond was not observed at all within the studied temperature range (up to 1500 °C).

In the case of homogeneous binary mixtures of $C_{10}H_8$ and $C_{10}F_8$, the mechanisms for thermal transformations of these compounds are essentially modified by the combined influence of volatile fluorine-containing destruction products of $C_{10}F_8$ on the processes of naphthalene carbonization and hydrogen-containing decomposition products of $C_{10}H_8$ on the processes of octafluoronaphthalene carbonization, respectively. This resulted in a significant reduction of the temperature thresholds for main transformation stages, observed for individual $C_{10}H_8$ and $C_{10}F_8$. So, according to Fig. 1, the formation of graphite in the binary system at 8.0 GPa was already observed at 800 °C, while diamond was formed at 1000 °C.

SEM images of diamonds, produced by the treatment of naphthalene and homogeneous $C_{10}H_8 - C_{10}F_8$ binary mixture (Fig. 2), show that diamonds obtained from pure $C_{10}H_8$ (Fig. 2a), appear as 5 – 40 micron monocrystals. The distinctive feature of the diamonds produced from a homogeneous $C_{10}H_8 - C_{10}F_8$ mixture, is that along with the micron size diamond fraction typical for naphthalene transformation, it also contains a considerable amount of nanosize diamonds appearing on Fig. 2b,c as shapeless agglomerates of nanoparticles.

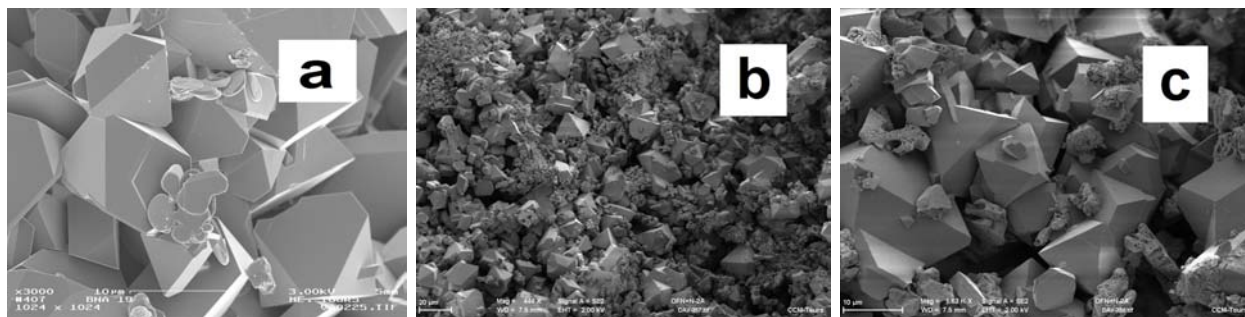


FIG. 2. SEM images of diamond materials obtained by treatment of naphthalene at 8.0 GPa and 1300 °C (a) and homogeneous mixture of $C_{10}H_8 - C_{10}F_8$ at 8.0 GPa and 1100 °C (b, c), taken at low magnification (b) and high magnification (c)

At first glance, the formation of two different size diamond fractions via the thermobaric treatment of organic compounds may have a purely thermodynamic explanation, according to which, the nano- and micron-size fractions of diamond can be considered as primary and secondary fractions during diamond formation. Indeed, according to p, T diagram of carbon [2], the formation of diamond from graphitization products at 8.0 GPa from 1000 – 1300 °C occurs within the p, T region of diamond stability, at a significant distance from the graphite-diamond equilibrium line. It is worth noting that the temperature of graphite-diamond phase equilibrium at 8.0 GPa is equal to ~ 2500 °C. That is, it can formally be said that in this case, diamond formation takes place at high degrees of overcooling. The realization of phase transition under such conditions enables the emergence of a large number of seeds for the new phase, and accordingly, the formation of a significant amount of nanodiamonds during the first stage of graphite-diamond phase transformation. However, since diamond is a higher density material than graphite, the formation of the primary diamond fraction is accompanied by a pressure drop in the reaction zone. As a result, the coordinates of the phase transition point on the p, T diagram become shifted towards the phase equilibrium line. Accordingly, the final stages of diamond formation occur under p, T parameters being much closer to the graphite-diamond phase equilibrium line. This matches the conditions favorable for the growth of a larger, micron size diamonds which can be considered as a ‘secondary’ transformation product. By taking into account that the degree of overcooling for the system during diamond formation from a binary $C_{10}H_8 - C_{10}F_8$ mixture is 300 °C higher than for the case of pure naphthalene, this can be suggested as a possible explanation for the elevated content of the nanosize diamond fraction present in the products of reactions using hydrocarbon and fluorocarbon mixtures as compared to pure hydrocarbons.

However, no notable quantities of nanodiamond have been detected among the products of $C_{10}H_8$ transformations, for which the degree of overcooling of the system relative to the temperature of the graphite-diamond phase equilibrium at 8.0 GPa was also quite high (~ 1200 °C). This allows one to assume that the formation of nanodiamonds from binary mixtures can be related to the difference in fractional composition of intermediate carbon states formed during carbonization and acting as direct precursors for diamond formation from $C_{10}H_8$ and $C_{10}H_8 - C_{10}F_8$ mixtures.

Since the relationship of the carbonization product to a particular starting component of the mixture cannot unambiguously be established for samples made from homogeneous mixtures, studies of the structure-morphology differences of $C_{10}H_8$ and $C_{10}F_8$ carbonization products have been carried out using samples of their heterogeneous mixtures, which consisted of two individual pellets of naphthalene and octafluoronaphthalene.

SEM images taken of the contact region in the sample of heterogeneous mixture (Fig. 3), treated at 8.0 GPa and 950 °C, clearly show differences in the morphology of the carbonization products of naphthalene and octafluoronaphthalene formed during thermal transformations of these compounds in a joint fluorine-hydrogen-containing environment. Flat-shaped graphite particles with lateral sizes of 0.5 – 1.0 microns (Fig. 3a,b) are major reaction products of $C_{10}H_8$. Unlike $C_{10}H_8$, the ultradispersed 10 – 20 nm nanoparticles (Fig. 3b,c), built from two-dimensional states of carbon, become a major component of $C_{10}F_8$ reactions under the considered conditions. The obtained data show that thermal transformations of the binary $C_{10}H_8 - C_{10}F_8$ mixture under high pressures and temperatures of $\sim 900 - 1000$ °C are indeed accompanied by the formation of nano- and micron-size fractions of carbon which can serve as precursors for the formation of nano- and micron-size diamond fractions. It is interesting

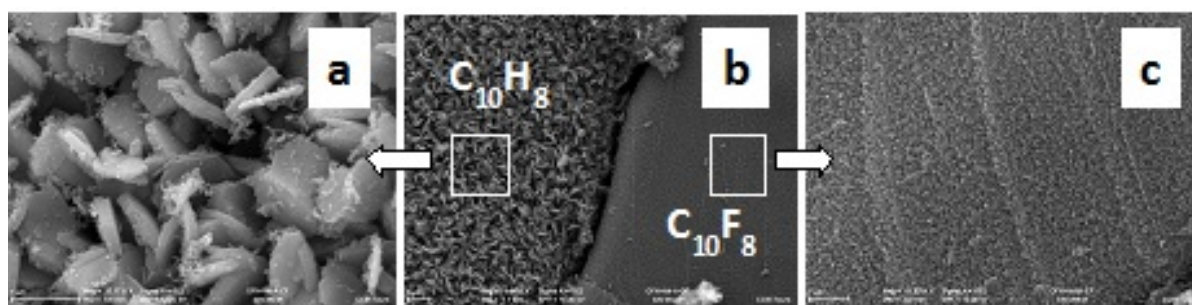


FIG. 3. SEM images of the products of thermal transformations of C₁₀H₈ (a,b) and C₁₀F₈ (b,c) taken from the region of contact area in the C₁₀H₈ – C₁₀F₈ heterogeneous mixture treated at 8.0 GP and temperature of 950 °C

to note that the micron-sized graphite and diamond fractions mainly originate from naphthalene carbonization products, while nano-size fractions were formed from octafluoronaphthalene carbonization products.

Thus, these results lead one to conclude that the main reason for the simultaneous formation of nano- and micron-size fractions of carbon materials in thermal transformations of different hydrocarbon-fluorocarbon mixtures at high pressures is the difference in the fractional compositions of the hydrocarbon- and fluorocarbon-based carbonization products under conditions of binary mixtures.

Acknowledgments

This work was supported by the Russian Foundation for Basic Research (Grant No. 12-03-00787).

References

- [1] Davydov V.A., Rakhmanina A.V., Agafonov V.N., Khabashesku V.N. Synergistic effect of fluorine and hydrogen on processes of graphite and diamond formation from fluorographite-naphthalene mixtures at high pressures. *The Journal of Phys. Chem. C*, **115**, P. 21000–21008 (2011).
- [2] Bundy F.P., Bassett W.A., et al. The pressure-temperature phase and transformation diagram for carbon. *Carbon*, **34** (2), P. 141–153 (1996).

SECONDARY NUCLEATION ON NANOSTRUCTURED CARBON FILMS IN THE PLASMA OF DIRECT CURRENT GLOW DISCHARGE

K. V. Mironovich¹, V. A. Krivchenko¹, P. V. Voronin¹, S. A. Evlashin¹

¹ Skobeltsyn Institute of Nuclear Physics, Lomonosov Moscow State University,
Moscow, Russia
mironbasket@mail.ru

PACS 68.55.A-

The high specific surface area of carbon nanowalls (CNWs) makes them an attractive catalyst support material or electrode material for energy storage devices (e.g. supercapacitors, Li-ion batteries). Secondary nucleation processes (formation of secondary nanowalls on the surface of pre-grown primary structures) play an important role in CNWs growth. It can significantly increase CNW film surface area, but at the same time be a limiting step for the production of films with an open pore structure. Both of these factors may be important for the applications mentioned above. In this work, we discuss possible mechanisms of secondary nucleation during CNW growth in the plasma of a direct current glow discharge. We also demonstrate a novel multi-step synthesis process with controllable secondary nucleation rates at different stages, which is an effective way to modulate CNW film morphology and produce films with desirable surface area and porosity.

Keywords: Carbon nanowalls, PECVD, Synthesis, Secondary nucleation, Morphology, Surface area.

1. Introduction

Carbon nanowall (CNW) films consist of graphite sheets standing almost vertically on the substrate and forming self-supported network of wall structures. Their unique structural properties such as high specific surface area and high aspect ratio make them useful for a number of different applications such as electrochemical devices (e.g. supercapacitors, Li-ion batteries [1]), catalyst support [2], and field emitters [3]. The potential use of CNWs in applications demands the ability to produce films with adjusted morphological properties, and this requires an understanding of their growth mechanisms. The most popular method for CNWs synthesis is chemical vapor deposition (CVD) in hydrocarbon-containing plasma of MW, RF, or DC discharge [4].

In this work, we continue our investigation of CNWs growth in the plasma of a DC glow discharge on substrates placed at the anode. Previously, we demonstrated that the distinctive feature of this method is the possible catalyst-free nucleation of conic-shaped carbon nanotubes (CNTs) upon CNWs and additionally, we proposed phenomenological models for CNWs and CNTs nucleation and growth [5]. Here, we focus our attention on the secondary nucleation (SN) process that forms secondary nanowalls (SCNWs) on the surface of pre-grown primary structures. This plays an important role in CNWs growth and can significantly increase CNW film surface area but at the same time it can be a limiting step for producing films with open pore structure. Both these factors may be important for electrochemical and catalyst support applications. We discuss possible mechanisms of

SN during CNWs growth in the plasma of a DC glow discharge. We also demonstrate a novel multi-step synthesis process with controllable SN rates at different stages, which is an effective way to modulate CNW film morphology and produce films with desirable surface area and porosity.

2. Experimental

CNWs were synthesized via DC plasma enhanced CVD in a mixture of methane and hydrogen. Polished *p*-doped 400 μm thick Si (100) wafers with an area of 1 cm^2 , were used as substrates and placed at the anode. Si wafers were previously ultrasonically treated in a diamond powder suspension for 5 min to assist the carbon film nucleation, then washed in distilled water and dried. Gas supply was realized with mass flow controllers, methane and hydrogen flow ratio defined their relative concentrations in gas mixture. Discharge current was controlled by a DC generator. Temperature was measured with a thermocouple connected to the bottom of Mo substrate holder. Typical experimental conditions were as follows: methane concentration 8–15%, hydrogen flow 10 l/h, pressure 150 Torr, discharge voltage and current 670 V and 0.6–0.9 A, respectively, and substrate holder temperature 680–800 $^{\circ}\text{C}$ (note that temperature of the substrate top surface was 150–200 $^{\circ}\text{C}$ higher). The duration of CNWs deposition was varied in from 20–35 min. After deposition, samples were studied by means of SEM (Carl Zeiss Supra 40 system) and Raman spectroscopy (Renishaw InVia).

3. Results and discussion

Fig. 1 (a) shows a typical CNW film, grown using the process described above at 700 $^{\circ}\text{C}$. The Raman spectrum of such a film (Fig. 2 (a)) presents three well-distinguished peaks at 1350 cm^{-1} , 1575 cm^{-1} and 2700 cm^{-1} (D-, G- and 2D-mode, respectively) and is typical for graphite materials. The ratio of the D and G mode intensities is usually used to evaluate film crystallinity. A typical I(D)/I(G) value was 0.6, revealing a sufficient number of defects in the CNWs structure. The shape and FWHM of the 2D mode doesn't depend on the presence of defects and is related to the number of graphene layers and their stacking order in the graphite structure. Analyzing the data presented in previous literature [6], we conclude that our CNWs consist of 10–15 graphene layers stacked in a turbostratic (disordered) manner. Previously, we suggested phenomenological model for CNWs nucleation and growth which considered nucleation of CNWs as a result of overlapping of horizontal graphite layers formed on the substrate surface at the early stage of growth [5]. Once nucleated, CNWs grow due to direct attachment of neutral hydrocarbon radicals to active sites at the edge of the CNW via hydrogen abstraction reactions.

Synthesis at higher temperature (800 $^{\circ}\text{C}$) is accompanied by catalyst-free growth of conical CNTs upon CNWs top edges (Fig. 1 (b)). Previously we showed that probable mechanism of their nucleation is folding of CNWs under high temperature in the presence of structural defects while their subsequent growth is mostly due to surface diffusion of hydrocarbon radicals from the bottom to the tip of the CNT [5]. Formation of such CNTs is a distinctive feature of DC PECVD synthesis probably due to absence of substrate bombardment by positive ions during growth. It should also be noted that higher temperature synthesis leads to the formation of less defective CNWs, as was confirmed by Raman spectroscopy analysis (I(D)/I(G) \sim 0.25).

Synthesis under the experimental conditions in a certain range led to the formation of films described above (Fig. 1 a, b). Increasing the methane concentration or synthesis duration induced a SN process that forms secondary nanowalls (SCNWs) on the surface of

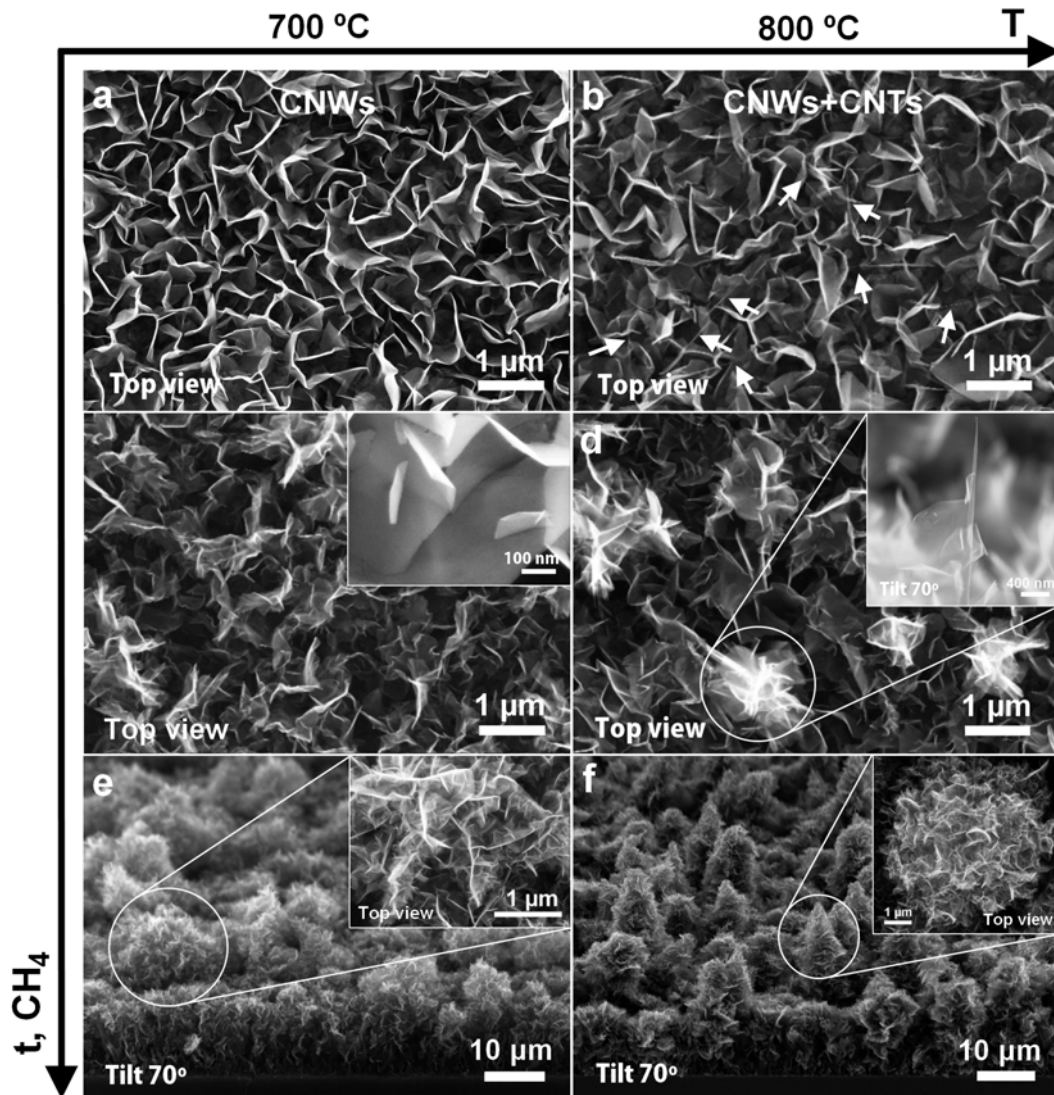


FIG. 1. CNW films obtained at different temperature, methane concentration and duration. White arrows mark CNTs

pre-grown primary structures. In the case of low temperature synthesis, SCNWs nucleated on the side surface of primary CNWs (Fig. 1 (c)) while at high temperatures, intense secondary nucleation took place at CNTs surface (Fig. 1 (d)). Further increasing of the duration or methane concentration led to the formation of globule-like clusters of SCNWs. At higher temperatures, these clusters grew in form of cones around primary CNTs (Fig. 1 (f)), while they had no definite shape in the absence of CNTs at lower temperatures (Fig. 1 (e)).

The probable mechanism of SN is as follows. As was mentioned above in our synthetic method, the role of building blocks is played by neutral hydrocarbon radicals. These radicals can be incorporated into the graphite lattice at a CNW edge, providing linear growth or be attached to defects on the CNW side surface. With increased radical density or duration, more radicals are attached to surface defects, forming additional graphene layers that broaden, overlap and give birth to SCNWs, just like nucleation of primary CNWs takes place on the substrate (Fig. 2 b, c). In addition, as was mentioned previously, CNWs obtained at lower temperatures have more defects, which increases the intensity of SN on their surface.

The SN process inevitably starts after some time, and there is no definite moment of its beginning, it gradually becomes more intense with CNWs growth. SN can significantly increase the CNW film surface area, but at the same time, it can be a limiting step for producing films with open pore structure. Both these factors may be important for electrochemical and catalyst support applications.

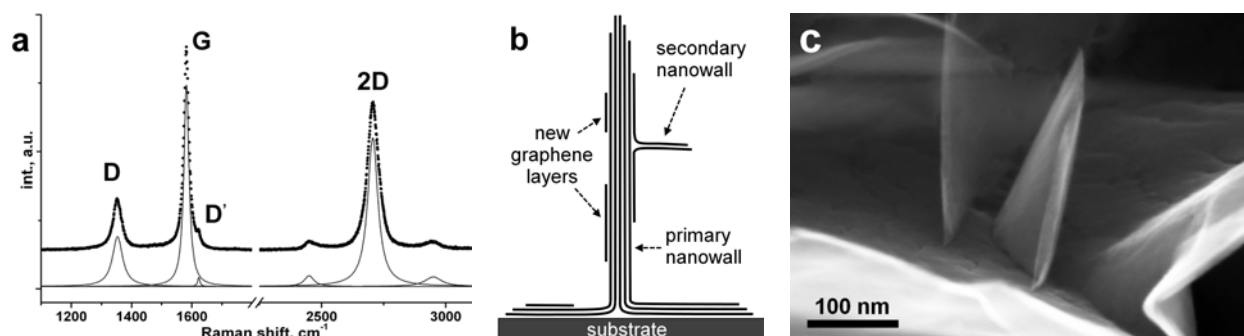


FIG. 2. (a) Typical Raman spectrum of obtained CNW films. (b) Schematic illustration of SN mechanism (c) SCNW on the surface of primary CNW

However, a controllable SN process gives one the opportunity to obtain films with a number of new morphologies. For this purpose, we suggest synthesizing CNWs in a multi-step process. In the first stage, deposition takes place under conditions that we call standard, leading to the formation of CNWs of certain size, before the beginning of SN process. At a certain time, the discharge conditions are abruptly changed (e.g. discharge current is increased), triggering an intense SN process. At this stage, prolonged growth of primary CNWs is accompanied by SCNWs nucleation and growth. It should be noted that the temperature at the first stage should be low enough to provide sufficient number of surface defects.

By varying the duration of each stage, it is possible to obtain films with an adjusted (in some range) size of primary and secondary CNWs and amount of the latter. The first column in Fig. 3 shows the CNWs obtained at 20, 25 and 30 minutes under standard conditions (150 Torr, relative methane concentration 10%, discharge current and voltage 0.6 A and 695 V, respectively at 680 °C). CNWs width and height increased proportionally with time (see inset). The other three columns demonstrate films obtained in different multi-step processes with SN initiated by an increase in the discharge current from 0.6 to 0.9 A (times of current change are depicted in the plots above the columns).

Fig. 3 (h) shows the film obtained after 20 minutes of standard growth followed by 5 minutes of high current regime. The primary vertical CNWs are covered with small SCNWs, while their width is almost the same as in the case of 25 minutes of standard synthesis without SN (Fig. 3 (b)). Similarly, the width of primary CNWs obtained in a process with a current increase after 25 minutes of standard growth (Fig. 3 (f)) corresponds to that of CNWs grown in standard process of the same total duration (Fig. 3 (c)). The amount of SCNWs and their size are higher than in the previously described film (Fig. 3 (h)), although the duration of the second stage was the same. This is due to the larger primary CNWs grown by the end of the first stage, in this case (see Fig. 3 (e)), in comparison to that of the film shown in Fig. 3 (h) (see Fig. 3 (g)), which implies more surface defects and thus, a more intense SN process.

Fig. 3 (i) shows the film obtained via the prolonged SN process, that led to an increase in the size and number of SCNWs, which in turn acted as a surface for nucleation

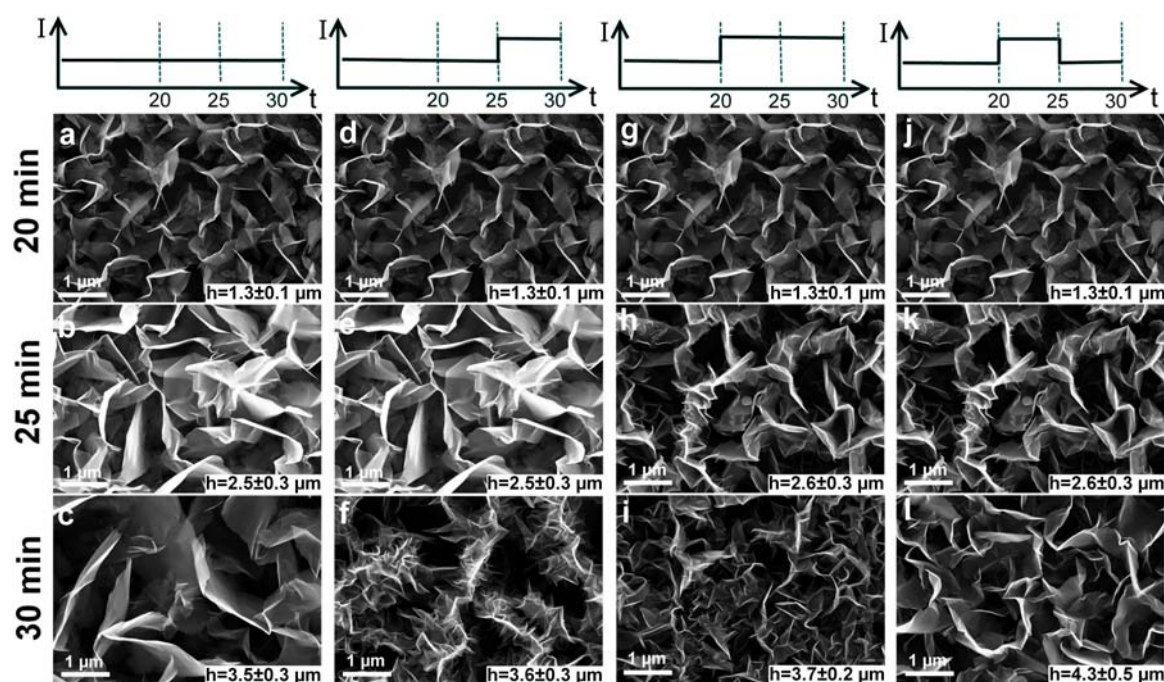


FIG. 3. CNW films obtained in different multi-step processes. Plots above denote times of current change. The right bottom corner of each image displays the height of the corresponding film

of tertiary CNWs and so on. This led to the formation of a densely branched network of CNWs, where the primary CNWs can't be identified. This film has considerably smaller pores in comparison to that of the film obtained in standard process of the same duration, while their heights are almost identical.

Fig. 3 (l) shows the film obtained in a three-step process. For the first 20 minutes, it grew under standard conditions (Fig. 3 (j)), then, the current was increased for 5 minutes, triggering a SN process (Fig. 3 (k)). For the last 5 minutes, current was decreased back to the initial value in order to suppress the SN process, thus only the primary and secondary CNWs present continued to grow without any change in number of the latter. This led to formation of CNW network with medium pore sizes in comparison to films c and i.

It should also be noted once more that the heights of all films presented in Fig. 3 depend only on the total process duration and were almost independent of the process type (within the error range). Thus, multi-step growth is a way to control film morphology without changing its height while these parameters are interrelated during conventional growth.

Acknowledgements

This work was financially supported by grant MK-2773.2014.2.

References

- [1] V.A. Krivchenko, D.M. Itkis, S.A. Evlashin, D.A. Semenenko, E.A. Goodilin, A.T. Rakhimov, A.S. Stepanov, N.V. Suetin, A.A. Pilevsky, P.V. Voronin. Carbon nanowalls decorated with silicon for lithium-ion batteries. *Carbon*, **50**, P. 1438–1442 (2012).
- [2] B.I. Podlovchenko, V.A. Krivchenko, Yu.M. Maksimov, T.D. Gladysheva, L.V. Yashina, S.A. Evlashin, A.A. Pilevsky. Specific features of the formation of Pt(Cu) catalysts by galvanic displacement with carbon nanowalls used as support. *Electrochimica Acta*, **76**, P. 137–144 (2012).

- [3] V.A. Krivchenko, A.A. Pilevsky, A.T. Rakhimov, B.V. Seleznev, N. V. Suetin, M.A. Timofeyev, A.V. Bepalov, O.L. Golikova. Nanocrystalline graphite: promising material for high current field emission cathodes. *J. Appl. Phys.*, **107**, P. 014315 (2010).
- [4] M. Hiramatsu, M. Hori. *Carbon Nanowalls, Synthesis and Emerging Applications*. Springer, Wien-NewYork, 161 p (2000).
- [5] V.A. Krivchenko, V.V. Dvorkin, N.N. Dzbanovsky, M.A. Timofeyev, A.S. Stepanov, A.T. Rakhimov, N.V. Suetin, O.Yu. Vilkov, L.V. Yashina. Evolution of carbon film structure during its catalyst-free growth in the plasma of direct current glow discharge. *Carbon*, **50**, P. 1477–1487 (2012).
- [6] D.S. Lee, C. Riedl, B. Krauss, K. Klitzing, U. Starke, J.H. Smet. Raman spectra of epitaxial grapheme on SiC and of epitaxial graphene transferred to SiO₂. *Nano Lett.*, **8**(12), P. 4320–4325 (2008).

FIELD ELECTRON EMISSION FROM A NICKEL-CARBON NANOCOMPOSITE

V. S. Protopopova, M. V. Mishin, A. V. Arkhipov, S. I. Krel, P. G. Gabdullin
Saint Petersburg State Polytechnic University, Saint Petersburg, Russia
max@mail.spbstu.ru, arkipov@rphf.spbstu.ru

PACS 79.70.+q; 79.60.Jv; 81.05.uj; 81.07.-b

The field-emission properties of nanocomposite films comprised of 10 – 20 nm-sized nickel particles immersed in a carbon matrix were investigated. The films were deposited onto silicon substrates by means of a metal-organic chemical vapor deposition (MOCVD) method. The composite's structure was controlled via deposition process parameters. Experiments demonstrated that the composite films can efficiently emit electrons, yielding current densities of up to 1.5 mA/cm² in electric fields below 5 V/μm. Yet, good emission properties were only shown in films with low effective thickness, when nickel grains did not form a solid layer, but left a part of the substrate area exposed to the action of the electric field. This phenomenon can be naturally explained in terms of the two-barrier emission model.

Keywords: Amorphous carbon, Nanocomposite, Thin film, Field electron emission.

1. Introduction

Many different varieties of carbon-based nanostructures demonstrate the property of facilitated field-induced electron emission, even those having a relatively smooth surface without protruding fibers, sharp tips or ribs [1–16]. The role of their nano-scale structure in the emission mechanism may lie with their long-term confinement of hot electrons at high-energy states without thermalization, which creates favorable conditions for the subsequent transfer of those electrons into a vacuum, even in a moderate electric field [17]. These hot electrons may be generated when current flows through tunnel junctions separating emitter nanodomains. The discussed hypothesis [17] explains facilitated emission from heterogeneous carbon films comprised by both sp^2 (conductive) and sp^3 (weakly conductive) carbon phases. In the presented work, we investigated properties of nanocomposite films produced via the joint deposition of carbon and nickel on silicon substrates. The conductive phase in the deposited film was represented by Ni and/or graphitic carbon, while nickel carbide and/or sp^3 -bonded carbon comprised a weakly conductive medium. Introduction of the second element provided additional flexibility to the technology, allowing manipulation of the composite structure via variation of the deposition process parameters.

In accordance with the two-barrier emission model [12–17], the size of the conductive crystallites can have dramatic effect on the emission properties of the film, while other parameters of this film's components are less important. Therefore the investigated Ni-C films could have been expected to demonstrate facilitated field electron emission with characteristics comparable to those of fully carbonic films of similar morphology [16].

2. Sample fabrication, structure and properties

The Ni-C thin films were prepared on Si substrates by the method of metal-organic chemical vapor deposition (MOCVD) with bis-(ethylcyclopentadienyl) nickel (EtCp)₂Ni as the precursor. The deposition process was carried out in a hot-wall horizontal low-pressure tube

silica reactor with temperature maintained from 350 – 650 °C. Details of this technology may be found elsewhere [18].

The effective thickness of the deposited Ni layers was determined by means of X-ray fluorescence (XRF) spectroscopy (Spectroscan MAX-GV), via measurement of intensity of a Ni characteristic line. Morphology of deposited films was studied by scanning electron microscopy (SEM) (microscope Supra 55 VP).

The performed experiments demonstrated that composite film structure could be efficiently controlled via deposition process parameters: deposition time, substrate temperature and partial pressures of the precursor $(\text{EtCp})_2\text{Ni}$, the H_2 and the buffer gas, Ar. In all cases, the film composition included carbon in an amorphous form. At the beginning of the deposition process, the Ni component was represented by separate nanoparticles occupying only a small part of the substrate surface. Then, the size and number of Ni particles increased until they merged into a solid film completely covering the substrate. Further deposition resulted in the formation of multi-layer films. The process affected not only the quantity of the precipitated metal but also the composite structure— both metallic particles and bonding carbon matrix. Fig. 1 presents a plot of surface electric resistivity for composite film samples versus deposition time (the latter was showed to be proportional to the effective Ni layer thickness). The data are given only for films with full area coverage. Surprisingly, the resistivity increases with film thickness. We explain this feature by two phenomena accompanying the deposition process. One of them involves the formation of carbide shells around Ni grains, which increases the insulating gaps separating adjacent crystallites and reduces the tunneling current between the grains. The percolation current flowing through grain contacts and conductive paths in the carbon matrix also decreases because of progressing graphitization of sp^3 carbon in the previously deposited film layers. The process results in increased film porosity (due to large difference in mass density between graphitic and the sp^3 -bonded carbon forms, leading to the development of local mechanical strains and deformations during the phase transition), reduction of contact areas between Ni grains and the appearance of new inter-crystallite boundaries at current paths.

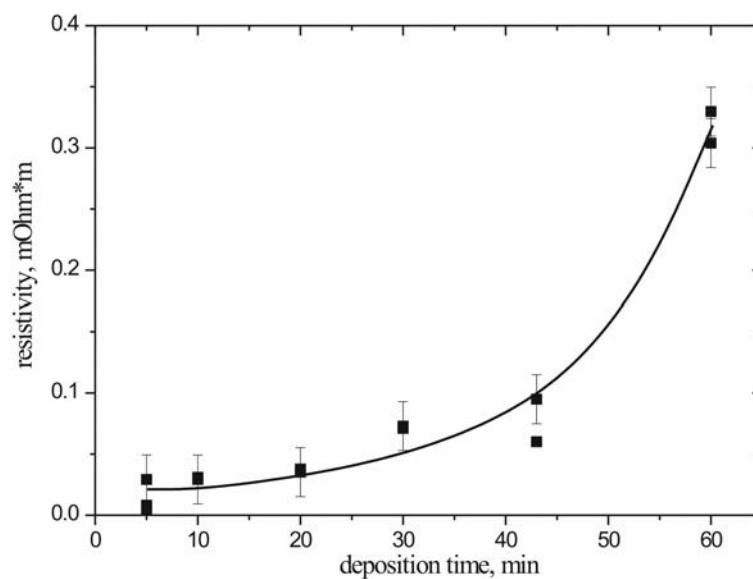


FIG. 1. Specific surface resistivity of Ni-C films deposited at 570 °C vs deposition time. Total pressure in reaction chamber 840 Pa, partial pressure of $(\text{EtCp})_2\text{Ni}$ and hydrogen – 75 and 210 Pa respectively

TABLE 1. Sample surface morphology and deposition process parameters¹

Sample	Temperature (°C)	Time (min)	Film morphology
1	390	60	Isolated particles, average size 11 nm
2	410	60	Isolated particles, average size 20 nm
3	570	5	Full monolayer of 20 nm particles, damaged during emission activation treatment
4	450	60	Full monolayer of 20 nm particles

¹Total pressure in all cases was 840 Pa, partial pressure of (EtCp)₂Ni and hydrogen – 75 and 210 Pa resp.

The substrate temperature maintained during the film fabrication process also had a strong effect on the resulting composite structure. The films deposited at higher temperatures were characterized by much greater porosity, lower density and higher surface resistivity. Also, substrate heating substantially increased the film growth rate.

For our emission experiments, we selected four samples with different film morphologies. The corresponding deposition process parameters and morphology types are listed in Table 1. Fig. 2 presents SEM images of the samples, showing mostly the Ni component of the composite. For the first two samples, the area density of Ni particles is low and they are isolated from each other. Hence, most of the weakly-conducting substrate's surface is open for penetration of external electric field. Mean particle size for samples 1 (Fig. 2(a)) and 2 (Fig. 2(b)) is equal to 11 nm and 20 nm, respectively. Samples 3 (Fig. 2(c)) and 4 (Fig. 2(d)) had full Ni grain monolayers completely covering the substrate. In the case of sample 3, the layer was deposited at a higher temperature (570 °C), and its mechanical strength was lower than that for sample 4, which was deposited in a much slower process at 450 °C. As a result, the former film was damaged in the course of emission activation treatment during the emission tests. (Fig. 2(c) shows its surface after the treatment). The film of sample 4 withstood the treatment without visible damage, as did samples 1 and 2, also deposited at low temperatures (390 °C and 410 °C respectively).

Besides Ni particles, the images of Fig. 2 show fiber-like structures that were identified as carbon nanocones [19], growing due to the high catalytic activity of Ni particles. According to [20] and references, the formation of silicon nanocones or combined Si/C structures is also possible under similar conditions (precursor pressure, Si substrate and its temperature). Though, efficient migration of silicon atoms through the silicon oxide layer and deposited film may be possible only in the presence of some activation factors. In [20], this role is ascribed to the flux of fast hydrogen ions generated in rf discharge and accelerated to the substrate by dc electric bias. In our case, the film deposition process did not engage application of either rf or dc field, hence we don't see any mechanisms for substrate atoms' mobility activation. In principle, the nanocones (either carbon or silicon) could substantially contribute to electron emission due to high local enhancement of applied electric field; hence their role in emission required a special investigation.

3. Emission tests

Field emission properties of the prepared Ni-C film samples were tested using the layout and experimental procedures described previously [21]. The electric field was applied in 0.5 – 0.6 mm-wide planar gap between the tested sample and tungsten cylindrical anode with ~ 30 mm² area. The tests were performed at a residual gas pressure of ~ 10⁻⁷ Torr. Emission characteristics were measured with slowly increasing gap voltage $U(t)$ up to a maximum value

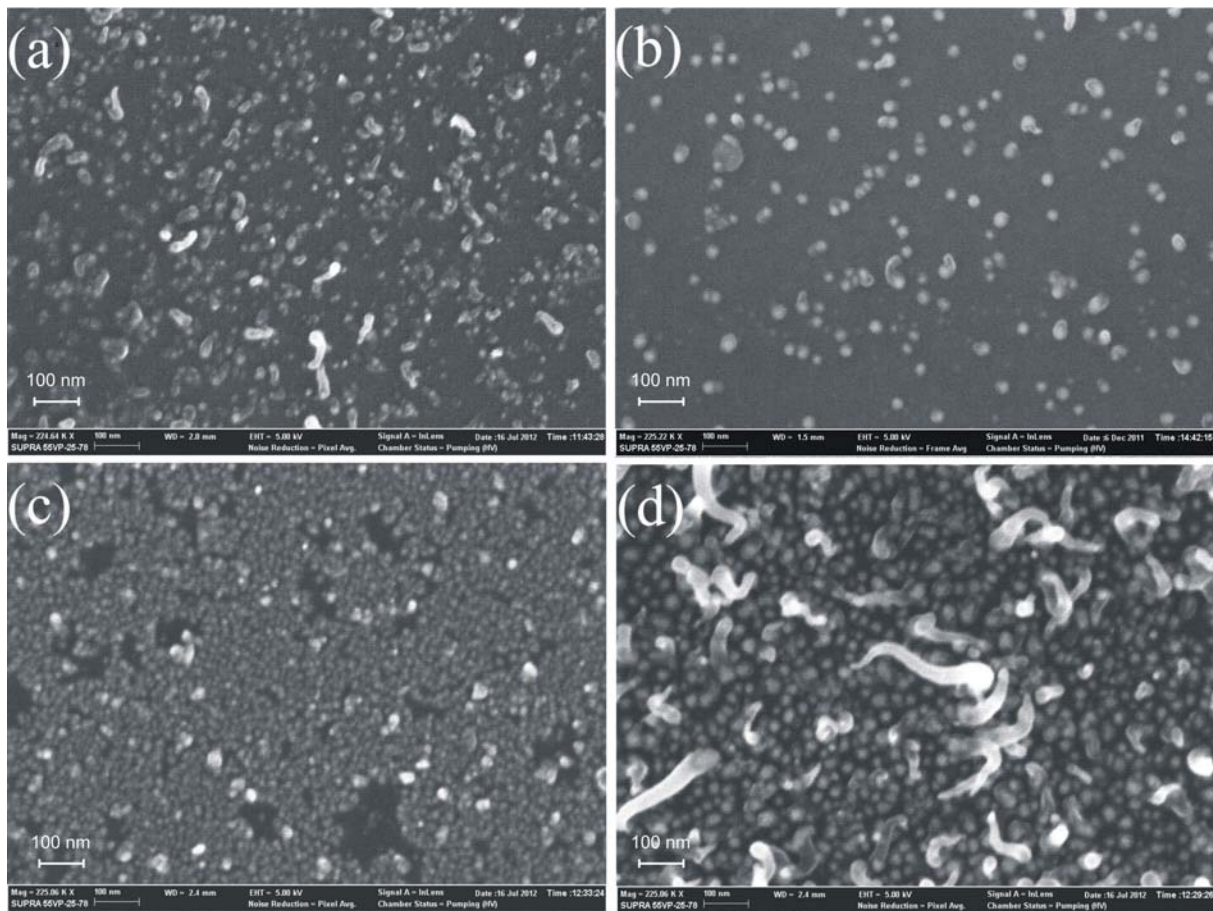


FIG. 2. SEM images of Ni-C films selected for the emission tests. (a) – sample 1; (b) – sample 2; (c) – sample 3 (after the tests); (d) – sample 4

U_{\max} . Then, the voltage was slowly decreased, and the ‘reverse’ branch of the characteristics was registered. The full cycle took approximately 65 seconds. This measurement was performed initially at room temperature and for relatively low U_{\max} . If no emission current appeared, the procedure was then repeated with greater U_{\max} and/or higher sample temperature, until a measurable current was yielded. Then the sample was maintained under conditions where the emission current amounted to a few μA . In this situation, the sample’s emission activity usually improved with time, and temperature and applied voltage were correspondingly decreased to stabilize the extracted current. After this activation treatment, the emission characteristics were measured repeatedly.

The performed experiments demonstrated that Ni-C film samples 1, 2 and 3 were capable of low-field electron emission. Their best emission characteristics are showed in Fig. 3. Emission started at threshold field values as low as 2 – 4 $\text{V}/\mu\text{m}$. Such values are very typical for numerous reported observations of low-field emission from various nanostructures, including different types of nanocarbon [1–17]. All characteristics were approximately linear in Fowler-Nordheim coordinates (bottom plot in Fig. 3), which gives evidence for the field-induced nature of the observed emission.

Figure 4 presents a typical temperature dependency of I–V emission plots for one of the samples. A temperature rise notably increased the emission current in comparison with its room-temperature value. Though, the dependency was relatively slow – sample heating to 380 °C resulted only in $\sim 100\%$ current growth. In Fowler-Nordheim coordinates (bottom

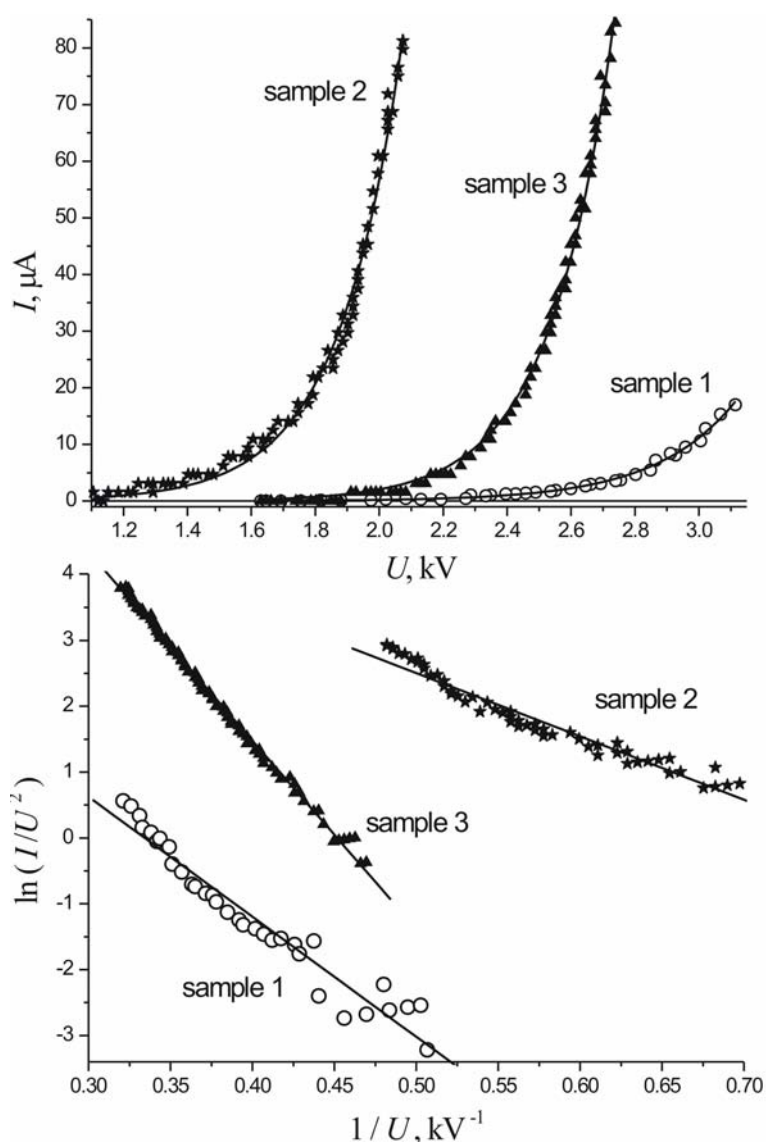


FIG. 3. Emission I-V plots of film samples measured in straight (top) and Fowler-Nordheim coordinates. The dependencies were measured at 380 °C

plot in Fig. 4) the linear emission plot was subject to approximately parallel displacement. The phenomenon of field emission thermal dependency is well known for different forms of nanocarbon [22–24]. It is usually explained by increased electron supply of emission sites due to substrate resistance reduction or increasing transparency of internal junctions, or by an increase of electron population of energy levels associated with surface, defects or dopant atom (that serve as intermediary states in emission mechanism), or by modification of emitter surface (due to out-gassing).

Sample 2 showed the best emission properties among the tested structures, with a threshold field value close to 2 V/μm. As it can be seen in Fig. 2, this film is comprised by separate 20 nm Ni particles. Previously, we observed [16] that purely graphitic carbon films of similar structure and dimensions also showed the best results. Sample 1, where the Ni grains were smaller (~ 11 nm), had an emission threshold that was twice as large. This observation is in good agreement with the estimates made in [17], demonstrating that the electric field induced

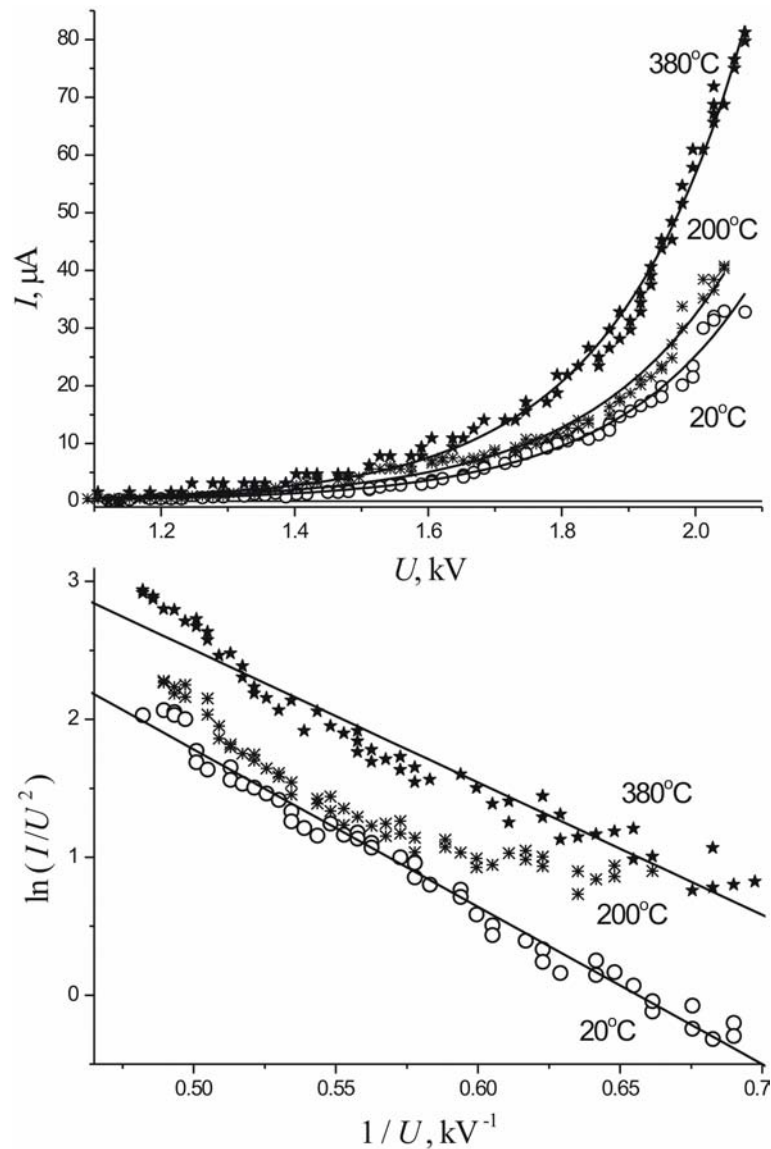


FIG. 4. Emission I-V plots of film sample 2 (see details in text and Table 1) measured at different temperatures

by an externally applied field between a substrate and an electrically insulated particle is proportional to particle size. Thus, the tunneling transport of electrons into a larger particle will produce hot electrons of a given energy (that can be responsible for facilitated emission) at lower value of the external field.

Emission from the sample 3 (that initially represented a solid film with 100% substrate coverage) appeared only after intensive activation treatment. We think that the activation which occurred was associated with the damage to the film caused by this procedure, opening a part of substrate surface (see in Fig. 2(c)) to the action of applied field. Its penetration under the film may have resulted in the generation of hot electrons. In contrast, sample 4 represented a film of similar morphology but with greater mechanical strength, that withstood the treatment undamaged. This sample never yielded any detectable emission current in the field up to $\sim 10 \text{ V}/\mu\text{m}$ at temperatures up to 470°C . Thus, we can associate emission with field penetration

in the sample. Surface conductivity of intact film (measured as approximately 10^4 S/m) is too high to allow substantial field penetration, which is necessary for generation of hot electrons.

The lack of emission for sample 4 also suggests that the nanocones (abundantly present at its surface, see Fig. 2d) did not play a key role in emission. This conclusion can be expanded onto the other samples, where concentration of the nanocones was much lower.

4. Summary

The experiments performed in the present work demonstrated that:

- Ni-C nanocomposite films can be fabricated by the MOCVD method from $(\text{EtCp})_2\text{Ni}/\text{H}_2$ gas mixture. The composite has the general form of 10 – 20 nm Ni particles in carbonic matrix. Physical characteristics of the composite can be controlled via parameters of the film deposition process;
- the composite films at silicon substrates can serve as efficient cold electron emitters producing mean current densities in the mA/cm^2 range in electric field below $5 \text{ V}/\mu\text{m}$;
- electron emission was observed only for the films with relatively low effective thickness, with at least a part of the substrate surface open for the action of the applied field. This observation can be naturally explained in the hot-electron emission model.

Acknowledgments

The work was supported by the Russian ministry of education and science (grant No. 11.G34.31.0041) and by the RFBR (grant 13-02-92709).

References

- [1] Okotrub A.V., Bulusheva L.G., et al. Field emission from products of nanodiamond annealing. *Carbon*, **42**, P. 1099–1102 (2004).
- [2] Shpilman Z., Michaelson Sh., Kalish R., Hoffman A. Field emission measurements from carbon films of a predominant nano-crystalline diamond character grown by energetic species. *Diamond and Related Materials*, **15**, P. 846–849 (2006).
- [3] Liu D., Benstetter G., Frammelsberger W. Nanoscale electron field emissions from the bare, hydrogenated, and graphitelike-layer-covered tetrahedral amorphous carbon films. *J. Appl. Phys.*, **99**, P. 044303 (2006).
- [4] ZhaoY., Zhang B., et al. Improved field emission properties from metal-coated diamond films. *Diamond and Related Materials*, **16**, P. 650–653 (2007).
- [5] Orlanducci S., Fiori A., et al. Nanocrystalline diamond films grown in nitrogen rich atmosphere: structural and field emission properties. *J. Nanosci. Nanotechnol.*, **8**, P. 3228–3234 (2008).
- [6] Panwar O.S., Rupesinghe N., Amaratunga G.A.J. Field emission from as grown and nitrogen incorporated tetrahedral amorphous carbon/silicon heterojunctions grown using a pulsed filtered cathodic vacuum arc technique. *J. Vac. Sci. Technol. B*, **26**, P. 566–575 (2008).
- [7] Xu L., Wang C., et al. Effects of bonding structure from niobium carbide buffer layer on the field electric emission properties of a-C films. *J. Appl. Phys.*, **105**, P. 074318 (2009).
- [8] Uppireddi K., Weiner B.R., Morell G. Field emission stability and properties of simultaneously grown micro-crystalline diamond and carbon nanostructure films. *J. Vac. Sci. Technol. B*, **28**, P. 1202–1205 (2010).
- [9] Huang P.-C., Shih W.-C., Chen H.-C., Lin I.-N. The induction of a graphite-like phase on diamond films by a Fe-coating/post-annealing process to improve their electron field emission properties. *J. Appl. Phys.*, **109**, P. 084309 (2011).
- [10] Masuzawa T., Sato Y., et al. Correlation between low threshold emission and C–N bond in nitrogen-doped diamond films. *J. Vac. Sci. Technol. B*, **29**, P. 02B119 (2011).
- [11] Nose K., Fujita R., Kamiko M., Mitsuda Y. Electron field emission from undoped polycrystalline diamond particles synthesized by microwave-plasma chemical vapor deposition. *J. Vac. Sci. Technol. B*, **30**, P. 011204 (2012).
- [12] Karabutov A.V., Frolov V.D., et al. Low-field electron emission of diamond/pyrocarbon composites. *J. Vac. Sci. Technol. B*, **19**, P. 965–970 (2001).

- [13] Obraztsov A.N., Zakhidov A.I. Low-field electron emission from nano-carbons. *Diamond and Related Materials*, **13**, P. 1044–1049 (2004).
- [14] Xie W.G., Chen Jun, et al. Effect of hydrogen treatment on the field emission of amorphous carbon film. *J. Appl. Phys.*, **101**, P. 084315 (2007).
- [15] Filip L.D., Palumbo M., Carey J.D., Silva S.R.P. Two-step electron tunneling from confined electronic states in a nanoparticle. *Phys. Rev. B*, **79** (24), P. 245429 (2009).
- [16] Arkhipov A.V., Gabdullin P.G., et al. Field-induced electron emission from graphitic nano-island films at silicon substrates. *Fullerenes, Nanotubes and Carbon Nanostructures*, **20** (4–7), P. 468–472 (2012).
- [17] Arkhipov A.V., Gabdullin P.G., Mishin M.V. On possible structure of field-induced electron emission centers of nanoporous carbon. *Fullerenes, Nanotubes and Carbon Nanostructures*, **19** (1–2), P. 86–91 (2011).
- [18] Alexandrov S.E., Protopopova V.S. Chemical vapor deposition of Ni-C films from bis-(ethylcyclopentadienyl) nickel. *Journal of Nanoscience and Nanotechnology*, **11**, P. 8259–8263 (2011).
- [19] Baylor L.R., Merkulov V.I., et al. Field emission from isolated individual vertically aligned carbon nanocones. *J. Appl. Phys.*, **91** (7), P. 4602–4606 (2002).
- [20] Orlanducci S., Toschi F., et al. A viable and scalable route for the homogrowth of Si nanocones and Si/C nanostructures. *Cryst. Growth Des.*, **12**, P. 4473–4478 (2012).
- [21] Bondarenko V.B., Gabdullin P.G., et al. Emissivity of powders prepared from nanoporous carbon. *Tech. Phys.*, **49**, P. 1360–1363 (2004).
- [22] Liao L., Zhang W.F., et al. Investigation of the temperature dependence of the field emission of ZnO nanorods. *Nanotechnology*, **18**, P. 225703 (2007).
- [23] Tordjman M., Bolker A., Saguy C., Kalish R. Temperature dependence of reversible switch-memory in electron field emission from ultrananocrystalline diamond. *Appl. Phys. Lett.*, **101**, P. 173116 (2012).
- [24] Arkhipov A.V., Gordeev S.K., et al. Nanodiamond composite as a material for cold electron emitters. *J. Phys.: Conf. Ser.*, **100**, P. 072047 (2008).

STRUCTURAL CHANGES IN INDUSTRIAL GLASSY CARBON AS A FUNCTION OF HEAT TREATMENT TEMPERATURE ACCORDING TO RAMAN SPECTROSCOPY AND X-RAY DIFFRACTION DATA

S. S. Bukalov^{*1}, Ya. V. Zubavichus^{2,3}, L. A. Leites^{1,2}, A. I. Sorokin⁴, A. S. Kotosonov⁴

¹Scientific and Technical Center on Raman Spectroscopy
of the Russian Academy of Sciences, Moscow, Russia

²A. N. Nesmeyanov Institute of Organoelement Compounds RAS, Moscow, Russia

³National Research Center “Kurchatov Institute”, Moscow, Russia

⁴State Scientific Research Institute of Graphite (NIIGrafit), Moscow, Russia
buklei@ineos.ac.ru, yzubav@googlemail.com

PACS S.81.05.-t, 82.80.Gk, 81.05.U

Changes in the structure of glassy carbon as a function of heat treatment temperature is investigated by Raman spectroscopy and X-ray diffraction measurements. It is shown that the glassy carbon samples studied can be described as poorly ordered turbostratic nanographite. An increase in temperature leads to some ordering with preservation of the general structural motif. Based on spectroscopic evidence, graphene sheet curvature in the high-temperature glassy carbon samples is suggested.

Keywords: Glassy carbon, nanographite, Raman spectroscopy, X-ray diffraction.

1. Introduction

Glassy carbon (GC)¹ is an sp² carbon material (CM) produced by the pyrolysis of suitable thermoreactive organic polymers. Due to GC's unique physicochemical properties, such as isotropy, chemical inertness, high mechanical strength, low density, impermeability to gases and liquids, extreme resistance to chemical attack, electrical conductivity, heat conduction, biocompatibility [1,2], this material is widely used in modern high-technologies. GC, produced by the carbonization of oxygen-containing polymers, belongs to the so-called “non-graphitizable” CM which do not transform to graphite even at temperatures of up to 3000 ° [2,4]. Several models were proposed for GC structure based on X-ray and neutron diffraction data as well as those of Raman spectroscopy, SEM, TEM and AFM [4-8], and on model calculations [9,10], however, its atomic-scale structure is not fully elucidated.

Our aim was to follow structural changes in the samples of a typical non-graphitized CM, fabricated at the pilot factory of the State Research Institute of Graphite (NIIGrafit, Moscow) by carbonization of phenol-formaldehyde resin SFG-3038, and heat-treated in a step-wise manner under an inert atmosphere in the interval from 1020 to 2700 °C (the samples are marked as GC1020 etc). To characterize the samples, elemental analysis, Raman spectroscopy and X-ray diffraction (XRD) data were used. The latter measurements were non-destructive and were carried out sequentially, without preliminary sample preparation.

¹“Glassy carbon” is a trademark commonly used instead of IUPAC recommended [1] term “glass-like carbon”.

2. Experimental

Raman spectra were obtained using a laser Raman spectrometer LabRAM (Jobin Yvon). The spectra were excited by a 632.8 nm line of a He-Ne laser, laser power not exceeding 1 mW. The spectra registered from different spots of the sample shears appeared identical, thus pointing to the sample homogeneity. X-ray diffraction patterns were measured in the Bragg-Brentano $\theta/2\theta$ geometry using a DRON-3 automated diffractometer (CuK α radiation, scanning step 0.02°). The curve-fitting analysis of the Raman band contours and diffraction patterns was carried out using a standard Origin 7.5 program with appropriate Lorentzian, Gaussian or Voight functions.

3. Results and Discussion

Raman spectra of GC from various origins have been published and interpreted in many papers, starting from the classical work of Koenig (see, e.g. [11-20]). First-order Raman spectra of GC differ from those of graphite in the widths of the D and G lines and in their intensity ratio, $I_D/I_G > 1$, the latter is also typical for other nano-sized disordered sp² CM [14-16,20], as well as in the presence of the line in the region of ~ 1100 cm⁻¹. The region 1000–3200 cm⁻¹ of the Raman spectra obtained for the samples studied is presented in Fig. 1 and characterized in Table 1. The overall spectral pattern agrees well with the literature data; in all spectra, the ratio $I_D/I_G > 1$. However, in the Raman spectrum of GC1020, the G and D lines are broadened compared to the spectrum of a typical GC [20]. The second-order Raman spectrum of this sample exhibits very broad and weak bands, typical for all strongly disordered sp² carbons [13,20]. All this is not surprising, because it is well-known [2,3,13] that at the initial stage of the resin pyrolysis (up to ~ 1400 °C), primary carbonization and polymerization of the organic substance takes place with the formation of randomly oriented graphene layers, however, containing an appreciable fraction of heteroatoms. Indeed, according to our elemental analysis data, the sample GC1020 contains only 75% of carbon. Thus, the sample marked GC1020 is in essence not a real glassy carbon. Heat-treatment of GC samples up to 1450 ° increases the carbon content to 98% and in the GC1650 sample it reaches the value of 99.5 %. The Raman spectra exhibit noticeable changes (Fig. 1,3,4, Table 1). The D and 2D lines shift slightly and gradually narrow. The G line becomes more and more asymmetric, and in the spectra of GC2100 and higher, a weak line at 1620 cm⁻¹ (D') becomes clearly visible, which points to a turbostratic structure, i.e., to the absence of strict periodicity along the **c** axis [19,20]. The latter conclusion is also confirmed by a gradual formation in the second-order spectrum of an intense symmetric line at 2650 cm⁻¹, corresponding to an overtone 2D. Thus, it is evident from the Raman spectra that an increase in the annealing temperature leads to partial ordering of the condensed aromatic clusters in the **ab** plane (two-dimensional “quasi-crystallization”) [19].

X-ray diffraction data are fully consistent with the above Raman spectroscopy data (Fig. 2). The diffraction pattern of GC1020 reveals three very broad peaks at $2\theta = 24.0$, 43.6 and 79.7°, which can be assigned to 002, 100 and 110 indices of the graphite lattice. No general-index lines (e.g., 101) were observed. Furthermore, the 100 and 110 lines were strongly asymmetric due to the Warren effect [21,22]. This indicates that the sample GC1020 can be formally described as a nanostructured turbostratic graphite without register in the orientation of adjacent graphene layers and with a very small size of ordered domains. In contrast to bulk graphite, this sample is not prone to preferred orientation. The sample GC2700 additionally contains an admixture of ordered polycrystalline graphite, which is evidenced by the occurrence of 002 line at 26.47° with FWHM of 0.65° (the area under the peak

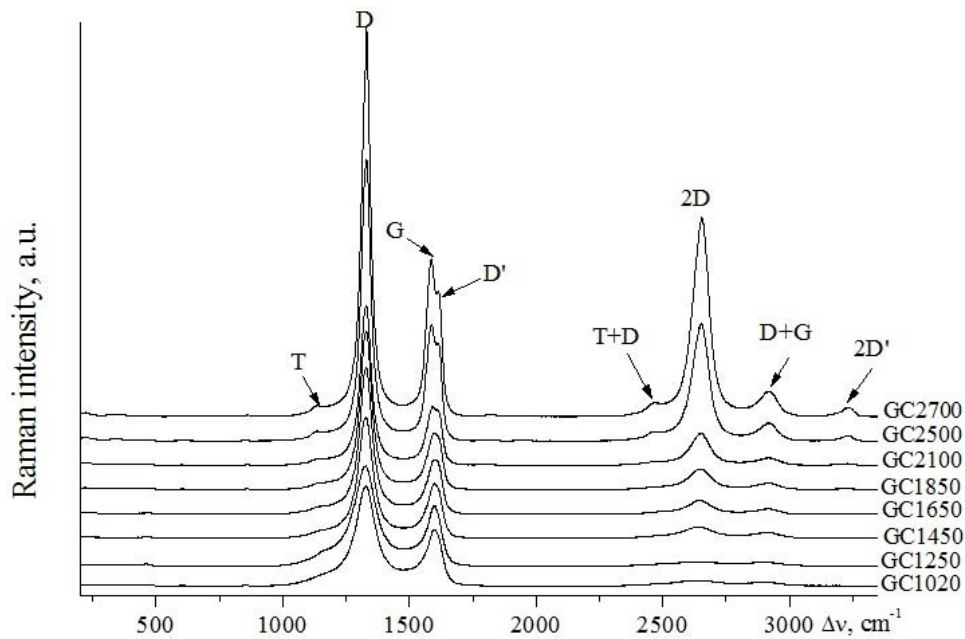


FIG. 1. Raman spectra of the GC samples annealed at different temperatures

TABLE 1. Frequencies ($\Delta\nu$) and half-widths (FWHM) of the D and 2D Raman lines *

Heat treatment temperature (°C)	$\Delta\nu$ of the D line (cm^{-1})	D line FWHM (cm^{-1})	$\Delta\nu$ of the 2D line (cm^{-1})	2D line FWHM (cm^{-1})
1020	1324.5	107	2637	233
1250	1326.5	92	2638	213
1450	1326.5	69	2639	148
1650	1328	59	2643	113
1850	1328	53	2645	102
2150	1328	48	2647	88
2450	1329	42	2649	72
2700	1329	40	2650	67

* The values presented are the results of averaging of 5 independent series of experiments.

corresponds to $\sim 15\%$ of that of the glassy carbon component). No graphite admixture was observed by other diffraction measurements using synchrotron radiation (to be published) on similarly prepared samples.

An increase in annealing temperature leads to the emergence of very weak bands in the low-frequency region of the Raman spectra from $200\text{--}500\text{ cm}^{-1}$ (Fig. 4). Analogous bands were observed for carbon tubular cones, whiskers, polyhedral crystals and nano-onions [23,24], the authors associate them with graphene sheet curvature. For the latter CM, a high Raman intensity of the 2D overtone was observed, the same is true for GC2500 and 2700 (Fig. 1). By analogy, it can be suggested that these facts speak for applicability to the high-temperature GC samples studied of the structural model proposed by Harris [7], which is based on fullerene-related basic units with a high curvature and on the presence of closed voids.

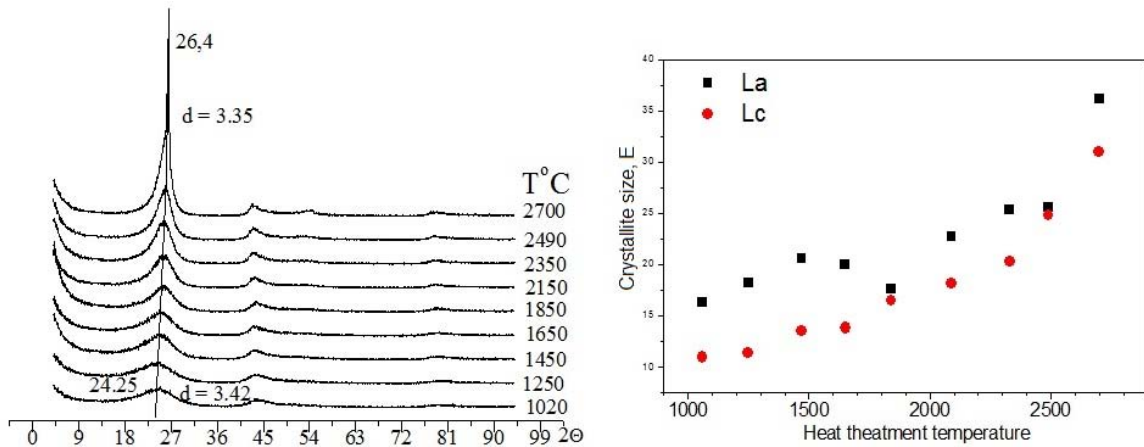


FIG. 2. X-ray diffraction patterns of glassy carbon samples treated at different temperatures (left) and estimates for crystallite sizes L_a and L_c (right)

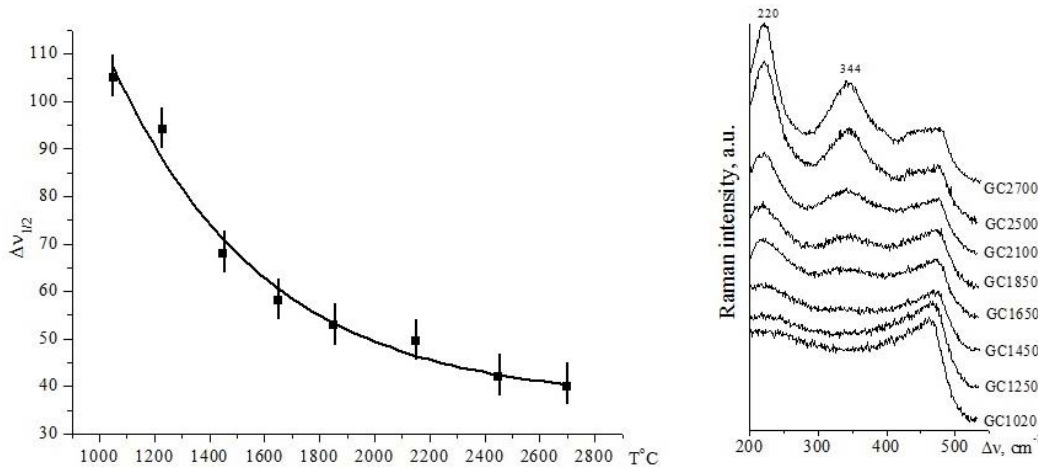


FIG. 3. Dependence of the D line half-width on the heat-treatment temperature

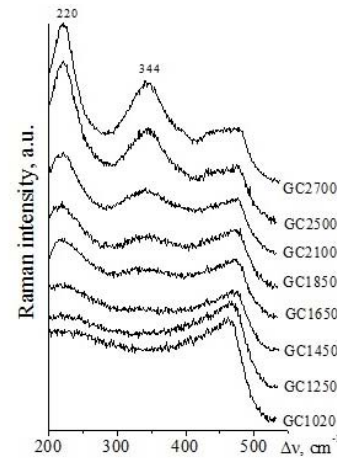


FIG. 4. Low frequency Raman region of the spectra obtained

Diffraction patterns of GC samples also evolve as the temperature increases (Fig. 2). The diffraction lines become narrower, the dominant 002 line slightly shifts to a larger scattering angle (to $2\theta \sim 25.5^\circ$), whereas the 110 line slightly shifts to smaller angles (Table 2).

All these changes clearly indicate that some ordering and an increase in effective crystallite size occurred with preservation of the graphite-like main structural motif.

To estimate dimensional characteristics of GC structural units, the X-ray diffraction data were used (a model approach with use of the Debye formula). The results are presented in Fig. 2, right panel.

Thus, both the X-ray and Raman data show that an increase in the heat-treatment temperature leads to a noticeable ordering of aromatic nanoclusters in directions parallel and normal to the graphene layers. However, the general structural motif, that is, poorly ordered turbostratic graphitic nano-particles is still preserved herewith. Gradual formation of a series of new low-frequency weak features in the Raman spectra suggests carbon layer curving which unfortunately has no distinct manifestation in the diffraction data.

TABLE 2. Changes in the profile parameters of 100 and 002 lines as a function of heat treatment temperature

Heat treatment temperature (°C)	FWHM of 100 line (°)	FWHM of 002 line (°)	Position of 002 line (°)
1020	4.2	7.7	23.97
1250	4.0	6.9	23.91
1450	3.2	5.8	24.58
1650	3.3	5.9	24.67
1850	2.9	5.2	24.92
2100	2.5	4.4	25.17
2450	2.5	3.9	25.21
2500	2.2	3.1	25.53
2700	2.4	2.8	25.34

Acknowledgements

The authors (S.S.B. and L.A.L.) acknowledge partial financial support from the Russian Foundation for Basic Research (# 13-03-00993).

References

- [1] IUPAC Recommended terminology for the description of carbon as a solid. *Pure and Appl. Chem.*, **67**, P. 474–506 (1995).
- [2] V.P. Sosedov, E.F. Chalykh. *Graphitization of carbon materials*. Metallurgy, Moscow, 176 p. (1987). [in Russian]
- [3] Carbon Materials for Advanced Technologies, ed. by Burchell T.D. Pergamon, Amsterdam, 535 p. (1999).
- [4] R. Franklin. The structure of graphitic carbons. *Acta Cryst.*, **4**, P. 253–261 (1951).
- [5] G.M. Jenkins, K. Kawamura, L.L. Ban. Formation and structure of polymeric carbons. *Proc. Roy. Soc. A*, **327**, P. 501–517 (1972).
- [6] L.A. Pesin, E.M. Baitinger. A new structural model of glass-like carbon. *Carbon*, **40**, P. 295–306 (2002).
- [7] P.J.F. Harris. Fullerene-related structure of commercial glassy carbons. *Phylos. Mag.*, **84**(29), P. 3159–3167 (2004). P.J.F. Harris. New perspectives on the structure of graphitic carbons. *Solid State Mater. Sci.*, **30**, P. 235–253 (2005).
- [8] P.M. Ossi, A. Miotello. Control of cluster synthesis in nano-glassy carbon films. *J. Non-Cryst. Solids*, **353**, P. 1860–1864 (2007).
- [9] R.C. Powles, N.A. Marks, D.W.M. Lau. Self-assembly of sp²-bonded carbon nanostructures from amorphous precursors. *Phys. Rev. B*, **79**, P. 075430 (2009).
- [10] T.C. Petersen, I.K. Snook, I. Yarovsky, D.G. McCulloch, B. O'Malley. Curved-surface atomic modeling of nanoporous carbon. *J. Phys. Chem. C*, **111**(2), P. 802–812 (2007).
- [11] F. Tuinstra, J.L. Koenig. Raman spectrum of graphite. *J. Chem. Phys.*, **53**, P. 1126–1130 (1970).
- [12] J.L. Lauer. Raman spectra of quasi-elemental carbon. In: Handbook of Raman Spectroscopy, ed. by Lewis I.R., Edwards H.G.M. Marcel Dekker Inc., N-Y, Basel, ch.22, P. 863–917 (2001).
- [13] A.C. Ferrari, J. Robertson. Interpretation of Raman spectra of disordered and amorphous carbon. *Phys. Rev. B*, **61**, P. 14095 (2000); Resonant Raman spectroscopy of disordered, amorphous and diamondlike carbon. *Phys. Rev. B*, **64**, P. 075414 (2001).
- [14] R.J. Nemanich, S.A. Solin. First- and second-order Raman scattering from finite-size crystals of graphite. *Phys. Rev. B*, **20**, P. 392–401 (1979).
- [15] R.P. Vidano, D.B. Fischbach, L.J. Willis, T.M. Loehr. Observation of Raman band with excitation wavelength for carbons and graphites. *Solid State Commun.*, **39**, P. 341–344 (1981).

- [16] A.V. Baranov, A.N. Bekhterev, Ya.S. Bobovich, V.I. Petrov. Interpretation of some peculiarities in the Raman spectra of graphite and glassy carbon. *Optics and Spectroscopy*, **62**(5), P. 1036–1041 (1987). [in Russian]
- [17] S.V. Kholodkevich, V.I. Beryozkin, V.Yu. Davydov. Peculiarities of the structure and temperature persistence of shungite carbon to graphitization. *Phys. Solid State*, **41**, P. 1291–1294 (1999); S.V. Kholodkevich, V.V. Poborchii. Raman spectra and enhanced stability of natural glassy carbon of shungites. *JETP Lett.*, **20**, P. 22–25 (1994).
- [18] A. Cuesta, P. Dhamelincourt, J. Laureyns, A. Martinez-Alonso, J.M.D. Tascón. Comparative performance of X-ray diffraction and Raman microprobe techniques for the study of carbon materials. *J. Mater. Chem.*, **8**, P. 2875–2879 (1998).
- [19] H. Wilhelm, M. Lelaurain, E. McRae, B. Humbert. Raman spectroscopic studies on well-defined carbonaceous materials of strong two-dimensional character. *J. Appl. Phys.*, **84**, P. 6552–6558 (1998).
- [20] S.S. Bukalov, L.A. Mikhailitsyn, Y.V. Zubavichus, L.A. Leites, Yu.N. Novikov. The study of the structure of graphites and some other sp^2 carbon materials by the methods of micro-Raman spectroscopy and X-ray diffractometry. *Mendeleev Chem. J.*, **1**, P. 83–91 (2006). [in Russian]
- [21] B.E. Warren. X-ray diffraction in random layer lattices. *Phys. Rev.*, **59**, P. 693–701 (1941).
- [22] B.E. Warren, P. Bodenstein. The diffraction pattern of fine particle carbon blacks. *Acta Crystallogr.*, **18**, P. 282–287 (1965).
- [23] P.H. Tan, S. Dimovsky, Yu. Gogotsi. Raman scattering of non-planar graphite: arched edges, polyhedral crystals, whiskers and cones. *Phil. Trans. R. Soc. Lond. A*, **362**, P. 2289–2310 (2004).
- [24] D. Roy, M. Chhowalla, H. Wang, N. Sano. Characterization of carbon nano-onions using Raman spectroscopy. *Chem. Phys. Lett.*, **373**, P. 52–56 (2003).

CARBON ENCAPSULATION OF MAGNETIC METAL NANOPARTICLES: CORRELATION BETWEEN NANOSCALE STRUCTURE OF CARBON MATRIX AND ELECTROMAGNETIC PROPERTIES

¹S. V. Kozyrev, ²V. I. Ivanov-Omskii, ²S. G. Yastrebov,
²T. K. Zvonareva, ²M. S. Chekulaev, ²A. V. Siklitskaya

¹ Center for Advanced Studies, St. Petersburg, Russia

² A.F.Ioffe Physicotechnical Institute RAS, St. Petersburg, Russia
SVKozyrev@spbcas.ru, Yastrebov@mail.ioffe.ru

PACS 81.05.ue

The dependence between the variation of microwave losses by $a - C : H(Co)$ films measured at 10 GHz and alteration of Co content in the film was investigated. It was shown that microwave losses attain maximal value at approximately 33at.% of cobalt. This dependence may be explained in terms of the formation of Co-containing clusters having various shapes. Because of property of conductive flakes to absorb microwaves, fragments of graphene modified with Co are considered as candidates for the microwave absorption. Estimations of the flake size using Raman and transmission electron microscopy data allow reproduce initial conditions for mathematical simulation of physical properties of the flakes.

Keywords: graphene, cobalt, intercalation, carbon, nanoclusters, encapsulation.

1. Introduction

Metal nanoclusters are promising materials for creation on their basis magnetic media for ultra-high density recording [1] and EM absorbers [2]. Methods for introducing metal clusters in a carbon matrix, also termed as “encapsulation”, are of two types (see, e.g., [3] and [4, 5]). In the first method, metallic clusters are encapsulated into carbon cages. In the second method, first developed in [4], nanoclusters are embedded into a matrix of amorphous carbon [4, 5]. This technique is less expensive, simpler and more effective than the first one [3] and compatible with thin film technologies for microelectronics. The ensembles of encapsulated clusters may show emerging quantum physical effects [6]. However, modification of hydrogenated amorphous carbon with Co is a more complex problem than encapsulation itself. That may be associated with modification of sp^2 part of amorphous carbon by metal [7]. In paper [7] modification of hydrogenated amorphous carbon with Co was performed by Raman spectroscopy that allows one to estimate mean size of graphene fragments. This observation is in a good agreement with sizes derived by transmission electron microscopy images [8], performed for the stacked graphene fragments that were termed in [8] as “graphite clusters”.

Actually, as one might expect for a relatively low concentration, Co atoms are stochastically scattering in the film and may interact with sp^2 constituent of the matrix not forming massive Co clusters. This sp^2 constituent consists of a set of grapheme plane fragments either embedded in an amorphous matrix and isolated from each other by spaces of amorphous material (sp^3 -bonded) or even forming a network percolating through the sample.

The valuable property of graphene fragments is the possibility to adsorb atoms that may occupy places above and below the planes. These atoms may form two-dimensional fragments of metallic surfaces that may absorb electromagnetic radiation. Actually, if a flake of graphene with adsorbed Co atoms may be formed, Co atoms may organize themselves in a fragment of two-dimensional Co layer attaching to a graphene fragment surface. At the same time classical electrodynamics predicts that two dimensional flakes (e.g. flat elliptical disks) may demonstrate a strong absorption of electromagnetic radiation through the mechanism of surface plasmon excitation. The absorption emerges at microwave frequency wavelengths for in-plane depolarization factor $L = 0$ that is typical for the flakes [9]. Thus, flat metallic particles may absorb microwaves of different polarizations, if the particles are randomly oriented in the volume of the sample. In this paper we revise the dependence of the microwave radiation losses on overall Co concentration for Co-modified films of a-C:H aiming explanation of this dependence.

2. Experimental

Films of $a - C : H(Co)$ were produced in our laboratory by simultaneous sputtering of graphite and cobalt targets by Argon (80%) -Hydrogen (20%) plasma in DC magnetron. The films were deposited on aramide tissue for microwave absorption experiments. Cobalt content was varied by a change of surface of sputtering Co target. Its concentration in the produced films was controlled by Rutherford backscattering method as previously described [7]. Microwave absorption experiments were performed using techniques published elsewhere [6].

3. Discussion and conclusions

We exploited previously published data for microwave absorption [6] for analysis as well as some unpublished data. The dependence of microwave losses measured at $10 GHz$ on Co content is presented in Fig.1. It is seen that the dependence attains a maximal value for a certain Co content, for approximately 33 at.%.

One may speculate that in the area of concentration of Co less than 33 at%, fragments of Co-modified graphene of limited size may exist and may work as absorber of microwaves through excitation of the surface plasmons. But it may mean that for bigger than 33at.% Co concentration, the formation mechanism for massive three dimensional clusters may dominate over mechanism of Co adsorption by graphene flakes. Quite naturally, for this case, the losses decrease with increased Co concentration, because the obvious change of the depolarization factor L varying from $L = 0$ for in-plane absorption by metal flakes (that corresponds to the absorption of microwaves) to $L = 1/3$ for spherical clusters (that corresponds to shift of maximum absorption of electromagnetic radiation from microwave to visual and ultraviolet regions [9]).

Thus, fragments of Co -intercalated graphene might be responsible for the absorption of microwaves. The hypothesis for the presence of the Co-modified graphene fragments in Co-doped amorphous carbon is consistent with the experimental data presented in [7]. The preliminary results published in [7] might be used for numerical investigation of physical properties of the fragments via *ab initio* methods. Moreover, TEM image analysis of amorphous carbon, together with analysis of Raman spectra of amorphous carbon modified with Co, provide us with some information about the mean diameter of a mean graphene fragment and mean number of hexagons constituting the fragment [7,8].

For further estimation, one may use a relation between mean number of atoms forming the fragment N and mean number of hexagons: $N = 2(2M + 1)$. If M fluctuates around 20,

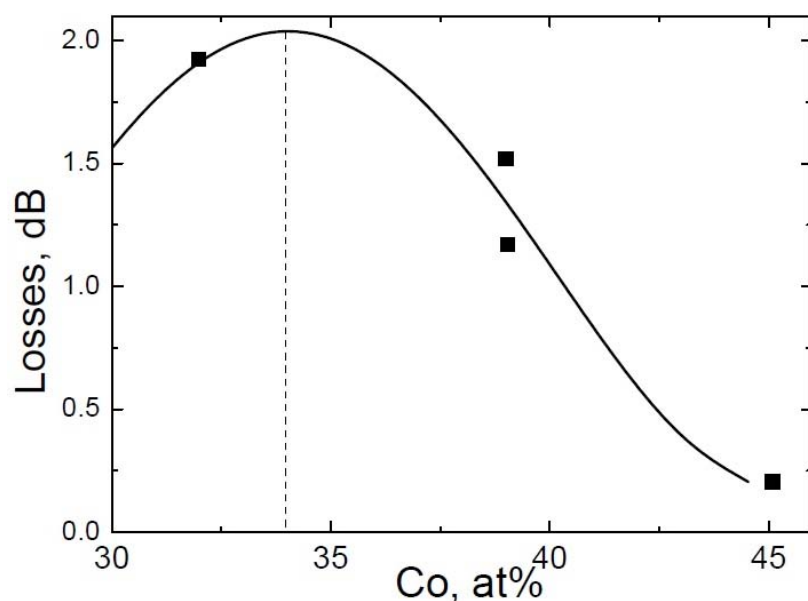


FIG. 1. Black squares stand for the dependence of losses of microwaves measured at 10 GHz on Co content for a-C:H(Co) samples. The curve shows the trend

therefore N oscillates near 82. For reconstruction of Co-intercalated fragment one may use number of Co atoms equal to number of hexagons.

Thus, the study performed predicts approximate initial conditions for mathematical simulation of fragments of graphene embedded in a matrix of hydrogenated amorphous carbon.

The dependence of microwave losses observed in Fig.1 may be explained exploiting concepts for the existence of conductive 2- dimensional graphene flakes and massive three dimensional Co clusters, contributing to the absorption for different Co concentrations.

References

- [1] T. Hayashi, S. Hirono, M. Tomita, S. Uremura. Magnetic thin films of cobalt nanocrystals encapsulated in graphite-like carbon. *Nature*, **381**, P. 772–774 (1996).
- [2] A. Alexeev, E. Shtager, S. Kozyrev. Physical Foundation of Stealth Technology. Saint-Petersburg.: VVM Ltd Publishing, 283 p. (2007).
- [3] E. Banhart, E. Hernandez, M. Terrones. Extreme superheating and supercooling of encapsulated metals in fullerene-like shells. *Phys. Rev. Lett.*, **90**, P. 185502/1–4 (2003).
- [4] V. I. Ivanov-Omskii, A. V. Tolmatchev, S. G. Yastrebov. Optical absorption of amorphous carbon doped with copper. *Philos. Mag. B*, **73**, P. 715–722 (1996).
- [5] V. I. Ivanov-Omskii, A. V. Kolobov, A. B. Lodygin, S. G. Yastrebov. Size distribution of cobalt nanoclusters in an amorphous carbon matrix. *Semiconductors*, **38**, P. 1416–1418 (2004).
- [6] L. V. Lutsev, S. V. Yakovlev, T. K. Zvonareva, A. P. Alexeyev, A. P. Starostin, S. P. Kozyrev. Microwave properties of granular amorphous carbon films with cobalt nanoparticles. *J. Appl. Phys.* **97**, P. 104327/1–6 (2005).
- [7] E. A. Smorgonskaya, T. K. Zvonareva, E. I. Ivanova, I. I. Novak, V. I. Ivanov-Omskii. One-Phonon Raman Spectra of Carbon in Composite Films prepared by modification of amorphous hydrogenated carbon by copper and cobalt. *Phys. Solid. State*, **45**, P. 1658–1668 (2003).
- [8] V. I. Ivanov-Omskii, A. A. Sitnikova, A. A. Suvorova, T. K. Zvonareva. Carbon clusters growth under ion sputtering of graphite. *Mol. Mat.* **8**, P. 99–102 (1996).
- [9] C.P. Bohren, D. Huffman. *Absorption and Scattering of Light by Small Particles*. Wiley, New York, 530 p. (1983).

USING ARTIFICIAL NEURAL NETWORKS FOR ELABORATION OF FLUORESCENCE BIOSENSORS ON THE BASIS OF NANOPARTICLES

S. A. Burikov^{*1}, S. A. Dolenko², K. A. Laptinskiy¹, I. V. Plastinin¹,
A. M. Vervald¹, I. I. Vlasov³, T. A. Dolenko¹

¹Moscow M. V. Lomonosov State University, Physics Department, Moscow, Russia

²D. V. Skobeltsyn Institute of Nuclear Physics, Moscow State University, Moscow, Russia

³General Physics Institute RAS, Moscow, Russia

burikov@lid.phys.msu.ru, dolenko@srd.sinp.msu.ru, laptinsky@lid.phys.msu.ru,
vervald@lid.phys.msu.ru, vlasov@nsc.gpi.ru, tdolenko@lid.phys.msu.ru

PACS 61.46.+w, 87.64.-t, 07.05.Kf, 87.85.fk

In this study, the results for the solution of the pattern recognition problem are presented — extraction of fluorescence contribution for carbon dots used as biomarkers from the background signals of natural fluorophores and the determination of relative nanoparticle concentration. To solve this problem, artificial neural networks were used. The principal opportunity for solution of the given problem was demonstrated. The used architectures for neural networks allow the detection of carbon dot-based fluorescence within the background of native fluorescent egg protein with sufficiently high accuracy (not lower than 0.002 mg/ml).

Keywords: fluorescence, carbon dots, biomarkers, egg protein, autofluorescence, artificial neural networks.

1. Introduction

One of the problems of modern biotechnologies is development of supersensitive methods for fast visualization of proteins, genes, cells. The latest achievements in the synthesis, bioadaptation and bioconjugation of nanoparticles has permitted the appearance of a new class of optical markers possessing properties capable of changing diagnostics and raise them to higher levels. Carbon dots and nanodiamonds relate to this new class of fluorescence biosensors, capable of replacing dye molecules traditionally used in biomedicine [1-4].

In spite of their ability to intensely fluoresce, organic dye molecules cannot be used for long-term *in vitro* and *in vivo* control because of fast photobleaching and cellular toxicity [5-7]. Quantum dots (QD) and nanodiamonds (ND) do not have these shortcomings. They have excellent photostability at room temperature and high quantum efficiency [1-4, 8]. Yet QD and ND have multi-functional surface which can be modified according to stated problems: for example functionalization of surface can increase biocompatibility of nanoparticles or reduce their cellular toxicity [8-11].

At the present time, the primary method for studying cellular processes is visualization using fluorescence. Background fluorescence represents a serious difficulty. This background fluorescence is the result of superposition of fluorescence bands from native tissue-based fluorophores in the range from 250 to 700 nm. The most important of these native fluorophores are tryptophan, phenylalanine, tyrosine, collagen, flavins and flavoproteins, beta-carotene, porphyrins, nucleic acids, vitamins, pigments etc [12, 13]. In Table 1 one can see optical characteristics for the mentioned native fluorophores of biomaterial.

TABLE 1. Optical characteristics of native fluorophores of biotissue [13]

Fluorophores	Absorption maxima	Emission maxima
collagen, elastin	325 nm	400 nm
Tryptophan	280 nm	350 nm
Tyrosine	275 nm	300 nm
Phenylalanine	260 nm	280 nm
Pyridoxine	324 nm	400 nm
NADH	260 nm	440 nm
Lipofuscin		430–540 nm
Eosinophils—circulating		440–550 nm

Autofluorescence significantly impedes the monitoring of ongoing processes and the motion of fluorescent nanoparticles. That is why the problem of separating the fluorescence signal of the nanoparticles-markers from the native fluorescence of biological tissue is very urgent. Currently, the problem of background fluorescence is solved either by experimental methods – in order to reduce the background signal, laser incident radiation is focused in very small volume [14] or by optimal choice of the nanoparticle’s properties and functionalization of their surface [10, 11, 15].

In this paper, a suggested means to solve the problem of separating nanoparticle fluorescence from the background native fluorescence of biomaterial is by the method of pattern recognition – by means of artificial neural networks [16]. Despite the very wide application of pattern recognition in biomedicine [17, 18], the authors of this paper are not aware of studies concerning the use of these methods to solve the problem of separating nanoparticle fluorescence from that of native biological tissue.

The aim of this work is the elaboration of a methodology using neural network algorithms to extract the optical response of a certain component of multi-component mixture from the background of overlapped optical responses of the other components.

2. Materials

Egg protein was used as biological tissue. Since the egg is a single cell, then such choice of bioobject excluded difficulties concerned with the introduction of nanoparticles into the cell.

It is known that nanoparticles synthesized via the oxidation of carbon materials have fluorescent properties, they are biocompatible, non-toxic and can be used as fluorescence biosensors [19–22]. In this study, biosensors were elaborated on the basis of carbon dots (CD) synthesized by oxidation of graphite with a mixture of sulfuric (95%) and nitric (68%) acids in a 3:1 ratio (CD were synthesized in International Technology Center, Raleigh, USA) [21].

In Fig. 1, Raman scattering (RS) and fluorescence (FL) spectra of an aqueous suspension of CD (0.01 mg/ml), egg protein and egg protein with introduced nanoparticles (concentration of CD in protein — 0.01 mg/ml) are shown. Excitation wavelength was 405 nm. Band with maximum near 470 nm corresponds to water RS valence band. Carbon dots fluoresce from 430 to 680 nm with a maximum near 500–505 nm (Fig. 1). The native fluorescence of egg protein represents a combination of an intense broad band from 430 to 730 nm with maximum near 480 nm and weaker bands with maxima of 640 nm, 655–660 nm and 675 nm. It follows from Fig. 1 and Table 1 that collagen, elastin, pyridoxine, NADF,

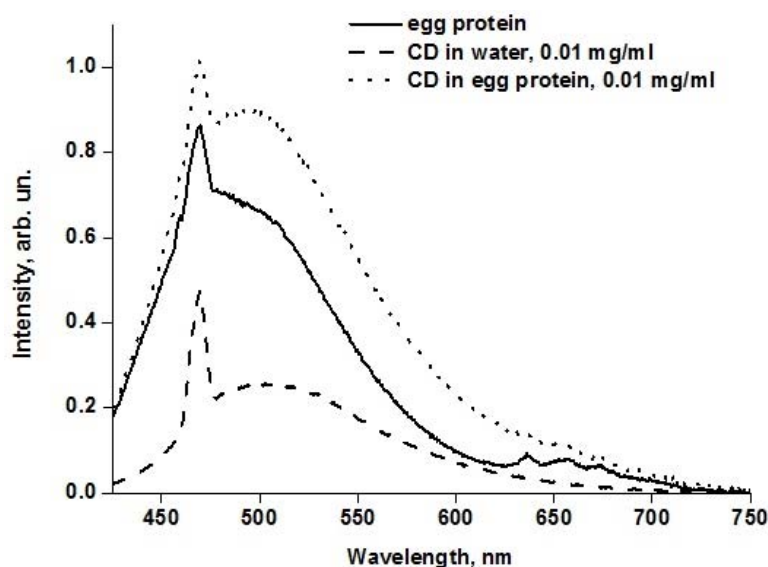


FIG. 1. Spectra of optical response of egg protein, suspension of CD in water and CD in egg protein under excitation at 405 nm

flavins and lipo-pigments make their fluorescence contribution in the main band of FL of egg protein. Weak bands near 640–670 nm are caused by porphyrin fluorescence.

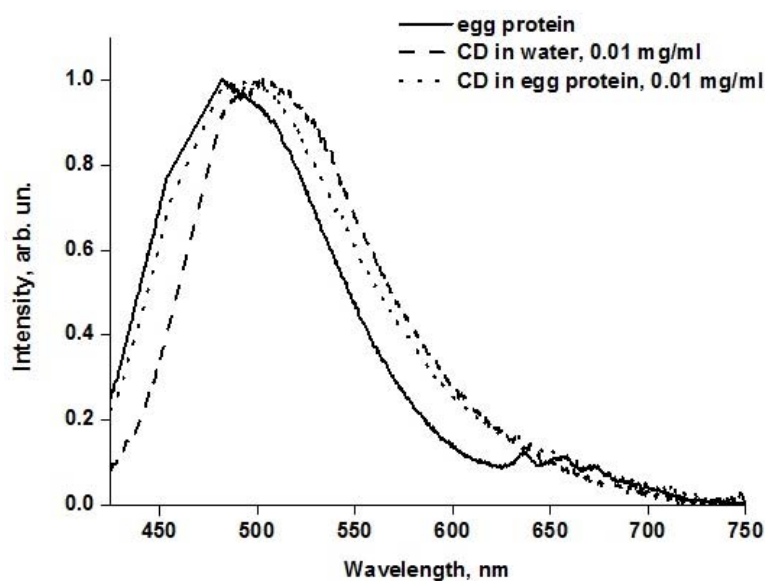


FIG. 2. Fluorescence spectra of egg protein, solution of CD in water and CD in egg protein. Water Raman valence band was subtracted, spectra were normalized by maximal intensity

Analysis of spectra shows that bands of CD fluorescence and egg protein strongly overlap but they differ by position of maximum (Fig. 2, Table 1). The FL spectrum of egg protein with introduced CD shows broad band from 400 to 730 nm with maximum near 490–495 nm (at CD concentration 0.01 mg/ml).

It is evident that the motion of nanoparticles in a biological object is among the processes exerting an influence on the intensity and shape of the nanoparticles' FL. At first, the concentration of CD changes and this changes the intensity of FL. Secondly, surface

functional groups on the nanoparticles interact with different components of biological tissues. These interactions are very complicated and are still far from being well understood, but they strongly change the FL of both native fluorophores and nanoparticles. Both significant quenching of the nanoparticles' FL and considerable intensification of FL are possible. That is why it is impossible to construct an analytical model for the change of total FL for egg protein and CD during the motion of nanoparticles in biomaterial. This means that it is impossible to directly solve the problem by usual mathematical methods, and therefore, the inverse problem of extracting the CD fluorescence contribution from the background of protein fluorescence during motion of nanoparticles in cells. In this study, algorithms of artificial neural networks (ANN) were used for the detection of CD fluorescence in the autofluorescence background of the protein.

3. Methods

ANN are widely used to solve problems of pattern recognition. ANN are class of mathematical algorithms showing very high efficiency during the solution of problems of intellectual data mining – problems of approximation, prediction, estimation, classification and pattern recognition. ANN are used for the solution of inverse problems because of their properties, e.g. training by example, high noise-immunity and resistance to contradictory data [16, 23].

In this study, the inverse problem was solved by ANN using an “experimental-based” — approach [24-26]. In this approach, experimental data are used for ANN training. The shortcoming of this approach is insufficient representativity of the data sets, since obtaining an immense amount of experimental material is incredibly tedious work. The main advantages of this approach are: the network is trained with real instrumental noise which raises the accuracy for inverse problem solutions, when ANN is trained directly on experimental data, all molecular interactions are taken into consideration [24-26]. This is very important for our problem, since the object of our research is living biological material whose condition can appreciably change as a result of long-term laser irradiation.

In this context, the following methods using ANN were elaborated in order to solve the stated inverse problem of optical biopsy:

1) Method for detection of CD fluorescence against the background of biotissue autofluorescence by fluorescence spectrum of the sample.

The considered problem is the simplest variant of a classification problem – determination of whether a pattern belongs to one of two non-crossing classes (nanoparticles present — no nanoparticles). A methodology for solving the problem of CD detection by their fluorescence in biological tissues would allow biomarker tracking and ensure targeted delivery of the biologically active supplements attached to the nanoparticle to the desired locations.

2) Method of determining the minimal CD concentration when the presence of nanoparticles is confidently detected against the background of proper biotissue fluorescence, i.e. determination of the threshold of sensitivity for the method as a whole.

3) Method for solving the inverse problem of nanoparticle concentration determination in biomaterials.

The considered inverse problem is rather complicated, but without its solution, the problem of drug delivery by fluorescing nanoparticles remains unsettled. In order to estimate the quantity of drugs or biologically active supplements delivered to the target receptors, it is necessary to determine concentration of nanoparticles that have reached their targets.

4. Experiment

Raman and FL spectra of egg protein with introduced CD were obtained using a laser spectrometer. For excitation of optical signal diode laser (wavelength 405 nm, incident power on the sample 50 mW) was used. Spectra were measured in a stepwise manner with registration by PMT from 430–750 nm. Spectral resolution was 0.5 nm. The temperature of samples during measurement was stabilized at 22.0 ± 0.1 °C. Spectra were corrected for laser power and accumulation time. Further mathematical processing of spectra consisted in subtraction of pedestal caused by elastic scattering of light in the cuvette with the sample, and normalization of spectra to the area of water Raman valence band.

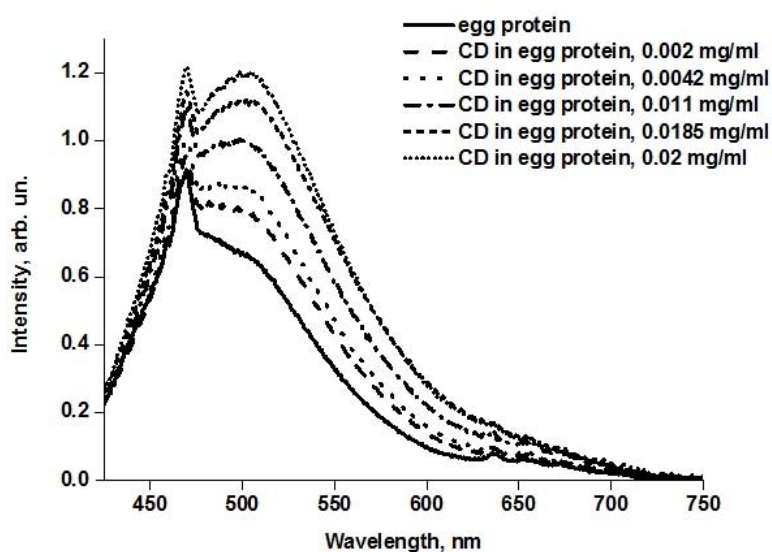


FIG. 3. Spectra of optical response of suspensions of CD in egg protein at different concentrations

Two series of RS and FL spectra were obtained in the experiment for two different egg proteins with introduced CD in the concentration range from 0 to 0.02 mg/ml with increments 0.00075 mg/ml. In Fig. 3, one can see some experimental RS and FL spectra for egg proteins with CD at different concentrations. The obtained data array was used to solve the stated inverse problem using ANN in the context of an “experimental-based” approach.

5. Use of ANN. Results and Discussion

To implement the “experiment-based” approach, both available series of experimental spectra were used: Series 1 (15 spectra in the CD concentration range from 0 to 0.02 mg/ml) and Series 2 (28 spectra in the same concentration range). All spectra in a series were obtained for the same protein, but different series were obtained for different proteins. That is why ANN was trained by data from Series 2, and Series 1 was used as independent data for examination of ANN and testing of its stability against change of protein.

All experimental data were divided into three sets: training (23 patterns), test (5) and examination (15). As the number of patterns was very small, 5 different divisions were used and quantitative results were averaged over all 5 divisions. Every division was performed in a regular manner (for example, every 5-th pattern in the order of increasing CD concentration was taken to the test set). The data of Series 1 were used as the examination set. So, operation of the obtained networks was assessed not just by independent data from

the same experiment, but by data from another experiment. This provided an estimate for the stability of the solution against changes in the object and experimental conditions.

The following adaptive algorithms were used to solve this problem: 1) Perception with one hidden layer, trained by the algorithm of error backpropagation [16]; 2) General regression neural network [23]; 3) Group method of data handling [27]. For all the calculations, software package NeuroShell 2 [28] was used.

TABLE 2. Values of the mean absolute error (MAE) of determination of CD concentration (in mg/ml) on various data sets for various algorithms of data processing

Algorithm \ Data set	Training	Test	Series 1
Perceptron	0.00034	0.00154	0.00405
GRNN, USF	0.00000	0.00164	0.00172
GRNN, ICSF	0.00000	0.00066	0.00176
GMDH	0.00064	0.00061	0.00584

In Table 2, the results obtained with the four described adaptive methods on three data sets (training, test, examination — Series 1) are presented. The results obtained on examination set are the most informative. The obtained results allow us to make the following conclusions.

1) Best results on examination set were demonstrated by both modifications of GRNN. Perceptron showed comparable results on training and test sets but turned out to be substantially less stable against changes in experimental conditions. This is demonstrated by the results obtained on examination set (Series 1).

2) As was expected, the worst stability was demonstrated by GMDH. With such a small number of patterns in the training array (28), the method can construct only very simple models showing sufficiently high results on the training array, but incapable of data generalization.

3) For both modifications of GRNN, mean absolute error on examination set (for Series 1) was about 0.0017 mg/ml (Table 2). This makes it possible to state that the minimum detectable CD concentration against the background of egg protein FL does not exceed 0.002 mg/ml.

The considered problem in its initial statement is characterized by the extremely unfavorable ratio of the number of patterns in the training set (23) and the number of input features (651). That is why the next direction of studies will be the consideration of algorithms which reduce the input dimensionality of the problem, i.e. reduce the number of data input features.

6. Conclusion

In this paper, the principle aim of solving the inverse problem of optical visualization — extraction of nanoparticle fluorescence from the background of an inherently fluorescent biological environment using neural network algorithms has been demonstrated. It has been shown that ANN allow the detection of CD fluorescence against the background of an inherently fluorescent egg protein with sufficiently low concentration threshold for detection (not greater than 0.002 mg/ml). It is worth noting that to obtain a contrasting image of nanoparticle fluorescence in living cells by confocal optical microscopy, the operating concentration of the aqueous suspension introduced into the cell may be 2 orders of magnitude higher than for the ANN method.

Acknowledgements

The authors of this paper wish to thank O. Shenderova from International Technology Center (North Carolina, USA) for the synthesis of CD. This work was supported in part by RFBR grants no. 12-01-31523-mol_a, 11-05-01160_a, 12-01-00958_a and 11-02-01432_a, the grant of RAS program no. 24, the grant of President of the Russian Federation for leading scientific schools no 3076.2012.

References

- [1] D. Ho (ed.). *Nanodiamonds, Applications in Biology and Nanoscale Medicine*. Springer, New York, 286 p. (2009).
- [2] J.-H. Liu, S.-T. Yang, X.-X. Chen, H. Wang. Fluorescent Carbon Dots and Nanodiamonds for Biological Imaging: Preparation, Application, Pharmacokinetics and Toxicity. *Current Drug Metabolism*, **13**, P. 1046–1056 (2012).
- [3] A.M. Schrand, S.A.C. Hens, O.A. Shenderova. Nanodiamond Particles: Properties and Perspectives for Bioapplications. *Critical Reviews in Solid State and Materials Sciences*, **34**, P. 18–74 (2009).
- [4] Y.Y. Hui, C.L. Cheng, H.C. Chang. Nanodiamonds for optical bioimaging. *J. Phys. D: Appl. Phys.*, **43**, P. 374021–374031 (2010).
- [5] C. Eggeling, J. Widengren, R. Rigler, C.A.M. Seidel. Photobleaching of Fluorescent Dyes under Conditions Used for Single-Molecule Detection: Evidence of Two-Step Photolysis. *Anal. Chem.*, **70**, P. 2651–2659 (1998).
- [6] A.M. Scutaru, A. Krüger, M. Wenzel, J. Richter, R. Gust. Investigations on the Use of Fluorescence Dyes for Labeling Dendrimers: Cytotoxicity, Accumulation Kinetics, and Intracellular Distribution. *Bioconjugate Chem.*, **21**, P. 2222–2226 (2010).
- [7] M. Haase, C.G. Hubner, F. Nolde, K. Mullen, T. Basche. Photoblinking and photobleaching of rylene diimide dyes. *Phys.Chem.Chem.Phys.*, **13**, P. 1776–1785 (2011).
- [8] V. Biju, T. Itoh, A. Anas, A. Sujith, M. Ishikawa. Semiconductor quantum dots and metal nanoparticles: syntheses, optical properties, and biological applications. *Anal. Bioanal. Chem.*, **391**, P. 2469–2495 (2008).
- [9] A.M. Schrand, H.J. Huang, C. Carlson, J.J. Schlager, E. Osawa, S.M. Hussain, L.M. Dai. Are diamond nanoparticles cytotoxic. *J. Phys. Chem. B*, **111**, P. 2–7 (2007).
- [10] E. von Haartman, H. Jiang, A.A. Khomich, J. Zhang, S.A. Burikov, T.A. Dolenko, J. Ruokolainen, H. Gu, O.A. Shenderova, I.I. Vlasov, J.M. Rosenholm. Core-shell designs of photoluminescent nanodiamonds with porous silica coatings for bioimaging and drug delivery I: Fabrication. *J. Mater. Chem. B*, **1**(18), P. 2358–2366 (2013).
- [11] N. Prabhakar, T. Nareoja, E. von Haartman, D.S. Karaman, H. Jiang, S. Koho, T.A. Dolenko, P. Haninen, D.I. Vlasov, V.G. Ralchenko, S. Hosomi, I.I. Vlasov, C. Sahlgren, J.M. Rosenholm. Core-shell designs of photoluminescent nanodiamonds with porous silica coatings for bioimaging and drug delivery II: Application. *Nanoscale*, **5**(9), P. 3713–3722 (2013).
- [12] M. Zellweger. Fluorescence spectroscopy of exogenous, exogenously- induced and endogenous fluorophores for the photodetection and photodynamic therapy of cancer. Thesis. Lausanne, Fevrier, 224 p. (2000).
- [13] R. Richards-Kortum, E. Sevick-Muraca. Quantitative Optical Spectroscopy for Tissue Diagnosis. *Annu. Rev. Phys. Chem.*, **47**, P. 555–606 (1996).
- [14] A.V. Feofanov. Spectral laser scanning confocal microscopy in biology researches. *Uspekhi biologicheskikh nauk*, **47**, P. 371–410 (2007) [in Russian].
- [15] J.M. Rosenholm, A. Penninkangas, M. Lindan. Amino-functionalization of large-pore mesoscopically ordered silica by a one-step hyperbranching polymerization of a surface-grown polyethyleneimine. *Chem. Commun.*, **37**, P. 3909–3911 (2006).
- [16] B.D. Ripley. *Pattern Recognition and Neural Networks*. Cambridge University Press, Cambridge, UK, 415 p. (1995).
- [17] E. Keedwell, A. Narayanan *Intelligent Bioinformatics: The Application of Artificial Intelligence Techniques to Bioinformatics Problems*. John Wiley&Sons Ltd, Chichester, UK, 294 p. (2005).
- [18] Yu.I. Neimark, Z.S. Batalova, Y.G. Vasin, M.D. Breido. *Pattern recognition and medical diagnostics*. Nauka, Moscow, 328 p. (1972) [in Russian].

- [19] R. Zhang, Y. Liu, L. Yu, Z. Li, S. Sun. Preparation of high-quality biocompatible carbon dots by extraction, with new thoughts on the luminescence mechanisms. *Nanotechnology*, **24**(22), P. 1-8 (2013).
- [20] L. Cao, X. Wang, M.J. Meziani, F.S. Lu, H.F. Wang, P.J.G. Luo, Y. Lin, B.A. Harruff, L.M. Vaca, D. Murray, S.Y. Xie, Y.P. Sun. Carbon Dots for Multiphoton Bioimaging. *J. Am. Chem. Soc.*, **129**, P. 11318–11319 (2007).
- [21] S.C. Hens, W. Lawrence, A.S. Kumbhar, O. Shenderova. Photoluminescent Nanostructures from Graphite Oxidation. *J. of Phys. Chem. C*, **116**, P. 20015–20022 (2012).
- [22] X. Sun, Z. Liu, K. Welsher, J.T. Robinson, A. Goodwin, S. Zaric, H. Dai. Nano-Graphene Oxide for Cellular Imaging and Drug Delivery. *Nano Res.*, **1**, P. 203–212 (2008).
- [23] D. Specht. A General Regression Neural Network. *IEEE Trans. on Neural Networks*, **2**(6), P. 568–576 (1991).
- [24] I.V. Gerdova (Boichuk), S.A. Dolenko, T.A. Dolenko, I.V. Churina, V.V. Fadeev. New approaches to solution of inverse problems of laser spectroscopy by the method of artificial neural networks. *Izvestiya RAS (seriya fizicheskaya)*, **66**(8), P. 1116–1124 (2002) [in Russian].
- [25] S.A. Dolenko, T.A. Dolenko, I.G. Persiantsev, V.V. Fadeev, S.A. Burikov. Solution of inverse problems of optical spectroscopy using of artificial neural networks. *Neurocomputers: elaboration and application*, **1-2**, P. 89–97 (2005) [in Russian].
- [26] S.A. Dolenko. Neural network based methods of solution of inverse problems. Proc. “Neuroinformatics-2013”: Lectures on Neuroinformatics. Moscow, Moscow Engineering Physical Institute, P. 214–269 (2013) [in Russian].
- [27] H.R. Madala, A.G. Ivakhnenko. *Inductive Learning Algorithms for Complex Systems Modeling*. CRC Press, 368 p. (1994).
- [28] <http://www.neuroproject.ru/aboutproduct.php?info=ns2info>



NANOSYSTEMS:

PHYSICS, CHEMISTRY, MATHEMATICS

Журнал зарегистрирован

Федеральной службой по надзору в сфере связи, информационных технологий и массовых коммуникаций

(свидетельство ПИ № ФС 77 - 49048 от 22.03.2012 г.)

ISSN 2220-8054

Учредитель: федеральное государственное бюджетное образовательное учреждение высшего профессионального образования «Санкт-Петербургский национальный исследовательский университет информационных технологий, механики и оптики»

Издатель: федеральное государственное бюджетное образовательное учреждение высшего профессионального образования «Санкт-Петербургский национальный исследовательский университет информационных технологий, механики и оптики»

Отпечатано в учреждении «Университетские телекоммуникации»
Адрес: 197101, Санкт-Петербург, Кронверкский пр., 49

Подписка на журнал НФХМ

На второе полугодие 2014 года подписка осуществляется через
ОАО Агентство «Роспечать»

Подписной индекс 57385 в каталоге «Издания органов научно-технической информации»